AALBORG UNIVERSITY
DENMARK

Contributions in Radio Channel Sounding, Modeling, and Estimation

Pedersen, Troels

Publication date:
2009

Document Version
Publisher's PDF, also known as Version of record

Link to publication from Aalborg University

Citation for published version (APA):
Pedersen, T. (2009). *Contributions in Radio Channel Sounding, Modeling, and Estimation* (1 ed.).

Contributions in Radio Channel
Sounding, Modeling, and Estimation

Contributions in Radio Channel Sounding, Modeling, and Estimation

Troels Pedersen

Ph.D. Thesis

Pedersen, Troels.
    Contributions in Radio Channel Sounding, Modeling, and Estimation

This Ph.D. thesis was defended January 12, 2009, at Aalborg University.

Assessment committee:
    Prof. Dr. Techn. Helmut Bölcskei, Swiss Federal Institute of Technology Zurich
    Prof. Dr. Sc. Techn. Pertti Vainikainen, Helsinki University of Technology
    Prof. Ph.D. Søren Holdt Jensen, Aalborg University (Chairman).

Supervisor:
    Prof. Dr. Sc. Techn. Bernard H. Fleury, Aalborg University.

Abstract

This thesis spans over three strongly related topics in wireless communication: channel-sounding, -modeling, and -estimation. Three main problems are addressed: optimization of spatio-temporal apertures for channel sounding; estimation of per-path power spectral densities (psds); and modeling of reverberant channels.

We develop a theory for optimization of spatio-temporal apertures used in multiple-input multiple-output (MIMO) channel sounding. Initially, we focus on joint estimation of bi-direction and Doppler frequency from time-division multiplexing (TDM) MIMO measurements. We introduce and analyze a bi-spatio-temporal ambiguity function for spatio-temporal channel sounding. The analysis reveals that by proper design of the spatio-temporal aperture, the maximum estimable Doppler frequency of a TDM-MIMO sounder is as high as that of a traditional single-input single-output sounder. We give the necessary and sufficient conditions for spatio-temporal apertures to minimize the Cramér-Rao lower bound on the joint bi-direction and Doppler frequency estimation. The spatio-temporal aperture also impacts on the accuracy of MIMO-capacity estimation from measurements impaired by colored phase noise. We present an improved capacity estimator, which exploits the second order statistics of the phase noise and the structure of the spatio-temporal aperture.

Next we turn to the problem of estimating the per-path psd resolved in directions and delay. We model the per-path psds using entropy maximizing probability density functions (pdfs); the pdfs are defined by their first- and second-order moments. We derive estimators of these parameters and illustrate their applicability on measurement data. The obtained spread estimates are significantly smaller, and the estimated psds are much more concentrated, than corresponding results from literature. These findings indicate that the per-path directional spreads (or cluster spreads) assumed in standard models are set too large.

Finally, we propose a model of the specular-to-diffuse transition observed in measurements of reverberant channels. The model relies on a "propagation graph" where vertices represent scatterers and edges represent the wave propagation conditions between scatterers. The graph has a recursive structure, which permits modeling of the transfer function of the graph. We derive a closed-form expression of the infinite-bounce impulse response. This expression is used for simulation of the impulse response of randomly generated propagation graphs. The obtained realizations exhibit the well-observed exponential power decay versus delay and specular-to-diffuse transition.

Dansk resumé

Denne Ph.D. afhandling omhandler tre stærkt forbunde emner: måling, modellering og estimering af radiokommunikationskanaler. Tre hovedproblemer behandles: optimering af rum-tid sampling i radiokanalmålesystemer, enkeltvis estimering af effektspektre af signalkomponenter i radiokanaler med flervejsudbredelse samt modellering af efterklangsfænomener.

Der udvikles en teori for optimering of rum-tid aperturer i multi-input multi-output (mimo) målesystemer. Der fokuseres først på samlet bestemmelse af dopplerfrekvens og udstrålings/indstrålings retninger ud fra tidsmultiplexede målinger af mimo kanaler. Derefter indføres en 'ambiguityfunktion' for dette estimeringsproblem. Analyse af ambiguityfunktionen viser, at den højeste dopplerfrekvens, der kan bestemmes entydigt, afhænger af rum-tid aperturet. Ved passende design af målesystemets rum-tid apertur er den øvre grænse for den estimerbare dopplerfrekvens for mimo systemer lige så høj som for traditionelle målesystemer med en sender- og en modtagerantenne. Der gives den nødvendige og tilstrækkelige betingelse for, at et givet rum-tid apertur minimerer Cramér-Rao begrænsningen på doppler-retnings bestemmelse. Rum-tid aperturet har også indflydelse på hvor nøjagtigt mimo-kanalkapaciteten kan estimeres når målesystemets fasestøj tages i betragtning. Ved at udnytte kendskab til fasestøjens autokorrelationsfunktion og strukturen af rum-tid aperturet, udledes en forbedret kapacitets estimator.

Dernæst behandles estimering af sprednings egenskaber for udbredelsesveje i et miljø med flervejsudbredelse. Effektspektret for en udbredelsesvej modelleres ved hjælp af en entropi-maximerende fordelingsfunktion (pdf). Denne pdf er givet ved det første og andet moment, for hvilke en estimator udledes. Estimatorens anvendelighed illustreres ved brug af måledata. De opnåede spredningsestimater er væsentligt mindre end tidligere publicerede estimater, hvor traditionelle metoder er anvendt. Estimeringsresultaterne indikerer, at signalspredningen for de enkeltvise signalveje kan være overvurderet i standardiserede radiokanalmodeller.

Til slut opstilles en model for overgangen fra separate til diffuse signalkomponenter som kan observeres i målinger af radiokanaler med efterklang. Modellen bygger på en 'udbredelsesgraf', hvori punkter repræsenterer objekter i udbredelses miljøet, og kanter repræsenterer bølgeudbredelsen mellem objekter. Der udledes et udtryk for grafens overføringsfunktion, der gælder for signalkomponenter der udbredes via et vilkårligt antal interaktioner. Overføringsfunktionen anvendes til simulering af impulsresponset af stokastisk genererede udbredelsesgrafer. Impulsresponserne udviser den førnævnte overgang fra separate til et diffust signalbidrag.

Preface

This thesis is submitted to the International Doctoral School of Technology and Science at Aalborg University, Denmark, in partial fulfillment of the requirements for the degree of doctor of philosophy. Chapters 1–4 provides an introduction and brief description of the contributions of the thesis. The main body consists of ten papers referred to as Paper A–Paper J published in peer-reviewed conferences and journals listed at pp. xv–xvi. The work has been carried out during the period September 2004 – August 2008 at the Department of Electronic Systems, Aalborg University. It has been supported in part by Elektrobit and in part by the project ICT-217033 Wireless Hybrid Enhanced Mobile Radio Estimators (WHERE). Parts of the work have been performed within the ICT-216715 FP7 Network of Excellence in Wireless COMmunication (NEWCOM++) and its predecessor NEWCOM.

Numerous people have in one way or another inspired my curiosity and encouraged me to pursue the study of radio communications. I am grateful to the members of the radio amateur club in Svendborg (OZ7FYN E.D.R. Svendborg Afdeling) who spurred my interest in radio communications. The first semester at Aalborg University took part in a student project on radio channel modeling supervised by the, now retired, Associate Professor Johan Brøndum. After completing the present thesis on the same topic, I can but admire his bravery of teaching the topic to freshmen!

As I flew to Dallas to present Paper A at the Globecom 2004 conference, I experienced a striking example of the unforeseeable nature of inspiration. It was my first conference and, in fact, my first trip outside Europe. It was a long flight Aalborg-Billund-Frankfurt-Dallas. At the boarding counter in Frankfurt airport, I had to answer a questionnaire about my profession, the purpose of the journey, etc. I handed in the filled-out form to a lady with a prominent smile. She briefly checked my answers and informed me that she had a few questions. 'Why are you going to USA?' she asked; 'I am going for a conference', I answered. 'What is the name of the conference?' was her next question. Mildly annoyed, I told her politely that I already gave her that information in the questionnaire. My answer did not please her, but she kept smiling. After a dozen questions, she concluded her interrogation by the asking:

> 'Can you please tell me, in layman's terms, what the topic of the paper you are going to present at the conference is?'

Her question took me by surprise. However simple the question was, I realized that answering it was not so easy. How do one explain the topic of optimi-

ix

zation of spatio-temporal apertures in channel sounding in layman's terms? I decided not to—*in lieu*, I attempted to explain what channel sounding is. After a moment of though I replied:

> 'Well, If you go down in your basement and shout "Hello" as loud as you can, you hear an echo.'

'Yes', she said, still smiling. I continued:

> '…and if you shout "Hello" in your living room, the echo sounds different.'

'Yes it does' she said and nodded heavily. I carried on;

> 'I shout "Hello" with radio waves and listen to the echo.'

The lady now smiled more than ever and replied in an excited high-pitched voice:

> 'Oooh! That's a *very* good explanation—*I* understood everything perfectly!'

Although I didn't answer her question exactly, I was allowed on board the flight to Dallas. The conference went well. I would like to thank that lady from American Airlines; her question inspired my further study of the analogy between acoustical and electromagnetic wave propagation and in turn inspired me to the radio channel model in Papers I and J of this thesis.

I wish to express my gratitude and thanks to my supervisor Professor, Dr. sc. techn. Bernard H. Fleury for providing me supervision and guidance of the past years. I deeply admire his persevering pursuit of the highest scientific standards. I also want to acknowledge my present and former colleagues and fellow PhD students at Aalborg University: Thomas Arildsen, Kazimieras Bagdonas, Mads Græsbøll Christensen, Joachim Dahl, Bin Hu, Jesper Højvang Jensen, Gunvor Elisabeth Kirkelund, Morten Holm Larsen, Hans Laurberg, Michael Nielsen, Laust Olsen, Romain Piton, Darius Plausinaitis, Steffen Præstholm, Christoffer Rødbro, Gerhard Steinböck, and Karsten V. Sørensen for many pleasant and inspiring discussions. I would like to direct a special thanks to my friend and former colleague Xuefeng Yin for the countless discussions of technical and non-technical nature. I will never forget his enthusiastic and curious approach to research, which I highly appreciate.

Last, but not least, I thank my friends and family, but most of all Mette, for her priceless help, understanding, and support.

<div align="right">

Troels Pedersen
Aalborg, December 2008

</div>

Contents

List of Papers

The main body of this PhD. thesis consists of the following ten papers:

Paper A T. Pedersen, C. Pedersen, X. Yin, B. H. Fleury, R. R. Pedersen, B. Bozinovska, A. Hviid, P. Jourdan, and A. Stucki, "Joint estimation of Doppler frequency and directions in channel sounding using switched Tx and Rx arrays," in *Proc. IEEE Global Telecommun. Conf. (Globecom)*, Dec. 2004.

Paper B T. Pedersen, C. Pedersen, X. Yin, and B. H. Fleury, "Optimization of Spatiotemporal apertures in channel sounding," *IEEE Trans. Signal Process.*, vol. 56, no. 10, pp. 4810–4824, Oct. 2008.

Paper C T. Pedersen, A. Taparugssanagorn, J. Ylitalo, and B. H. Fleury, "On the impact of TDM in estimation of MIMO channel capacity from phase-noise impaired measurements," in *Proc. Int. Zurich Seminar on Commun. (IZS)*, Mar. 2008.

Paper D T. Pedersen, X. Yin, and B. H. Fleury, "Estimation of MIMO channel capacity from phase-noise impaired measurements," in *IEEE Global Commun. Conference (IEEE Globecom)*, New Orleans, USA, Nov.–Dec. 2008.

Paper E X. Yin, T. Pedersen, N. Czink, and B. H. Fleury, "Parametric characterization and estimation of bi-azimuth dispersion of path components," in *Proc. IEEE Int. Workshop on Signal Processing Advances for Wireless Commun. (SPAWC)*, Nice, France, July 2006.

Paper F X. Yin, T. Pedersen, N. Czink, and B. H. Fleury, "Parametric characterization and estimation of bi-azimuth and delay dispersion of path components," in *Proc. European Conf. on Antennas and Propagation (EuCAP)*, Acropolis, Nice, France, Nov. 2006.

Paper G X. Yin, L. Liu, D. Nielsen, T. Pedersen, and B. Fleury, "A SAGE algorithm for estimation of the direction power spectrum of individual path components," in *Proc. IEEE Global Telecommun. Conference (Globecom)*, Nov. 2007.

Paper H X. Yin, L. Liu, T. Pedersen, D. K. Nielsen, and B. H. Fleury, "Modeling and estimation of the direction-delay power spectrum of the propagation channel," in *Proc. International Symposium on Communications, Control and Signal Processing ISCCSP*, Mar. 2008.

Paper I T. Pedersen and B. H. Fleury, "A realistic radio channel model based on stochastic propagation graphs," in *Proc. 5ᵗʰ Vienna Symposium on Mathematical Modelling (MATHMOD)*, vol. 1,2, Feb. 2006, ISBN 3–901608–30–3.

Paper J T. Pedersen and B. H. Fleury, "Radio channel modelling using stochastic propagation graphs," in *Proc. IEEE International Conference on Communications (ICC)*, June 2007.

Additionally, the following papers were co-authored by Troels Pedersen during his PhD. studies:

Paper 1 X. Yin, B. H. Fleury, T. Pedersen, and J.-P. Nuutinen, "Azimuth spread estimation for slightly distributed scatterers using the generalized array manifold model," in *Proc. IEEE 16th International Symposium on Personal, Indoor and Mobile Radio Commun. (PIMRC)*, vol. 1, 2005, pp. 604–608.

Paper 2 J. Figueiras, T. Pedersen, and H.-P. Schwefel, "Wireless positioning based on a segment-wise linear approach for modeling the target trajectory," in *IEEE Global Commun. Conference (Globecom)*, New Orleans, USA, Nov.–Dec. 2008.

Paper 3 X. Yin, T. Pedersen, G. Steinböck, G. E. Kirkelund, P. Blattnig, A. Jaquier, and B. H. Fleury, "Tracking of the multi-dimensional time-variant parameters of a target signal using particle filtering," in *Proc. IEEE Radar Conference*, Rome, Italy, May 2008.

Paper 4 X. Yin, G. Steinböck, G. E. Kirkelund, T. Pedersen, P. Blattnig, A. Jaquier, and B. H. Fleury, "Tracking of time-variant radio propagation paths using particle filtering," in *Proc. IEEE International Conference on Commun. (ICC)*, May 2008, pp. 920–924.

Paper 5 G. Lechner, T. Pedersen, and G. Kramer, "Exit chart analysis of binary message-passing decoders," in *IEEE International Symposium on Information Theory*, June 2007, pp. 871–875.

Introduction and Motivation

Radio communications is an indispensable technology of a modern society. Its applications range from pure convenience, such as the remote keys for cars, to the essential mobile communications for emergency use. Radio communications is naturally applied when wired communication is impractical (*e.g.* in mobile telephony) or impossible (*e.g.* data transfer from the ground to aircraft or satellites). Radio communication systems exist for nearly any range; from cable replacement in the so-called personal area networks to communications between the Earth and distant space probes.

A radio communication system consists of one or more transmitters which create a dynamic electromagnetic field, and one or more receivers away from the transmitters sensing the electromagnetic field. The field at the receiver is to some degree related to the emitted field. Thus, provided acceptable propagation conditions exist, one may encode information in the field emitted at the transmitter and recover parts of this information by sensing the field at the receiver. Obviously, the engineering of a radio communication system relies on specified requirements to the system, such as the type of information to be transmitted, the required quality and reliability of the transmission, *etc.* These specifications are, however, insufficient by themselves to guarantee successful design of a communication system. In addition to these predefined requirements, invention, design, testing, and optimization of radio communication systems rely heavily on knowledge of the relation between the electromagnetic field generated at the transmitter and the sensed field at the receiver site. Thus, knowledge of this relation is a prerequisite for the engineering of modern wireless communication systems.

For the purpose of studying or designing communication systems, it brings great conceptual simplification to model such a system as a collection of basic constituents as depicted schematically in Fig. 1.1: the transmitter, the transmit antennas, the receive antennas, the receiver, and the propagation environment. The transmitter generates the input (vector) signal $\mathbf{x}(t)$ (the voltage or current) applied to the input ports of the transmitter antennas. The transmitter antennas excite an electromagnetic wave which propagates throughout the environment. As the electromagnetic wave reaches the receiver antennas, it induces a signal $\mathbf{y}(t)$ (voltage or current) at their output ports. We define the *radio channel* as the system where the input signal $\mathbf{x}(t)$
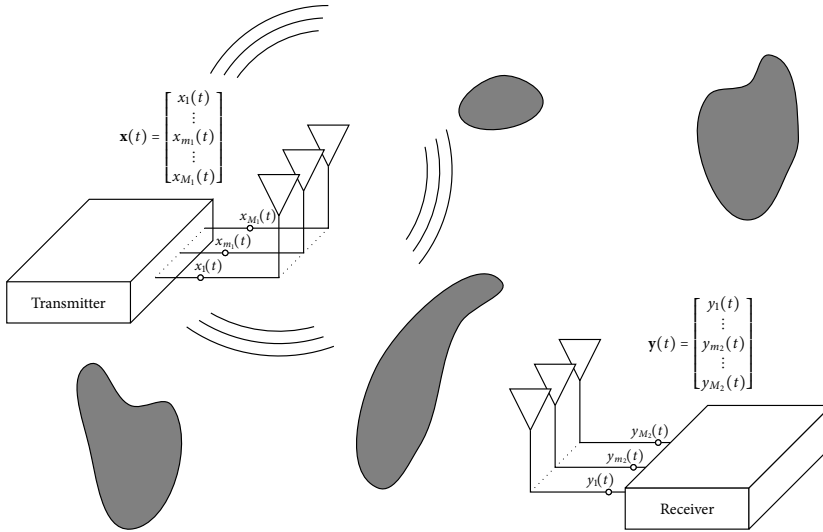
Fig. 1.1: A radio communication system with M_1 transmit antennas and M_2 receive antennas. The transmitter applies the signal $\mathbf{x}(t)$ to the inputs of the transmit antennas. Thereby the antennas emit an electromagnetic field which propagates through the environment and interacts with obstacles illustrated by the gray objects. Away from the transmitter, the field induces the signal $\mathbf{y}(t)$ at the outputs of the receive antennas.

is applied and the output $\mathbf{y}(t)$ is observed, *i.e*, from the input of the transmit antenna array to the output of the receive antenna array. The problem at hand is to obtain knowledge on the radio channel necessary for designing, testing, or optimizing wireless communication systems.

In the remainder of this chapter we define and motivate the key crafts of radio channel characterization: channel *sounding*, *modeling* and *estimation*. In Section 1.1 the interconnections between these three crafts are outlined. We further detail their definitions and purposes in Sections 1.2–1.5.

1.1   Channel Characterization: The Trinity of Sounding, Estimation, and Modeling

The problem of radio channel characterization consists of three mutually dependent crafts: *sounding*, *modeling*, and *estimation*. As summarized in Fig. 1.2, various kinds of information are exchanged between these three crafts. In the following we discuss these three crafts and the exchanged information in further detail.

In *channel sounding* channel measurements are performed by applying a known signal to the transmit antennas and observing the output signal of
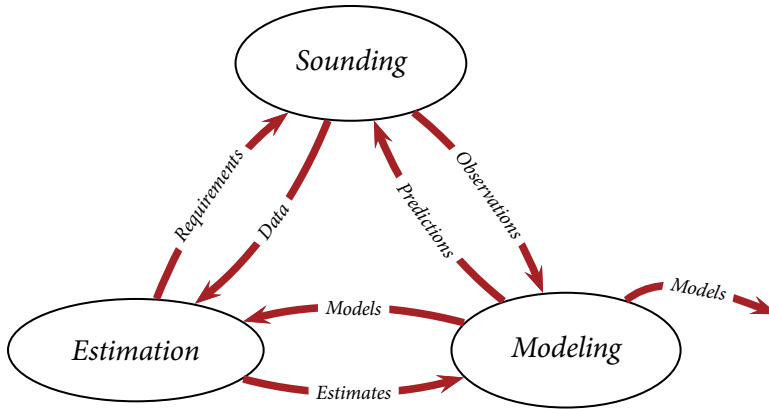
Fig. 1.2: *The trinity of channel characterization: sounding, modeling, and estimation.*

the receive antennas. Since the transmitted signal is known, information on the relation between the transmitted and received signals can be gathered. The output of channel sounding is the measurement data. It is sometimes possible to observe a phenomenon directly from the measurement data. These observations may then inspire the channel modeling process. The design and planning of experiments relies on *a priori* information. This information allows for the planner to decide upon which antennas to apply, which scenario to investigate, at which frequency to transmit, *etc*. The information takes the form of predictions of phenomena of interest, and specification of the measurement settings required to obtain the necessary estimation accuracy.

Channel modeling is the craft of creating (mathematical) representations or descriptions of the radio channel. Models can be based on theoretical considerations as well as on measurements. The models give, however, only approximate descriptions of the propagation conditions, and thus, there is no guarantee that their predictions hold true. One main objective of modeling is to organize available information about the channel in a form useful for the design of communication systems. This process relies on channel observations and estimates of model parameters. The design of estimators thus naturally depends on the models.

Channel estimation is concerned with extracting parameter values from channel measurements.[1] To do so, estimators of the considered model parameters must be developed. The input data to a channel estimator is the measurement data. To allow for a certain precision of the parameter estimates,

---

[1] We are here concerned only with channel estimation for the use in channel sounding and modeling, and not with channel estimators for receiver algorithms.

the estimator requires certain properties of the measurement data. This can be requirements on the measurement design, the type of measurement signal, the measurement bandwidth, *etc.*

The end-result of the channel characterization process is the knowledge gained about the features of the channel, which is essential for system design. This knowledge may be qualitative or quantitative information on the observed phenomena. This information is often conveyed in form of a channel model. As previously stated, the system developer relies on this information for the design of radio communication systems. The knowledge allows the system designer to approach the questions of "how can the observed phenomena be exploited", "how can the best performance of the communication system be achieved", and "what is the performance of the system". It should, however, be kept in mind that *none* of the three crafts of *sounding*, *modeling*, or *estimation* are directly relevant to the designers of radio communication systems; only the outcome of the process, *i.e.*, the model, is.

1.2 Definition of a (Mathematical) Model

In this thesis we will frequently use mathematical models. It is therefore worthwhile to define the concept of a (mathematical) model. We first give a definition of this concept and then refine the definition to the particular case of a mathematical model. There are numerous definitions of the concept of a "model" available in the literature. The interested reader is referred to [1–3] for further examples of definitions. The following definition will serve as an outset for our subsequent discussion of radio channel models:

Definition 1.2.1 (Model): *A model is a representation of a part of the real world created for a particular purpose.*

This definition is inspired from the definitions given in the references [1] and [2]. Definition 1.2.1 consists of three basic components[2]:

Purpose: The purpose of a model.

Scope: The part of the real world which the model is supposed to represent.

Formulation: The type of representation used in the model.

Of these three components, the purpose is the most fundamental: it can be well-defined without having a scope or a formulation in mind. On the contrary, it is meaningless to settle upon a scope unless we know what the purpose of the model is; nor is it sensible to formulate something we do not know what it is. To some extent, the purpose dictates the scope and

---

[2]In the references [1] and [2] only the "purpose" is discussed; the "scope" and "formulation" are not discussed in relation with the definition of a model.

determines, at least partly, the type of formulation. A model is evaluated with respect to its purpose [2]: To evaluate a model one must answer the question "Does the model suit the purpose?" A model well-suited for a specific purpose might render completely useless for another.

The representation can take different forms: Architects often use cardboard, whereas physicists and engineers frequently use mathematical representations. Since we are solely interested in mathematical models of radio communication channels, a further precision of the concept of a mathematical model is beneficial. We shall adhere to the definition from [1]:

Definition 1.2.2 (Mathematical model): *A mathematical model is an abstract, simplified mathematical construct related to a part of reality and created for a particular purpose.*

Compared to Definition 1.2.1, Definition 1.2.2 has been delimited to mathematical models; the basic components (purpose, scope, formulation) remain. For reasons of brevity, we use the term "model" for "mathematical model" throughout.

1.3 Purposes of Radio Channel Models

Channel models for radio communications are used for (at least) three different purposes:

1. for the *study* of propagation effects,

2. for the *design* of communication systems, and

3. for the *simulation* of communication systems.

This observation suggests that models may be categorized according to their purpose as respectively *study*, *design*, and *simulation models*.

Study models are used as tools to better understand the propagation phenomena governing the radio channel. Understanding the impact of propagation effects is useful to a system designer—without this understanding the designer has no clue of the existence of propagation phenomena which should be mitigated or could possibly be exploited. Often the models are inspired by measurements or by simplifications of Maxwell's theory of electromagnetism [4, 5]. The scope of a model falling into this category naturally depends on the particular phenomenon of interest and thus numerous different types of formulations exist. Since their purpose is to help the understanding of phenomena, study models are evaluated on their explanatory qualities, analytic simplicity, and prediction accuracy. There are numerous study models throughout literature, of which we give two examples. In the seminal work [6], Clarke proposes a model for studying the correlation properties of the

received signal envelope. Our second example is the more recent model by Franceschetti [7], which describes the effect of environment parameters on the delay-power spectrum.

Design models are the mathematical models assumed in the design of communication systems. These models form the basis for analytical treatment of (parts of) the communications systems to be designed. Communication systems are usually complex enough by themselves. Hence analytic simplicity is crucial for design models. But the models should still represent, at least in a simplistic way, the specific phenomena considered. Typically design models are inspired and/or justified by a certain study model. Illustrative examples can be found in the development of detection/demodulation algorithms, which relies on simplified channel models. The models used in the design of narrow-band receivers include the additive white Gaussian noise channel, and the Raleigh fading channel [8, 9].

Simulation models are used to evaluate the performance of (parts of) a communication system by simulation. Performance measures, like bit-error-rates, are in most cases intractable for mathematical analysis [8]. To evaluate the performance of communication systems we must, therefore, resort to numerical methods. It is common practice to perform numerical simulations using various Monte Carlo methods [10]. To this end, stochastic simulation models of the radio channel are necessary. Obviously, one could use a simulation model with the same assumptions as the design model. This provides a test whether the design is good *if the model assumptions hold true*. But such a test cannot be used as an indication of how the equipment performs in a real-world scenario. Another option is to use a more realistic model to test the equipment. A simulation model therefore has (at least) two conflicting objectives: it should 1) mimic the propagation mechanisms accurately, and, as a great number of model realizations are necessary, 2) have low computational complexity. An early example of a simulation model is the model by Jakes [11], which is essentially a simulation version of the model by Clarke [6]. A more recent examples include the bi-directional simulation models [12–14]. Most standardized models, such as the 3GPP [15], WINNER [16], COST 259 [17, 18], and IEEE 802.16 [19] are simulation models.

Considering the mutually contradicting requirements to a model dictated by the above model purposes, it is evident that no single model can satisfy them all. Consequently, the literature on radio channel models is rich on models for various purposes, scopes, and formulations.

Commonly, users of channel models work in fields of communication engineering. The users may be experts in the field of receiver design or testing. Naturally those engineers are specialists within their field, but cannot be expected to have expertise in the creation of channel models too. The users

of channel models must chose among the great many existing models to find one *suiting their purpose*. One cannot expect these engineers to read detailed scientific papers on the development and validation of specific models. *In lieu*, to choose an appropriate model, they may rely on textbooks, tutorials, reviews, or surveys written by channel modeling experts. A number of such overviews exists in papers (*e.g.*, [20–27]) and books (*e.g.*, [28–36]). It appears, however, that none of these overviews base their approach on a *definition* of the model concept—at least none of the publications [20–36] states their definition. Instead, the most often followed the procedure is to categorize models according to the phenomena which they describe, or which assumptions they rely on. As a result, different models are compared with respect to their computational complexity, disregarding their purposes. To a channel modeling expert this might be of minor concern; but to the non-expert such approaches may lead to an unbalanced view of the virtues and shortcomings of models.

1.4 Purposes of Channel Sounding

Why do we perform measurements of the radio channel? Parsons [28, p. 221] states two objectives:

> "It is often of interest to make measurements which shed some light on the propagation mechanisms that exist in the radio channel but engineers are usually more interested in obtaining parameters that can be used to predict the performance, or performance limits, of communication systems intended to operate in the channel."

The two different objectives can be reformulated as: 1) *gaining insight into the propagation mechanisms* and 2) *to extract model parameters from measurement data*. Objective 1 is a matter of extracting knowledge of the channel through measurements. However, scientific knowledge can only be gained by use of a proper scientific method [37]. This method requires according to [37] a separation between the *hypothesis statement* and the *hypothesis test*. Therefore, the first objective contains *two* purposes: one is to make observations and to state hypothesis; another is to test the hypothesis, or in model terms, to *validate* the model. Objective 2 is a matter of estimation of model parameters from the measurement data. We call this procedure *"model calibration"*. In addition to these three purposes, it is often necessary to evaluate the applicability of estimation algorithms using measurement data.

We therefore find it useful to distinguish between four different purposes of channel measurements:

Observation of propagation phenomena: The measurement data can be used for observing new propagation phenomena. Such observations are essential to the statement of new hypotheses in the form of study models.

Model validation: It is usually possible to predict phenomena from a study model. It is thus a natural validity test to design experiments specifically with the purpose to check if the predictions hold true.

Model calibration: According to the discussion of the purposes of radio channel models in Section 1.3, simulation models are generally designed from available study models. The settings of these parameters are sometimes known from the description of the intended propagation environment. It is, however, often necessary to "calibrate" a model by estimating parameter values from measurement data.

Test of estimation algorithms: When testing parameter estimators it is often necessary to assess whether the estimation methods are robust enough to be used for real measurements. To this end, it is necessary to use a set of measurement data to test, and possibly adjust, the implementation of the estimators.

Due to a number of reasons, measurement campaigns are seldom made—and almost never used—for a single purpose only. Measurement campaigns are time-consuming and expensive. They are therefore usually planned for multiple purposes. Another reason is that propagation phenomena are often discovered while testing estimators or during model calibration and validation. This process is quite natural and cost-effective. There is, however, a caveat: to observe a phenomenon from a set of data, create a model to fit these data, and thereafter to use the same set of data to validate the model is a circular argument [37] which potentially leads to erroneous conclusions. An excellent example of how to avoid this problem is the contribution by Turin *et al.* [38]: The authors first state an initial model (*i.e.* their hypothesis), then perform the measurements, validate the model, and finally, inspired by observations made while validating their initial model, propose a revised model (*i.e.* a new hypothesis). The revised model is not validated with the same measurement data. Instead, its validation is left to future measurement campaigns.

1.5   *Purposes of Channel Estimation Algorithms*

The purpose of channel estimation algorithms can be defined in a more straightforward manner compared to the previous discussion of modeling

and sounding. The purpose of a channel estimation algorithm is to extract values for model parameters from measurement data. Parameters estimates are necessary for model validation, where estimates are compared to the predictions of a model. Similarly, they are used for model calibration, where parameters of a model are determined from calibration measurements.

As an example of the estimation process, we consider the parameter estimation of a probabilistic channel model. Let us consider the case where we have made a measurement and recorded the observation data d. Now, we state a model for d and make the *assumption* that d is an outcome $d = Z$ of a random variable $Z \sim f_Z(z; \theta)$, where $f_Z(z; \theta)$ denotes the probability density function (pdf) of Z specified by the unknown parameter θ. An estimate of θ can be obtained as $\hat{\theta} = T(d)$, where T is a mapping of d into the parameter space. The example shows, that both the channel model $f_Z(z; \theta)$ and the data d are part of the estimation process. Clearly, the model defines what to estimate from the data and, thus, the model can be considered as an input for the estimation process. In this example we have considered a statistical channel model, but the estimation process is essentially the same for deterministic models.

According to the preceding discussion, channel estimation relies on two principal inputs: the sounding data and the model. The types of parameters to be estimated are determined by the channel model under consideration. Here, the term "parameters" is used in a fairly broad sense; *e.g.* a power spectrum can be considered a parameter for some models. Due to the great number of different models with different scopes, the type of entities to be estimated are rather diverse. Also the kind and amount of measurement data influence which types of parameters are estimable, as well as the achievable precision. Thus, to enable estimation of the desired model parameters at the necessary precision, certain requirements must be accounted for in the design of measurement equipment, and planning of measurement campaigns.

1.6   Organization of the Thesis

This chapter has discussed the motivation for radio channel characterization for use in the engineering of radio communication systems. We defined channel characterization as a process in which the three crafts of sounding, modeling, and estimation interact. The outcome of the characterization process is knowledge of the relationship between the transmitted and received signals. This outcome is often provided in the form of mathematical models. We discern between study, design, and simulation models according to their purposes.

The remaining parts of the thesis are organized as follows:

Chapter 2 defines the mathematical notation and concepts which we rely on in Chapters 3 and 4

Chapter 3 presents the three topics of the thesis. Each topic description is concluded by the statement of a question.

Chapter 4 outlines the contributions of the thesis with respect to the questions posed in Chapter 3. This chapter is shaped as a brief overview and summary of Papers A–J. Conclusions and outlook are provided at the end of the chapter.

Papers A–J are ten contributions published in peer-reviewed conferences and journals. The layouts of the papers have been adapted to the thesis, but the wording and notation are kept *tel quel* in the original published versions. Thus, the notation used in the papers differs from the one in Chapters 2–4.

Some Preliminaries

In Chapter 1 we defined the notion of radio channel models and related them to channel sounding and parameter estimation. In this chapter we develop a general model for the study of multiple-input multiple-output (MIMO) radio channels. The purpose of the model is to introduce the notation and concepts used in Chapters 3 and 4.

2.1   A Generic Representation of Radio Communication Channels

We consider a radio communication system with M_1 transmit antennas and M_2 receive antennas as depicted in Fig. 2.1. We represent the transmitted and received signals by their complex baseband [8] (vector) signals

$$\mathbf{x}(t) = \begin{bmatrix} x_1(t) \\ \vdots \\ x_{m_1}(t) \\ \vdots \\ x_{M_1}(t) \end{bmatrix} \quad \text{and} \quad \mathbf{y}(t) = \begin{bmatrix} y_1(t) \\ \vdots \\ y_{m_2}(t) \\ \vdots \\ y_{M_2}(t) \end{bmatrix}, \tag{2.1}$$
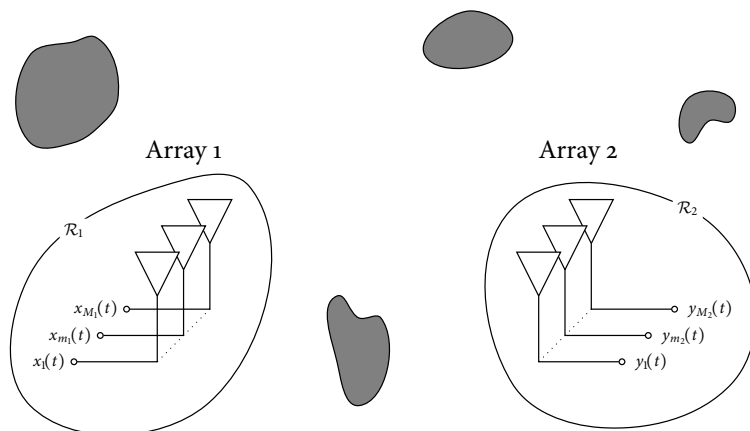
Fig. 2.1: A radio communication system where Array 1 transmits and Array 2 receives. The signal $\mathbf{x}(t)$ *is applied to the* M_1 *inputs of Array 1; the signal* $\mathbf{y}(t)$ *is observed at* M_2 *outputs of Array 2. The elements of Array k are confined in a region* $\mathcal{R}_k$, $k = 1, 2$.

respectively. Here, $x_{m_1}(t)$ is the input signal of transmit antenna m_1 and $y_{m_2}(t)$ is the output signal of receiver antenna m_2. We represent the observed signal as the sum of two components

$$\mathbf{y}(t) = \mathbf{s}(t) + \mathbf{n}(t), \tag{2.2}$$

where $\mathbf{s}(t)$ denotes the $\mathbf{x}(t)$-dependent *signal component*. The signal $\mathbf{n}(t)$ in (2.2) represents any interfering signal or noise contribution unrelated to the transmitted signal $\mathbf{x}(t)$. As an example $\mathbf{n}(t)$ could represent thermal noise in the receiver itself. Therefore, $\mathbf{n}(t)$ is termed the *noise component*.

In this thesis the main interest lies in the characterization of the signal component. We shall therefore not consider the properties of the noise component in much detail. The remainder of the chapter is devoted to the representation of the signal component.

2.2 The Delay-Spread Function

We assume that the signal component can be represented by the integral equation

$$\mathbf{s}(t) = \int \mathbf{H}(t, \tau)\mathbf{x}(t - \tau) \, \mathrm{d}\tau, \tag{2.3}$$

where we have introduced the $M_2 \times M_1$ integral kernel $\mathbf{H}(t, \tau)$. This kernel is the matrix equivalent of the *input delay-spread function* in Bello's terminology [39]. There exist other kernels equivalent to $\mathbf{H}(t, \tau)$ [39]; but for our use, the delay-spread function suffices. For short we refer to $\mathbf{H}(t, \tau)$ as the *delay-spread function*. In (2.3) the variable t denotes the time at which the signal is observed by the receive array, whereas $t - \tau$ is the time at which the signal is applied to the input of the transmit array. Therefore, τ is called the *(propagation) delay*.

Referring to (2.3), for a given delay-spread function the signal component can be obtained for any transmitted signal. Thus, neglecting the noise component in (2.2), the radio channel is represented entirely by its delay-spread function. The delay-spread function allows for the representation of delay dispersion in time-variant channels. It is practical to consider the special cases where a channel is time-invariant, non-dispersive in delay, or both.

Definition 2.2.1 (Time-invariant channel): *A time-invariant channel has a delay-spread function of the form* $\mathbf{H}(t, \tau) = \mathbf{H}_t(\tau)$, *where* $\mathbf{H}_t(\tau)$ *is is the channel impulse response. The signal component of a time-invariant channel reads*

$$\mathbf{s}(t) = \int \mathbf{H}_t(\tau)\mathbf{x}(t - \tau)\mathrm{d}\tau. \tag{2.4}$$

Definition 2.2.2 (Channel, non-dispersive in delay): *The delay-spread function of a channel, which is non-dispersive delay, is of the form* $\mathbf{H}(t, \tau) = \mathbf{H}_{\mathrm{n}}(t) \cdot \delta(\tau)$. *Here* $\mathbf{H}_{\mathrm{n}}(t)$ *is the time-varying (MIMO) channel matrix. The signal component thus reads*

$$\mathbf{s}(t) = \mathbf{H}_{\mathrm{n}}(t)\mathbf{x}(t). \tag{2.5}$$

Definition 2.2.3 (Time-invariant channel non-dispersive in delay): *A channel that is non-dispersive in delay and time-invariant, has a delay-spread function of the form* $\mathbf{H}(t, \tau) = \mathbf{H}_{\mathrm{tn}} \cdot \delta(\tau)$. *The term* $\mathbf{H}_{\mathrm{tn}}(t)$ *is the (MIMO) channel matrix. The signal component reads in this case*

$$\mathbf{s}(t) = \mathbf{H}_{\mathrm{tn}}\mathbf{x}(t). \tag{2.6}$$

The symbol $\delta(\cdot)$ used in Definitions 2.2.2 and 2.2.3 denotes the Dirac delta.

Time-invariance may be assumed for environments where changes occur slowly enough to be neglected for the considered transmission time duration. Similarly, a channel can be assumed non-dispersive in delay if the Fourier transform of the delay-spread function $\mathcal{F}_\tau\{\mathbf{H}(t, \tau)\}(f)$ with respect to the delay variable is (approximately) constant for frequencies within the bandwidth of the transmitted signal.

2.3 The Bi-Directional Delay-Spread Function

We now describe a channel representation using the delay-spread function. The terminology "bi-directional " indicates that the function can describe both the direction of departure and the direction of arrival of waves propagating from the transmitter to the receiver.

A characterization of first- and second-order moments of directional spread functions is given in [40]. Bi-directional channel representations are implicitly used in ray-tracing simulations [27, 28]. The bi-directional property also underlies the angular extensions of the model by Saleh and Valenzuela [41] proposed in [42, 43]. In the contribution by Zwick [13] a "spatial impulse response" is introduced which is essentially the same idea. The term "directional impulse response" is used in [43]. In [44] the "double-directional model" is described relying on the bi-directional representation. The bi-directional delay-spread function is also used in conjunction with stochastic models for Monte Carlo simulations as in, *e.g.*, [12].

Again, we consider the propagation environment depicted in Fig. 2.1, but introduce two assumptions:

Plane waves: Following [45], we assume that the far-field condition holds, such that a plane wave approximation can be applied in a region $\mathcal{R}_2$
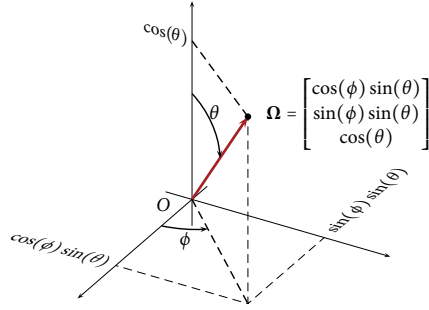
Fig. 2.2: Definition of the direction vector $\boldsymbol{\Omega}$ with respect to the coordinate system O. The direction vector can be uniquely related to its azimuth angle ϕ and co-elevation angle θ by the expression shown in the figure.

surrounding Array 2 when Array 1 transmits, and *vice versa*. This assumption implies that the same set of plane waves impinge on all elements of Array k when the other array transmits. The plane-wave assumption allows us to characterize the antennas by their complex field patterns [11, 32, 46].

Constant geometry: We assume that the gross geometries of the propagation paths remain constant throughout the observation time. Thus, the directions, delays, Doppler frequencies, and polarization properties are assumed to be constant.

In addition we make two assumptions on the transmit and receive arrays:

Time-invariant antennas: We assume for simplicity that the complex field patterns of the antennas [11, 32, 46] are constant over time.

Antennas with no delay dispersion: We assume that the array elements are non-dispersive in delay.

The complex electric field pattern of element m_k of Array k is a two-dimensional complex function [11, 32, 46]

$$\mathbf{c}_{k,m_k}(\boldsymbol{\Omega}) = \begin{bmatrix} c_{k,m_k}^{(\theta)}(\boldsymbol{\Omega}) \\ c_{k,m_k}^{(\phi)}(\boldsymbol{\Omega}) \end{bmatrix}, \tag{2.7}$$

where (2.7) $c_{k,m_k}^{(\theta)}(\boldsymbol{\Omega})$, and $c_{k,m_k}^{(\phi)}(\boldsymbol{\Omega})$ are, respectively, the vertical and horizontal components of its complex electric field pattern. The direction vector $\boldsymbol{\Omega}$ is defined as in Fig. 2.2. We define the $2 \times M_k$ polarimetric steering matrix of Array k to be

$$\mathbf{C}_k(\boldsymbol{\Omega}) = \begin{bmatrix} \mathbf{c}_{k,1}(\boldsymbol{\Omega}) & \cdots & \mathbf{c}_{k,m_k}(\boldsymbol{\Omega}) & \cdots & \mathbf{c}_{k,M_k}(\boldsymbol{\Omega}) \end{bmatrix}. \tag{2.8}$$

The field patterns in (2.8) are all measured with respect to the same coordinate system O_k with origin in $\mathcal{R}_k$. With this definition the delay-spread function can be formulated as

$$\mathbf{H}(t, \tau) = \int_{\mathbb{S}_2} \int_{\mathbb{S}_2} \mathbf{C}_2(\mathbf{\Omega}_2)^{\mathsf{T}} \mathbf{H}(t, \tau, \mathbf{\Omega}_1, \mathbf{\Omega}_2) \mathbf{C}_1(\mathbf{\Omega}_1) \mathrm{d}\mathbf{\Omega}_1 \mathrm{d}\mathbf{\Omega}_2, \qquad (2.9)$$

where the 2×2 complex kernel $\mathbf{H}(t, \tau, \mathbf{\Omega}_1, \mathbf{\Omega}_2)$ is the *bi-directional delay-spread function* of the radio channel. In (2.9), $[\cdot]^{\mathsf{T}}$ denotes the transpose operator. Its entries are named according to

$$\mathbf{H}(t, \tau, \mathbf{\Omega}_1, \mathbf{\Omega}_2) = \begin{bmatrix} h^{\theta\theta}(t, \tau, \mathbf{\Omega}_1, \mathbf{\Omega}_2) & h^{\theta\phi}(t, \tau, \mathbf{\Omega}_1, \mathbf{\Omega}_2) \\ h^{\phi\theta}(t, \tau, \mathbf{\Omega}_1, \mathbf{\Omega}_2) & h^{\phi\phi}(t, \tau, \mathbf{\Omega}_1, \mathbf{\Omega}_2) \end{bmatrix}, \qquad (2.10)$$

where the superscripts denote the transmit-receive polarization pair. It appears from (2.9) that by the aforementioned assumptions on the environment we have achieved a separation of the delay-spread function into an environment-related kernel $\mathbf{H}(t, \tau, \mathbf{\Omega}_1, \mathbf{\Omega}_2)$ and the two system-dependent steering matrices $\mathbf{C}_1(\mathbf{\Omega}_1)$ and $\mathbf{C}_2(\mathbf{\Omega}_2)$.

Invoking Definition 2.2.1–2.2.3 in (2.9), the corresponding bi-directional delay-spread functions reads

$$\mathbf{H}(t, \tau, \mathbf{\Omega}_1, \mathbf{\Omega}_2) = \begin{cases} \mathbf{H}_{\mathrm{t}}(\tau, \mathbf{\Omega}_1, \mathbf{\Omega}_2) & \text{by Definition 2.2.1} \\ \mathbf{H}_{\mathrm{n}}(t, \mathbf{\Omega}_1, \mathbf{\Omega}_2) \cdot \delta(\tau) & \text{by Definition 2.2.2} \\ \mathbf{H}_{\mathrm{tn}}(\mathbf{\Omega}_1, \mathbf{\Omega}_2) \cdot \delta(\tau) & \text{by Definition 2.2.3} \end{cases} \qquad (2.11)$$

with the same naming convention for the entries of the 2×2 kernels as in (2.10).

The main limitations of the bi-directional representation are directly related to those of the assumptions underlying its derivation. In particular, the plane-wave assumption over both arrays is an issue for some environments. The assumption of constant geometry limits the time-duration for which the representation is valid. The assumption of time-invariant antenna responses is relevant in, *e.g.*, cellular phones where the hand and the head of the user influence the antenna field patterns. The assumption of non-delay-dispersive antenna elements is not valid for ultra-wideband systems. The representation can, however, be extended to account for delay dispersion of the antennas. We let the bi-directional representation rest for now. We will return to it later in Section 2.5.

2.4 The Multipath Propagation Assumption

We now introduce the frequently used multipath propagation assumption. Multipath propagation is an elegant and intuitive way to describe many observed phenomena such as fast fading, delay- and Doppler-power spectra, *etc.* [6, 21, 28, 31, 32, 34]. The assumption of multipath propagation simplifies the mathematical representation of the radio channel in heterogeneous environments. The multipath assumption also allows for physical interpretations of observed phenomena.

Due to its conceptual and analytical simplicity, the multipath assumption or similar ideas appear in numerous different models. In fact, most modern simulation and design models for mobile and indoor communications rely on some sort of multipath description of the propagation scenario. Multipath propagation is assumed so frequently that it is often referred to as a fact, see *e.g.* [11, 28, 34, 47]. However, multipath propagation cannot be directly observed, but can only be inferred from the behavior of observed signal. We therefore stress that multipath propagation is indeed assumed in the formulation of a channel model.

The received signal is modeled as a superposition of L signal components contributed by waves propagating along different *paths*

$$\mathbf{s}(t) = \sum_{\ell=1}^{L} \mathbf{s}_\ell(t). \tag{2.12}$$

The signal $\mathbf{s}_\ell(t)$ denotes the portion of $\mathbf{s}(t)$ which is contributed by the wave propagating via Path ℓ.

The concept of a propagation path implies an approximation of the propagation mechanisms. The approximation depends on the particular definition of what a propagation path is. The precise definition of the term "path" varies throughout the literature. One frequently used definition is that a path consists of the trajectory along which a wave or ray travels from the transmitter to the receiver, under interaction with a number of so-called *scatterers*.

Definition 2.4.1 (Propagation path): *A (propagation) path is defined as a sequence of scatterers and the corresponding wave interactions.*

For the multipath model we obtain a decomposition of the delay-spread function according to

$$\mathbf{H}(t, \tau) = \sum_{\ell=1}^{L} \mathbf{H}_\ell(t, \tau), \tag{2.13}$$

where $\mathbf{H}_\ell(t, \tau)$ denotes the delay-spread function of Path ℓ. Furthermore, the assumptions in Definitions 2.2.1–2.2.3 carry over to the delay-spread function

of each path; thus:

$$\mathbf{H}_t(\tau) = \sum_{\ell=1}^{L} \mathbf{H}_{t,\ell}(\tau), \quad \mathbf{H}_n(t) = \sum_{\ell=1}^{L} \mathbf{H}_{n,\ell}(t), \quad \text{and} \quad \mathbf{H}_{tn} = \sum_{\ell=1}^{L} \mathbf{H}_{tn,\ell}. \quad (2.14)$$

2.5 *The Bi-Directional Multipath Representation*

We now rewrite the bi-directional delay-spread function defined in Section 2.3 when the the multipath assumption holds.

Assuming that the plane-wave assumption holds for each path and invoking (2.9) we can express the delay-spread function of Path ℓ as

$$\mathbf{H}_\ell(t, \tau) = \int_{\mathbb{S}_2} \int_{\mathbb{S}_2} \mathbf{C}_2(\mathbf{\Omega}_2)^\mathsf{T} \mathbf{H}_\ell(t, \tau, \mathbf{\Omega}_1, \mathbf{\Omega}_2) \mathbf{C}_1(\mathbf{\Omega}_1) \mathrm{d}\mathbf{\Omega}_1 \mathrm{d}\mathbf{\Omega}_2, \quad (2.15)$$

where $\mathbf{H}_\ell(t, \tau, \mathbf{\Omega}_1, \mathbf{\Omega}_2)$ is the bi-directional delay-spread function of Path ℓ. Thus by (2.13), the delay-spread function can be recast as

$$\begin{aligned} \mathbf{H}(t, \tau) &= \sum_{\ell=1}^{L} \mathbf{H}(t, \tau) \\ &= \sum_{\ell=1}^{L} \int_{\mathbb{S}_2} \int_{\mathbb{S}_2} \mathbf{C}_2(\mathbf{\Omega}_2)^\mathsf{T} \mathbf{H}_\ell(t, \tau, \mathbf{\Omega}_1, \mathbf{\Omega}_2) \mathbf{C}_1(\mathbf{\Omega}_1) \mathrm{d}\mathbf{\Omega}_1 \mathrm{d}\mathbf{\Omega}_2 \\ &= \int_{\mathbb{S}_2} \int_{\mathbb{S}_2} \mathbf{C}_2(\mathbf{\Omega}_2)^\mathsf{T} \left[\sum_{\ell=1}^{L} \mathbf{H}_\ell(t, \tau, \mathbf{\Omega}_1, \mathbf{\Omega}_2) \right] \mathbf{C}_1(\mathbf{\Omega}_1) \mathrm{d}\mathbf{\Omega}_1 \mathrm{d}\mathbf{\Omega}_2. \quad (2.16) \end{aligned}$$

Comparing this result to (2.9) it follows that the bi-directional delay-spread function reads

$$\mathbf{H}(t, \tau, \mathbf{\Omega}_1, \mathbf{\Omega}_2) = \sum_{\ell=1}^{L} \mathbf{H}_\ell(t, \tau, \mathbf{\Omega}_1, \mathbf{\Omega}_2). \quad (2.17)$$

Making use of (2.17) in Definitions 2.2.1–2.2.3 yields

$$\mathbf{H}_t(\tau, \mathbf{\Omega}_1, \mathbf{\Omega}_2) = \sum_{\ell=1}^{L} \mathbf{H}_{t,\ell}(\tau, \mathbf{\Omega}_1, \mathbf{\Omega}_2), \quad (2.18)$$

$$\mathbf{H}_n(t, \mathbf{\Omega}_1, \mathbf{\Omega}_2) = \sum_{\ell=1}^{L} \mathbf{H}_{n,\ell}(t, \mathbf{\Omega}_1, \mathbf{\Omega}_2), \quad (2.19)$$

and

$$\mathbf{H}_{tn}(\mathbf{\Omega}_1, \mathbf{\Omega}_2) = \sum_{\ell=1}^{L} \mathbf{H}_{nt,\ell}(\mathbf{\Omega}_1, \mathbf{\Omega}_2). \quad (2.20)$$

17

2.6   The Specular Bi-Directional Multipath Representation

The interactions along a propagation path may, due to the geometric extents and electromagnetic properties of the scatterers, disperse the signal in delay, Doppler, bi-direction, and in polarization under each scatterer-interaction. We refer to this dispersion phenomenon as "per-path dispersion". The per-path dispersion is small compared to inter-path dispersion and may in some cases be neglected. This simplification leads to the modeling of a path as a series of successive specular reflections. This motivates the use of the attribute "specular" in connection with a propagation path when it is non-dispersive in delay, Doppler, and bi-direction.

Definition 2.6.1 (Specular path): *A path is specular when its bi-directional delay-spread function reads*

$$\mathbf{H}_\ell(t, \tau, \mathbf{\Omega}_1, \mathbf{\Omega}_2) = \mathbf{\Gamma}_\ell \exp(-j2\pi\nu_\ell t)\delta(\tau - \tau_\ell)\delta(\mathbf{\Omega}_1 - \mathbf{\Omega}_{1,\ell})\delta(\mathbf{\Omega}_2 - \mathbf{\Omega}_{2,\ell}). \tag{2.21}$$

The parameters of a specular path are: the 2×2 complex polarization matrix $\mathbf{\Gamma}_\ell$, the Doppler frequency ν_ℓ, the delay τ_ℓ, and the two unit vectors $\mathbf{\Omega}_{1,\ell}$, and $\mathbf{\Omega}_{2,\ell}$ specifying the direction of departure and direction of arrival, respectively, as shown in Fig. 2.3.

   We use the term "dispersive path" to refer to a path that is non-specular.

   The remainder of the chapter is devoted to the characterization of bi-direction delay Doppler dispersion under the specular-path assumption. This form of representation is especially relevant since most available high-resolution channel parameter estimators are derived based on it.

   The entry of $\mathbf{H}(t, \tau)$ corresponding to transmit antenna m_1 and receive antenna m_2, which we call the delay-spread function of *subchannel* (m_1, m_2), reads

$$\left[\mathbf{H}_\ell(t, \tau)\right]_{m_2 m_1} = \int_{\mathbb{S}_2} \int_{\mathbb{S}_2} \mathbf{c}_{m_2}(\mathbf{\Omega}_2)^{\mathsf{T}}\mathbf{H}_\ell(t, \tau, \mathbf{\Omega}_1, \mathbf{\Omega}_2)\mathbf{c}_{m_1}(\mathbf{\Omega}_1)\mathrm{d}\mathbf{\Omega}_1\mathrm{d}\mathbf{\Omega}_2. \tag{2.22}$$

After inserting (2.21) in (2.22) and integrating over $\mathbf{\Omega}_1$ and $\mathbf{\Omega}_2$ we obtain

$$\left[\mathbf{H}_\ell(t, \tau)\right]_{m_2 m_1} = \mathbf{c}_{m_2}(\mathbf{\Omega}_{2,\ell})^{\mathsf{T}}\mathbf{\Gamma}_\ell \, \mathbf{c}_{m_1}(\mathbf{\Omega}_{1,\ell})\delta(\tau - \tau_\ell)\exp(-j2\pi\nu_\ell t). \tag{2.23}$$

Thus, the bi-directional delay-spread function of Path ℓ is determined by the parameter set

$$\boldsymbol{\theta}_\ell = \{\mathbf{\Gamma}_\ell, \mathbf{\Omega}_{1,\ell}, \mathbf{\Omega}_{2,\ell}, \tau_\ell, \nu_\ell\}. \tag{2.24}$$

Recalling that $\mathbf{\Gamma}_\ell$ is a complex matrix with four entries and that the two unit vectors $\mathbf{\Omega}_{1,\ell}$ and $\mathbf{\Omega}_{1,\ell}$ can be represented by their azimuth and co-elevation
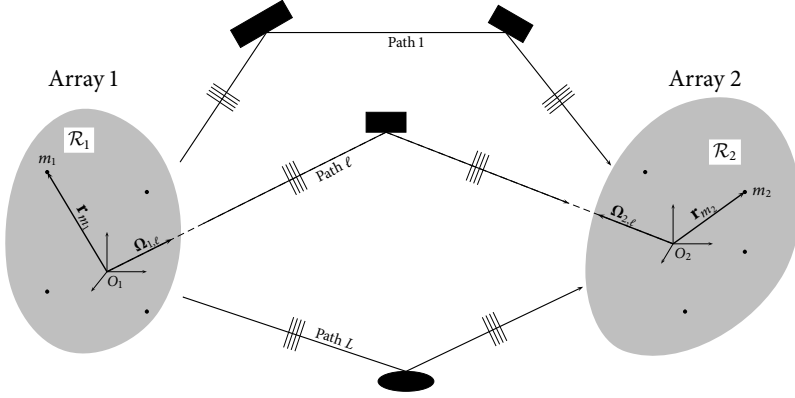
Fig. 2.3: A specular multi-path propagation environment [Paper B]. The black dots indicate the position of the antenna elements. The M_1 transmit antennas of Array 1 are confined in a region $\mathcal{R}_1$. Antenna m_1 is at position $\mathbf{r}_{m_1}$ with respect to the origin O_1 measured in carrier wave-lengths. Similarly the M_2 receive antennas of Array 2 are in the region $\mathcal{R}_2$ with the position of antenna m_2 given by $\mathbf{r}_{m_2}$ with respect to O_2. The signal propagates via L paths from Array 1 to Array 2. The direction of departure of Path ℓ is determined by the unit vector $\mathbf{\Omega}_{1,\ell}$. Similarly, the direction of arrival is determined by $\mathbf{\Omega}_{2,\ell}$.

angles, in total 14 parameters are required to specify one path. Thus, the delay-spread function $\mathbf{H}(t, \tau)$ is specified by totally $14L$ parameters. It is possible, however, to simplify the model by introducing further assumptions.

An important example of such a simplified bi-directional representation is obtained by assuming isotropic[1] antenna elements. This assumption implies for subchannel (m_1, m_2) that

$$\mathbf{c}_{m_2}(\mathbf{\Omega}_{2,\ell})^\mathsf{T}\mathbf{\Gamma}_\ell\,\mathbf{c}_{m_1}(\mathbf{\Omega}_{1,\ell}) = \alpha_\ell\exp\big(j2\pi\mathbf{\Omega}_{1,\ell}^\mathsf{T}\mathbf{r}_{m_1} + j2\pi\mathbf{\Omega}_{2,\ell}^\mathsf{T}\mathbf{r}_{m_2}\big), \qquad (2.25)$$

where α_ℓ is termed the complex gain of Path ℓ and the antenna positions are given by the vectors $\mathbf{r}_{m_1}$, $\mathbf{r}_{m_2}$ defined in Fig. 2.3. Thus, in this case

$$\big[\mathbf{H}_\ell(t, \tau)\big]_{m_2,m_1} = \alpha_\ell\exp\big(j2\pi v_\ell t + j2\pi\mathbf{\Omega}_{1,\ell}^\mathsf{T}\mathbf{r}_{m_1} + j2\pi\mathbf{\Omega}_{2,\ell}^\mathsf{T}\mathbf{r}_{m_2}\big)\delta(\tau-\tau_\ell). \quad (2.26)$$

In total 8 parameters are necessary to determine the delay-spread function in (2.26).

Further simplifications can be obtained by applying Definitions 2.2.1, 2.2.2, and 2.2.3. For the time-invariant case (Definition 2.2.1) we have the

---

[1] Expression (2.25) is valid provided that each of the arrays consists of antenna elements with identical responses, apart from a phase-shift due to the displacement from the origin of the array. Obviously, this condition is fulfilled for isotropic array elements. In this general case, however, α_ℓ may depend on $\mathbf{\Omega}_{1,\ell}$ and $\mathbf{\Omega}_{2,\ell}$.

expression

$$\left[\mathbf{H}_{\mathrm{t},\ell}(t,\tau)\right]_{m_2 m_1} = \alpha_\ell \exp\left(j2\pi\boldsymbol{\Omega}_{1,\ell}^{\mathsf{T}}\mathbf{r}_{m_1} + j2\pi\boldsymbol{\Omega}_{2,\ell}^{\mathsf{T}}\mathbf{r}_{m_2}\right)\delta(\tau - \tau_\ell) \qquad (2.27)$$

with 7 parameters. For a channel non-dispersive in delay (Definition 2.2.2) we also need 7 parameters:

$$\left[\mathbf{H}_{\mathrm{n},\ell}(t)\right]_{m_2 m_1} = \alpha_\ell \exp\left(j2\pi\nu_\ell t + j2\pi\boldsymbol{\Omega}_{1,\ell}^{\mathsf{T}}\mathbf{r}_{m_1} + j2\pi\boldsymbol{\Omega}_{2,\ell}^{\mathsf{T}}\mathbf{r}_{m_2}\right). \qquad (2.28)$$

Finally, in the time-invariant and delay non-dispersive case (Definition 2.2.3) we obtain

$$\left[\mathbf{H}_{\mathrm{tn},\ell}(t,\tau)\right]_{m_2 m_1} = \alpha_\ell \exp\left(j2\pi\boldsymbol{\Omega}_{1,\ell}^{\mathsf{T}}\mathbf{r}_{m_1} + j2\pi\boldsymbol{\Omega}_{2,\ell}^{\mathsf{T}}\mathbf{r}_{m_2}\right) \qquad (2.29)$$

with 6 parameters.

The bi-directional multipath representation and derivatives thereof are used in both study models (see *e.g.* [27, 44, 45]) and simulation models (see *e.g.* [12–14, 17, 48]). The bi-directional specular multipath representation can be used as a study model in channel estimation. To this end, estimation algorithms must be derived. When used in simulation models, a common approach is to draw the path parameters according to an assumed probability density function, which then needs to be determined by calibration measurements (*cf* Section 1.4).

Topics of the Thesis

In this chapter we describe the three main topics covered in the Papers A–J included in the thesis. We conclude each topic description with a statement of the questions considered in these papers. The first topic presented in Section 3 regards sounding systems. More specifically, we are here concerned with sounding systems for measurement of the spatial properties of the channel. The second topic discussed in Section 3.2 is concerned with modeling and estimation of the per-path dispersion in delay and bi-direction. The last topic stated in Section 3.3 is the modeling of reverberant indoor channels.

3.1 *Spatio-Temporal Channel Sounding*

Due to the many different model types and scopes, there exist numerous different sounding techniques for collecting various kinds of measurement data [28, 47, 49–51]. Also spatially resolved measurements can be obtained by different methods. The sounding systems may use one of the following four approaches to obtain spatial resolution at the transmitter, at the receiver, or at both sites:

Directional antenna: Measurements are performed with a highly directive antenna [46] oriented in different directions [42]. While the hardware necessary for this sounding method is relatively simple, this method is slow (in the range of seconds or minutes [34]) due to the rotation of the antenna. Therefore this method is suitable only for measurements of stationary environments.

Antenna array: Measurements are performed using an array of antenna elements [52–55]. The directional resolution is obtained via array processing methods. The measurements can be performed continuously, and therefore there are practically no constraints on the stationarity of the measurement environment. The hardware complexity and cost is high because of the required parallel transmitters and/or receivers. The calibration of the transmitter/receiver chains is also cumbersome. In the case of parallel transmitters, the sounding signals must be chosen to allow for separation of the received signals into its components from each of the transmitters.

Synthetic antenna array: An antenna array is simulated by taking measurements with a single antenna placed at a number of different positions. The positions of the antenna are thereafter considered as element positions of a synthetic array [56]. Provided that the environment remains constant during the whole measurement, it is possible to process the measurement data by standard array processing methods [56]. As with the rotated directional antenna this method is time-consuming, and can therefore only be applied in stationary environments.

Switched antenna array: The sounder is connected to the transmit/receive antenna array via a switch. The switch makes it possible to transmit or receive with one antenna element at the time. This technique is several orders of magnitudes faster than that using a synthetic array or directional antenna [51, 57–61]. The complexity and calibration effort is limited since only one transmitter/receiver is necessary. Due to the limitations in switching speed, the environment is required to be quasi-stationary. Additionally, since the measurements are not performed simultaneous for all antennas, phase and frequency stability of the oscillators of the transmitter or receiver is an issue. One further weakness of using a switched antenna array at the transmitter is the rather limited power that the switch can accommodate. This limitation is especially critical in outdoor measurements.

It is thus possible to obtain spatial resolution at the transmitter or at the receiver site, or both. Indeed, modern sounding systems commonly apply spatial resolution techniques at both sites. The above techniques may be combined. For instance, the sounder presented in [51] relies on a combination of a switched transmitter antenna array and an antenna array the receiver with fully parallel receivers. Another example is the channel sounder presented in [62]. Here, 16 fully parallel transmitters are connected directly to the transmit array, while the 32 receive antennas are sensed by via 8 switches via 8 parallel receivers. Commercially available sounders are most often equipped with switched arrays at both the transmitter and the receiver [51, 57, 59–61]. We therefore discuss this sounding technique in further detail.

Fig. 3.1 shows a time-division-multiplexing (TDM) or a *switched* sounding system. Switch 1 feeds the sounding signal to the inputs of the Array 1 elements. Similarly, the outputs of the Array 2 elements are sensed by the receiver via Switch 2. In this way any subchannel can be measured. The sounding signal $u(t)$ can be chosen as a sum of time-shifted sounding pulses

$$u(t) = \sum_{i=1}^{I} p_i(t). \tag{3.1}$$
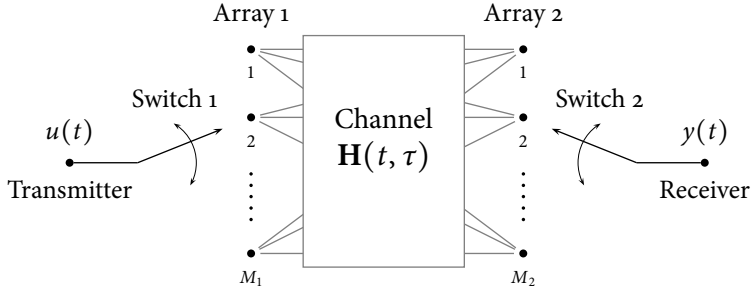
Fig. 3.1: A switched sounding system. The known sounding signal $u(t)$ is applied to the transmitter antenna via a Switch 1. The output terminals of the receiver antennas is sensed via Switch 2. Thus, a time-division-multiplexed channel measurement $y(t)$ is obtained.

Different types of sounding pulses may be considered. Often applied sounding pulses consist of a maximum-length sequence [45]. Another option is a chirp signal [51]. The signal component $s(t)$ of the observed signal $y(t) = s(t) + n(t)$ is a superposition

$$s(t) = \sum_{i=1}^{I} s_i(t), \tag{3.2}$$

where the ith signal component $s_i(t)$ is obtained with Switch 1 in position $m_1(i)$ and Switch 2 in position $m_2(i)$:

$$s_i(t) = \int \left[\mathbf{H}(t, \tau) \right]_{m_2(i)m_1(i)} p_i(t - \tau) d\tau. \tag{3.3}$$

In the case where the temporal variations of $\mathbf{H}(t, \tau)$ are small for the duration of $p_i(t)$ we can make use of the following approximation

$$\mathbf{H}(t, \tau) \approx \mathbf{H}(t_i, \tau), \quad \text{for } t \in \mathcal{T}_i \tag{3.4}$$

where *sample time* t_i is the center time of the support $\mathcal{T}_i$ of $p_i(t)$. Under this approximation, the signal component $s_i(t)$ is the form

$$s_i(t) = \int \left[\mathbf{H}(t_i, \tau) \right]_{m_2(i)m_1(i)} p_i(t - \tau) d\tau. \tag{3.5}$$

It appears from (3.5) that the signal component $s_i(t)$ is the ith sounding pulse filtered by a channel specified by the sample time t_i, and the two antenna indices $m_1(i)$, and $m_2(i)$. We define the *i*th *spatiotemporal sample* as one signal component $s_i(t)$ impaired by the noise component of $y(t)$.

A switched [1] sounding system allows for acquisition of one sample at each of the sample times $t_1, \ldots, t_I$. In this case the channel coefficient of $s_i(t)$ is

---

[1] We present here a simplified version of the theory developed fully in Paper B. In the more general theory of Paper B we can define spatiotemporal samples and sounding modes for systems with an arbitrary numbers of parallel transmitters and receivers.

thus fully specified by the triplet of indices

$$(i, m_1(i), m_2(i)) \in \{1, \ldots, I\} \times \{1, \ldots, M_1\} \times \{1, \ldots, M_2\}. \tag{3.6}$$

We define a *sounding mode* as the set of triplets from which measurements are obtained:

$$\mathcal{M} = \{(i, m_1(i), m_2(i)) : i = 1, \ldots, I\}. \tag{3.7}$$

If the radio channel varies between consecutive sample times, *i.e.*, if the channel matrix $\mathbf{H}(t_i, \tau)$ is not constant for $i = 1, \ldots, I$, then the acquired set of channel measurement data is affected by the order in which the subchannels are measured. Consequently, estimators relying on these data will be affected by the choice of sounding mode. In the following we are concerned with two such estimation problems where the sounding mode is of importance.

Estimation of Doppler Frequency and Bi-Direction in Switched Sounding

We now consider the estimation of the parameters of the non-delay-dispersive channel model given in (2.26). The set of parameters to be estimated is $\boldsymbol{\theta} = \{\boldsymbol{\theta}_1, \ldots, \boldsymbol{\theta}_L\}$ with $\boldsymbol{\theta}_\ell = \{\alpha_\ell, v_\ell, \boldsymbol{\Omega}_{1,\ell}, \boldsymbol{\Omega}_{2,\ell}\}$.

The ith spatiotemporal sample is obtained at time t_i from transmitter antenna $m_1(i)$ at position $\mathbf{r}_{m_1(i)}$ and receiver antenna $m_2(i)$ positioned at $\mathbf{r}_{m_2(i)}$. Insertion in (2.26) yields for the channel coefficient of sample i

$$[\mathbf{H}_n(t_i)]_{m_2(i)m_1(i)} = \sum_{\ell=1}^{L} \alpha_\ell \exp\left(j2\pi \mathbf{a}_i^\mathsf{T} \boldsymbol{\vartheta}_\ell\right), \tag{3.8}$$

where

$$\mathbf{a}_i = \begin{bmatrix} t_i \\ \mathbf{r}_{m_1(i)} \\ \mathbf{r}_{m_2(i)} \end{bmatrix} \quad \text{and} \quad \boldsymbol{\vartheta}_\ell = \begin{bmatrix} v_\ell \\ \boldsymbol{\Omega}_{1,\ell} \\ \boldsymbol{\Omega}_{2,\ell} \end{bmatrix}. \tag{3.9}$$

The observed channel coefficients in (3.8) are thus specified by the *spatio-temporal aperture matrix*:

$$\mathbf{A} = \begin{bmatrix} \mathbf{a}_1, \ldots, \mathbf{a}_i, \ldots, \mathbf{a}_I \end{bmatrix}. \tag{3.10}$$

Given a set of sample times $\{t_1, \ldots, t_I\}$ and the layouts of the two antenna arrays, the sounding mode completely specify $\mathbf{A}$.

As apparent from (3.8), the data available for estimation of $\boldsymbol{\theta}$ depend on the aperture matrix (and thus on the sounding mode). Consequently, the performance of the estimator in terms of accuracy and noise-robustness is influenced by the spatiotemporal aperture.

In the design of a sounding system, there is a degree of freedom to select the timing scheme and sounding mode. It is, however, a standard approach to

group the measurement of sub-channels into sounding cycles [34, 61]. In each sounding cycle all sub-channels are measured once. The cycle time denoted by T_{cy} between the start of two successive sounding cycles fulfills the inequality

$$T_{cy} \geq M_1 M_2 T_r, \tag{3.11}$$

where T_r denotes the minimal time between successive spatio-temporal samples. It is commonly believed, by an intuitive argument [34, 61], that the maximum estimable Doppler frequency is given by invoking the Nyquist-Shannon Sampling Theorem [63] as $(2T_{cy})^{-1}$. With this result the maximum estimable Doppler frequency is accordingly reduced by a factor $(M_1 M_2)^{-1}$ compared to a single-input single-output (SISO) sounding system [34, 61]. For sounding systems with a large number of transmitter and receiver antennas this results in a significant limitation on the maximum Doppler frequency, and thus on the maximum velocity of any moving object in the measurement environment.

To illustrate the importance of this limitation we consider an example where the transmitter moves directly toward the receiver at a speed V emitting a carrier with wavelength λ_c. The signal component propagating directly from the transmitter to the receiver (the direct component) has Doppler frequency V/λ_c [28, 32, 34]. We are interested in computing the highest speed denoted by V_{max}, such that the Doppler frequency of the direct component is estimable. We let the maximum estimable Doppler frequency equal $(2T_r M_1 M_2)^{-1}$, hence

$$V_{max} = \frac{\lambda_c}{2 T_r M_1 M_2}. \tag{3.12}$$

As a numerical example consider the measurements presented in Paper A. The carrier wave length is $\lambda_c = 0.12$ m, and the sounding system is equipped with $M_1 = 54$ transmitter antennas and $M_2 = 32$ receiver antennas, yielding $M_1 M_2 = 1728$. We obtain by setting $T_r = 5.1\,\mu s$, for the two cases $M_1 M_2 = 1$ (SISO) and $M_1 M_2 = 1728$ (MIMO)

$$V_{max} = \frac{0.12\,\text{m}}{2 \cdot 5.1\,\mu s \cdot M_1 M_2} = \begin{cases} 20 \cdot 10^3\,\text{km/h}, & M_1 M_2 = 1, \\ 12\,\text{km/h}, & M_1 M_2 = 1728. \end{cases} \tag{3.13}$$

In the SISO case, the speed limit does not pose problems for use in terrestrial applications, whereas it severely limits the applicability in the MIMO case.

It is important to notice that the Nyquist-Shannon Sampling Theorem [63] gives the minimum sampling frequency by which one can represent a band-limited signal and still recover the original signal without error. For Doppler frequency and direction estimation, it is, however, not the objective to be able to recreate the signal without error. It suffices to be able to estimate
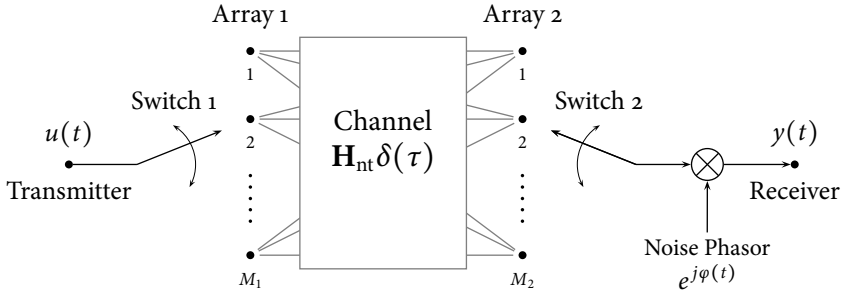
Fig. 3.2: Measurement of a time-invariant, delay non-dispersive channel with a switched sounding system impaired by phase noise. The noise phasor $e^{j\varphi(t)}$ represents the concatenated phase noise of the transmitter and receiver oscillators.

the parameters of interest with a small error. Thus the Nyquist-Shannon Sampling Theorem cannot be directly applied for the determination of the maximum estimable Doppler frequency.

It was shown in [64] that by appropriately selecting the temporal sampling scheme, the maximum estimable Doppler frequency is limited by $(2T_r)^{-1}$ even for MIMO sounders. The results of [64] include Doppler frequency estimation, but does not consider estimation of bi-direction. A question arises from this observation: *How to select the spatio-temporal aperture such that the estimation accuracy of joint Doppler frequency and bi-direction is optimum?*

Phase-Noise Impaired Switched Sounding

Another situation where the sounding mode influences the measurement results is the case of phase-noise impaired switched sounding [65, 66]. To illustrate the problem, we consider the system depicted in Fig. 3.2.

We measure a time-invariant channel that is non-dispersive in delay with a phase-noise impaired sounder. We represent the impairment by single phase noise process $\varphi(t)$ concatenating phase noise of the oscillators in the transmitters and receivers. Although the propagation channel $\mathbf{H}_{tn}\delta(\tau)$ is time-invariant, phase noise causes the measured channel to vary over time. An expression for the signal contribution $s_i(t)$ is obtained from (3.3) by inserting $\mathbf{H}_{tn}\delta(\tau)e^{j\varphi(t)}$ for $\mathbf{H}(t, \tau)$:

$$s_i(t) = \int \left[\mathbf{H}_{tn}\delta(\tau)e^{j\varphi(t)}\right]_{m_2(i)m_1(i)} p_i(t - \tau)\, d\tau \qquad (3.14)$$

$$= \left[\mathbf{H}_{tn}\right]_{m_2(i)m_1(i)} e^{j\varphi(t)} p_i(t). \qquad (3.15)$$

For a sounding pulse of sufficiently short duration, the following approximation is valid for a band-limited phase noise process $\varphi(t)$:

$$e^{j\varphi(t)}p_i(t) \approx e^{j\varphi(t_i)}p_i(t). \tag{3.16}$$

Making use of this approximation, we achieve from (3.15)

$$s_i(t) = g_i p_i(t), \quad g_i = [\mathbf{H}_{\mathrm{tn}}]_{m_2(i)m_1(i)} \cdot e^{j\varphi(t_i)}. \tag{3.17}$$

From this expression it appears that g_i depends on t_i, $m_1(i)$ and $m_2(i)$. Due to the random noise phasor, the obtained coefficients $\{g_1, \ldots, g_I\}$ are stochastic variables. The phase of coefficient g_i reads

$$\angle g_i = \angle \left([\mathbf{H}_{\mathrm{tn}}]_{m_2(i)m_1(i)}\right) + \varphi(t_i). \tag{3.18}$$

As a result, the expectation of $\angle g_i$ is

$$\mathsf{E}[\angle g_i] = \angle \left([\mathbf{H}_{\mathrm{tn}}]_{m_2(i)m_1(i)}\right) + \mathsf{E}[\varphi(t_i)], \tag{3.19}$$

where $\mathsf{E}[\cdot]$ denotes the expectation operator. It appears from (3.19) that the sequence $\{\mathsf{E}[\angle g_i]\}$ depends on the sounding mode. It follows similarly, that for correlated $\{\varphi(t_i)\}$, the cross correlations of $\{\angle g_i\}$ depend on the sounding mode as well. We thus reach the conclusion that the sounding mode affects the statistical properties of $\{g_i\}$ and in turn the estimators relying on the measurement $y(t)$.

A specific estimation problem where the phase stability of the sounding system is of importance is the problem of estimating the MIMO channel capacity from measurement data [65–70]. The capacity of a time-invariant, non-delay-dispersive deterministic MIMO channel is defined as [71, 72]

$$C = \max_{\boldsymbol{\Sigma}:\mathrm{tr}\,(\boldsymbol{\Sigma})=M_1} \log_2 \det \left(\mathbf{I} + \frac{\rho}{M_1}\mathbf{H}_{\mathrm{tn}}\boldsymbol{\Sigma}\mathbf{H}_{\mathrm{tn}}^{\mathsf{H}}\right), \tag{3.20}$$

where $\boldsymbol{\Sigma}$ is the covariance matrix of the transmitted signal $\mathbf{x}(t)$ normalized such that $\mathrm{tr}\,(\boldsymbol{\Sigma}) = M_1$ and $\rho = \mathsf{E}[\mathbf{x}(t)^{\mathsf{H}}\mathbf{x}(t)]/N_0$ is the signal-to-noise ratio with N_0 denoting the one-sided spectral height of the noise component. Rather than performing the maximization required to evaluate (3.20), it is customary to consider the case, where the channel is unknown to the transmitter, and thus select $\boldsymbol{\Sigma} = \mathbf{I}$. This choice leads to

$$C(\mathbf{H}_{\mathrm{tn}}\mathbf{H}_{\mathrm{tn}}^{\mathsf{H}}) = \log \det \left(\mathbf{I} + \frac{\rho}{M_1}\mathbf{H}_{\mathrm{tn}}\mathbf{H}_{\mathrm{tn}}^{\mathsf{H}}\right). \tag{3.21}$$

This quantity is, despite the fact that it is merely a mutual information between the transmitted signal and the received signal, commonly referred to as the MIMO channel capacity with no channel knowledge at the transmitter [73]. Recently, measurements of the MIMO capacity have been reported in a great number of publications.

Due to the noise phasor, the matrix $\mathbf{H}_{tn}$ in (3.21) is unknown and, consequently, the capacity cannot be computed. Instead, the capacity must to be estimated from a set of measurement data. The standard estimate of $C(\mathbf{H}_{tn}\mathbf{H}_{tn}^{H})$ from a noisy measurement $\mathbf{G}$ of $\mathbf{H}_{tn}$ impaired by both additive and phase noise is $C(\mathbf{G}\mathbf{G}^{H})$ [65–70].

The contribution [74] considers the effect of additive measurement noise on the standard capacity estimate. It is shown that the additive noise leads to an overestimation of the channel capacity. It has been shown recently that phase noise of the sounding system affects the estimation of MIMO channel capacity when using the standard capacity estimate [65–67]. The effect of phase noise on MIMO capacity estimation is studied in [67] assuming that phase noise is a random walk process. Theoretical investigations reported in [65, 66] show that, provided phase noise is white and Gaussian, it leads to large measurement errors in terms of estimated channel capacity when the channel matrix has low rank. In [66] analytical results are given under the assumptions that the sounding mode fulfills a separability condition and that the phase noise process is white. However, experimental studies reported in [70] show that phase noise cannot be assumed to be white or a random walk on the time-scale of a measurement period [68, 70]. Furthermore, the spatio-temporal arrays optimized for joint Doppler-direction estimation do not in general fulfill the separability condition.

This leads us to a second question regarding the selection of sounding mode: *How does the sounding mode in combination with the correlated phase noise of the sounding system affect the estimation of MIMO channel capacity, and how can the sounding mode be accounted for in the capacity estimator?*

3.2 *Modeling and Estimation of Per-Path Dispersion*

As described in Chapter 2, modern stochastic channel models commonly rely on the multipath assumption, *i.e.*, the response of the channel is modeled as a superposition of components where each component represents the response of one propagation path which may be dispersive or specular.

It is shown in [75–78] that the per-path dispersion has an impact on important metrics of a channel model, such as, the MIMO channel capacity and diversity. Realistic models including the per-path dispersion are therefore important to accurately assess the impact on system performance with respect to these metrics.

Several models of per-path dispersion have been proposed in the literature. The most wide-spread approach, pioneered by Saleh and Valenzuela [41] and extended by others [13, 14, 42, 43], is to model the per-path response as a

superposition of specular components. Assuming uni-polarized antennas, and dropping the polarization superscript in (2.11) we have for the time-invariant case in (2.28)

$$h_{t,\ell}(\tau, \mathbf{\Omega}_1, \mathbf{\Omega}_2) = \sum_q \alpha_{\ell q} \delta(\tau - \tau_{\ell q}) \delta(\mathbf{\Omega}_1 - \mathbf{\Omega}_{1,\ell q}) \delta(\mathbf{\Omega}_2 - \mathbf{\Omega}_{2,\ell q}), \quad (3.22)$$

where the complex gain $\alpha_{\ell q}$, the delay $\tau_{\ell q}$, the direction of departure $\mathbf{\Omega}_{1,\ell q}$, and the direction of $\mathbf{\Omega}_{2,\ell q}$ are random variables. The specular components belonging to path ℓ are assumed to be grouped or "clustered" around a center of gravity in the bi-direction-delay domain.

We remark that the term "cluster" introduced in [41] has been used in several differing meanings in the literature. The large intra-cluster delays of [41] suggests that the term originally referred to a group of signal components arriving via different paths, and not the decomposition of the response of a single path as in (3.22). In directionally resolved measurements, where the spatial resolution admit resolution of the responses of individual paths, the term cluster has been used in the meaning of the response of a single path [42, 79, 80].

For simulation models it is necessary to generate realizations of the random parameters in (3.22). This includes choosing realistic pdfs of these parameters. Similarly, for design models, parameters describing the per-path dispersion must be chosen realistically in order to yield systems that will work under realistic conditions. These pdfs are generally not readily available, but must be inferred from measurements. Hence, for this purpose it is important to be able to reliably estimate the per-path dispersion parameters from measurement data.

The *clustering approach* proposed in [41] and later applied by other researchers [42, 79–84] comprises three steps:

1. Estimate a number of specular components.

2. Group the obtained estimates according to a clustering rule.

3. Estimate the cluster parameters of the defined clusters.

The first step is typically performed by applying a high-resolution estimation method such as CLEAN [42, 85], MUSIC [86, 87], ESPRIT [57, 88], RIMAX [89, 90], or SAGE [45, 91]. In step two, various heuristic clustering rules and algorithms have been proposed and applied to measurement data [41, 42, 79–84]. Most of these techniques rely on visual clustering performed by a *trained operator* [41, 42, 79, 81, 82]. In the third step cluster parameters, most often first- and second-order moments of each cluster, are estimated.

As the cluster model is an extension of the specular model, the clustering approach extends the specular estimation techniques. There are, however, a

few issues to be considered. The clustering approach relies on accuracy of a high-resolution method; but these methods are most often derived for *well-separated specular* components—a condition which is obviously not fulfilled for estimation of per-path dispersion. Under such conditions the output of the high-resolution estimators may contain estimation artifacts not related to the propagation conditions. An example of this problem follows from the analysis presented in [92] where a slightly dispersive path results in a heavy-tailed distribution of the estimated specular components. Hence, relying on this type of estimator, may result in large variances of the spread estimates. The applied clustering rules are also problematic from a scientific viewpoint. The use of visual inspection does not only make a systematic evaluation of the accuracy of these methods difficult but renders their repeatability and objectivity questionable. From a practical point of view, the clustering methods require large amounts of time-consuming manual work. The amount of manual work has been alleviated by the introduction of (semi-)automatic clustering methods [79–81, 83, 84], but to be replaced by another set of heuristics involving parameter setting of these algorithms. The accuracy of these methods, however, remains cumbersome to analyze statistically due to the heuristic nature of their clustering rules.

Another approach to the estimation of per-path dispersion parameters is to rely on a non-specular path model and to estimate the parameters of this model directly [93]. Hence, in contrast to the clustering approach, this procedure requires the development of new high-resolution estimators for the parameters of each path model. The available methods are reviewed in [93]. Rather than modeling the response of a path, we focus on modeling and estimation of the per-path power spectral density (psd). The psd of a path is defined as follows. Assuming that the spread functions of the paths are uncorrelated and wide-sense stationary complex (zero-mean) orthogonal stochastic measures [40] we have

$$\mathsf{E}\big[h_{\mathrm{t},\ell}(\tau, \mathbf{\Omega}_1, \mathbf{\Omega}_2)h^*_{\mathrm{t},\ell'}(\tau', \mathbf{\Omega}'_1, \mathbf{\Omega}'_2)\big] =$$
$$P_\ell(\tau, \mathbf{\Omega}_1, \mathbf{\Omega}_2)\delta_{\ell\ell'}\delta(\tau - \tau')\delta(\mathbf{\Omega}_1 - \mathbf{\Omega}'_1)\delta(\mathbf{\Omega}_2 - \mathbf{\Omega}'_2). \quad (3.23)$$

In (3.23) $\delta_{\ell\ell'}$ is the Kronecker delta. The bi-direction delay psd $P_\ell(\tau, \mathbf{\Omega}_1, \mathbf{\Omega}_2)$ in (3.22) of Path ℓ reads

$$P_\ell(\tau, \mathbf{\Omega}_1, \mathbf{\Omega}_2) = \mathsf{E}\big[|h_{\mathrm{t},\ell}(\tau, \mathbf{\Omega}_1, \mathbf{\Omega}_2)|^2\big]. \quad (3.24)$$

For a model of the type (3.22), fulfilling the uncorrelated scattering (us) condition [39, 40], i.e, each of the terms in (3.22) are statistically uncorrelated, the per-path psd can be interpreted as follows: Since the psd is non-negative and since the integral

$$\iiint P_\ell(\tau, \mathbf{\Omega}_1, \mathbf{\Omega}_2) \mathrm{d}\tau \mathrm{d}\mathbf{\Omega}_1 \mathrm{d}\mathbf{\Omega}_2 = P_\ell \qquad (3.25)$$

is finite, the psd of Path ℓ can be recast as a product of P_ℓ and a non-negative function integrating to unity

$$P_\ell(\tau, \mathbf{\Omega}_1, \mathbf{\Omega}_2) = P_\ell \cdot f(\tau, \mathbf{\Omega}_1, \mathbf{\Omega}_2; \boldsymbol{\theta}_\ell), \qquad (3.26)$$

where the vector $\boldsymbol{\theta}_\ell$ holds the parameters of $f(\tau, \mathbf{\Omega}_1, \mathbf{\Omega}_2; \boldsymbol{\theta}_\ell)$. We may thus *interpret* the function $f(\tau, \mathbf{\Omega}_1, \mathbf{\Omega}_2; \boldsymbol{\theta}_\ell)$ as the joint pdf of the random variables $\tau_{\ell q}$, $\mathbf{\Omega}_{1,\ell q}$, and $\mathbf{\Omega}_{2,\ell q}$ in (3.22). Thus by assuming a particular pdf, the estimation problem at hand amounts to estimating the parameters $\boldsymbol{\theta}_\ell$ defining the pdf in (3.26), and the power P_ℓ.

In the literature there exists a number of contributions proposing various pdfs for estimation of dispersion in various dispersion domains [93–95]. It is, however, not obvious which pdf to select. Since this choice affects the the accuracy of the corresponding estimators [93] this issue merits further consideration. We are particularly interested in estimating the first- and second-order moments of the psd since these parameters are required in numerous design and simulation models. It thus appears natural to pose the question: *"How should the model of the non-specular path be chosen for the purpose of estimating the second order moments of path components dispersed in delay and direction from measurement data?"*

3.3 Reverberation Models for Indoor Radio Channels

The third topic treated in this thesis is modeling of the channel impulse responses of indoor radio channels. In particular, we study the "specular-to-diffuse" transition observed in experimentally obtained channel impulse responses.

In the ultra-wide-band measurements presented in [96], it is observed that the impulse response of an indoor channel exhibits a specular-to-diffuse transition. For the purpose of describing the problem we consider the channel impulse response $h_\mathrm{t}(\tau)$ of a single-input single-output communication system operating in a time-invariant channel. The transition effect is illustrated in Fig. 3.3. The early part of the response is dominated by specular components while the later part is a diffuse 'tail', of which the power decreases exponentially as the delay increases.

The simulation models presented in [96–98] take this transition effect into account by modeling the impulse response as a sum of specular components and a single exponentially decaying diffuse term:

$$h_\mathrm{t}(\tau) = h_\mathrm{specular}(\tau) + h_\mathrm{diffuse}(\tau), \qquad (3.27)$$
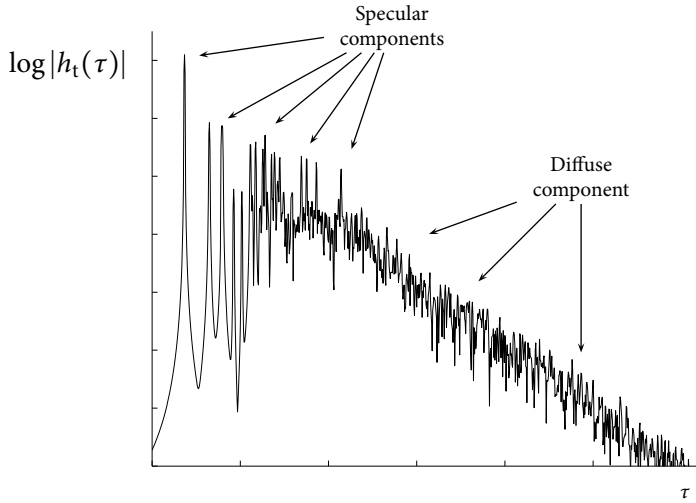
Fig. 3.3: An example of a channel impulse response illustrating the specular-to-diffuse transition. The magnitude of $h_t(\tau)$ is depicted on a logarithmic scale versus the delay τ. The early part of the response is predominantly specular, while the later part consists of an exponentially decaying diffuse 'tail'.

where $h_{\text{specular}}(\tau)$ is modeled as a superposition of specular components

$$h_{\text{specular}}(\tau) = \sum_{\ell=1}^{L} \alpha_\ell \delta(\tau - \tau_\ell) \tag{3.28}$$

and the diffuse component $h_{\text{diffuse}}(\tau)$ is an zero-mean complex Gaussian random process with delay-power spectrum

$$\mathsf{E}\big[|h_{\text{diffuse}}(\tau)|^2\big] = \begin{cases} 0 & \tau < \tau_{\text{diff}} \\ P_{\text{diff}} \exp(-\tau/T), & \tau \geq \tau_{\text{diff}}. \end{cases} \tag{3.29}$$

This approach is reasonable for simulation models but is, however, inadequate as a study model since it does not reflect the propagation mechanisms leading to the transition effect.

A different approach is followed by Franceschetti in [7, 99, 100], where the radio propagation mechanism is modeled as a "stream of photons" performing a continuous random walk in an isotropically cluttered environment. When a photon interacts with an obstacle, it is either absorbed (with a certain probability) or scattered in a random direction. The delay power spectrum is derived in a closed-form expression directly reflecting the impact of the environment parameters. The obtained expression consists of a "coherent part"

corresponding to the direct component and a "non-coherent part" stemming from scattered power. While able to jointly describe the direct (the coherent part) and the diffuse components (the non-coherent part), Franceschetti's model does not represent the specular-to-diffuse transition.

As does the radio channel, the delay-power spectrum of the acoustical channel exhibits an exponential decay [101]. In the field of room acoustics there is a well-developed theory quantifying this decay rate. A key feature of the room acoustical response is the "reverberance time" of a room for which several models exists [101–104]. The reverberance time is directly related to the power decay rate of the impulse response [101]. Also, a similar specular-to-diffuse transition effect is well-known in acoustics [101]. This effect is also attributed to a reverberation phenomenon [101].

As a matter of fact there exist a well-developed statistical theory for reverberant electromagnetic fields in convex cavities [105]. Most of the results are, however, derived under the assumption that the boundaries are perfect conductors. The theory is well-suited for analysis of the so-called "reverberation chambers" with metal clad walls used for electromagnetic compatibility testing; but the theory does not apply directly to the normal indoor propagation environments with finitely conducting walls.

There exists a number of contributions [106–112] where the analogy between reverberant acoustical and electromagnetic fields is exploited to model the delay-power spectrum. The earliest work appears to be [106] by Holloway *et al.* Here, the statistical acoustical reverberation theory by Sabine [102] and Eyring [103] is applied with slight modifications to model the delay-power spectrum of reverberant indoor radio propagation environments. The model is further refined in [107, 109]. In the contributions [108, 110], acoustical reverberation theory has been applied to analyze the electromagnetic field in reverberation chambers. Recently, Andersen *et al.* [111, 112] have transcribed Sabine's acoustical reverberation theory to electromagnetic reverberation in large room environments.

From this discussion of the available models describing the delay-power spectrum of reverberant indoor channels it appears that these models are in general not well-suited as study models to describe the specular-to-diffuse transition effect. Therefore, to investigate the effect further—and in particular to determine how it depends on the propagation environment—it is necessary to develop a suitable study model which jointly describes specular and diffuse signal components. We thus arrive at the question: *How can the specular and diffuse components of the channel impulse response be modeled jointly?*

Contributions of the Thesis

This chapter summarizes the contributions of the thesis. The contributions fall into three categories. In each of the three categories, we have found a number of questions to be addressed in the thesis. For ease of reference we name these questions as:

Q1 How to select the spatio-temporal array such that the estimation accuracy of joint Doppler frequency and bi-direction is optimized? How does the sounding mode in combination with the correlated phase noise of the sounding system affect the estimation of MIMO channel capacity, and how can the sounding mode be accounted for in the capacity estimator?

Q2 How should the model of the non-specular paths be chosen for the purpose of estimating the first- and second-order moments of path components dispersed in delay and direction from measurement data?

Q3 How can the specular and diffuse components of the channel impulse response be modeled jointly?

We provide an overview of the contributions of Papers A–J in Table 4.1. In the table we indicate which questions and which fields the papers address.

Paper	Field of Contribution			Question
	Sounding	Estimation	Modeling	
A	✓	✓		
B	✓	✓		Q1
C	✓	✓		
D	✓	✓		
E		✓	✓	
F		✓	✓	Q2
G		✓	✓	
H		✓	✓	
I			✓	Q3
J			✓	

Table 4.1: A tabular overview of the questions and contributions of the papers presented in this thesis. The labels Q1,Q2, and Q3 refer to the questions stated in the text.

4.1 *Optimization of Spatio-Temporal Apertures in Channel Sounding*

Papers A–D deal with the research question Q1. Papers A and B focus on the selection of spatio-temporal arrays for joint Doppler and bi-direction estimation. In Paper C and Paper D we study how phase noise of the channel sounder affects the measurement accuracy. In particular we focus on how phase noise affects the estimation of MIMO channel capacity. In Paper C the problem is analyzed, and in Paper D we propose an improved capacity estimator, that can account for the spatio-temporal array.

Paper A We study the effect of the spatio-temporal aperture on the estimation of Doppler frequency and bi-direction. We analyze the objective function of the SAGE algorithm [64, 113, 114] and show that extension of the Doppler frequency estimation range as proposed in [64] leads to an ambiguity in the joint estimation of Doppler and bi-direction. It is also shown that the occurrence of this ambiguity effect is determined by the sounding mode. More specifically, it is shown that on the one hand the so-called modulo-type sounding modes, including the most commonly used identity sounding mode, all lead to the ambiguity effect. On the other hand, one can select sounding modes such that the ambiguity effect does not occur. Simulations indicate that the root-mean-square error of the Doppler-direction estimator depends heavily on the normalized magnitude of the side lobes of the objective function. This finding motivates the definition and use of the normalized side-lobe level as a figure of merit to assess the sounding modes. Finally, experimental results show that by using an appropriate sounding mode the Doppler frequency can be estimated up to the range proposed in [64], even in a practical multipath scenario.

Paper B The signal model assumed in Paper A is based on the signal models from previous papers [64, 113, 114], which where created for the purpose of developing estimators. In Paper A these models are modified to include the spatio-temporal aperture. While the previous signal models are appropriate for describing the estimation algorithms, they significantly complicate the analysis of the impact of the spatio-temporal apertures on the estimation accuracy. In particular they are inadequate to describe parallel sounding systems. Therefore, a more general signal model is developed in Paper B in which the spatio-temporal aperture is represented in a straight-forward manner. Based on this new system model, we introduce the Doppler-(bi-)direction ambiguity function. The definition is inspired by the ambiguity theory used in the analysis and design of radar systems. It can be shown that the ambiguity

function is proportional to the objective function for the noise-less one-path scenario analyzed in Paper A. The results of the ambiguity analysis generalize the results presented in Paper A. We derive the Cramér-Rao lower bound (CRLB) on the estimation error for Doppler frequency and bi-direction. The spatio-temporal aperture appears directly in the expression of the CRLB. This leads to the derivation of a necessary and sufficient condition for spatio-temporal aperture to minimize the CRLBs for Doppler and bi-direction estimation in the one-path scenario. In essence the condition is that the apertures in time and space should all be mutually orthogonal. We prove that the same orthogonality condition is necessary to yield the minimum Bayesian CRLB in the multipath scenario.

Paper C We analyze the combined impact of phase-noise correlation and sounding mode in a TDM-MIMO sounding system on the capacity estimation based on the standard channel matrix estimator using the experimentally obtained phase-noise model developed in [115]. Monte Carlo simulations show that the predicted error of the ergodic capacity estimate is reduced compared to the case where phase-noise is white and Gaussian. We also show that the estimated ergodic capacity is highly influenced by the choice of the spatio-temporal aperture [Paper B]. It is found that there exist non-separable apertures which lead to the same capacity estimation error as separable apertures. However, the observations presented in Paper C raise a major concern regarding the feasibility of the standard capacity estimator, when applied to phase-noise impaired channel measurements.

Paper D In this paper we propose a new MIMO channel capacity estimator. The estimator is designed for the case where the available channel measurements are impaired by both phase-noise and additive noise. The proposed estimator exploits knowledge of the phase-noise autocorrelation function, which can be obtained by calibration measurements of the channel sounder. The accuracy of the proposed estimator is assessed by Monte Carlo simulations. The proposed estimator yields reliable estimates at signal-to-noise ratios relevant for wireless communication systems. The simulation results reveal an interesting phenomenon related to the spatio-temporal aperture. While a non-separable aperture deteriorates the estimation accuracy of the conventional capacity estimator, it oppositely improves accuracy of the proposed estimator.

4.2   Modelling and Estimation of the Per-Path Power Spectra

The Papers E, F, G, and H are concerned with Q2. We approach this problem by formulating a study model of the power spectral density (psd), designing an estimator of the model parameters, testing the applicability on measurement data, and finally, using the estimator on measurement data. The steps of the methodology require significant amounts of work and some of the steps need to be revised; as the models improve, the estimators need to be adapted as well. We present preliminary results of this ongoing process in Papers E, F, G, and H.

Paper E   In this contribution, we propose a characterization of the *bi-azimuth* (azimuth of arrival and azimuth of departure) dispersion of individual paths. For this purpose we introduce a bivariate generalized von-Mises-Fisher pdf and a maximum-likelihood estimator for its parameters. This distribution maximizes the entropy under the constraint that its first- and second-order moments are specified.

Preliminary experimental investigations were conducted to assess the applicability of the proposed characterization in real situations. The experimental results show that the estimated per-path psds are noticeably more concentrated in the bi-azimuth plane compared to the corresponding estimates obtained with the classical Bartlett spectrum.

Paper F   We propose a characterization of *bi-azimuth-delay* dispersion of individual paths. As in Paper E, the characterization relies on an entropy maximizing psd. Again, the obtained experimental results show that the per-path bi-azimuth-delay dispersion is significantly smaller than that one might infer from the corresponding footprints in the Bartlett spectrum. The obtained results also indicate dependency between dispersion in the azimuth and the delay dimensions.

Paper G   We characterize the *directional* per-path psd paths using the Fisher-Bingham-5 pdf. We derive a SAGE estimator for the model parameters, and apply the estimator to measurement data. The estimated per-path psd are more concentrated than the corresponding footprints in the Bartlett spectrum

Paper H   We model the per-path psd in the *direction-delay* domain. We use a SAGE algorithm to estimate the parameters of the direction–delay power spectral densities from measurement data.

4.3 Channel Modelling Using Stochastic Propagation Graphs

Paper I and Paper J focus on Q3. We develop a study model with the purpose of investigating the transition effect described in Section 3.3.

Paper I In this contribution we propose a channel model for the purpose of studying the specular-to-diffuse transition effect. We model the propagation environment by using random graphs. The vertices of a "propagation graph" represent scatterers and its edges model the propagation path in between scatterers. We propose a method to randomly generate propagation graphs with the intent to simulate a single-room scenario. Since the graph is not assumed cycle-free, reverberation phenomena can be modeled. Due to its recursive scattering structure the obtained model predicts an exponentially decaying delay-power spectrum as commonly reported from measurements. Furthermore, the obtained impulse responses exhibit a specular-to-diffuse transition.

Paper J In this contribution the propagation graph model proposed in Paper I is extended to include multiple transmitters and receivers. We develop a closed-form analytical expression for the transfer matrix of the propagation graph. This expression allows for faster computation of the received signal for a given propagation graph. This property makes the model feasible for computer simulations.

4.4 Discussion and Outlook

The thesis concerns three strongly related crafts in wireless communications: channel-sounding, -modeling, and -estimation. We have addressed three topics of central relevance to these crafts: optimization of spatio-temporal apertures for channel sounding, estimation of per-path power spectral densities (psds), and modeling of reverberant channels.

We have developed a theory for optimization of spatio-temporal apertures used in multiple-input multiple-output (mimo) channel sounding. We first focused on joint estimation of bi-direction and Doppler frequency from time-division multiplexing (tdm) mimo measurements. We have derived the necessary and sufficient conditions for spatio-temporal apertures to minimize the Cramér-Rao lower bound for the joint estimation of bi-direction and Doppler frequency. We introduced and analyzed a bi-spatio-temporal ambiguity function for spatio-temporal channel sounding. The analysis revealed that by proper design of the spatio-temporal aperture, the maximum estimable Doppler frequency of a tdm-mimo sounder coincides with that of a traditional single-input single-output sounder. The derived ambiguity function is

39

a means to test for "rank-1 ambiguity", *i.e.*, to test whether ambiguity occurs in the one-path case. Consequently, the developed theory applies only in the strict sense to the one-path case. However, the measurement results presented in Paper A demonstrate the utility of the theory in real measurement scenarios. The theory of spatio-temporal array optimization for joint estimation of Doppler frequency and bi-direction can be applied to other systems than radio channel sounding, *e.g.*, in the design of bi-static MIMO radar systems.

It was shown that the spatio-temporal aperture affects the accuracy of MIMO-capacity estimation from measurements impaired by colored phase-noise. We have proposed an improved capacity estimator, which exploits the second-order statistics of phase noise and the structure of the spatio-temporal aperture. We found that the proposed estimator, in contrast to previously published capacity estimators, works well for spatio-temporal arrays optimized for joint estimation of Doppler frequency and bi-direction. The derivation of the estimator relies on three main assumptions. Firstly, we have derived the capacity assuming a wide-sense stationary phase-noise process. Thus, we have neglected the non-stationary nature of phase-noise. Further work is necessary to clarify if the capacity estimator can be extended to account for this effect. Secondly, we have derived a capacity estimator for the MIMO channel including the antennas of the measurement system. Since the antenna arrays of measurement systems in most cases differ from the antennas of a communication systems, this effect should be investigated further. Secondly, we assumed that the MIMO channel matrix is time-invariant throughout the measurement. This assumption may not be fulfilled for real measurement scenarios. The considered capacity metric, which assumes a static channel, is not valid for the time-variant case. A more relevant approach would be to develop an estimator of the ergodic capacity.

The second topic considered in the thesis is estimation of the per-path psds resolved in directions and delay. We modeled the per-path psds using entropy-maximizing probability density functions (pdfs); the pdfs are defined by their first- and second-order moments. We have derived estimators of these parameters. The applicability of these estimators has been tested by using them to process measurement data. The main intent with this test was to evaluate the estimators in real measurement scenarios. Nonetheless, we were able to make an important empirical observation from this preliminary work: The obtained spread estimates are significantly smaller and the estimated psds are much more concentrated than corresponding results found in the literature. These findings indicate that the per-path directional spreads assumed in standard models are set too large. Further experimental investigations are needed to confirm this hypothesis. Initially, this can be done by processing already available measurement data. Theoretically, however, a test of this

hypothesis should be made from experiments designed especially for this purpose, and not from previously available data. If the observation holds true, this effect should by considered in (standardized) simulation models including direction dispersion.

Finally, we proposed a model of the specular-to-diffuse transition observed in measurements of reverberant channels. The model relies on a "propagation graph" where vertices represent scatterers and edges represent the wave propagation conditions between scatterers. The graph has a recursive structure, which permits modeling of the transfer function of the graph. We derived a closed-form expression of the infinite-bounce impulse response. This expression is used for simulation of the impulse response of randomly generated propagation graphs. The obtained realizations exhibit the well-observed exponential power decay versus delay and specular-to-diffuse transition. One interesting virtue of this type of model is that a diffuse component can be modeled by assuming specular interactions. The specular-to-diffuse transition occurs in the model because of a gradually increasing arrival rate of specular components. After a certain delay threshold, the individual specular components can no longer be considered as separate. Instead, the sum of specular components must be considered as a single diffuse component. This phenomenon is not accounted for in traditional channel models where the arrival rate is typically assumed constant over time. The proposed model has not yet been validated experimentally. To this end, key features such as the slope of the delay-power spectrum, must be derived to permit comparison of the model with measurement data. Work is currently ongoing in this direction.

References

[1] E. A. Bender, *An Introduction To Mathematical Modelling.*   John Wiley and Sons, 1978.

[2] D. Mooney and R. Swift, *A Course in Mathematical Modeling.*   The Mathematical Association of America, Inc., 1999.

[3] F. R. Giodano, M. D. Weir, and W. P. Fox, *A First Course in Mathematical Modeling*, 3rd ed.   Brooks/Cole, 2003.

[4] J. C. Maxwell, *Treatise on Electricity and Magnetism*, 3rd ed.   Dover Publications, June 1954, vol. 1.

[5] ——, *Treatise on Electricity and Magnetism*, 3rd ed.   Dover Publications, 1954, vol. 2.

[6] R. H. Clarke, "A statistical theory of mobile-radio reception," *Bell Labs Systems Technical Journal*, vol. 47, pp. 957–1000, July 1968.

[7] M. Franceschetti, "Stochastic rays pulse propagation," *IEEE Trans. Antennas Propag.*, vol. 52, no. 10, pp. 2742–2752, Oct. 2004.

[8] J. G. Proakis and M. Salehi, *Communications Systems Engineering*, 2nd ed.   Prentice-Hall, Inc., 2002.

[9] S. Verdú, *Multiuser Detection.*   Cambridge University Press, 1998.

[10] J. M. Hammersley, *Monte Carlo Methods.*   London: Methuen, 1964.

[11] W. C. Jakes, *Microwave Mobile Communications.*   New York: IEEE Press, 1974.

[12] H. Xu, D. Chizhik, H. Huang, and R. Valenzuela, "A generalized space-time multiple-input multiple-output (MIMO) channel model," *IEEE Trans. Wireless Commun.*, vol. 3, no. 3, pp. 966–975, May 2004.

[13] T. Zwick, C. Fischer, D. Didascalou, and W. Wiesbeck, "A stochastic spatial channel model based on wave-propagation modeling," *IEEE J. Sel. Areas Commun.*, vol. 18, no. 1, pp. 6 –15, Jan. 2000.

[14] T. Zwick, C. Fischer, and W. Wiesbeck, "A stochastic multipath channel model including path directions for indoor environments," *IEEE J. Sel. Areas Commun.*, vol. 20, no. 6, pp. 1178 – –1192, Aug. 2002.

[15] ETSI 3rd Generation Partnership Project (3GPP), "Universal mobile telecommunications system (UMTS); spatial channel model for multiple input multiple output (MIMO) simulations," ETSI, Tech. Rep. 3GPP TR 25.996 version 7.0.0 Release 7, June 2007.

[16] WINNER, "WINNER II channel models," WINNER II, Tech. Rep. D1.1.2 V1.2, 2008.

[17] A. F. Molisch, H. Asplund, R. H. M. Steinbauer, and T. Zwick, "The COST259 directional channel model—part i: Overview and methodology," *IEEE Trans. Wireless Commun.*, vol. 5, no. 12, pp. 3421–3433, Dec. 2006.

[18] H. Asplund, A. A. Glazunov, Molisch, K. I. Pedersen, and M. Steinbauer, "The COST 259 directional channel model—part ii: Macrocells," *IEEE Trans. Wireless Commun.*, vol. 5, no. 12, pp. 3434–3450, Dec. 2006.

[19] V. Erceg and *et al.*, "Channel models for fixed wireless applications," IEEE 802.16 Broadband Wireless Access Working Group, Tech. Rep. IEEE 802.16.3c-01/29r4, 2001.

[20] D. Molkdar, "Review on radio propagation into and within buildings," *Microwaves, Antennas and Propagation, IEE Proceedings H*, vol. 138, no. 1, pp. 61–73, 1991.

[21] H. Hashemi, "The indoor radio propagation channel," *Proc. IEEE*, vol. 81, no. 7, pp. 943–968, July 1993.

[22] J. B. Andersen, T. S. Rappaport, and S. Yoshida, "Propagation measurements and models for wireless communications channels," *IEEE Commun. Mag.*, vol. 33, no. 1, pp. 42–49, Jan. 1995.

[23] W. Tam and V. Tran, "Propagation modelling for indoor wireless communication," *Electronics & Communication Engineering Journal*, vol. 7, no. 5, pp. 221–228, 1995.

[24] B. H. Fleury and P. E. Leuthold, "Radiowave propagation in mobile communications: an overview of European research," *IEEE Commun. Mag.*, vol. 34, no. 2, pp. 70–81, Feb. 1996.

[25] K. Yu and B. Ottersten, "Models for MIMO propagation channels: a review," *Wireless Communications and Mobile Computing*, vol. 2, no. 7, pp. 653–666, Nov. 2002.

[26] T. Sarkar, J. Zhong, K. Kyungjung, A. Medouri, and M. Salazar-Palma, "A survey of various propagation models for mobile communication," *IEEE Antennas Propag. Mag.*, vol. 45, no. 3, pp. 51–82, June 2003.

[27] P. Almers, E. Bonek, A. Burr, N. Czink, M. Debbah, V. Degli-Esposti, H. Hofstetter, P. Kyolsti, D. Laurenson, G. Matz, A. Molisch, C. Oestges, and H. Ozcelik, "Survey of channel and radio propagation models for wireless MIMO systems," *Eurasip Journal on Wireless Communications and Networking*, vol. 12, pp. 1–19, 2007.

[28] J. D. Parsons, *The Mobile Radio Transmission Channel*, 2nd ed. Chichester, England: John Wiley and Sons, Ltd., 2000.

[29] H. L. Bertoni, *Radio Propagation for Modern Wireless Systems*. Prentice Hall, 2000.

[30] L. W. Barclay, *Propagation of Radiowaves*, 2nd ed. The Institute of Electrical Engineers, 2003.

[31] G. D. Durgin, *Space-Time Wireless Channels*. Prentice Hall, 2003.

[32] R. Vaughan and J. B. Andersen, *Channels, Propagation and Antennas for Mobile Communications*. Institution of Electrical Engineers, 2003.

[33] H. Sizun, *Radio Wave Propagation for Telecommunication Applications*, 3-540-40758-8, Ed. Springer-Verlag, 2005.

[34] A. F. Molisch, *Wireless Communications*. John Wiley & Sons, 2005.

[35] C. Oestges and B. Clerckx, *MIMO Wireless Communications*. Elsevier, 2007.

[36] K. Siwiak and Y. Bahreini, *Radiowave Propagation and Antennas for Personal Communications*, 3rd ed. Artech House, 2007.

[37] H. G. Gauch, *Scientific Method in Practice*. Cambridge University Press, 2003.

[38] G. Turin, F. Clapp, T. Johnston, S. Fine, and D. Lavry, "A statistical model of urban multipath propagation channel," *IEEE Trans. Veh. Technol.*, vol. 21, pp. 1–9, Feb. 1972.

[39] P. A. Bello, "Characterization of randomly time-invariant linear channels," *IEEE Trans. Commun. Syst.*, vol. CS-11, pp. 360–393, Dec. 1963.

[40] B. H. Fleury, "First- and second-order characterization of direction dispersion and space selectivity in the radio channel," *IEEE Trans. Inf. Theory*, vol. 46, no. 6, pp. 2027–2044, Sept. 2000.

[41] A. A. M. Saleh and R. A. Valenzuela, "A statistical model for indoor multipath propagation channel," *IEEE J. Sel. Areas Commun.*, vol. SAC-5, no. 2, pp. 128–137, Feb. 1987.

[42] Q. H. Spencer, B. Jeffs, M. Jensen, and A. Swindlehurst, "Modeling the statistical time and angle of arrival characteristics of an indoor multipath channel," *IEEE J. Sel. Areas Commun.*, vol. 18, no. 3, pp. 347–360, 2000.

[43] J. W. Wallace and M. A. Jensen, "Modeling the indoor MIMO wireless channel," *Antennas and Propagation, IEEE Transactions on*, vol. 50, no. 5, pp. 591–599, May 2002.

[44] M. Steinbauer, A. F. Molisch, and E. Bonek, "The double-directional radio channel," *IEEE Antennas Propag. Mag.*, vol. 43, no. 4, pp. 51–63, Aug. 2001.

[45] B. H. Fleury, M. Tschudin, R. Heddergott, D. Dahlhaus, and K. L. Pedersen, "Channel parameter estimation in mobile radio environments using the SAGE algorithm," *IEEE J. Sel. Areas Commun.*, vol. 17, no. 3, pp. 434–450, Mar. 1999.

[46] C. Balanis, *Antenna Theory: Analysis and Design*, 2nd ed. John Wiley and Sons, 1997.

[47] J. D. Parsons, D. A. Demery, and A. M. D. Turkmani, "Sounding techniques for wideband mobile radio channels: a review," *IEE Proceedings–I Communications, Speech and Vision*, vol. 138, no. 5, pp. 437–446, Oct. 1991.

[48] A. G. Burr, "Capacity bounds and estimates for the finite scatterers MIMO wireless channel," *IEEE J. Sel. Areas Commun.*, vol. 21, no. 5, pp. 812–818, 2003.

[49] P. J. Cullen, P. C. Fannin, and A. Molina, "Wide-band measurement and analysis techniques for the mobile radio channel," *IEEE Trans. Veh. Technol.*, vol. 42, no. 4, pp. 589–603, 1993.

[50] A. F. Molisch, K. Balakrishnan, D. Cassioli, C.-C. Chong, S. Emami, A. Fort, J. Karedal, J. Kunisch, H. Schantz, , and K. Siwiak, "A comprehensive model for ultrawideband propagation channels," in *Proc. IEEE Global Telecommun. Conf., Globecom 2005.*, 2005.

[51] S. Salous, P. Filippidis, R. Lewenz, I. Hawkins, N. Razavi-Ghods, and M. Abdallah, "Parallel receiver channel sounder for spatial and MIMO characterisation of the mobile radio channel," *IEE Proc. Commun.*, vol. 152, no. 6, pp. 912– 918, Dec. 2005.

[52] C. C. Martin, J. H. Winters, H. H. Z. N. R. Sollenberger, and A. Dixit, "Multiple-input multiple-output (MIMO) radio channel measurements and experimental implementation for EDGE," in *Conference Record of the Thirty-Fourth Asilomar Conference on Signals, Systems and Computers*, vol. 1, 2000, pp. 738–742.

[53] C. C. Martin, J. H. Winters, and N. R. Sollenberger, "Multiple-input multiple-output (MIMO) radio channel measurements," in *Proc. IEEE 52nd Vehicular Technology Conference Fall 2000, VTC2000-Fall.*, vol. 2, 774–779 2000.

[54] ——, "Multiple-input multiple-output (MIMO) radio channel measurements," in *2001 Digest IEEE Antennas and Propagation Society International Symposium.*, 2001, pp. 418–421.

[55] D. Chizhik, J. Ling, P. W. Wolniansky, R. A. Valenzuela, N. Costa, and K. Huber, "Multiple-input-multiple-output measurements and modeling in Manhattan," *IEEE J. Sel. Areas Commun.*, vol. 21, no. 3, pp. 321–331, Apr. 2003.

[56] D. H. Johnson and D. E. Dudgeon, *Array Signal Processing.* Prentice Hall, 1993.

[57] R. S. Thomä, D. Hampicke, A. Richter, G. Sommerkorn, A. Schneider, U. Trautwein, and W. Wirnitzer, "Identification of time-variant directional mobile radio channels," *IEEE Trans. Instrum. Meas.*, vol. 49, no. 2, pp. 357– 364, Apr. 2000.

[58] R. D. Tingley and K. Pahlavan, "Space-time measurement of indoor radio propagation," *IEEE Trans. Instrum. Meas.*, vol. 50, no. 1, pp. 22–31, Feb. 2001.

[59] A. Stucki, "PROPSound System Specifications Document: Concept and Specifications," Elektrobit AG, Switzerland," Internal Report, 2001.

[60] B. H. Fleury, P. Jourdan, and A. Stucki, "High-resolution channel parameter estimation for MIMO applications using the SAGE algorithm," in *Int. Zurich Seminar on Broadband Commun., Proceedings*, vol. 30, Feb. 2002, pp. 1–9.

[61] R. S. Thomä, M. Landmann, A. Richter, and U. Trautwein, *Multidimensional high-resolution channel sounding measurement.* Hindawi Publishing Corporation, 2005, ch. 13, pp. 241–270.

[62] J. Ø. Nielsen, J. B. Andersen, P. C. F. Eggers, G. F. Pedersen, K. Olesen, E. H. Sørensen, and H. Suda, "Measurements of indoor 16x32 wideband MIMO channels at 5.8 GHz," in *Proceedings of the 2004 International Symposium on Spread Spectrum Techniques and Applications*, Aug. 2004, pp. 864–868.

[63] C. E. Shannon, "Communication in the precense of noise," *Proc. of the IRE*, vol. 37, no. 1, pp. 10–21, 1949.

[64] X. Yin, B. Fleury, P. Jourdan, and A. Stucki, "Doppler frequency estimation for channel sounding using switched multiple-element transmit and receive

antennas," in *Proc. IEEE Global Telecommun. Conf., Globecom 2003*, vol. 4, Dec. 2003, pp. 2177–2181.

[65] D. S. Baum and H. Bölcskei, "Impact of phase noise on MIMO channel measurement accuracy," in *Proc. 2004 IEEE Vehicular Technology Conf.*, Sept. 2004.

[66] ——, "Information-theoretic analysis of MIMO channel sounding," Sept. 2007, submitted to the IEEE Tran. on Inf. Theory. [Online]. Available: http://www.nari.ee.ethz.ch/commth/pubs/p/phase07

[67] P. Almers, S. Wyne, F. Tufvesson, and A. Molisch, "Effect of random walk phase noise on MIMO measurements," in *Proc. IEEE 61st Vehicular Technology Conference, VTC2005-Spring*, vol. 1, 2005, pp. 141–145 Vol. 1.

[68] A. Taparugssanagorn and J. Ylitalo, "Reducing the impact of phase noise in the MIMO capacity estimation." in *Proc. Wireless Personal Multimedia Communications, WPMC*, sep 2005, pp. 527–531.

[69] A. Taparugssanagorn, X. Yin, J. Ylitalo, and B. Fleury, "Phase noise mitigation in channel parameter estimation for TDM MIMO channel sounding," in *Conference Record of the Forty-First Asilomar Conference on Signals, Systems and Computers, ACSSC*, Nov. 2007, pp. 656–660.

[70] A. Taparugssanagorn, J. Ylitalo, and B. Fleury, "Phase-noise in TDM-switched MIMO channel sounding and its impact on channel capacity estimation," in *Proc. IEEE Global Telecommun. Conf., Globecom 2007*, Nov. 2007, pp. 4559–4564.

[71] I. E. Telatar, "Capacity of multi-antenna Gaussian channels," Lucent Technologies, Bell laboratories," Technical Memorandum, Oct. 1995.

[72] ——, "Capacity of multi-antenna Gaussian channels," *European Trans. on Telecommun.*, vol. 10, pp. 585–595, 1999.

[73] A. Paulraj, R. Nabar, and D. Gore, *Introduction to Space-time Wireless Communications*. Cambridge University Press, 2003.

[74] P. Kyritsi, R. A. Valenzuela, and D. C. Cox, "Channel and capacity estimation errors," *IEEE Commun. Lett.*, vol. 6, no. 12, pp. 517–519, Dec. 2002.

[75] K.-H. Li, M. Ingram, and A. Van Nguyen, "Impact of clustering in statistical indoor propagation models on link capacity," *IEEE Trans. Commun.*, vol. 50, no. 4, pp. 521–523, Apr. 2002.

[76] H. Bölcskei, D. Gesbert, and A. Paulraj, "On the capacity of OFDM-based spatial multiplexing systems," *IEEE Trans. Commun.*, vol. 50, no. 2, pp. 225–234, Feb. 2002.

[77] Z. Tang and A. S. Mohan, "Impact of clustering in indoor MIMO propagation using a hybrid channelmodel," *EURASIP Journal of Applied Signal Processing*, vol. 2005, no. 11, pp. 1698–1711, 2005.

[78] T. Betlehem, T. D. Abhayapala, and T. A. Lamahewa, "Space-time MIMO channel modelling using angular power distributions," *Communications Theory Workshop, 2006. Proceedings. 7th Australian*, pp. 165–170, Feb. 2006.

[79] N. Czink, "The random-cluster model," Ph.D. dissertation, Forschungszentrum Telekommunikation Wien (ftw.), Dec. 2007.

[80] K. Mammasis, R. W. Stewart, and E. Pfann, "3-dimensional channel modeling using spherical statistics for multiple input multiple output systems," in *IEEE Wireless Communications and Networking Conference, WCNC,* Apr. 2008, pp. 769–774.

[81] C.-C. Chong, C.-M. Tan, D. I. Laurenson, S. McLaughlin, M. A. Beach, and A. R. Nix, "A new statistical wideband spatio-temporal channel model for 5-GHz band WLAN systems," *IEEE J. Sel. Areas Commun.,* vol. 21, no. 2, pp. 139–150, Feb. 2003.

[82] K. Yu, Q. Li, D. Cheung, and C. Prettie, "On the tap and cluster angular spreads of indoor WLAN channels," in *Proc. of the 59th IEEE Veh. Technol. Conf. (VTC),* vol. 1, 2004, pp. 218–222.

[83] N. Czink, P. Cera, , J. Salo, E. Bonek, J.-P. Nuutinen, and J. Ylitalo, "A framework for automatic clustering of parametric MIMO channel data including path powers," in *Proc. of the 64th IEEE Veh. Technol. Conf. (VTC),* 2006, pp. 1–5.

[84] N. Czink, C. Mecklenbräuker, and G. del Galdo, "A novel automatic cluster tracking algorithm," in *Proc. IEEE 17th Int. Symposium on Personal, Indoor and Mobile Radio Commun. PIMRC 2006,* 2006, pp. 1–5.

[85] J. A. Högbom, "Aperture synthesis with a non-regular distribution of interferometer baselines," *Astronomy and Astrophysics Supplement Series,* vol. 15, no. 3, pp. 417–426, 1974.

[86] R. O. Schmidt, "Multiple emitter location and signal parameter estimation," *IEEE Trans. Antennas Propag.,* vol. AP-34, no. 3, pp. 276–280, Mar. 1986.

[87] M. c. Vanderveen, C. B. Papadias, and A. Paulraj, "Joint angle and delay estimation (JADE) for multipath signals arriving at an antenna array," *IEEE Commun. Lett.,* vol. 1, no. 1, pp. 12–14, Jan. 1997.

[88] R. Roy and T. Kailath, "Esprit-estimation of signal parameters via rotational invariance techniques," *IEEE Trans. Aerosp. Electron. Syst.,* vol. 37, no. 7, pp. 984–995, July 1989.

[89] A. Richter, M. Landmann, and R. S. Thomä, "Maximum likelihood channel parameter estimation from multidimensional channel sounding measurements," in *The 57th IEEE Semiannual Vehicular Technology Conference,* vol. 2, Apr. 2003, pp. 1056–1060.

[90] R. Thoma, M. Landmann, G. Sommerkorn, and A. Richter, "Multidimensional high-resolution channel sounding in mobile radio," in *Proc. 21st IEEE Instrumentation and Measurement Technology Conf., IMTC,* vol. 1, May 2004, pp. 257–262.

[91] J. A. Fessler and A. O. Hero, "Space-alternating generalized expectation-maximization algorithm," *IEEE Trans. Signal Process.,* vol. 42, no. 10, pp. 2664–2677, Oct. 1994.

[92] M. Bengtsson and B. Volcker, "On the Estimation of Azimuth Distributions and Azimuth Spectra," in *Proc. of the 54th IEEE Veh. Technol. Conf. (VTC)*, vol. 3, Oct. 2001, pp. 1612–1615 vol.3.

[93] X. Yin, "High-resolution parameter estimation for MIMO channel sounding," Ph.D. dissertation, Aalborg University, July 2006.

[94] C. B. Ribeiro, E. Ollila, and V. Koivunen, "Stochastic maximum-likelihood method for MIMO propagation parameter estimation," *IEEE Trans. Signal Process.*, vol. 55, no. 1, pp. 46–55, Jan. 2007.

[95] C. B. Ribeiro, "Propagation parameter estimation in MIMO systems," Ph.D. dissertation, Helsinki University of Technology, Apr. 2008.

[96] J. Kunisch and J. Pamp, "Measurement results and modeling aspects for the UWB radio channel," in *IEEE Conf. on Ultra Wideband Systems and Technologies, 2002. Digest of Papers*, May 2002, pp. 19–24.

[97] ——, "An ultra-wideband space-variant multipath indoor radio channel model," in *Ultra Wideband Systems and Technologies, 2003 IEEE Conf. on*, Nov. 2003, pp. 290–294.

[98] ——, "UWB radio channel modeling considerations," in *Proc. ICEAA 2003*, Turin, Sept. 2003.

[99] M. Franceschetti, "Power delay profile in a cluttered environment," in *Proc. 2004 IEEE Int. Conf. on Commun., ICC*, vol. 6, June 2004, pp. 3188–3192.

[100] M. Franceschetti, J. Bruck, and L. J. Schulman, "A random walk model of wave propagation," *IEEE Trans. Antennas Propag.*, vol. 52, no. 5, pp. 1304–1317, May 2004.

[101] H. Kuttruff, *Room Acoustics*. London: Taylor & Francis, 2000.

[102] W. C. Sabine, *Collected Papers on Acoustics by Wallace Clement Sabine*. New York: Dover, 1964, originally publiced by Harvard University Press, 1922.

[103] C. F. Eyring, "Reverberation time in 'dead' rooms," *The Journal of the Acoustical Society of Amarica*, vol. 1, no. 2, p. 241, 1930.

[104] R. Gerlach, "The reverberation process as Markoff chain-theory and initial model experiments," in *Auditorium Acoustics, The Proceedings of an International Symposium on Architectural Acoustics*, R. Mackenzie, Ed. Applied Science Publishers, 1975, pp. 101–114.

[105] T. H. Lehman, "A statistical theory of electromagnetic fields in complex cavities," Otto von Guericke University of Magdeburg, Tech. Rep., May 1993.

[106] C. Holloway, M. Cotton, and P. McKenna, "A model for predicting the power delay profile characteristics inside a room," *IEEE Trans. Veh. Technol.*, vol. 48, no. 4, pp. 1110–1120, July 1999.

[107] R. Rudd and S. Saunders, "Statistical modelling of the indoor radio channel - an acoustic analogy," in *Proc. Antennas and Propagation Twelfth International Conference on (Conf. Publ. No. 491)*, vol. 1, 31 March–3 April 2003, pp. 220–224.

[108] M. Otterskog, "Modelling of propagation environments inside a scattered field chamber," in *IEEE 61st Vehicular Technology Conference, VTC 2005-Spring*, vol. 1, May 2005, pp. 102–105.

[109] R. F. Rudd, "The prediction of indoor radio channel impulse response," in *Antennas and Propagation, 2007. EuCAP 2007. The Second European Conference on*, Nov. 2007, pp. 1–4.

[110] O. Delangre, P. D. Doncker, M. Lienard, and P. Degauque, "Delay spread and coherence bandwidth in reverberation chamber," *Electronics Letters*, vol. 44, pp. 328–329, Feb. 2008.

[111] J. B. Andersen, J. Ødum. Nielsen, G. Bauch, and M. Herdin, "The large office environment-measurement and modeling of the wideband radio channel," in *The 17th Annual IEEE Int. Symposium on Personal Indoor and Mobile Radio Commun.*, 2006.

[112] J. B. Andersen, J. Ø. Nielsen, G. F. Pedersen, G. Bauch, and J. M. Herdin, "Room electromagnetics," *IEEE Antennas Propag. Mag.*, vol. 49, no. 2, pp. 27–33, Apr. 2007.

[113] X. Yin, B. Fleury, P. Jourdan, and A. Stucki, "Polarization estimation of individual propagation paths using the SAGE algorithm," in *Proc. 14th IEEE on Personal, Indoor and Mobile Radio Communications, PIMRC*, vol. 2, Sept. 2003, pp. 1795–1799.

[114] B. H. Fleury, X. Yin, P. Jourdan, and A. Stucki, "High-resolution channel parameter estimation for communication systems equipped with antenna arrays," in *Proc. 13th IFAC Symposium on System Identification (SYSID 2003), Rotterdam, The Netherlands*, no. ISC-379, 2003.

[115] A. Taparugssanagorn, M. Alatossava, V. M. Holappa, and J. Ylitalo, "Experimental study on impact of phase noise in MIMO channel sounder on SAGE," 2007, accepted for publication at IET Proceedings Microwaves, Antennas & Propagation.

Joint Estimation of Doppler Frequency and Directions in Channel Sounding Using Switched Tx and Rx Arrays

Troels Pedersen, Claus Pedersen, Xuefeng Yin, Bernard H. Fleury,
Rene R. Pedersen, Biljana Bozinovska, Asger Hviid, Patrik Jourdan,
and Andreas Stucki

Abstract

To save hardware equipment and reduce the effort to calibrate the system, channel sounding with Tx and Rx antenna arrays is commonly performed in a time division multiplexing (TDM) mode where the array elements are successively switched. We refer to this technique as TDM-MIMO (multiple-input multiple-output) channel sounding. A recent study [1] shows that the ISI-SAGE algorithm [2], [3] applied in combination with TDM-MIMO channel sounding makes it possible to extend the Doppler frequency (DF) estimation range (DFER) by a factor at least equal to the product of the element numbers of the Tx and Rx arrays compared to the traditionally used DFER. The extension is significant when arrays with large element numbers are employed.

In this paper we derive the signal model for TDM-MIMO channel sounding and report analytical investigations showing that the above DFER extension requires selection of switching modes (SMs) tailored to the array characteristics. The SM of a switched array is the temporal order in which the array elements are switched. In fact, the traditionally used SMs of uniform linear and planar arrays where the elements are switched according to their natural spatial ordering prove to be inappropriate as they lead to an ambiguity in the joint estimation of DF and directions. We also introduce the concept of normalized side-lobe level (NSL) associated to the SM of a switched array. We show that minimizing the NSL is a sensible criterion for the identification of SM leading to DF and direction estimates with nearly optimum performance in terms of root mean square estimation error. Finally experimental investigations illustrate the impact of the SM of a uniform planar array on the behaviour of the DF and direction of arrival estimates computed with the ISI-SAGE algorithm.

A.1 Introduction

Deploying multiple-element antennas at the transmitter (Tx) and the receiver (Rx) combined with space-time coding can substantially increase the capacity of mobile radio communication systems [4], [5] and [6]. A system or technique using multiple-element Tx and Rx antennas is called a multiple-input multiple-output (MIMO) system or technique. The design and optimization of MIMO communication systems require realistic models of the propagation channel that incorporate dispersion in direction or equivalently space selectivity jointly at both Tx and Rx sites. High-resolution parameter estimation has become an essential tool to extract the critical model parameters from measurement data. The improved-search-and-initialization space-alternating generalized expectation-maximization (ISI-SAGE) algorithm [2], [3] has recently been proposed for joint estimation of the polarization matrix, relative

delay, Doppler frequency (DF), direction, i.e. azimuth and co-elevation angles, of departure (DoD), and direction of arrival (DoA) of propagation paths between the Tx site and the Rx site. Experimental investigations in [2], [3] demonstrate the high potential of the algorithm for detailed propagation studies.

MIMO channel sounders commonly operate in a time-division multiplex (TDM) mode in order to save hardware equipment and reduce the effort to calibrate the system. The sounding signal is fed successively at the ports of the array elements at the Tx, and while any one of these elements transmits, the ports of the antenna elements at the Rx are sensed successively. We understand an element pair to be a pair containing an element of the Tx array in first position and an element of the Rx array in second position. A measurement cycle denotes the process where all element pairs are switched once. A cycle interval is the period separating the beginning of two consecutive measurement cycles. The separation between the beginning of two consecutive sensing periods within one measurement cycle is called the switching interval. The cycle rate and the switching rate are the inverses of the cycle interval and the switching interval respectively. Notice that the ratio of the switching rate to the cycle rate is at least equal to the product of the element numbers of the two arrays.

It was traditionally believed, that the maximum absolute DF that can be estimated using the TDM-MIMO sounding technique equals half the cycle rate. Therefore, by keeping the switching rate unchanged, large element numbers in the arrays result in a low cycle rate and consequently lead to a small DF estimation range (DFER). However, a recent study [1] has shown that the maximum absolute DF that can be estimated using the TDM-MIMO sounding technique actually equals half the switching rate. This enlarged DFER is independent of the element numbers of the arrays.

In this paper, we show that the extension of the DFER proposed in [1] may result in an ambiguity in the estimation of the DF and directions (DoD and DoA). The estimates of the path parameters are computed in the maximization (M-) step of the ISI-SAGE algorithm to be the solution that maximizes a given objective function. The ambiguity occurs when this objective function exhibits multiple maxima. This situation may happen when the DFER is enlarged from minus to plus half the switching rate depending on the switching mode (SM) and the characteristics (e.g. the layouts and the element radiation patterns) of the arrays. The SM of an array describes the temporal order in which the array elements are switched. This paper analyses the impact of the SMs of the arrays in TDM-MIMO sounding on the joint estimation of DF and directions using the ISI-SAGE algorithm by means of theoretical and experimental investigations combined with Monte-Carlo simulations.
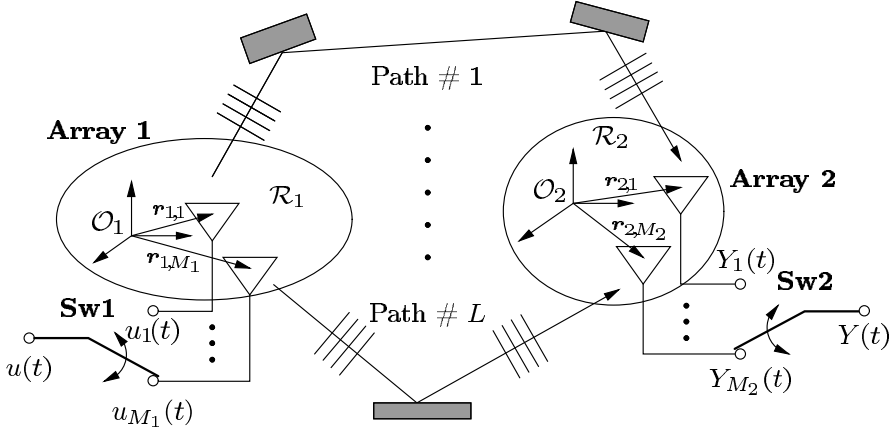
Fig. A.1: Signal model for the TDM-MIMO sounding technique.

The paper is organized as follows. The MIMO radio channel model is introduced in Section A.2. Section A.3 presents the signal model for TDM-MIMO channel sounding. In Section A.4 the objective function used in the M-step of the ISI-SAGE algorithm is derived. Investigations of a case study considering TDM-SIMO (single-input multiple-output) channel sounding with a uniform linear array give insight into the ambiguity problem and the necessary and sufficient conditions for it to occur. In Section A.5 the impact of the SM on the root mean square estimation errors (RMSEEs) of the DF and DoA estimates is assessed via Monte Carlo simulations. In Section A.6 experimental investigations compare the performance of the DF and DoA estimators when applying the conventionally used SM and an optimized SM to a uniform planar array. Finally, concluding remarks are addressed in Section A.7.

A.2 Signal Model for MIMO Systems

Let us consider the propagation environment depicted in Fig. A.1. A certain number, L, of waves propagate along different paths from the M_1 antenna elements forming Array 1 to the M_2 antenna elements forming Array 2. Along its path a wave interacts with a certain number of scatterers. We use the index $k \in \{1, 2\}$ for the arrays. Following [7], we assume that the far-field condition holds, and that the elements of Array k are confined in a region $\mathcal{R}_k$, in which the plane wave approximation is accurate. A coordinate system is specified at an arbitrary origin $\mathcal{O}_k$ in $\mathcal{R}_k$. The individual locations of the elements of

Array k are determined by the vectors $\mathbf{r}_{k,m} \in \mathbb{R}^3, m = 1, \ldots, M_k$. Here, $\mathbb{R}$
denotes the real line.

Let $\mathbf{u}(t) \doteq [u_1(t), \ldots, u_{M_1}(t)]^\mathsf{T}$ denote the (complex baseband represen-
tation of the) signal vector at the input of Array 1. Here, $[\cdot]^\mathsf{T}$ is the transpose
operator. The contribution of the ℓth wave to the outputs of Array 2 can be
written in vector notation as

$$\mathbf{s}(t; \boldsymbol{\theta}_\ell) = \alpha_\ell \exp\{j2\pi\nu_\ell t\}\mathbf{c}_2(\boldsymbol{\Omega}_{2,\ell})\mathbf{c}_1(\boldsymbol{\Omega}_{1,\ell})^\mathsf{T}\mathbf{u}(t - \tau_\ell). \qquad \text{(A.1)}$$

In this expression, $\boldsymbol{\theta}_\ell \doteq [\boldsymbol{\Omega}_{1,\ell}, \boldsymbol{\Omega}_{2,\ell}, \tau_\ell, \nu_\ell, \alpha_\ell]$ is a vector whose entries are
the parameters characterizing the ℓth path: $\boldsymbol{\Omega}_{1,\ell}, \boldsymbol{\Omega}_{2,\ell}, \tau_\ell, \nu_\ell$, and α_ℓ denote,
respectively its DoD, DoA, propagation delay, DF, and complex weight (or
gain). We describe a direction as a unit vector $\boldsymbol{\Omega}$ with initial point anchored
at the reference location, or equivalently as the terminal point of this vector,
i.e. a point located on a unit sphere centered at the reference point. Then, $\boldsymbol{\Omega}$
is uniquely determined by its spherical coordinates $(\phi, \theta) \in [-\pi, \pi) \times [0, \pi]$
according to $\boldsymbol{\Omega} = [\cos(\phi)\sin(\theta), \sin(\phi)\sin(\theta), \cos(\theta)]^\mathsf{T}$. The angles ϕ and
θ are referred to as respectively the azimuth and the co-elevation of $\boldsymbol{\Omega}$. The
M_k-dimensional complex vector $\mathbf{c}_k(\boldsymbol{\Omega})$ represents the response of Array k
to a wave impinging from direction $\boldsymbol{\Omega}$. Provided coupling effects between
the array elements are negligible, $\mathbf{c}_k(\boldsymbol{\Omega}) = [f_{k,m}(\boldsymbol{\Omega}) \exp\{j\frac{2\pi}{\lambda_0}(\boldsymbol{\Omega}^\mathsf{T}\mathbf{r}_{k,m})\}; m = 1, \ldots, M_k]^\mathsf{T}$. The function $f_{k,m}(\boldsymbol{\Omega})$ is the complex electric radiation patterns
of the mth element in Array k, and λ_0 denotes the carrier wavelength.

The signal vector $\mathbf{Y}(t) \doteq [Y_1(t), \ldots, Y_{M_2}(t)]^\mathsf{T}$ representing the outputs
of Array 2 is given by

$$\mathbf{Y}(t) = \sum_{\ell=1}^{L} \mathbf{s}(t; \boldsymbol{\theta}_\ell) + \sqrt{\tfrac{N_0}{2}}\mathbf{W}(t), \qquad \text{(A.2)}$$

where $\mathbf{W}(t) \doteq [W_1(t), \ldots, W_{M_2}(t)]^\mathsf{T}$ is standard M_2-dimensional complex
temporally and spatially white Gaussian noise, and N_0 is a positive constant.

A.3   TDM Channel Sounding Technique

Sounding of the propagation channel is performed in a TDM mode according
to the time structure depicted in Fig. A.2. As depicted in Fig. A.1, the sounding
signal is fed via Switch 1 (Sw1) during a sounding period T_t successively to the
ports of the elements of Array 1. While any element of Array 1 is active, the
ports of the elements of Array 2 are sensed during T_s successively by Switch
2 (Sw2). The period separating two consecutive sensing intervals is denoted
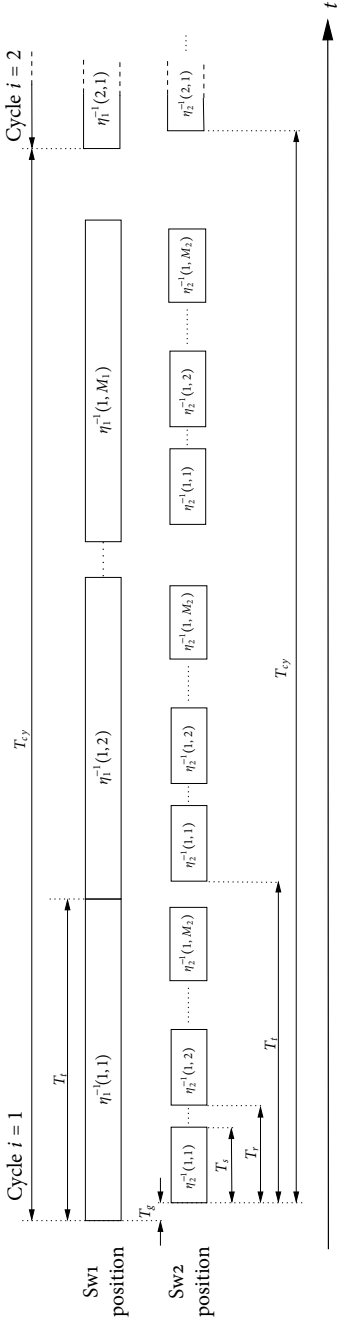by T_r. Clearly, $T_r \geq T_s$ and $T_t = M_2 T_r$. A measurement cycle during which all

Fig. A.2: *The considered TDM measurement mode.*

element pairs are switched once lasts $M_1 T_t$ seconds. The separation between the beginnings of two consecutive measurement cycles is called the measurement cycle interval and is denoted by T_{cy}. The cycle repetition rate is the ratio $R \doteq \frac{T_{cy}}{M_1 T_t} \geq 1$. Notice that the switching rate T_r^{-1} is related to the measurement cycle rate T_{cy}^{-1} according to $T_r^{-1} = M_1 M_2 R T_{cy}^{-1}$. The guard interval T_g in Fig. A.2 is irrelevant in the subsequent investigations. The motivation for introducing this interval can be found in [7]. One measurement run consists of I cycles.

To characterize the SM of a switched array, we first need to define a (spatial) indexing of the array elements which is then kept fixed. The natural element indexing for a uniform linear array is according to the element spatial ordering, starting at one end. Similarly the natural element indexing of a uniform planar array is determined first by the order of the element row and then by the element order inside its row. The SM of an array during one cycle is entirely defined by a permutation of the element indices. Let $\eta_k(i, \cdot)$ denote (the permutation describing) the SM of Array k during the ith cycle. Referring to Fig. A.2, the beginning of the interval when the element pair (m_1, m_2) is switched in the ith cycle is $t_{i,m_1,m_2} \doteq \left(i - \frac{I+1}{2}\right) T_{cy} + \left(\eta_1(i, m_1) - \frac{M_1+1}{2}\right) T_t + \left(\eta_2(i, m_2) - \frac{M_2+1}{2}\right) T_r$. Clearly, $\eta_k(i, m_k)$ is the time index of the interval during which the m_kth element of Array k is switched during the ith cycle ($m_k = 1, \ldots, M_k$). Hence, $\eta_k(i, \cdot)$ maps a spatial index onto a time index. The inverse mapping $\eta_k^{-1}(i, \cdot)$ (reported on Fig. A.2) determines the temporal order in which the elements of Array k are sequentially switched in the ith cycle. Notice that the SM of Array 2 does not depend on which element of Array 1 is active during each cycle, i.e. $\eta_2(i, \cdot)$ does not depend on m_1. For notational convenience we identify the permutation $\eta_k(i, \cdot)$ with the vector $\boldsymbol{\eta}_k(i) = [\eta_k(i, m_k), m_k = 1, \ldots, M_k]$. If $\boldsymbol{\eta}_k(i) = \boldsymbol{\eta}_k, i = 1, \ldots, I$, the SM is called cycle-independent. The identity SM $\boldsymbol{\eta}_k = [1, \ldots, M_k]$ switches the elements of Array k in their spatial order.

Following the same notation as in [7], the scalar signal at the output of Sw2 reads

$$Y(t) = \sum_{\ell=1}^{L} s(t; \boldsymbol{\theta}_\ell) + \sqrt{\tfrac{N_0}{2}} q_2(t) W(t), \tag{A.3}$$

where $W(t)$ denotes standard complex white Gaussian noise and $q_2(t)$ is an indicator function, i.e. with range $\{0,1\}$, which takes value one if, and only if, some element of Array 2 is switched by Sw2. Moreover,

$$s(t; \boldsymbol{\theta}_\ell) = \alpha_\ell \exp\{j 2\pi \nu_\ell t\} \mathbf{c}_2(\boldsymbol{\Omega}_{2,\ell})^\mathsf{T} \mathbf{U}(t; \tau_\ell) \mathbf{c}_1(\boldsymbol{\Omega}_{1,\ell}),$$

where $\mathbf{U}(t; \tau_\ell)$ is the $M_2 \times M_1$ sounding matrix $\mathbf{U}(t; \tau_\ell) \doteq \mathbf{q}_2(t) \mathbf{q}_1(t)^\mathsf{T} u(t - \tau_\ell)$, with $u(t)$ denoting the signal at the input of Sw1. The M_2 dimensional vector-valued functions $\mathbf{q}_k(t)$ characterize the timing of Swk. More specifi-

cally, the m_kth entry of $\mathbf{q}_k(t)$ is an indicator function which takes value one, if and only if, Swk switches the m_kth element of Array k [7].

A.4 Objective Function used in the Estimation of the DF and the Directions

A.4.1 TDM-MIMO Channel Sounding

According to [7] at each iteration of the ISI-SAGE algorithm, the parameter estimates of the ℓth path are updated successively in the M-step of the algorithm. This step computes the argument maximizing an objective function $|z(\bar{\boldsymbol{\theta}}_\ell; \hat{x}_\ell)|$, where $\bar{\boldsymbol{\theta}}_\ell \doteq [\boldsymbol{\Omega}_{1,\ell}, \boldsymbol{\Omega}_{2,\ell}, \tau_\ell, \nu_\ell]$ and $|\cdot|$ denotes the norm of the scalar or the vector given as an argument. Notice that the objective function coincides with the maximum-likelihood estimate (MLE) of $\hat{\boldsymbol{\theta}}_\ell$ in a one-path scenario, in which case $\hat{x}_\ell(t) = y(t)$. The function $z(\bar{\boldsymbol{\theta}}_\ell; \hat{x}_\ell)$ is given by

$$z(\bar{\boldsymbol{\theta}}_\ell; \hat{x}_\ell) \doteq \tilde{\mathbf{c}}_2(\boldsymbol{\Omega}_{2,\ell})^{\mathsf{H}} \mathbf{X}_\ell(\tau_\ell, \nu_\ell; \hat{x}_\ell) \tilde{\mathbf{c}}_1(\boldsymbol{\Omega}_{1,\ell})^* \qquad \text{(A.4)}$$

with $[\cdot]^{\mathsf{H}}$ denoting the Hermitian operator, $[\cdot]^*$ representing the complex conjugate, and $\tilde{\mathbf{c}}_k(\boldsymbol{\Omega}) \doteq |\mathbf{c}_k(\boldsymbol{\Omega})|^{-1} \mathbf{c}_k(\boldsymbol{\Omega})$ being the normalized response of Array k. The entries of the $M_2 \times M_1$ dimensional matrix $\mathbf{X}(\tau_\ell, \nu_\ell; \hat{x}_\ell)$ read

$$X_{\ell, m_2, m_1}(\tau_\ell, \nu_\ell; \hat{x}_\ell) = \sum_{i=1}^{I} \Big[\exp\left\{-j2\pi\nu_\ell t_{i,m_1,m_2}\right\}$$
$$\cdot \int_0^{T_s} u^*(t - \tau_\ell) \exp\{-j2\pi\nu_\ell t\} \hat{x}_\ell(t + t_{i,m_1,m_2}) \, dt \Big], \quad \text{(A.5)}$$

$m_k = 1, \ldots, M_k$, $k = 1, 2$. In (A.5) $\hat{x}_\ell(t) = y(t) - \sum_{\ell'=1, \ell' \neq \ell}^{L} s(t; \hat{\boldsymbol{\theta}}_{\ell'})$, with $\hat{\boldsymbol{\theta}}_{\ell'}$ denoting the current estimate of $\boldsymbol{\theta}_{\ell'}$, is an estimate of the so-called admissible hidden data $X_\ell(t) = s(t; \boldsymbol{\theta}_\ell) + \sqrt{\frac{N_0}{2}} q_2(t) W(t)$ calculated in the expectation (E-) step of the ISI-SAGE algorithm. The reader is referred to [8] for the properties of the SAGE algorithm and the related terminology.

In the subsequent analysis of the behavior of the objective function versus the DF, the DoD and DoA we make the following four simplifying assumptions: (A) The antenna elements are isotropic; (B) The phase change due to the DF within T_s is neglected, i.e. the term $\exp\{-j2\pi\nu_\ell t\}$ in (A.5) is set equal to 1. As shown in [1] this effect can be easily included into the model and its impact on the performance of the DF estimate proves to be negligible; (C) We assume that the remaining interference contributed by the waves ℓ', $\ell' = \{1, \ldots, L\}/\{\ell\}$ in the estimate $\hat{x}_\ell(t)$ computed in the E-step of Path ℓ is negligible, i.e.

$$\hat{x}_\ell(t) = s(t; \boldsymbol{\theta}_\ell) + \sqrt{\frac{N_0}{2}} q_2(t) W(t).$$

Under this assumption, the M-step of Path ℓ is derived based on an equivalent
signal model where only Path ℓ is present. If we further focus the attention on
one particular path, which without loss of generality is selected to be Path 1,
then (A.3) with $L = 1$ is the equivalent signal model for the derivation of the
M-step of Path 1. In this case, $\hat{x}_1(t) = y(t)$ and the MLE of $\bar{\boldsymbol{\theta}}_1$ is computed
in the M-step. For notational convenience we shall drop the indexing for the
parameters of Path 1 in the sequel; (D) As the focus is on the estimation of
the DF, DoD, and DoA, we further assume that the ISI-SAGE algorithm has
perfectly estimated the delay of Path 1 or has knowledge of it. As a result
$z(\bar{\boldsymbol{\theta}}; y)$ reduces to a function of $\boldsymbol{\Omega}_1$, $\boldsymbol{\Omega}_2$, and v according to

$$
z(v, \boldsymbol{\Omega}_1, \boldsymbol{\Omega}_2; y) = \sum_{i=1}^{I} \sum_{m_2=1}^{M_2} \sum_{m_1=1}^{M_1} \tilde{c}_{1,m_1}(\boldsymbol{\Omega}_1)^* \tilde{c}_{2,m_2}(\boldsymbol{\Omega}_2)^*
$$
$$
\cdot \exp\{-j2\pi v t_{i,m_1,m_2}\} \int_0^{T_s} u(t - \tau')^* y(t + t_{i,m_1,m_2}) \, dt. \quad \text{(A.6)}
$$

The notation $(\cdot)'$ designates the true value of the parameter given as an
argument.

Under the above assumptions, by dropping a constant term and normal-
izing by $\frac{1}{IM_1M_2}$, (A.6) can be cast as

$$
z(v, \boldsymbol{\Omega}_1, \boldsymbol{\Omega}_2; y) = \sum_{i=1}^{I} R_i(\check{v}) S_i(\check{\boldsymbol{\Omega}}_1, \check{v}) T_i(\check{\boldsymbol{\Omega}}_2, \check{v}) + V(v, \boldsymbol{\Omega}_1, \boldsymbol{\Omega}_2) \quad \text{(A.7)}
$$

with the notational convention $(\check{\cdot}) \doteq (\cdot)' - (\cdot)$. Moreover,

$$
R_i(\check{v}) \doteq \frac{1}{I} \exp\{j2\pi\check{v}\left(i - \tfrac{I+1}{2}\right) T_{cy}\},
$$
$$
S_i(\check{\boldsymbol{\Omega}}_1, \check{v}) \doteq \frac{1}{M_1} \sum_{m_1=1}^{M_1} \exp\left\{j2\pi \frac{\check{\boldsymbol{\Omega}}_1^{\mathsf{T}} \mathbf{r}_{1,m_1}}{\lambda_0} + j2\pi\check{v}\left(\eta_1(i, m_1) - \tfrac{M_1+1}{2}\right) T_t\right\},
$$
$$
T_i(\check{\boldsymbol{\Omega}}_2, \check{v}) \doteq \frac{1}{M_2} \sum_{m_2=1}^{M_2} \exp\left\{j2\pi \frac{\check{\boldsymbol{\Omega}}_2^{\mathsf{T}} \mathbf{r}_{2,m_2}}{\lambda_0} + j2\pi\check{v}\left(\eta_2(i, m_2) - \tfrac{M_2+1}{2}\right) T_r\right\}.
$$
$$
\text{(A.8)}
$$

The noise term $V(v, \boldsymbol{\Omega}_1, \boldsymbol{\Omega}_2)$ can be derived analogously to $V(v)$ in [1]. Notice
that the expressions in the arguments of the exponential terms in the sum-
mands of $S_i(\check{\boldsymbol{\Omega}}_1, \check{v})$ and $T_i(\check{\boldsymbol{\Omega}}_2, \check{v})$ reveal respectively a coupling depending
on $\eta_1(i, \cdot)$ in the estimation of the DoD and the DF and a coupling depending
on $\eta_2(i, \cdot)$ in the estimation of the DoA and the DF.

A.4.2 Case Study: TDM-SIMO Channel Sounding with Uniform Linear Array

In this subsection we investigate in detail the above mentioned coupling and in particular how the SM affects the objective function of the DF and direction MLEs. To keep the discussion simple we restrict the attention to a special case where Array 1 consists of one element ($M_1 = 1$) and Array 2 is uniform and linear. In this case, the DoD cannot be estimated and (A.7) reduces to

$$z(\nu, \mathbf{\Omega}_2; y) = \sum_{i=1}^{I} R_i(\check{\nu}) T_i(\check{\mathbf{\Omega}}_2, \check{\nu}) + V(\nu, \mathbf{\Omega}_2). \tag{A.9}$$

We investigate the behavior of the absolute value of (A.9) in the noiseless case ($V(\nu, \mathbf{\Omega}_2) = 0$). Array 2 consists of M_2 equidistant isotropic elements with locations $\mathbf{r}_{2,m_2} = \left[\frac{m_2 \lambda_0}{2}, 0, 0\right]^\mathsf{T}$, $m_2 = 1, \ldots, M_2$. The inner products arising in the response of this array are calculated as $\mathbf{\Omega}_2^\mathsf{T} \mathbf{r}_{2,m_2} = \omega \frac{m_2 \lambda_0}{2}$, $m_2 = 1, \ldots, M_2$, where $\omega \doteq \cos(\phi_2) \sin(\theta_2)$. The parameter ω can be interpreted as a spatial frequency. It can be also written as $\omega = \cos(\psi)$ where ψ is the angle between the impinging direction and the array axis. This angle is the only characteristic of the incident direction that can be uniquely determined with a linear array.

The absolute value of (A.9) reads in this case

$$|z(\nu, \mathbf{\Omega}_2; y)| = |z(\check{\nu}, \check{\omega}; y)|. \tag{A.10}$$

If the SM is cycle-independent, the right-hand expression in (A.10) factorizes according to

$$|z(\check{\nu}, \check{\omega}; y)| = |G(\check{\nu})| \cdot |T(\check{\omega}, \check{\nu})|, \tag{A.11}$$

where

$$G(\check{\nu}) \doteq \frac{\sin(\pi \check{\nu} I T_{cy})}{I \sin(\pi \check{\nu} T_{cy})},$$

$$T(\check{\omega}, \check{\nu}) \doteq \frac{1}{M_2} \sum_{m_2=1}^{M_2} \exp\left\{ j m_2 \pi \check{\omega} + j 2\pi \check{\nu}[\eta_2(m_2) - \tfrac{M_2+1}{2}] T_r \right\}.$$

We investigate the impact of different SMs on (A.11) for the setting of the TDM-SIMO system and the one-wave scenario specified in Table A.1. The wave is incident perpendicular to the array axis and its DF is 0 Hz. Notice that from (A.10) the behaviour of the objective function only depends on the DF deviation from the true DF so that the choice of the latter within the range $\left(-\frac{1}{2T_r}, \frac{1}{2T_r}\right]$ is irrelevant. Fig. A.3(a), A.3(b), and A.3(c) depict the graphs of respectively $|G(\check{\nu})|$, $|T(\check{\omega}, \check{\nu})|$, and $|z(\check{\nu}, \check{\omega}; y)|$ in (A.11), when the conventionally used identity SM, is applied. Notice that the range of $\check{\nu}$ is $\left(-\frac{1}{2T_r}, \frac{1}{2T_r}\right] = (-200, 200]$ Hz.

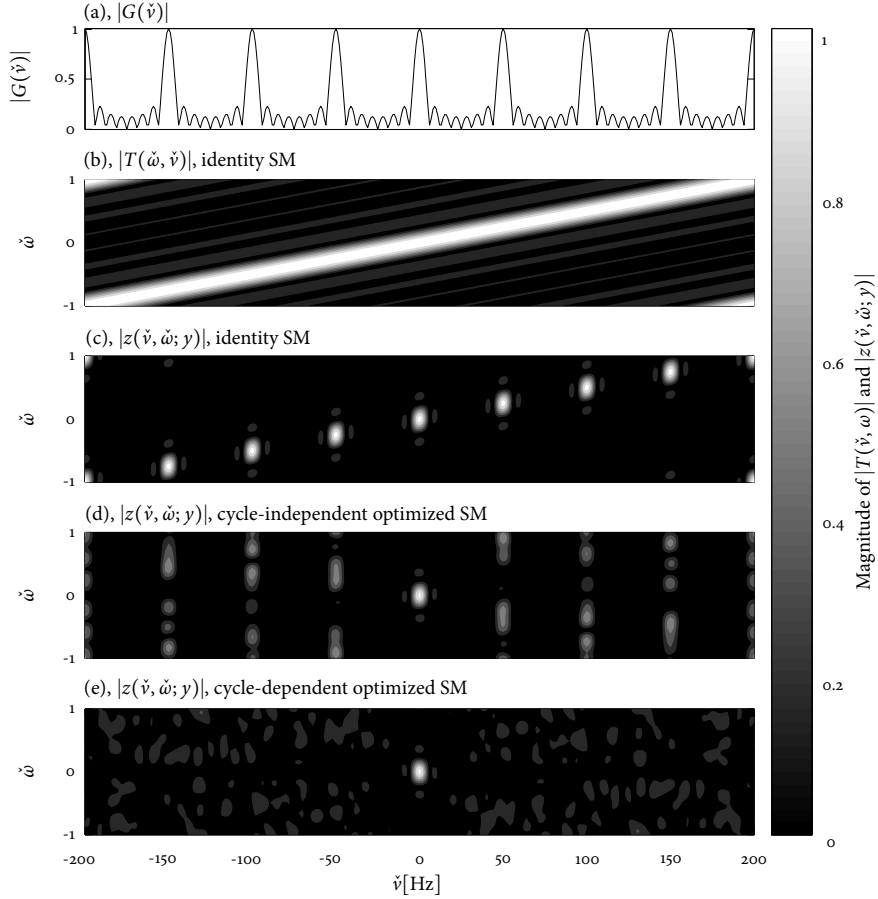*Fig. A.3: Objective functions for the joint DF and DoA MLEs in the case study (TDM-SIMO with uniform linear array) where the following SMs are selected: $\boldsymbol{\eta}_2 = [1, 2, \ldots, 8]$ (c), $\boldsymbol{\eta}_2(i) = [4, 2, 1, 8, 5, 7, 3, 6]$ (d), and a randomly selected cycle-dependent SM (e). Fig. A.3 (a) and (b) depict the factors of the objective function (see (A.11)) for the identity SM.*

Table A.1: Case study: Setting of the TDM-SIMO system and parameters of the incident wave

I	M_1	M_2	R	T_{cy} [s]	v' [Hz]	ω'
8	1	8	1	0.02	0	0

Clearly, the period of $|G(\check{v})|$ is $\frac{1}{T_{cy}}$ = 50 Hz. The loci of the pairs $(\check{v}, \check{\omega})$ where $|T(\check{\omega}, \check{v})|$ equals its maximum value (= 1) is the line $\check{\omega} = \check{v} T_r$. As can be observed in Fig. A.3 (c) the product of these two functions, i.e. $|z(\check{v}, \check{\omega}; y)|$, exhibits multiple maxima along the above line separated by $\frac{1}{T_{cy}}$ in $\check{v}$. These multiple maxima cause an ambiguity in the joint ML estimation of the DF and DoA when the DFER is selected equal to $\left(-\frac{1}{2T_r}, \frac{1}{2T_r}\right]$. Notice that $|z(\check{v}, \check{\omega}; y)|$ exhibits one unique maximum if $\check{v} \in \left(-\frac{1}{2T_{cy}}, \frac{1}{2T_{cy}}\right]$. Thus, if this SM is used, the DFER has to be restricted to the above interval in order to avoid the ambiguity problem.

Fig. A.3(d) and Fig. A.3(e) report respectively the graphs of $|z(\check{v}, \check{\omega}; y)|$ for the cycle-independent SM $\boldsymbol{\eta}_2 = [4, 2, 1, 8, 5, 7, 3, 6]$ and a cycle-dependent randomly selected SM. With this selection of the SMs, $|z(\check{v}, \check{\omega}; y)|$ exhibits a unique maximum and therefore the ambiguity problem does not occur. One can still see clearly the impact of the periodic behavior of $|G(\check{v})|$ on the objective function depicted in Fig. A.3(d) as side-lobe stripes at the loci of the maxima of $|G(\check{v})|$ when the SM is cycle-independent. As exemplified by Fig. A.3(e) this pattern vanishes completely when using a cycle-dependent SM. Furthermore, the side-lobes of the third depicted objective function have much lower magnitude than those of the second objective function.

This study shows that in the worst case (using the identity SM), the operational DFER is $\left(-\frac{1}{2T_{cy}}, \frac{1}{2T_{cy}}\right]$. By appropriately selecting the SM the DFER can be extended to $\left(-\frac{1}{2T_r}, \frac{1}{2T_r}\right]$, i.e., by a factor M_2 = 8 in this case study or in general by $M_1 M_2 R$. Furthermore, Fig. A.3(c)–(e) make it evident that the SMs significantly affect the magnitudes of the side-lobes of the objective function. This impact is investigated in more detail in Section A.5.

A.4.3   *Analysis of the Ambiguity Effect for the Case Study*

In this subsection we derive a necessary and sufficient condition for a cycle-independent SM to lead to an objective function exhibiting multiple maxima. We also show that modulo-type SMs (and among them the identity SM) cause the ambiguity problem when the cycle repetition rate R is integer.

The function $z(\check{v}, \check{\omega}; y)$ in (A.10) is of the form

$$z(\check{v}, \check{\omega}; y) = \frac{1}{IM_2} \sum_{i=1}^{I} \sum_{m_2=1}^{M_2} \exp\{j\Phi_{i,m_2}\},$$

where $\Phi_{i,m_2} \doteq 2\pi\check{v}\left(i - \frac{I+1}{2}\right)T_{cy} + 2\pi\check{v}\left(\eta_2(i, m_2) - \frac{M_2+1}{2}\right)T_r + \pi\check{\omega}m_2$. When $\check{\omega} = 0$ and $\check{v} = 0$, $|z(\check{v}, \check{\omega}; y)|$ equals its maximum value 1. However, a necessary and sufficient condition for $|z(\check{v}, \check{\omega}; y)| = 1$ to hold is that all the phases in the double sum are congruent modulo 2π. This will be the case if, and only if,

$$\Phi_{i,m_2} - \Phi_{i+1,m_2} \equiv 0 \pmod{2\pi}$$
$$m_2 = 1, \ldots, M_2, \ i = 1, \ldots, I-1 \tag{A.12}$$

and

$$\Phi_{i,m_2} - \Phi_{i,m_2+1} \equiv 0 \pmod{2\pi}$$
$$m_2 = 1, \ldots, M_2 - 1, \ i = 1, \ldots, I. \tag{A.13}$$

Hence $|z(\check{v}, \check{\omega}; y)|$ exhibits multiple maxima if, and only if, the system of equations defined by (A.12) and (A.13) has one or more non-trivial solutions $(\check{v}, \check{\omega}) \in \left(-\frac{1}{2T_r}, \frac{1}{2T_r}\right] \times [\omega' - 1, \omega' + 1]$. The trivial solution is $(\check{v}, \check{\omega}) = (0, 0)$.

In the sequel, we focus on cycle-independent SMs. In this case $\eta_2(i, m_2) - \eta_2(i + 1, m_2) = 0$ and (A.12) reduces to $\check{v}T_{cy} = K$ for $K \in \mathbb{Z} \cap \left(-\frac{RM_2}{2}, \frac{RM_2}{2}\right]$, where $\mathbb{Z}$ is the set of integers. Inserting this identity in (A.13) yields

$$K \cdot \frac{\dot{\eta}_2(m_2)}{RM_2} \equiv \frac{\check{\omega}}{2} \pmod{1}, \ m_2 = 1, \ldots, M_2 - 1, \tag{A.14}$$

where $\dot{\eta}_2(m_2) \doteq \eta_2(m_2) - \eta_2(m_2 + 1)$. Hence, provided the SM is cycle-independent, a necessary and sufficient condition for the ambiguity problem to occur is that the equation system (A.14) has at least one non-trivial solution $(K, \check{\omega}) \in \left(\mathbb{Z} \cap \left(-\frac{RM_2}{2}, \frac{RM_2}{2}\right]\right) \times [\omega' - 1, \omega' + 1]$.

A modulo-type SM fulfills the congruence $(\eta_2(m_2) - 1) \equiv Jm_2 + K \pmod{M_2}$ for some $J, K \in \mathbb{Z}$ with J and M_2 being relatively prime. As an example, the commonly used identity SM $\boldsymbol{\eta}_2 = [1, 2, \ldots, M_2]$ is a modulo-type SM with $J = 1$ and $K = 0$. For any modulo-type SM, $\{\dot{\eta}_2(m_2); m_2 = 1, \ldots, M_2 - 1\} = \{J, J - M_2\}$. Hence (A.14) consists of two different congruences. Elimination of $\check{\omega}$ yields $K = RK'$, with K' taking any value in $\mathbb{Z} \cap \left(-\frac{M_2}{2}, +\frac{M_2}{2}\right]$. When $R \in \mathbb{Z}$, the non-trivial solutions for K are the $RM_2 - 1$ values in $\mathbb{Z} \cap \left(-\frac{RM_2}{2}, \frac{RM_2}{2}\right] \setminus \{0\}$. Notice that this result is in accordance with the 8 maxima (corresponding to the 7 non-trivial solutions plus the trivial solution) that can be observed in Fig. A.3(c).

A.5   Performance Simulations

The theoretical investigations of the study case reported in the previous sub-section show that the SM strongly affects the side-lobes of the objective function of the DF and DoA MLEs. As a consequence the SM will also affect the robustness of the estimators toward noise since this robustness directly depends on the magnitudes of the side-lobes.

We define the normalized side-lobe level (NSL) associated with a SM to be the magnitude of the highest side-lobe of the corresponding objective function. It is obvious that objective functions with NSL equal to one have multiple maxima and therefore lead to an ambiguity in the estimation of DF and DoA, whereas objective functions with NSL less than 1 have a unique maximum.

We show by means of Monte-Carlo simulations that the NSL associated with a SM can be used as a figure of merit of this SM for the optimisation of the performance of the DF and DoA MLEs. The parameter setting of the considered scenario is the same as that used in the case study (see Table A.1). Fig. A.4 depicts the RMSEEs of the MLEs $\hat{v}$ and $\hat{\psi}$ versus the output signal-to-noise ratio $\gamma_o \doteq IM_2 P |\alpha|^2 |\mathbf{c}_1(\Omega_1)|^2 |\mathbf{c}_2(\Omega_2)|^2 / (\frac{N_0}{T_s})$ [1] for four SMs leading to NSLs equal to 0.28, 0.58, 0.80, and 0.85 respectively. The symbol P in the above expression denotes the transmitted signal power. The RMSEEs are compared to the corresponding individual Cramér-Rao lower bounds (CRLBs) calculated in [8] assuming parallel SIMO channel sounding.

As shown in Fig. A.4 all curves exhibit the same behavior, i.e. when γ_o is larger than a certain threshold, γ_o^{th}, the RMSEEs of $\hat{v}$ and $\hat{\psi}$ are close to the corresponding CRLBs. When $\gamma_o < \gamma_o^{th}$, the RMSEEs increase dramatically as already shown in [1]. Further simulations show that γ_o^{th} increases along with the NSL. This behavior can be explained as follows: The probability of the event that the maximum of any side-lobe of the objective function is higher than the maximum of its main-lobe is larger when these side-lobes have high magnitudes. Notice that the threshold effect is well-known in non-linear estimation such as frequency estimation [9].

We can use the RMSEE curve of the DF MLE under the hypothesis that all other parameters but the complex gain of the path are known as a benchmark for the DF MLE performance when all path parameters are unknown. This curve is indeed a lower bound for the RMSEE curve of the latter DF estimates. Monte Carlo simulations not reported here show that this benchmark curve exhibits a threshold γ_o^{th} = 15 dB and is close to the CRLB of $\hat{v}$ for $\gamma_o > \gamma_o^{th}$. From Fig. A.4 we observe that the threshold γ_o^{th} of the RMSEE curve of $\hat{v}$ obtained for the SM leading to NSL=0.28 is 0.5 dB apart from that of the benchmark curve. Hence, the former threshold is close to the minimum
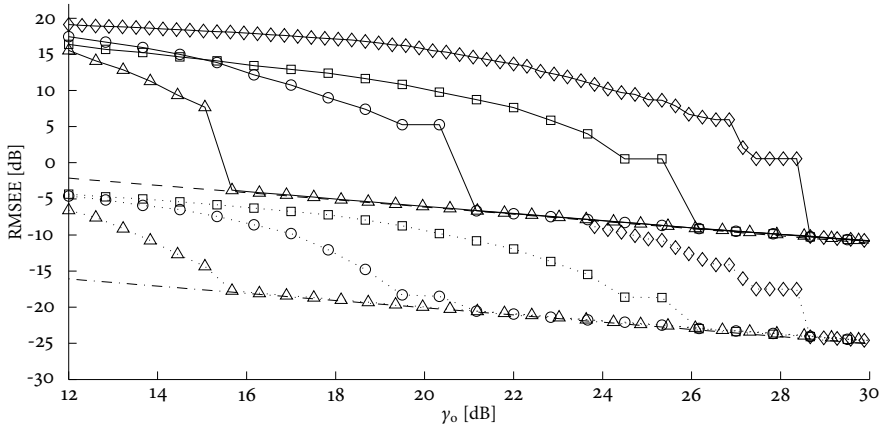
Fig. A.4: RMSEEs of $\hat{v}$ (solid curves) and $\hat{\psi}$ (dotted curves) versus γ_o computed using the setting given in Table A.1 for different SMs. The dashed and the dash-dotted lines represent the CRLBs of $\hat{v}$ and $\hat{\psi}$ respectively. The curves with symbols $\diamond$, $\square$, $\bigcirc$, $\triangle$ have been obtained using 3 cycle-independent SMs and 1 cycle-dependent SM leading to NSL = 0.85, 0.80, 0.58, and 0.28 respectively.

achievable threshold. This observation confirms that the NSL is a suitable figure of merit for the selection of "good" SMs, i.e. leading to MLEs operating close to optimum.

A.6 Experimental Investigations

In this section, we present experimental investigations that illustrate the impact of the SM on the objective function used in the ISI-SAGE algorithm to estimate the DF and DoA of propagation paths based on measurement data. The measurements were performed with the TDM-MIMO channel sounder PROPSound [10]. The Tx array consisted of 3 conformal sub-arrays of 8 dual-polarized patches uniformly spaced on a cylinder together with a uniform rectangular 2×2 sub-array of 4 dual-polarized patches placed on top of the cylinder ($M_1 = 54$). At the Rx a 4×4 planar array with 16 dual-polarized patches was used ($M_2 = 32$). The spacing between the Rx array elements and the elements of the four Tx sub-arrays is half a wavelength. The selected carrier frequency was 2.45 GHz. The sounding signal was a pseudo-noise (PN) sequence of length $K = 255$ chips with chip duration $T_c = 10$ ns. The sensing interval coincided with one period of the PN-sequence, i.e. $T_s = K T_c = 2.55$ μs. The transmitted power was 100 mW.

The Rx array was mounted outside a window on the 3rd floor of the Elektrobit AG building in Bubikon, Switzerland. The Tx array was mounted

Table A.2: *Settings of the channel sounder for measurement Scenarios I and II*

Parameters	Scenario I	Scenario II
SM at Array 2	Patch-wise identity SM	Patch-wise optimized SM
T_r [μs]	3.05	5.10
T_{cy} [ms]	6.2	47.2
Selected DFER [Hz]	$\left(-\frac{1}{2T_{cy}}, \frac{1}{2T_{cy}}\right] =$ $(-81.3, 81.3]$	$\left(-\frac{1}{2T_r}, \frac{1}{2T_r}\right] =$ $(-98\,039, 98\,039]$

on the roof of a van moving with approximately 8 m/s away from the building. The measurements were performed twice along the same route with different settings of the sounding equipment (see Table A.2). The van was driving at approximately the same velocity during both measurement recordings to ensure propagation scenarios with almost identical DFs. The azimuth of arrival (AoA), the elevation of arrival (EoA) and the DF of the LOS path can be calculated from the location of the Rx as well as the position and the velocity of the van to be approximately 5°, 20° and -59 Hz respectively. The two settings of the sounding equipment were selected in such a way that the maximum DF is in $\left(-\frac{1}{2T_{cy}}, \frac{1}{2T_{cy}}\right]$ in Scenario I and outside this range but in $\left(-\frac{1}{2T_r}, \frac{1}{2T_r}\right]$ in Scenario II. These intervals were then selected as the corresponding DFERs for the two scenarios. As explained later, the SM at the Tx is irrelevant in the investigated situation. At the Rx, we apply a patch-wise identity SM in Scenario I and a patch-wise optimized SM in Scenario II. The term "patch-wise" indicates that the two elements of each patch are always switched consecutively. This is done to mitigate phase noise effect for accurate polarization estimation.

The ISI-SAGE algorithm is applied to the measurement data to estimate the individual parameter vectors of $L = 4$ propagation paths using $I = 4$ measurement cycles. The parameter estimates of the four paths are initialized successively with a Non-Coherent Maximum Likelihood (NC-ML) technique described in [3]. Once the initialization is completed, the E- and M-steps of the ISI-SAGE are performed as described in [7]. It can be shown that the objective function used for the joint initialization of $\hat{v}_\ell$ and $\hat{\mathbf{\Omega}}_{2,\ell}$ after the initial delay estimate $\hat{\tau}_\ell(0)$ has been computed is similar to the absolute value of (A.9) with $\tau_\ell = \hat{\tau}_\ell(0)$ and $\hat{x}_\ell(t) = y(t) - \sum_{\ell'=1}^{\ell-1} s(t; \hat{\boldsymbol{\theta}}'_{\ell'}(0))$. Since at that stage, the DoD of the ℓth path has not been estimated yet, the NC-ML technique is used to initialize $\hat{v}_\ell$ and $\hat{\mathbf{\Omega}}_{2,\ell}$ jointly. The SM at the Tx is irrelevant when this method is applied. Hence, we can use the initialization procedure

of the ISI-SAGE algorithm to experimentally investigate scenarios similar
to the case study described in Subsection A.4.2. The differences between
the experimental scenarios and the case study are as follows: (1) the SIMO
antenna system considered in the case study is replaced by a MIMO system
in the experimental scenario; (2) a uniform planar array with dual-polarized
elements is used instead of a uniform linear array; (3) the array elements are
not isotropic; (4) in the calculation of $\hat{x}_\ell(t)$ the contribution of the waves but
the ℓth one were either not or only partially cancelled.

In the sequel we restrict the attention to the LOS path indexed $\ell = 1$. To
visualize the behavior of the objective function versus v_1, we compute

$$F(v_1) \doteq \max_{\mathbf{\Omega}_{2,1}} |z(v_1, \mathbf{\Omega}_{2,1}; \hat{x}_1 = y)|^2$$

with $z(v_1, \mathbf{\Omega}_{2,1}; y)$ given in (A.9). Notice that $T_i(\check{\mathbf{\Omega}}_{2,1}, \check{v}_1)$ (see (A.8)) depends
on the real response of the Rx array, i.e. includes the radiation patterns of
the elements in the array. Inserting (A.9) with the noise term omitted in the
definition of $F(v_1)$ we obtain

$$\begin{aligned}
F(v_1) &= \max_{\check{\mathbf{\Omega}}_{2,1}} |\sum_{i=1}^{I} R_i(\check{v}_1) T_i(\check{\mathbf{\Omega}}_{2,1}, \check{v}_1)|^2 \\
&= \max_{\check{\mathbf{\Omega}}_{2,1}} |G(\check{v}_1) T(\check{\mathbf{\Omega}}_{2,1}, \check{v}_1)|^2 \\
&= |T'(\check{v}_1)|^2 \cdot |G(\check{v}_1)|^2
\end{aligned}$$
(A.15)

with
$$T'(\check{v}_1) \doteq \max_{\check{\mathbf{\Omega}}_{2,1}} T(\check{\mathbf{\Omega}}_{2,1}, \check{v}_1).$$

The second line follows similarly to (A.11) since the SM is cycle-independent.
Hence, the SM only affects $F(v_1)$ via $|T'(\check{v}_1)|^2$.

The right hand expression in (A.15) will be useful for understanding the
behavior of $F(v_1)$ computed from the measurement data. This function is
plotted versus v_1 ranging in $(-81.3\,\text{Hz}, 81.3\,\text{Hz}]$ in Fig. A.5 (top) for both
scenarios. The pulse-train-like behavior of the curves is due to the factor
$|G(\check{v}_1)|^2$ in (A.15), which is periodic with period $1/T_{cy}$. The maximum of $F(v_1)$
in Scenario I (with DFER $(-\frac{1}{2T_{cy}}, \frac{1}{2T_{cy}}]$), is located at -52 Hz. In Scenario
II (with DFER $(-\frac{1}{2T_r}, \frac{1}{2T_r}]$) the maximum of $F(v_1)$ is located at -81 Hz.
Notice that these values are the initial DF estimates of the LOS path returned
by the ISI-SAGE algorithm. After four iterations of the algorithm the DF
estimates of the LOS path have converged to $-52.5\,\text{Hz}$, and the AoA and EoA
estimates equal 4.6^o and 27° respectively in Scenario I. In Scenario II the DF
estimate converges to $-60\,\text{Hz}$, and the AoA and EoA estimates equal 5.3^o and
18.7^o respectively. All these values are in accordance with the theoretically
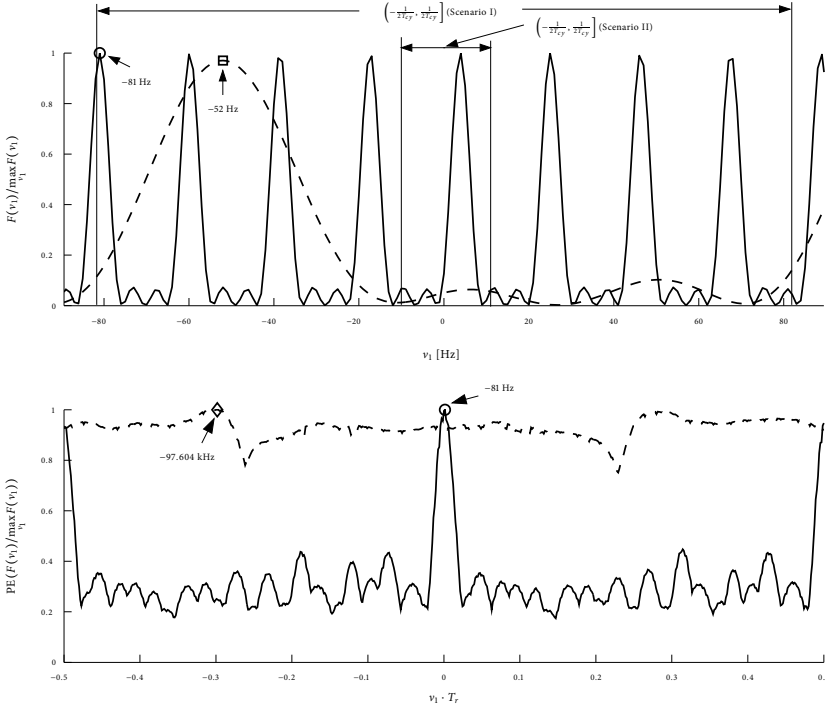
Fig. A.5: Normalized $F(v_1)$ (top) and pseudo-envelope $\text{PE}(F(v_1))$ (bottom) computed from the measurement data obtained in Scenario I (dashed lines) and Scenario II (solid lines). The marks □ and ◇ denote the maxima of $F(v_1)$ in Scenario I when the DFER is respectively $\left(-\frac{1}{2T_{cy}}, \frac{1}{2T_{cy}}\right]$ and extended to $\left(-\frac{1}{2T_r}, \frac{1}{2T_r}\right]$. The mark ∘ denotes the maximum of $F(v_1)$ in Scenario II (DFER $= \left(-\frac{1}{2T_r}, \frac{1}{2T_r}\right]$).

calculated values. The deviation between the two sets of the estimates is due to the difference in the velocities and the positions of the van during the measurement recordings.

The pulse-train-behavior of $F(v_1)$ due to $|G(v_1)|^2$ makes it difficult to visualize the effect of the SM (embodied in $|T'(\check{v}_1)|^2$) on the former function when $\check{v}$ ranges in $\left(-\frac{1}{2T_r}, \frac{1}{2T_r}\right]$. To circumvent this problem we compute an approximation of $|T'(\check{v}_1)|$ from $F(v_1)$ as follows: $\text{PE}(F(v_1))$ is a pseudo-envelope (PE) obtained by dividing the range of v_1 into multiple bins with equal width of $\frac{1}{T_{cy}}$ and connecting the maxima of $F(v_1)$ within each bin using linear interpolation. Fig. A.5 (bottom) reports the computed PE curves for both scenarios. For Scenario I, $\text{PE}(F(v_1))$ remains close to one over the entire range $\left(-\frac{1}{2T_r}, \frac{1}{2T_r}\right]$. This behavior is due to the identity SM used for the 4×4 planar array. In Scenario II, $\text{PE}(F(v_1))$ exhibits a dominant lobe and multiple

side-lobes with significant lower amplitude. The width of the main lobe is in accordance with the analytically derived value of $\frac{2}{M_2}\frac{1}{T_r}$ for the separation between the zero points of the main lobe.

In case the DFER is extended to $\left(-\frac{1}{2T_r}, \frac{1}{2T_r}\right]$ in Scenario I, the maximum of $F(\nu_1)$ is located at -97.604 kHz in the initialization step (as shown in Fig. A.5 (bottom)), and stays at this value after 4 iterations. The AoA and EoA estimates are respectively 70° and 2°. These estimates are obviously artifacts that result due to the identity SM used at the Rx array.

Notice that the high side-lobes at the boundary of the DF estimation range are due to the patch-wise switching of the arrays. When the DF is very low compared to the switching rate as it is the case here, the resulting phase-shift due to the DF between consecutive sensing intervals of the elements of a patch is close to zero, which leads to an effective doubling of T_r. As a result, the graph of $\mathrm{PE}(F(\nu_1))$ exhibits two segments of similar shape as shown in Fig. A.5 (bottom).

The above investigations show experimentally the ambiguity effect that occurs when the DFER is extended to $\left(-\frac{1}{2T_r}, \frac{1}{2T_r}\right]$ and the identity SM combined with a planar array is used. It also demonstrates that this problem is avoided by appropriately selecting the SM.

A.7 Conclusion

In this contribution we investigate the behavior of the Doppler frequency (DF) and direction estimates obtained with the ISI-SAGE algorithm [2] and [3] when the scheme is used in combination with TDM-MIMO channel sounding.

Theoretical analysis combined with simulations show that when the DF estimation range (DFER) is selected to be from minus to plus half the switching rate as proposed in [1] the switching modes (SMs) of the arrays have to be selected suitably. It is shown that traditionally used SMs of uniform linear and planar arrays where the elements are switched according to their natural spatial ordering are inappropriate as they lead to an ambiguity in the joint estimation of DF and directions. The investigations also reveal that the objective function of the DF and direction estimates and in particular the levels of its side-lobes are strongly affected by the choice of the SM.

We propose to associate to any SM the so-called normalized side-lobe level (NSL) of the objective function resulting from selecting this SM. Monte Carlo simulations show that the NSL is a sensible figure of merit for the identification of SMs leading to DF and direction estimates performing close to optimum in terms of root mean square estimation error.

The above theoretical studies are confirmed by experimental investigations using the ISI-SAGE algorithm. These investigations show that consecutive switching of the two elements of dual polarized patches in an array reduce the DFER by a factor two. However this reduction is in practice irrelevant as the switching rate implemented in measurement equipments is usually several orders of magnitude larger than the maximum Doppler frequency observable in radio propagation environments.

References

[1] X. Yin, B. H. Fleury, P. Jourdan, and A. Stucki, "Doppler frequency estimation for channel sounding using switched multiple transmit and receive antennae," *Proc. IEEE Global Communications Conference, Globecom2003*, vol. 4,1-5, pp. 2177–2181, 2003.

[2] B. H. Fleury, X. Yin, P. Jourdan, and A. Stucki, "High-resolution channel parameter estimation for communication systems equipped with antenna arrays," *Proc. 13th IFAC Symposium on System Identification (SYSID 2003), Rotterdam, The Netherlands*, no. ISC-379, 2003.

[3] X. Yin, B. H. Fleury, P. Jourdan, and A. Stucki, "Polarization estimation of individual propagation paths using the SAGE algorithm," *The 14th IEEE International Symposium on Personal, Indoor and Mobile Radio Communications, PIMRC2003*, vol. 2, pp. 1795–1799, 2003.

[4] I. E. Telatar, "Capacity of multi-antenna Gaussian channels," *European Transactions on Telecommunication*, vol. 10, pp. 585–595, 1999.

[5] G. J. Foschini and M. J. Gans, "On limits of wireless communications in a fading environment when using multiple antennas," *Wireless Personal Communications*, vol. 6, pp. 311–335, 1998.

[6] D. Chizhik, G. J. Foschini, and R. A. Valenzuela, "Capacities of multi-element transmit and receive antennas: Correlations and keyholes," *IEE Electronics Letters*, vol. 36, no. 13, pp. 1099–1100, June 2000.

[7] B. H. Fleury, P. Jourdan, and A. Stucki, "High-resolution channel parameter estimation for MIMO applications using the SAGE algorithm," *2002 Int. Zurich Seminar on Broadband Communications*, vol. 30, pp. 1–9, 2002.

[8] B. H. Fleury, M. Tschudin, R. Heddergott, D. Dahlhaus, and K. L. Pedersen, "Channel parameter estimation in mobile radio environments using the SAGE algorithm," *IEEE Journal on Selected Areas in Communications*, vol. 17, no. 3, pp. 434–450, Mar. 1999.

[9] D. C. Rife and R. R. Boorstyn, "Single tone parameter estimation from discrete-time observations," *IEEE Trans. Information Theory*, 1974.

[10] A. Stucki *et. al.*, "PROPSound System Specifications Document: Concept and Specifications," Elektrobit AG, Switzerland," Internal Report, 2001.

Optimization of Spatio-Temporal Apertures in Channel Sounding

Troels Pedersen, Claus Pedersen, Xuefeng Yin, and Bernard H. Fleury.

Abstract

In this paper we investigate the impact of the spatio-temporal aperture of a channel sounding system equipped with antenna arrays at the transmitter and receiver on the accuracy of joint estimation of Doppler frequency and bi-direction. The contribution of this work is three-fold. Firstly, we state a spatio-temporal model which can describe parallel as well as switched sounding systems. The proposed model is applicable for arbitrary layouts of the spatial arrays. To simplify the derivations we investigate the special case of linear spatial arrays. However, the results obtained for linear arrays can be generalized to arbitrary arrays. Secondly, we give the necessary and sufficient conditions for a spatio-temporal array to yield the minimum Cramér-Rao lower bound in the single-path case and Bayesian Cramér-Rao Lower Bound in the multipath case. The obtained conditions amount to an orthogonality condition on the spatio-temporal array. Thirdly, we define the Doppler-bi-direction ambiguity function and derive the necessary and sufficient conditions for a linear spatio-temporal array to be ambiguous. Based on the ambiguity function we define the normalized side-lobe level, which we propose to use as a figure of merit in the design of spatio-temporal arrays.

B.1 Introduction

The design and optimization of multiple-input multiple-output (MIMO) communication systems require realistic models of the propagation channel, which incorporate dispersion in delay, Doppler frequency, direction of departure, direction of arrival, and polarization. In order to develop realistic parametric models of the channel response it is of great importance to be able to accurately measure the dispersive behavior of the propagation channel, that is, simultaneously measure dispersions in the above dispersion dimensions. Dispersion of the propagation channel in one dimension can be estimated from an observation using an aperture in the corresponding Fourier domain. For example, if Doppler frequency is to be estimated, observations at different time instants are required.

The focus of the paper is on the joint estimation of direction of departure, direction of arrival and Doppler frequency from observations obtained by exciting the propagation channel via a *spatial aperture* and sensing the output of the channel via another spatial aperture at different time instants, i.e. via a *temporal aperture*. All together these three apertures constitute a bi-spatio-temporal aperture, or a *spatio-temporal aperture* for short. A spatio-temporal aperture can be implemented using antenna arrays at the transmitter and receiver sites. Spatio-temporal sounding systems fall in two groups: parallel and switched sounding systems.

A *parallel* sounding system (such as [1]) is equipped with one transmitter for each transmit antenna element and one receiver per receive antenna element. All transmit array elements are active simultaneously and all outputs of the receive array elements are observed simultaneously. Snapshots of the channel are collected at different time instances. Each of the parallel transmitters must transmit a unique signal. The transmitted sounding signals must be carefully chosen such that their cross- and auto-correlation properties allow for their separation and sufficient delay resolution respectively.

In *switched* sounding systems (such as the one used in [2–5]) the sounding signal generated by a single transmitter is applied to the elements of the transmit array via a switch. The output of the receive array is sensed via another switch. In this way observations from all antenna pairs of one transmit antenna and one receive antenna can be achieved. Despite the added switches, the hardware complexity of switched systems is lower than that of parallel systems. Furthermore, the cross-correlation properties of the sounding signals is not an issue in switched channel sounding systems and therefore any code sequence with the desired autocorrelation property may be applied.

Various algorithms for the estimation of directions and Doppler shifts from data obtained from spatio-temporal arrays have been proposed, see e.g. [2–5] and references therein. It is shown in [5] that the design of spatio-temporal apertures is critical to the joint estimation of Doppler frequency and bi-direction. Until recently, it was believed that the maximum absolute Doppler frequency that can be estimated with a switched sounding system is inversely proportional to the product of the number of elements of the transmit and receive arrays. This limitation was considered a major draw-back of switched systems [1]. However, as shown in [4] and [5], this limitation is an effect caused by the (inappropriate) choice of the spatio-temporal aperture and is not a fundamental (Nyquist) limit. This inappropriate choice leads to an ambiguity in the estimation of Doppler frequency and direction [5]. An intuitive interpretation of this effect is that the phase changes induced by a plane wave at the outputs of the array elements may result either due to the fact that the wave exhibits a Doppler frequency or due to the wave's impinging direction, when switching sounding is used. The ambiguity effect occurs when it is not possible to distinguish which effect has really caused this phase changes. In particular it was shown in [5] that by appropriately selecting the spatio-temporal aperture it is possible to extend the above maximum Doppler frequency to the largest value that can be estimated with a similar single-input single-output sounding system. As illustrated by these results, the theoretical understanding of the impact of the spatio-temporal aperture on joint bi-direction and Doppler estimators requires a joint treatment of the spatio-temporal aperture.

In this paper we investigate the impact of the spatio-temporal aperture on the accuracy of joint estimation of Doppler frequency and bi-direction. The contribution of this work is three-fold. Firstly, we state a spatio-temporal model which can describe parallel as well as switched sounding systems. The proposed model is applicable for arbitrary layouts of the spatial arrays. However, to simplify the derivations we investigate the special case of linear spatial arrays. Secondly, we give the necessary and sufficient conditions for a spatio-temporal array to yield the minimum Cramér-Rao lower bound (CRLB) in the single-path case and Bayesian Cramér-Rao Lower Bound (BCRLB) in the multipath case. The obtained conditions amount to an orthogonality condition on the spatio-temporal array. A similar condition for azimuth and elevation estimation has been derived in the single-path case for planar arrays in [6] and three dimensional arrays in [7]. Thirdly, we define the Doppler-bi-direction ambiguity function for the proposed spatio-temporal model. The ambiguity function [8] is a standard means to asses the resolution ability of radar waveforms and a rich literature exists on ambiguity functions and related results for various radar systems, see e.g. [9, 10] and references therein. In the recent work [11] the ambiguity function has been defined for MIMO bi-static radar systems with parallel transmitters and receivers. The interested reader is referred to this contribution for an overview and discussion of recent results in ambiguity functions for mono- and bi-static radar. The bi-static radar estimation problem is essentially the same as the problem of parameter estimation of single-bounce propagation paths in the field of channel sounding for MIMO wireless communications. However, in real propagation environments single-bounce only propagation cannot be assumed, and consequently the available radar results do not apply directly. In the channel sounding literature however, the use of ambiguity functions has been fairly limited so far. In [12, 13] the delay-Doppler ambiguity function is computed. To our best knowledge, the ambiguity function has not previously been defined and calculated for (bi-)spatio-temporal channel sounding. The ambiguity function presented in this contribution is valid for both parallel and switched sounding systems. It is a special case of the general ambiguity function defined in [9]. Based on this ambiguity function we derive the necessary and sufficient conditions for a linear spatio-temporal array to be ambiguous. The obtained result generalizes the result from [5] and resembles the results of the well-studied type-1 (or rank-1) ambiguity effect for spatial arrays; see e.g. [14–16]. Based on the ambiguity function we also define the normalized side-lobe level (NSL), which we propose to use as a figure of merit in the design of spatio-temporal arrays.

The paper is organized as follows. In Section B.2 we introduce a model of the spatio-temporal sounding system capable of describing both parallel
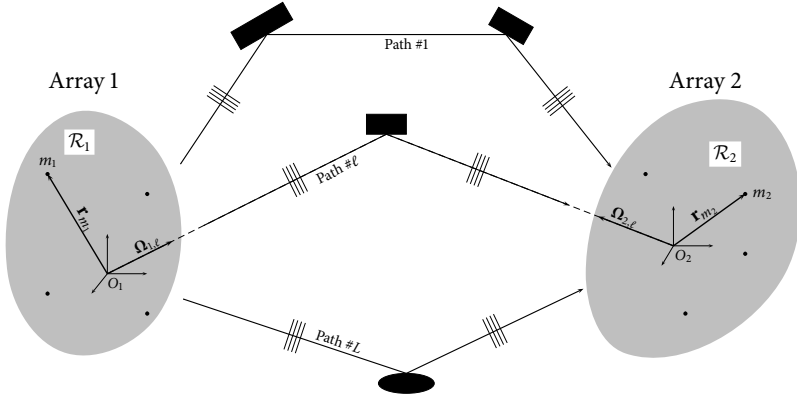
Fig. B.1: The considered multi-path propagation environment. The black dots in the regions $\mathcal{R}_1$ and $\mathcal{R}_2$ indicate the positions of the array elements.

and switched systems. In Section B.3 the impact of the spatio-temporal array on the CRLB and the BCRLB is investigated. In Section B.4 we define the Doppler-bi-direction ambiguity function which is then used for the analysis of the above-mentioned ambiguity effect. In Section B.5 we investigate the effect of the spatio-temporal aperture on the estimation performance by means of Monte-Carlo simulations. Concluding remarks are stated in Section B.6.

Notation: Throughout this contribution, the following notation is used. Vectors and matrices have bold faced symbols. Sets are printed in calligraphic letters (such as $\mathcal{A}$). The notations $[\cdot]^*$, $[\cdot]^\mathsf{T}$, and $[\cdot]^\mathsf{H}$ denote complex conjugation, transposition and Hermitian transposition, respectively. The notations $[\mathbf{a}]_p$ and $[\mathbf{A}]_{p,q}$ mean the pth element of the vector $\mathbf{a}$, and element (p,q) of the matrix $\mathbf{A}$. The symbol $\otimes$ denotes the Kronecker product. The notation $\mathbf{A} \succeq \mathbf{B}$ means that the matrix $\mathbf{A} - \mathbf{B}$ is positive semidefinite. We denote a p-dimensional column vector with unity entries by $\mathbf{1}_p$. The notation $|\cdot|$ stands for the Euclidean norm of a scalar or vector and the cardinal number of a set. Expectation is denoted by $\mathsf{E}[\cdot]$. The least integer larger than or equal to a is denoted by $\lceil a \rceil$. The symbols $\mathbb{Z}$, $\mathbb{R}$ and $\mathbb{C}$ stand for the set of integers, the real line, and the complex plane, respectively.

B.2   System Model

Let us consider the propagation environment depicted in Fig. B.1. The sounding system consists of two antenna arrays referred to as Array 1 and Array 2, respectively. The index $k \in \{1, 2\}$ is used to distinguish the transmitter ($k = 1$) from the receiver ($k = 2$). The number of elements in Array k is denoted by

M_k. At Array k the coordinates are given in carrier wavelengths with respect to the coordinate system O_k. The displacement of Array k element m_k from the origin of the coordinate system O_k is denoted by $\mathbf{r}_{k,m_k} \in \mathbb{R}^3$. To simplify the notation we write $\mathbf{r}_{m_k}$ for $\mathbf{r}_{k,m_k}$. The time variable is denoted by $t \in \mathbb{R}$.

Referring to Fig. B.1, a certain number L of waves propagate along different paths from Array 1 to Array 2. Along its path a wave interacts with a certain number of scatterers. We make the following assumptions on the propagation environment:

A) Following [2], we assume that the far-field condition holds, such that a plane wave approximation can be applied in a region $\mathcal{R}_k \subset \mathbb{R}^3$ surrounding Array k when the other array transmits. This implies that the set of parameters describing each path is independent of the array element positions.

B) The propagation paths are assumed to be specular.

C) We assume that the geometry of the propagation paths is constant throughout the observation window $\mathcal{T}$. In other words, the parameters of the propagation paths remain constant for the whole measurement run.

D) We consider the narrow-band case only. Hence, without loss of generality propagation delays are assumed to be zero.

E) We assume that the elements of Array 1 and Array 2 are isotropic.

Under Assumptions A–D, the ℓth path can be described by the parameter vector $\boldsymbol{\theta}_\ell \triangleq [\nu_\ell, \boldsymbol{\Omega}_{1,\ell}^{\mathsf{T}}, \boldsymbol{\Omega}_{2,\ell}^{\mathsf{T}}, \alpha_\ell]^{\mathsf{T}}$, where ν_ℓ is the Doppler frequency of Path ℓ and $\boldsymbol{\Omega}_{k,\ell}$ is a unit vector with the initial point anchored at the origin of O_k pointing towards the direction of Path ℓ in $\mathcal{R}_k$ (see Fig. B.1). We denote the complex gain of path ℓ as α_ℓ. The $8L$-dimensional vector $\boldsymbol{\theta} \triangleq [\boldsymbol{\theta}_1^{\mathsf{T}}, \dots, \boldsymbol{\theta}_L^{\mathsf{T}}]^{\mathsf{T}}$ contains the parameters of all L paths.

B.2.1 Signal Model

Let $p_{m_1}(t)$ be the (complex base-band representations of the) sounding signal applied to the input of Array 1 element m_1. We consider J non-overlapping sounding intervals of length T. The center time instant of the jth sounding interval is denoted by t_j. Thus the jth sounding interval reads $\mathcal{T}_j = [t_j - \frac{T}{2}, t_j + \frac{T}{2})$. The center time instants $t_1, \dots t_J$ are selected such that $\mathcal{T}_1, \dots, \mathcal{T}_J$ are disjoint. For both parallel and switched systems, the observation window $\mathcal{T} = \bigcup_{j=1}^{J} \mathcal{T}_j$ equals the union of the sounding intervals. Element m_1 of Array 1 is said to be *active* during $\mathcal{T}_j$ if $\mathcal{T}_j$ is a subset of the support of the signal $p_{m_1}(t)$, i.e. if the sounding waveform is fed to its input terminal. Similarly, an element of Array 2 is active during $\mathcal{T}_j$ if its output terminal is sensed during

$\mathcal{T}_j$. Furthermore, we say that the antenna pair (m_1, m_2) is active during $\mathcal{T}_j$ if Array 1 element m_1 and Array 2 element m_2 are both active during $\mathcal{T}_j$.

For the sake of clarity we first introduce the notation for a parallel sounding system. Thereafter we consider switched sounding and describe a common model for both switched and parallel systems.

Let $p_{j,m_1}(t)$ be the sounding pulse with support $\mathcal{T}_j$ applied to the input of Array 1 element m_1 of a parallel sounding system. Then $p_{m_1}(t)$ is of the form

$$p_{m_1}(t) = \sum_{j=1}^{J} p_{j,m_1}(t). \tag{B.1}$$

We consider the case where the sounding pulses have same energy E and are mutually orthogonal, i.e.

$$\int_{\mathcal{T}} p_{j,m_1}(t) p_{j',m_1'}^*(t) \mathrm{d}t = E \cdot \delta_{jj'} \cdot \delta_{m_1 m_1'}, \tag{B.2}$$

where $\delta_{..}$ is the Kronecker delta function. This orthogonality restriction ensures that the signal contributions of different transmitted sounding pulses can be extracted from the received signal without interference from the other pulses. Furthermore, it implies that the noise contributions in the extracted sounding pulses are uncorrelated for different sounding pulses. In practice, the sounding pulses must be chosen to fulfill (B.2), at least approximately, e.g. by letting the sounding pulses at different transmitters be differently shifted versions of the same pseudo-noise sequence.

The output signal of Array 2 element m_2 is given as

$$Y_{m_2}(t) = \sum_{m_1=1}^{M_1} \sum_{j=1}^{J} s_{j,m_1,m_2}(t, \boldsymbol{\theta}) + N_{m_2}(t), \quad t \in \mathcal{T}, \tag{B.3}$$

where $s_{j,m_1,m_2}(t; \boldsymbol{\theta})$ and $N_{m_2}(t)$ denotes respectively the *signal contribution* due to the jth sounding pulse applied to the input of Array 1 element m_1 and the *noise contribution* to $Y_{m_2}(t)$. The noise contributions across the Array 2 element outputs are assumed to be spatially and temporally white circularly symmetric complex Gaussian processes, i.e. fulfilling

$$\mathsf{E}\big[N_{m_2}(t) N_{m_2'}(t+\tau)^* \big] = N_0 \cdot \delta_{m_2, m_2'} \cdot \delta(\tau), \tag{B.4}$$

where N_0 is a positive constant and $\delta(\cdot)$ denotes the Dirac delta function.

Under the Assumptions A–E we can write the signal $s_{j,m_1,m_2}(t; \boldsymbol{\theta})$ as

$$s_{j,m_1,m_2}(t; \boldsymbol{\theta}) = \sum_{\ell=1}^{L} \alpha_\ell \exp\big(j2\pi(v_\ell t + \boldsymbol{\Omega}_{1,\ell}^\mathsf{T} \mathbf{r}_{m_1} + \boldsymbol{\Omega}_{2,\ell}^\mathsf{T} \mathbf{r}_{m_2})\big) p_{j,m_1}(t). \tag{B.5}$$

B.2.2 *Maximum-Likelihood Estimation of Path Parameters*

First we introduce a notation which clearly distinguishes between the parameter of the propagation paths, their estimates, and the free parameter in the log-likelihood function. We adhere to the following notational convention: $(\hat{\cdot})$ is an estimate of the parameter given as argument, and $(\bar{\cdot})$ is a free parameter in the log-likelihood function. As an example the symbol ν_ℓ denotes the Doppler frequency of Path ℓ of which the estimate $\hat{\nu}_\ell$ is obtained by joint maximization of the log-likelihood function $\Lambda(\bar{\boldsymbol{\theta}})$ with respect to $\bar{\nu}_\ell$ and the remaining free parameters of $\bar{\boldsymbol{\theta}}$.

In the sequel we consider the maximum-likelihood estimator of the parameter vector $\boldsymbol{\theta}$:

$$\widehat{\boldsymbol{\theta}} = \arg \max_{\bar{\boldsymbol{\theta}} \in \mathcal{E}_{\boldsymbol{\theta}}} \Lambda(\bar{\boldsymbol{\theta}}), \tag{B.6}$$

where $\Lambda(\bar{\boldsymbol{\theta}})$ is the log-likelihood of $\bar{\boldsymbol{\theta}}$ given an observation $y_1(t), \ldots, y_{M_2}(t)$ of the processes $Y_1(t), \ldots, Y_{M_2}(t)$ and $\mathcal{E}_.$ denotes the estimation range of the parameter given as index. The maximization in (B.6) is over the $8L$-dimensional domain $\mathcal{E}_{\boldsymbol{\theta}}$.[1]

The log-likelihood of $\bar{\boldsymbol{\theta}}$ given an observation $y_1(t), \ldots, y_{M_2}(t)$ of $Y_1(t)$, $\ldots, Y_{M_2}(t)$ reads [2, 17]:

$$\Lambda(\bar{\boldsymbol{\theta}}) = \sum_{m_2=1}^{M_2} \left\{ 2\Re\left[\int_{\mathcal{T}} \sum_{j=1}^{J} y_{m_2}(t) \sum_{m_1=1}^{M_1} s_{j,m_1,m_2}^*(t;\bar{\boldsymbol{\theta}}) \mathrm{d}t \right] \right.$$
$$\left. - \int_{\mathcal{T}} \left| \sum_{j=1}^{J} \sum_{m_1=1}^{M_1} s_{j,m_1,m_2}(t;\bar{\boldsymbol{\theta}}) \right|^2 \mathrm{d}t \right\}. \tag{B.7}$$

Due to the orthogonality (B.2) of the transmitted pulses, all "cross terms" in the leftmost integral of (B.7) vanish. Thus, (B.7) simplifies to the triple sum

$$\Lambda(\bar{\boldsymbol{\theta}}) = \sum_{j=1}^{J} \sum_{m_1=1}^{M_1} \sum_{m_2=1}^{M_2} \Lambda_{j,m_1,m_2}(\bar{\boldsymbol{\theta}}), \tag{B.8}$$

where the summands are defined as

$$\Lambda_{j,m_1,m_2}(\bar{\boldsymbol{\theta}}) \triangleq 2\Re\left\{ H_{j,m_1,m_2}(\bar{\boldsymbol{\theta}}) \right\} - E_{j,m_1,m_2}(\bar{\boldsymbol{\theta}}), \tag{B.9}$$

with

$$H_{j,m_1,m_2}(\bar{\boldsymbol{\theta}}) \triangleq \int_{\mathcal{T}_j} y_{m_2}(t) s_{j,m_1,m_2}^*(t;\bar{\boldsymbol{\theta}}) \mathrm{d}t \tag{B.10}$$

---

[1]The maximization over $\mathcal{E}_{\boldsymbol{\theta}}$ is computationally prohibitive. However a low-complexity approximation of the maximum likelihood estimate can be obtained using a space-alternating generalized expectation-maximization (SAGE) algorithm [2–5].

and

$$E_{j,m_1,m_2}(\bar{\boldsymbol{\theta}}) \triangleq \int_{\mathcal{T}_j} \left| s_{j,m_1,m_2}(t;\bar{\boldsymbol{\theta}}) \right|^2 \mathrm{d}t.$$ (B.11)

The integral $H_{j,m_1,m_2}(\bar{\boldsymbol{\theta}})$ can be split into a signal term and a noise term. Inserting (B.3) and dropping the terms that are zero due to the orthogonality condition given in (B.2) we obtain

$$H_{j,m_1,m_2}(\bar{\boldsymbol{\theta}}) = \int_{\mathcal{T}_j} s_{j,m_1,m_2}(t,\boldsymbol{\theta}) s^*_{j,m_1,m_2}(t,\bar{\boldsymbol{\theta}}) \mathrm{d}t + \underbrace{\int_{\mathcal{T}_j} N_{m_2}(t) s^*_{j,m_1,m_2}(t,\bar{\boldsymbol{\theta}}) \mathrm{d}t}_{\triangleq N_{j,m_1,m_2}(\bar{\boldsymbol{\theta}})}.$$

(B.12)

Remembering that the noise contributions are temporally and spatially white, and applying the orthogonality assumption (B.2), the complex Gaussian random variables $N_{j,m_1,m_2}(\bar{\boldsymbol{\theta}})$ are uncorrelated:

$$\mathsf{E}\left[N_{j,m_1,m_2}(\bar{\boldsymbol{\theta}}) N^*_{j',m'_1,m'_2}(\bar{\boldsymbol{\theta}}) \right] = E_{j,m_1,m_2}(\bar{\boldsymbol{\theta}}) N_0 \delta_{j,j'} \delta_{m_1,m'_1} \delta_{m_2,m'_2}.$$ (B.13)

B.2.3 Sounding Modes and Their Spatio-Temporal Aperture Matrices

In the following we generalize the system model such that it can account for any configuration of switched and parallel transmitters and receivers.

Motivated by the particular form of (B.8) we use the term *spatio-temporal sample* to denote the signal component which was transmitted from Array 1 element m_1, received at Array 2 element m_2 during $\mathcal{T}_j$. Each sample results in one term of the sum in (B.8). Therefore each spatio-temporal sample can be indexed by the triplet (j, m_1, m_2). In (B.8) the spatio-temporal samples are obtained from all combinations of one Array 1 element and one Array 2 element for every sounding interval. It follows readily from the derivation of (B.8) that if any of the spatio-temporal samples are left out, the corresponding terms in (B.8) will disappear. For instance in a switched system, $\Lambda(\bar{\boldsymbol{\theta}})$ have a similar form, but the triple sum in (B.8) will only be over a subset of the set of all triplets (j, m_1, m_2).

Definition B.2.1 (Sounding mode): *A sounding mode is a subset $\mathcal{M}$ of* $\{1, \ldots, J\} \times \{1, \ldots, M_1\} \times \{1, \ldots, M_2\}$.

The log-likelihood function of $\bar{\boldsymbol{\theta}}$ associated to the sounding mode $\mathcal{M}$ is given by

$$\Lambda(\bar{\boldsymbol{\theta}}) = \sum_{(j,m_1,m_2)\in\mathcal{M}} \Lambda_{j,m_1,m_2}(\bar{\boldsymbol{\theta}}).$$ (B.14)

We enumerate the elements of a sounding mode $\mathcal{M}$ by the index i, i.e. we define a bijection

$$\{1, \ldots, I\} \to \mathcal{M}, \ i \mapsto (j(i), m_1(i), m_2(i)). \tag{B.15}$$

Thus, $j(i)$ specifies in which sounding interval sample i was generated. Similarly, the indices $m_1(i)$ and $m_2(i)$ specify which element of Array 1 and which element of Array 2 respectively is used to generate sample i. The total number of spatio-temporal samples acquired in a measurement run is $I = |\mathcal{M}|$. Thus for a parallel sounding system, where $\mathcal{M} = \{1, \ldots, J\} \times \{1, \ldots, M_1\} \times \{1, \ldots, M_2\}$, the number of samples is $I = JM_1M_2$. For a switched sounding system where one sample is acquired in each sounding interval we have $I = J$.

Defining $\Lambda_i(\bar{\boldsymbol{\theta}}) \triangleq \Lambda_{(j(i), m_1(i), m_2(i))}(\bar{\boldsymbol{\theta}})$ we can now recast (B.14) as

$$\Lambda(\bar{\boldsymbol{\theta}}) = \sum_{i=1}^{I} \Lambda_i(\bar{\boldsymbol{\theta}}). \tag{B.16}$$

The choice of indexing in (B.15) is not unique. The particular enumeration of the elements of a sounding mode only determines the order of the terms in the sum (B.16) which is irrelevant in the further development. The indexing can therefore be selected arbitrarily by the system designer. In switched sounding systems it is natural to select the indices such that $j(i) = i$ and $t_1 < t_2 < \cdots < t_I$. In parallel sounding systems however, indexing purely according to the temporal order is not possible because the sounding pulses overlap in time.

We define the vector

$$\mathbf{a}_i \triangleq [t(i), \mathbf{r}_1(i)^{\mathsf{T}}, \mathbf{r}_2(i)^{\mathsf{T}}]^{\mathsf{T}} \in \mathbb{R}^7, \tag{B.17}$$

where $t(i) \triangleq t_{j(i)}$, $\mathbf{r}_1(i) \triangleq \mathbf{r}_{m_1(i)}$, and $\mathbf{r}_2(i) \triangleq \mathbf{r}_{m_2(i)}$. We say that $\mathbf{a}_i$ is the center point of the ith spatio-temporal sample.

Definition B.2.2 (Spatio-temporal aperture matrix): *The $7 \times I$ spatio-temporal aperture matrix* $\mathbf{A}$ *is determined as*

$$\mathbf{A} \triangleq [\mathbf{a}_1, \ldots, \mathbf{a}_i, \ldots, \mathbf{a}_I] \in \mathbb{R}^{7 \times I} \tag{B.18}$$

with $\mathbf{a}_i$ *defined in* (B.17).

Without loss of generality we select the origin of the spatio-temporal coordinate system such that the columns of $\mathbf{A}$ fulfill

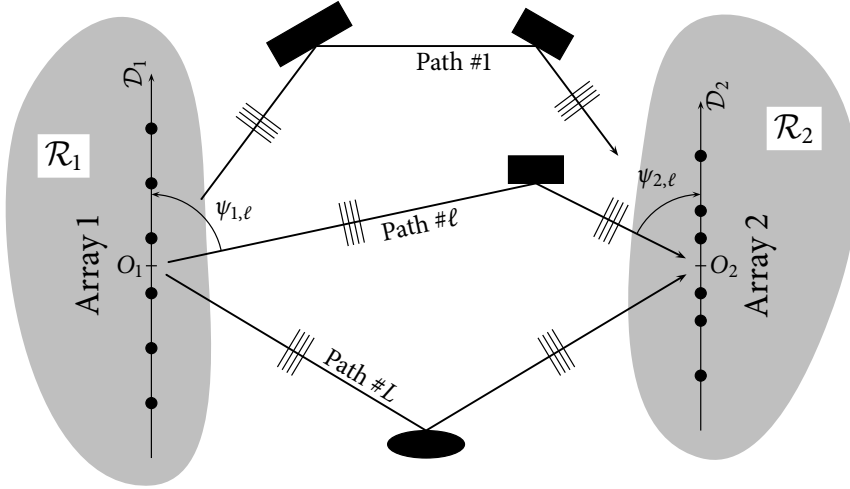$$\sum_{i=1}^{I} \mathbf{a}_i = \mathbf{0}. \tag{B.19}$$

Fig. B.2: A sounding system with linear arrays. The black dots indicate the centroids of the antenna elements.

However, as we will see in Subsection B.3.1 this condition has some optimality property, in the sense that it ensures decoupling in the Fisher information matrix between the linear (α_ℓ) and non-linear ($\boldsymbol{\vartheta}_\ell$) parameters of path ℓ. The spatio-temporal aperture is uniquely defined by the spatio-temporal aperture matrix **A** together with the pulse length T.

B.2.4 *Linear Antenna Arrays*

For sounding systems with linear antenna arrays, as the one depicted in Fig. B.2, the signal model can be simplified. We say that Array k is linear if its elements are located along a straight line $\mathcal{D}_k$ through the origin of O_k, i.e. $\mathbf{r}_k \in \mathcal{D}_k \cap \mathcal{R}_k$. In this case, the position of a point on the array axis $\mathcal{D}_k$ is specified by the signed distance $d_k \in \mathbb{R}$ from the origin of O_k. Likewise, $d_k(i)$ denotes the centroid position of the ith temporal sounding pulse at Array k. Obviously, the full $\boldsymbol{\Omega}_{k,\ell}$-vector cannot be estimated in this case but only its projection onto the array axis $\mathcal{D}_k$. Therefore we replace $\boldsymbol{\Omega}_{k,\ell}$ by this projection denoted by $\omega_{k,\ell}$. It can be noticed that $\omega_{k,\ell} = \cos(\psi_{k,\ell})$ where $\psi_{k,\ell}$ is the angle between the array axis $\mathcal{D}_k$ and $\boldsymbol{\Omega}_{k,\ell}$. We call $\omega_{k,\ell}$ the *spatial frequency* of Path ℓ at Array 1. In the sequel we assume one-dimensional arrays and replace $\mathbf{r}_k$ by d_k, and $\boldsymbol{\Omega}_{k,\ell}$ by $\omega_{k,\ell}$. Consequently, $\mathbf{a}_i = [t(i), d_1(i), d_2(i)]^\mathsf{T} \in \mathbb{R}^3$, $\boldsymbol{\theta}_\ell = [\alpha_\ell, \nu_\ell, \omega_{1,\ell}, \omega_{2,\ell}]^\mathsf{T} \in \mathbb{C} \times \mathbb{R}^3$, and $\boldsymbol{\theta} = [\boldsymbol{\theta}_1^\mathsf{T}, \ldots, \boldsymbol{\theta}_L^\mathsf{T}]^\mathsf{T}$ is a $4L$-dimensional vector throughout the remainder of this paper. We also define $\boldsymbol{\vartheta}_\ell \triangleq [\nu_\ell, \omega_{1,\ell}, \omega_{2,\ell}]^\mathsf{T} \in \mathbb{R}^3$ and $\boldsymbol{\vartheta} \triangleq [\boldsymbol{\vartheta}_1^\mathsf{T}, \ldots, \boldsymbol{\vartheta}_L^\mathsf{T}]^\mathsf{T}$ for the subsequent investigations.

B.2.5   Specific Examples of Systems Using Linear Arrays

In numerical examples we will consider two switched systems named "MIMO-ULA" and "SIMO-ULA", respectively. The MIMO-ULA system is equipped with two uniformly spaced linear arrays consisting of M_k antenna elements with half-a-wavelength inter-element spacing. The position of element $m_k(i)$ is given by $d_k(i) \triangleq \frac{1}{2}\left(m_k(i) - \mu_k\right)$, where μ_k is selected such that (B.19) is fulfilled. We define the antenna element index vector $\mathbf{m}_k \triangleq \left[m_k(1), \ldots, m_k(I)\right]^{\mathsf{T}}$. The SIMO-ULA system is a MIMO-ULA system with $M_1 = 1$. For both MIMO-ULA and SIMO-ULA the uniform temporal sampling

$$t(i) \triangleq \left(i - \tfrac{I+1}{2}\right) T_r, \quad T_r \geq T \tag{B.20}$$

is selected. Here, T_r denotes the time-period between consecutive samples. With this definition $\sum_{i=1}^{I} t(i) = 0$, as required from (B.19). Hence, the spatio-temporal aperture matrix $\mathbf{A}$ of the MIMO-ULA system is fully defined by the vectors $\mathbf{m}_1$ and $\mathbf{m}_2$. For the SIMO-ULA system it suffices to specify $\mathbf{m}_2$.

For the MIMO-ULA system the estimation range $\mathcal{E}_{\boldsymbol{\vartheta}_\ell}$ of $\boldsymbol{\vartheta}_\ell$ is given as

$$\mathcal{E}_{\boldsymbol{\vartheta}_\ell} = \mathcal{E}_\nu \times \mathcal{E}_{\omega_1} \times \mathcal{E}_{\omega_2} \tag{B.21}$$

with $\mathcal{E}_\nu = \left(-\frac{1}{2T_r}, +\frac{1}{2T_r}\right]$ and $\mathcal{E}_{\omega_k} = (-1, +1]$. For the SIMO-ULA system, where $\omega_{1,\ell}$ is not estimable, we select $\mathcal{E}_{\omega_1} = \{0\}$.

B.3   Fisher Information Matrix and Cramér-Rao Lower Bounds

In this section we investigate the effect of the spatio-temporal aperture matrix $\mathbf{A}$ on the (conditional) Cramér-Rao lower bound (CRLB) and on the Bayesian Cramér-Rao lower bound (BCRLB) for the estimation of the entries of the parameter vector $\boldsymbol{\theta}$. The CRLB is a function of $\boldsymbol{\theta}$, whereas the BCRLB depends on an assumed prior density function for $\boldsymbol{\theta}$ [18].

In the following subsections we first derive the CRLB for the estimator and show which criterion the aperture matrix should fulfill in order to yield the minimum CRLB in a scenario with one propagation path ($L = 1$). Thereafter we show that the same criterion minimizes the BCRLB in the multipath case.

B.3.1   The Conditional Cramér-Rao Lower Bound

The CRLB on the variance of the estimation error of an unbiased estimator of $[\boldsymbol{\theta}]_{p,p}$ can be calculated as the pth diagonal of the inverted Fisher information matrix:

$$\mathrm{CRLB}([\hat{\boldsymbol{\theta}}]_p) \triangleq \left[\mathbf{F}(\boldsymbol{\theta})^{-1}\right]_{p,p}. \tag{B.22}$$

In Appendix B.I the Fisher information matrix $\mathbf{F}(\boldsymbol{\theta})$ for the estimation of $\boldsymbol{\theta}$ is shown to be of the form

$$\mathbf{F}(\boldsymbol{\theta}) \triangleq \begin{bmatrix} \mathbf{F}_{\boldsymbol{\theta}_1\boldsymbol{\theta}_1} & \cdots & \mathbf{F}_{\boldsymbol{\theta}_1\boldsymbol{\theta}_L} \\ \vdots & \ddots & \vdots \\ \mathbf{F}_{\boldsymbol{\theta}_L\boldsymbol{\theta}_1} & \cdots & \mathbf{F}_{\boldsymbol{\theta}_L\boldsymbol{\theta}_L} \end{bmatrix} \tag{B.23}$$

where the sub-matrix $\mathbf{F}_{\boldsymbol{\theta}_\ell,\boldsymbol{\theta}_{\ell'}}$ is partitioned as

$$\mathbf{F}_{\boldsymbol{\theta}_\ell\boldsymbol{\theta}_{\ell'}} = \begin{bmatrix} F_{\alpha_\ell\alpha_{\ell'}} & \mathbf{F}_{\alpha_\ell\vartheta_{\ell'}} \\ \mathbf{F}_{\vartheta_\ell\alpha_{\ell'}} & \mathbf{F}_{\vartheta_\ell\vartheta_{\ell'}} \end{bmatrix}. \tag{B.24}$$

Defining the *normalized element factor* of sounding pulse i (see also Section B.4) as

$$\mathrm{EF_n}(v;i) \triangleq \frac{1}{E} \int |p_i(t)|^2 \exp(j2\pi vt)\,\mathrm{d}t \tag{B.25}$$

with $p_i(t) \triangleq p_{j(i),m_1(i)}(t)$, the entries $\mathbf{F}_{\alpha_\ell\alpha_{\ell'}}, \mathbf{F}_{\vartheta_\ell\alpha_{\ell'}} = \mathbf{F}^{\mathsf{H}}_{\alpha_{\ell'},\vartheta_\ell}$, and $\mathbf{F}_{\vartheta_\ell\vartheta_{\ell'}}$ of $\mathbf{F}_{\boldsymbol{\theta}_\ell\boldsymbol{\theta}_{\ell'}}$ read

$$\mathbf{F}_{\alpha_\ell\alpha_{\ell'}} = \frac{E}{N_0}\Re\left\{ \sum_{i=1}^{I} \exp(j2\pi(\vartheta_\ell-\vartheta_{\ell'})^{\mathsf{T}}\mathbf{a}_i)\mathrm{EF_n}(v_\ell-v_{\ell'};i) \right\}, \tag{B.26}$$

$$\mathbf{F}_{\vartheta_\ell\alpha_{\ell'}} = \frac{2\pi E}{N_0}\Re\left\{ (j-1)\alpha_{\ell'} \sum_{i=1}^{I} \mathbf{a}_i \cdot \exp(j2\pi(\vartheta_\ell-\vartheta_{\ell'})^{\mathsf{T}}\mathbf{a}_i)\mathrm{EF_n}(v_\ell-v_{\ell'};i) \right\}, \tag{B.27}$$

and

$$\mathbf{F}_{\vartheta_\ell\vartheta_{\ell'}} = \frac{8\pi^2 E}{N_0}\Re\left\{ \alpha_\ell\alpha_{\ell'}^* \sum_{i=I}^{I} \mathbf{a}_i\mathbf{a}_i^{\mathsf{T}} \cdot \exp(j2\pi(\vartheta_\ell-\vartheta_{\ell'})^{\mathsf{T}}\mathbf{a}_i)\mathrm{EF_n}(v_\ell-v_{\ell'};i) \right\}. \tag{B.28}$$

As can be noticed from (B.26)–(B.28), the matrix $\mathbf{F}_{\boldsymbol{\theta}_\ell\boldsymbol{\theta}_{\ell'}}$ in general depends on the parameter vectors $\boldsymbol{\theta}_\ell$ and $\boldsymbol{\theta}_{\ell'}$. For $\ell = \ell'$, the factor $\mathrm{EF_n}(v;i)$ in (B.25) and the exponential terms in (B.26)–(B.28) are all unity. Therefore, making use of the condition (B.19) and the identity $\sum_{i=1}^{I} \mathbf{a}_i\mathbf{a}_i^{\mathsf{T}} = \mathbf{A}\mathbf{A}^{\mathsf{T}}$ we obtain

$$\mathbf{F}_{\alpha_\ell\alpha_\ell} = \frac{EI}{N_0}, \quad \mathbf{F}_{\vartheta_\ell\alpha_\ell} = \mathbf{0}, \quad \text{and} \quad \mathbf{F}_{\vartheta_\ell\vartheta_\ell} = \frac{8\pi^2 E|\alpha_\ell|^2}{N_0}\mathbf{A}\mathbf{A}^{\mathsf{T}}. \tag{B.29}$$

As is apparent from (B.29), the matrix $\mathbf{F}_{\vartheta_\ell\vartheta_\ell}$ depends only on $|\alpha_\ell|$ and not on the remaining entries of $\boldsymbol{\theta}$. Notice, that the choice of a coordinate system satisfying (B.19) ensures that $\mathbf{F}_{\vartheta_\ell\alpha_\ell} = \mathbf{0}$ holds. Similar effects have previously been noticed for radar systems [19], for direction estimation [6], and for switched sounding systems [2].

B.3.2 *The One-Path Case, Orthogonal Aperture*

For the one-path case ($L = 1$) we have $\boldsymbol{\theta} = \boldsymbol{\theta}_1$. For simplicity we drop the path index $\ell = 1$. It follows from (B.23), (B.24) and (B.29) that the Fisher information matrix reads

$$\mathbf{F}(\boldsymbol{\theta}) = \begin{bmatrix} \frac{EI}{N_0} & \mathbf{0}^\mathsf{T} \\ \mathbf{0} & \mathbf{F}_{\vartheta\vartheta} \end{bmatrix}, \tag{B.30}$$

with

$$\mathbf{F}_{\vartheta\vartheta} = 8\pi^2\gamma_0 \frac{1}{I}\mathbf{A}\mathbf{A}^\mathsf{T} = 8\pi^2\gamma_0 \frac{1}{I} \begin{bmatrix} \mathbf{t}^\mathsf{T}\mathbf{t} & \mathbf{t}^\mathsf{T}\mathbf{d}_1 & \mathbf{t}^\mathsf{T}\mathbf{d}_2 \\ \mathbf{d}_1^\mathsf{T}\mathbf{t} & \mathbf{d}_1^\mathsf{T}\mathbf{d}_1 & \mathbf{d}_1^\mathsf{T}\mathbf{d}_2 \\ \mathbf{d}_2^\mathsf{T}\mathbf{t} & \mathbf{d}_2^\mathsf{T}\mathbf{d}_1 & \mathbf{d}_2^\mathsf{T}\mathbf{d}_2 \end{bmatrix}, \tag{B.31}$$

where $\gamma_0 \triangleq |\alpha|^2 \frac{EI}{N_0}$ is the signal to noise ratio (SNR) and $\mathbf{t} \triangleq [t(1), \ldots, t(I)]^\mathsf{T}$, $\mathbf{d}_k \triangleq [d_k(1), \ldots, d_k(I)]^\mathsf{T}$, $k = 1, 2$, denote the rows of $\mathbf{A}$.

By inspection of (B.31) we see that the pth diagonal element of $\mathbf{F}_{\vartheta\vartheta}$ depends only on the squared norm of the pth row of $\mathbf{A}$, e.g. element $(1,1)$ depends only on $|\mathbf{t}|^2$. The off-diagonal elements of $\mathbf{F}_{\vartheta\vartheta}$ are cross-terms involving scalar products of different rows of $\mathbf{A}$. For example the off diagonal element $[\mathbf{F}_{\vartheta\vartheta}]_{2,1}$ is proportional to $\mathbf{d}_1^\mathsf{T}\mathbf{t}$.

Theorem B.3.1: *The CRLBs for the estimation of the Doppler and spatial frequencies fulfill the inequalities*

$$\mathrm{CRLB}(\hat{\omega}_k) \geq \frac{1}{8\pi^2\gamma_0\frac{1}{I}|\mathbf{d}_k|^2}, \ k = 1, 2, \quad and \quad \mathrm{CRLB}(\hat{v}) \geq \frac{1}{8\pi^2\gamma_0\frac{1}{I}|\mathbf{t}|^2}. \tag{B.32}$$

Moreover, equality in all three inequalities is achieved simultaneously in (B.32) *if, and only if, the rows of* $\mathbf{A}$ *are orthogonal, i.e.*

$$\mathbf{t}^\mathsf{T}\mathbf{d}_1 = 0, \quad \mathbf{t}^\mathsf{T}\mathbf{d}_2 = 0, \ and \ \mathbf{d}_1^\mathsf{T}\mathbf{d}_2 = 0. \tag{B.33}$$

Proof. It is shown in [20, pp. 231] that $[\mathbf{F}]_{p,p}^{-1} \leq [\mathbf{F}^{-1}]_{p,p}$ for any p, i.e. $[\mathbf{F}]_{p,p}^{-1}$ lower bounds the CRLB for parameter $[\boldsymbol{\theta}]_p$. Using Lemma B.II.3 given in Appendix B.II we see that the equality $[\mathbf{F}_{\theta\theta}]_{p,p}^{-1} = [\mathbf{F}_{\theta\theta}^{-1}]_{p,p}$ is obtained *for all* p if, and only if, $\mathbf{F}_{\theta\theta}$ is diagonal. By inspection of (B.30) we see that $\mathbf{F}_{\theta\theta}$ is diagonal if, and only if, the rows of $\mathbf{A}$ fulfill (B.33). □

Restricting the comparison to the class of apertures with equal diagonal elements in their associated Fisher information matrices we have the corollary:

Corollary B.3.2: *Within the class of spatio-temporal apertures with identical values of $|\mathbf{t}|^2$, $|\mathbf{d}_1|^2$, and $|\mathbf{d}_2|^2$, the minimum CRLB is obtained if, and only if, the rows of the aperture matrix are orthogonal.*

A result analog to Theorem B.3.1 for the joint estimation of elevation and azimuth and elevation of arrival of a single path has previously been published. As shown in [6, 7], the minimum CRLB for joint estimation of azimuth and elevation from data collected with a three-dimensional array is achieved if, and only if, the non-diagonal terms of the matrix $\sum_{i=1}^{I} \mathbf{r}_2(i)\mathbf{r}_2(i)^\mathsf{T}$ vanish.

B.3.3   *Specific Examples (Continued)*

In the following we demonstrate the impact of the spatio-temporal aperture on the CRLB in the one-path case. We consider the CRLB of a MIMO-ULA system with $I = M_1 M_2$, and the commonly used sequential sounding mode

$$m_1(i) = \lceil i/M_2 \rceil , \text{ and} \tag{B.34}$$

$$m_2(i) = (i - 1 \mod M_2) + 1. \tag{B.35}$$

Equivalently, $\mathbf{m}_1 = [1, 2, \dots, M_1]^\mathsf{T} \otimes \mathbf{1}_{M_2}$ and $\mathbf{m}_2 = \mathbf{1}_{M_1} \otimes [1, 2, \dots, M_2]^\mathsf{T}$. We chose $T_r = T$. This selection of $m_k(i)$ ensures that all pairs of one Array 1 element and one Array 2 element are active once, and, as we will show in Section B.3.5, that $\mathbf{d}_1^\mathsf{T}\mathbf{d}_2 = 0$. The resulting spatio-temporal aperture matrix yields a non-diagonal Fisher information matrix because $\mathbf{t}^\mathsf{T}\mathbf{d}_k \neq 0$ and the minimum CRLB is not obtained. If in addition $M_1 = M_2$, the Fisher information matrix is non-invertible, and hence the CRLB is infinite. For instance in the case where $M_1 = 10$ and $M_2 = 9$ the ratios between the CRLBs obtained for the selected aperture matrix $\mathbf{A}$ resulting from (B.34) and (B.35) and the minimum CRLB for ν, ω_1, and ω_2 are calculated as $\left[\mathbf{F}_{\theta\theta}^{-1}\right]_{2,2} \cdot \left[\mathbf{F}_{\theta\theta}\right]_{2,2} \approx$ 15.4 dB, $\left[\mathbf{F}_{\theta\theta}^{-1}\right]_{3,3} \cdot \left[\mathbf{F}_{\theta\theta}\right]_{3,3} \approx 15.3$ dB, and $\left[\mathbf{F}_{\theta\theta}^{-1}\right]_{4,4} \cdot \left[\mathbf{F}_{\theta\theta}\right]_{4,4} \approx 1.27$ dB, respectively.

In the above example the spatial sounding was selected such that all antenna array elements are active the same number of times during one measurement run. In the next example we compare this case to the case where some antenna elements are active more frequently than others.

With $M_k = 8$, $k = 1, 2$ we see that $|\mathbf{d}_k|^2 = 84$ if all Array k elements are active 8 times. For comparison we select the spatial sampling schemes such that $m_k(i) \in \{1, 2, 7, 8\}$, i.e. we use only four of the eight elements of each array. In this case, provided all the used antenna array elements are active the same number of times (i.e. 16 times) during the measurement run, we have $|\mathbf{d}_k|^2 = 148$. If both spatio-temporal apertures fulfill (B.33) we see that

the CRLB in the latter case is lower than in the former case. The difference amounts to approximately 2.46 dB.

These two examples clearly show that the sounding mode highly affects the CRLBs for the estimation of spatial and Doppler frequencies in the one-path case.

B.3.4   Orthogonal Apertures in the Multipath Case

Motivated by the above orthogonality criterion that applies to the one-path case, it is of interest to see if this condition holds true in the multipath case as well. As remarked in Section B.3.1, the Fisher information matrix depends on the parameters to be estimated. In particular the off-diagonals of the Fisher information matrix which enters the proof of Theorem B.3.1 depend on the path parameters. Thus it is difficult to give a characterization of the minimum CRLB in the multipath case. To circumvent this obstacle we investigate the BCRLB.

The BCRLB for the estimation of $\boldsymbol{\theta}$ is [18]

$$\text{BCRLB} \triangleq (\mathbf{G} + \mathbf{P})^{-1}, \tag{B.36}$$

where $\mathbf{G}$ is the Fisher information matrix averaged with respect to the prior density $\lambda(\boldsymbol{\theta})$

$$\mathbf{G} \triangleq \int \mathbf{F}(\boldsymbol{\theta})\lambda(\boldsymbol{\theta}) \, \mathrm{d}\boldsymbol{\theta} \tag{B.37}$$

and the matrix $\mathbf{P}$ depends only on the prior (and is independent of the aperture matrix). The particular choice of prior does not affect our analysis in the following.

By (B.23) we see that $\mathbf{G}$ can be written as

$$\mathbf{G} = \begin{bmatrix} \mathbf{G}_{\boldsymbol{\theta}_1 \boldsymbol{\theta}_1} & \cdots & \mathbf{G}_{\boldsymbol{\theta}_1 \boldsymbol{\theta}_L} \\ \vdots & \ddots & \vdots \\ \mathbf{G}_{\boldsymbol{\theta}_L \boldsymbol{\theta}_1} & \cdots & \mathbf{G}_{\boldsymbol{\theta}_L \boldsymbol{\theta}_L} \end{bmatrix}, \tag{B.38}$$

with

$$\mathbf{G}_{\boldsymbol{\theta}_\ell \boldsymbol{\theta}_{\ell'}} \triangleq \int \mathbf{F}_{\boldsymbol{\theta}_\ell \boldsymbol{\theta}_{\ell'}} \lambda(\boldsymbol{\theta}) \mathrm{d}\boldsymbol{\theta}. \tag{B.39}$$

We remark that the diagonal blocks of $\mathbf{G}$ read

$$\mathbf{G}_{\boldsymbol{\theta}_\ell, \boldsymbol{\theta}_\ell} = \begin{bmatrix} G_{\alpha_\ell \alpha_\ell} & \mathbf{0}^{\mathsf{T}} \\ \mathbf{0} & \mathbf{G}_{\vartheta_\ell \vartheta_\ell} \end{bmatrix} \tag{B.40}$$

with

$$\mathbf{G}_{\vartheta_\ell \vartheta_\ell} = 8\pi^2 \frac{\mathsf{E}\big[|\alpha_\ell|^2\big] \cdot E}{N_0} \mathbf{A}\mathbf{A}^\mathsf{T}, \quad \ell = 1, \dots, L, \tag{B.41}$$

where $\mathsf{E}\big[|\alpha_\ell|^2\big]$ denotes the expectation with respect to the prior of α_ℓ.

We are now able to give the following characterization of the aperture matrices which yields the lowest BCRLB in the multipath case:

Theorem B.3.3: *Let* $\mathrm{BCRLB}_{\tilde{\mathbf{A}}}$ *be the BCRLB resulting from the aperture matrix* $\tilde{\mathbf{A}}$ *and similarly* $\mathrm{BCRLB}_{\mathbf{A}}$ *the BCRLB resulting from an arbitrary aperture matrix* $\mathbf{A}$ *with the property that* $\mathrm{diag}(\mathbf{A}\mathbf{A}^\mathsf{T}) = \mathrm{diag}(\tilde{\mathbf{A}}\tilde{\mathbf{A}}^\mathsf{T})$. *If the inequality*

$$\mathrm{BCRLB}_{\mathbf{A}} \ge \mathrm{BCRLB}_{\tilde{\mathbf{A}}} \tag{B.42}$$

is fulfilled for any such aperture matrix $\mathbf{A}$ *then the rows of* $\tilde{\mathbf{A}}$ *are orthogonal.*

Proof. We prove Theorem B.3.3 by proving that if the BCRLB of an aperture matrix $\tilde{\mathbf{A}}$ is lower than or equal to the BCRLB of an orthogonal aperture matrix $\mathbf{A}$, then $\tilde{\mathbf{A}}$ is orthogonal as well. By the assumption (B.42),

$$(\mathbf{G} + \mathbf{P})^{-1} \ge (\tilde{\mathbf{G}} + \mathbf{P})^{-1} \tag{B.43}$$

is fulfilled for any $\mathbf{G}$ such that $\mathrm{diag}(\mathbf{A}\mathbf{A}^\mathsf{T}) = \mathrm{diag}(\tilde{\mathbf{A}}\tilde{\mathbf{A}}^\mathsf{T})$. Making use of (B.69) given in Appendix B.II and eliminating the $\mathbf{P}$ terms we obtain from (B.43)

$$\tilde{\mathbf{G}} \ge \mathbf{G}. \tag{B.44}$$

Then, by invoking Lemma B.II.2 in Appendix B.II, and inserting (B.40) we obtain after elimination of some irrelevant terms

$$[(\mathbf{A}\mathbf{A}^\mathsf{T})^{-1}]_{p,p} \ge [(\tilde{\mathbf{A}}\tilde{\mathbf{A}}^\mathsf{T})^{-1}]_{p,p}, \quad \text{for all } p. \tag{B.45}$$

Now, suppose that $\mathbf{A}$ is row-orthogonal. Then $\mathbf{A}\mathbf{A}^\mathsf{T}$ is diagonal and $[(\mathbf{A}\mathbf{A}^\mathsf{T})^{-1}]_{p,p} = 1/[\mathbf{A}\mathbf{A}^\mathsf{T}]_{p,p}$ for all p. Inserting in (B.45) yields

$$\frac{1}{[(\mathbf{A}\mathbf{A}^\mathsf{T})]_{p,p}} \ge [(\tilde{\mathbf{A}}\tilde{\mathbf{A}}^\mathsf{T})^{-1}]_{p,p} \quad \text{for all } p. \tag{B.46}$$

From [21, Theorem 7.7.8] we have that $[(\tilde{\mathbf{A}}\tilde{\mathbf{A}}^\mathsf{T})^{-1}]_{p,p} \ge 1/[\tilde{\mathbf{A}}\tilde{\mathbf{A}}^\mathsf{T}]_{p,p}$ for any p. Since $\mathrm{diag}(\mathbf{A}\mathbf{A}^\mathsf{T}) = \mathrm{diag}(\tilde{\mathbf{A}}\tilde{\mathbf{A}}^\mathsf{T})$ then $1/[\mathbf{A}\mathbf{A}^\mathsf{T}]_{p,p} = 1/[\tilde{\mathbf{A}}\tilde{\mathbf{A}}^\mathsf{T}]_{p,p}$ for any p. Hence $[(\tilde{\mathbf{A}}\tilde{\mathbf{A}}^\mathsf{T})^{-1}]_{p,p} \ge 1/[\mathbf{A}\mathbf{A}^\mathsf{T}]_{p,p}$ for any p. Combining this additional inequality with (B.46) we obtain for any p

$$\frac{1}{[\mathbf{A}\mathbf{A}^\mathsf{T}]_{p,p}} \ge [(\tilde{\mathbf{A}}\tilde{\mathbf{A}}^\mathsf{T})^{-1}]_{p,p} \ge \frac{1}{[\mathbf{A}\mathbf{A}^\mathsf{T}]_{p,p}}, \tag{B.47}$$

$$\Rightarrow [(\tilde{\mathbf{A}}\tilde{\mathbf{A}}^\mathsf{T})^{-1}]_{p,p} = \frac{1}{[\mathbf{A}\mathbf{A}^\mathsf{T}]_{p,p}}. \tag{B.48}$$

By Lemma B.II.3 given in Appendix B.II, the two inequalities in (B.47) are fulfilled for all p if, and only if, $\tilde{\mathbf{A}}\tilde{\mathbf{A}}^\mathsf{T}$ is diagonal. Hence, $\tilde{\mathbf{A}}$ is row-orthogonal.

□

It is worth noticing the difference between Theorem B.3.1 and Theorem B.3.3. Theorem B.3.1 states that (in the one-path case), the orthogonality condition (B.33) is a *necessary and sufficient condition* for the minimum CRLB to be achieved. The result in Theorem B.3.3 states a *necessary* (but not sufficient) condition for an aperture matrix to yield the minimum BCRLB in the sense of (B.42). The reason for this seemingly weaker result is that the cross-terms $\mathbf{G}_{\ell,\ell'}, \ell \neq \ell'$ in the matrices $\tilde{\mathbf{G}}$ and $\mathbf{G}$ are removed in the step from (B.44) to (B.45). If the off-diagonal blocks should be taken into consideration, more specific assumptions must be made about the prior. Considering a prior and a group of apertures such that $\mathbf{G}_{\ell,\ell'} = \mathbf{0}, \ell \neq \ell'$, one can prove that row-orthogonality is a necessary and sufficient condition for an aperture matrix to yield the minimum BCRLB. The proof is similar to the proof of Theorem B.3.1.

B.3.5   Uniform and Parallel Spatio-Temporal Apertures

In the following, we define the concept of uniformity of a spatio-temporal aperture matrix and show that uniformity implies that this matrix is row-orthogonal. For convenience we define the row indices p, q, and r of $\mathbf{A}$ such that $\{p, q, r\} = \{1, 2, 3\}$ is fulfilled. Let $\mathbf{b}$ be a column of $\mathbf{A}$, i.e. $\mathbf{b} \in \{\mathbf{a}_1, \ldots, \mathbf{a}_I\}$. Then the number of columns of $\mathbf{A}$ that coincide with $\mathbf{b}$ in the pth and qth elements can be written as

$$\varphi_{p,q}(\mathbf{b}) \triangleq \left| \left\{ i \in \{1, \ldots, I\} : ([\mathbf{b}]_p, [\mathbf{b}]_q) = ([\mathbf{a}_i]_p, [\mathbf{a}_i]_q) \right\} \right|.$$

Definition B.3.4: A spatio-temporal aperture matrix $\mathbf{A}$ is (p, q)-uniform if, and only if, there exists a constant $\varphi_{p,q}$ such that $\varphi_{p,q}(\mathbf{b}) = \varphi_{p,q}$, for all $\mathbf{b} \in \{\mathbf{a}_1, \ldots, \mathbf{a}_I\}$.

We can now prove a simple lemma which turns out to be helpful for the design of row-orthogonal spatio-temporal aperture matrices.

Lemma B.3.5: Row p and row q of a (p, q)-uniform spatio-temporal aperture matrix $\mathbf{A}$ are orthogonal.

Proof. Let $\mathbf{c}_r^\mathsf{T} = [c_{r,1}, \ldots, c_{r,I}]$ denote the rth row of $\mathbf{A}$ and $\mathcal{C}_r = \bigcup_{i=1}^I \{c_{r,i}\}$. Then $\sum_{i=1}^I c_{p,i} = \varphi_{p,q}|\mathcal{C}_q| \sum_{c_p \in \mathcal{C}_p} c_p$. Therefore,

$$\mathbf{c}_q^\mathsf{T}\mathbf{c}_p = \sum_{i=1}^I c_{q,i}c_{p,i} = \varphi_{p,q} \sum_{c_q \in \mathcal{C}_q} c_q \sum_{c_p \in \mathcal{C}_p} c_p.$$

By convention $\sum_{i=1}^I c_{p,i} = 0$, which implies $\sum_{c_p \in \mathcal{C}_p} c_p = 0$. Thus $\mathbf{c}_q^\mathsf{T}\mathbf{c}_p = 0$.   □

As an example, a $(2, 3)$-uniform (i.e., *spatially uniform*) aperture is a spatio-temporal aperture where all pairs of antenna array elements (m_1, m_2) are active $\varphi_{2,3}$ times during one measurement run. For all spatially uniform aperture matrices the condition $\mathbf{d}_1^\mathsf{T} \mathbf{d}_2 = 0$ is fulfilled. For instance, the spatio-temporal aperture matrix defined by (B.34) and (B.35) is spatially uniform with $\varphi_{2,3} = 1$ and therefore, $\mathbf{d}_1^\mathsf{T} \mathbf{d}_2 = 0$ in this case.

For a parallel sounding system with M_1 transmitters and M_2 receivers where all antenna pairs are active simultaneously, we see that $I = J M_1 M_2$. In this case, $\mathbf{A}$ is $(1, 2)$-uniform with $\varphi_{1,2} = M_2$, $(1, 3)$-uniform with $\varphi_{1,3} = M_1$, and $(2, 3)$-uniform with $\varphi_{2,3} = J$. Therefore, such a system always fulfills (B.33). This result agrees with the result in [22, 23], that $\left[\mathbf{F}_{\boldsymbol{\vartheta}_\ell \boldsymbol{\vartheta}_\ell}\right]_{1,3} = \left[\mathbf{F}_{\boldsymbol{\vartheta}_\ell \boldsymbol{\vartheta}_\ell}\right]_{3,1} = 0$ always hold for a parallel system with $M_1 = 1$.

From the observation that parallel systems always fulfill (B.33), it might seem tempting to conclude that parallel systems are preferable to switched systems. However, the comparison of the CRLBs of different spatio-temporal apertures must be done with the same SNR and thus with the same I for all considered apertures. To illustrate the comparison problem we consider the case where all antenna pairs are active once during the measurement run. In a parallel system this condition implies that all samples are taken simultaneously and therefore $|\mathbf{t}|^2 = 0$. Hence, in this case, Doppler frequency estimation is not possible. In a switched sounding system the same condition implies that $|\mathbf{t}|^2 > 0$ and thus a spatio-temporal aperture with finite CRLB can be constructed. In general one can always construct a spatio-temporal aperture of a switched sounding system with a value $|\mathbf{t}|^2$ larger than that of a parallel sounding system with the same number of samples. An additional major difference between parallel and switched systems is that parallel systems do not allow for adjustments of $|\mathbf{d}_k|^2$ without changing the geometry of the antenna arrays, as do switched systems.

B.4   Spatio-Temporal Ambiguity Function

In this section we define a (bi-)spatio-temporal ambiguity function for channel sounding. To our best knowledge, this problem has not previously been addressed in published work yet.

Definition B.4.1: *The* Doppler-(bi-)direction ambiguity function *of a (bi-)spatio-temporal channel sounding system is defined to be*

$$\chi(\boldsymbol{\vartheta}, \bar{\boldsymbol{\vartheta}}) \triangleq \frac{1}{E I \alpha^* \bar{\alpha}} \sum_{i=1}^{I} \int_{\mathcal{T}_{j(i)}} s_i^*(t; \boldsymbol{\theta}) s_i(t; \bar{\boldsymbol{\theta}}) \mathrm{d}t, \tag{B.49}$$

where $s_i(t; \boldsymbol{\theta}) \triangleq s_{j(i), m_1(i), m_2(i)}(t; \boldsymbol{\theta})$ *with* $s_{j, m_1, m_2}(t; \boldsymbol{\theta})$ *defined in* (B.5).

The magnitude of the ambiguity function ranges from zero to unity. For any $\boldsymbol{\vartheta} \in \mathcal{E}_{\boldsymbol{\vartheta}}$, $|\chi(\boldsymbol{\vartheta}, \boldsymbol{\vartheta})| = 1$. In the case where there exists a vector $\bar{\boldsymbol{\vartheta}} \in \mathcal{E}_{\boldsymbol{\vartheta}}$, $\bar{\boldsymbol{\vartheta}} \neq \boldsymbol{\vartheta}$ such that $|\chi(\boldsymbol{\vartheta}, \bar{\boldsymbol{\vartheta}})| = 1$, two signal components with parameter vectors $\boldsymbol{\vartheta}$ and $\bar{\boldsymbol{\vartheta}}$ respectively are indistinguishable. This effect we call the ambiguity effect.

Due to the particular form of the sounding pulses (see e.g. (B.5)), the ambiguity function in (B.49) can be recast as

$$\chi(\boldsymbol{\vartheta}, \bar{\boldsymbol{\vartheta}}) = \frac{1}{I} \sum_{i=1}^{I} \exp\left(-j2\pi(\boldsymbol{\vartheta} - \bar{\boldsymbol{\vartheta}})^{\mathsf{T}} \mathbf{a}_i\right) \cdot \mathrm{EF}_{\mathrm{n}}(\nu - \bar{\nu}; i). \tag{B.50}$$

Thus, $\chi(\boldsymbol{\vartheta}, \bar{\boldsymbol{\vartheta}})$ is a function of the difference vector $\boldsymbol{\vartheta} - \bar{\boldsymbol{\vartheta}}$, i.e. $\chi(\boldsymbol{\vartheta}, \bar{\boldsymbol{\vartheta}}) = \chi_0(\boldsymbol{\vartheta} - \bar{\boldsymbol{\vartheta}})$. For simplicity we refer to both $\chi(\boldsymbol{\vartheta}, \bar{\boldsymbol{\vartheta}})$ and $\chi_0(\boldsymbol{\vartheta})$ as "ambiguity function". It suffices to investigate the behaviour of $\chi_0(\boldsymbol{\vartheta})$ defined as

$$\chi_0(\boldsymbol{\vartheta}) = \chi(\boldsymbol{\vartheta}, \mathbf{0}) \tag{B.51}$$

$$= \frac{1}{I} \sum_{i=1}^{I} \exp\left(-j2\pi\boldsymbol{\vartheta}^{\mathsf{T}} \mathbf{a}_i\right) \cdot \mathrm{EF}_{\mathrm{n}}(\nu; i). \tag{B.52}$$

Notice that while the definition of Woodward's ambiguity function [8] involves the transmitted signal only, the definition (B.49) includes both the transmitted temporal-signal and the spatial aperture. A more general class of ambiguity functions is derived in [9], whereof the definition given in (B.49) is a special case. It is shown in Appendix B.III that the Doppler-direction ambiguity function fulfills a constant volume property as does Woodward's ambiguity function. Due to this property, ambiguity volume can be moved from one region of the estimation range to another, but not canceled. Thus, if a side-lobe of the ambiguity function is suppressed, the corresponding suppressed ambiguity volume appears elsewhere.

Inspired by the terminology used in antenna theory [24], we call $\mathrm{EF}_{\mathrm{n}}(\nu; i)$ the *normalized element factor* of the sounding pulse i. When all element factors are equal, i.e. $\mathrm{EF}_{\mathrm{n}}(\nu; i) = \mathrm{EF}_{\mathrm{n}}(\nu)$, the ambiguity function simplifies to

$$\chi_0(\boldsymbol{\vartheta}) = \mathrm{EF}_{\mathrm{n}}(\nu) \cdot \mathrm{AF}_{\mathrm{n}}(\boldsymbol{\vartheta}; \mathbf{A}), \tag{B.53}$$

where

$$\mathrm{AF}_{\mathrm{n}}(\boldsymbol{\vartheta}; \mathbf{A}) \triangleq \frac{1}{I} \sum_{i=1}^{I} \exp\left(-j2\pi\boldsymbol{\vartheta}^{\mathsf{T}} \mathbf{a}_i\right) \tag{B.54}$$

is the *normalized spatio-temporal array factor* or *array factor* for short.

The factorization of (B.53) is analogous to the well-known factorization in the theory of antenna systems. The radiation pattern of an antenna array

with identical elements is the product of an element factor and an array factor [24]. This factorization splits the impacts on the ambiguity function of the array elements, reflected via the element factor, and of the aperture configuration, reflected via the array factor. The main concern of this contribution is the impact of the configuration of the spatio-temporal aperture of a MIMO channel sounder. Thus, the factor of interest in the product (B.53) is the array factor. Two equivalent conceptual approaches can be followed to investigate the effect of the aperture configuration only. The first approach consists merely in restricting the attention to the array factor of the aperture. The second approach consists in considering an ambiguity function induced by the aperture with the impact of the element factor dropped. This is achieved by assuming that the element factor is constant. This assumption is often valid since the duration of a measurement run is typically large compared to the duration of a sounding pulse. The fact that both conceptual approaches are equivalent follows from (B.53).

It follows from the definition (B.54) that the array factor achieves its maximum value at $\vartheta = 0$, namely $|\mathrm{AF_n}(0; A)| = 1$. If there exists a non-zero $\vartheta \in \mathcal{E}_\vartheta$ such that $|\mathrm{AF_n}(\vartheta; A)| = 1$ is fulfilled, the ambiguity effect occurs, provided that the element factor is constant. This observation leads to the following definition.

Definition B.4.2 (Ambiguous array factor)*: A spatio-temporal array factor* $\mathrm{AF_n}(\vartheta; A)$ *is ambiguous if there exist a* $\vartheta \neq 0$ *in* $\mathcal{E}_\vartheta$ *such that* $|\mathrm{AF_n}(\vartheta; A)| = 1$.

A spatio-temporal array factor that is not ambiguous is termed a *non-ambiguous array factor*. If a spatio-temporal aperture yields an ambiguous array factor we say that *the aperture is ambiguous*.

In the following we analyze how the spatio-temporal aperture affects the array factor. In particular we state a necessary and sufficient condition for a spatio-temporal aperture to be ambiguous.

B.4.1 Specific Examples (Continued)

The following numerical examples illustrate the behavior of the array factor for different spatio-temporal apertures. We consider a SIMO-ULA system with $I = 64$ and $M_2 = 8$. Fig. B.3 reports the magnitude of the array factors corresponding to four different spatio-temporal apertures for $(v, \omega_2) \in (-\frac{1}{2T_r}, +\frac{1}{2T_r}] \times (-1, +1]$. In Fig. B.3 (a), $m_2(i)$ is given by (B.35). It is apparent from the figure that the absolute value of the array factor exhibits multiple maxima of unit magnitude and is therefore ambiguous. In Fig. B.3 (b), $m_2(i)$ is defined by $m_2(i) = \lceil i/8 \rceil$, i.e., each Array 2 element is active 8 times in succession. As shown in Fig. B.3 (b) this yields a non-ambiguous array factor
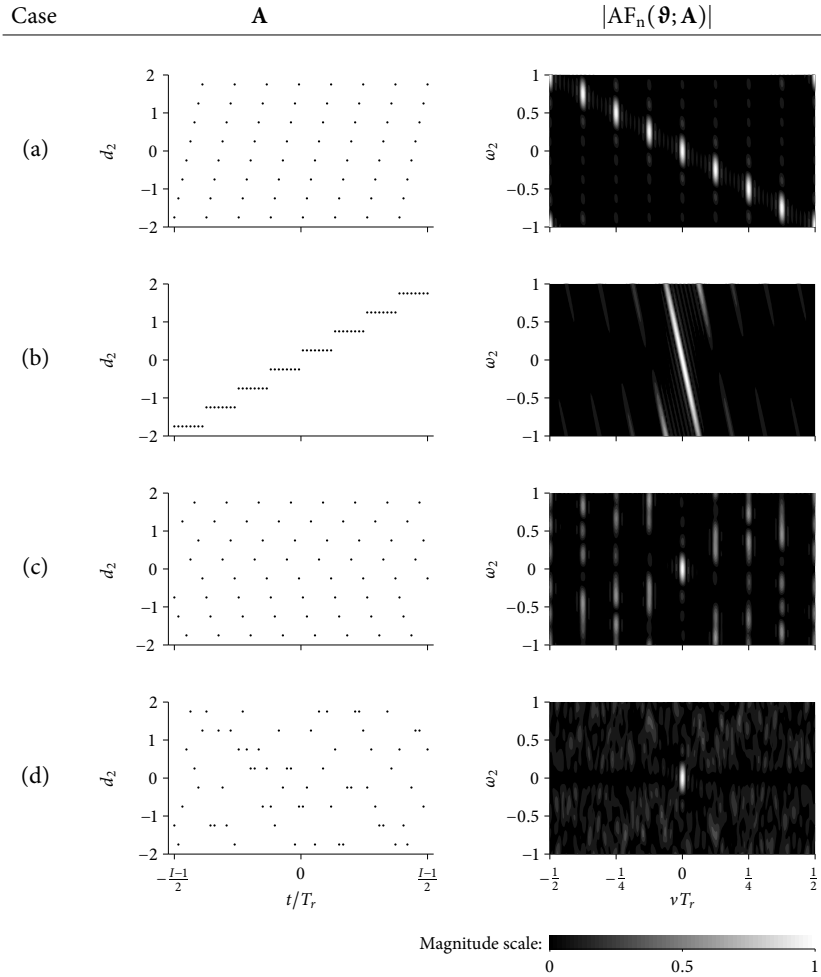
Fig. B.3: *The spatio-temporal arrays (left plots) and corresponding magnitude of the array factors (right plots) in the four cases (a), (b), (c), and (d) described in the text. Each dot of the aperture plots denotes one $(t(i), d_2(i))$ point, i.e. the centroid of one spatio-temporal sample.*

with a unique maximum, but a wide main-lobe. Hence high variances of $\hat{v}$ and $\hat{\omega}_2$ are to be expected in this case at large SNRs. Furthermore, since the main-lobe is tilted, an error in the Doppler frequency estimate affects the error in the direction estimate and vice-versa. The two estimators are statistically dependent. In Fig. B.3 (c), $\mathbf{m}_2$ is defined by $\mathbf{m}_2 = \mathbf{1}_8 \otimes [3, 2, 7, 1, 5, 8, 6, 4]^\mathsf{T}$. This spatial array corresponds to permuting the array element indices and then applying the spatial sounding given in (B.35). It is apparent from Fig. B.3 (c) that the array factor is non-ambiguous in this case and its main lobe is narrower than the one depicted in Fig. B.3 (b). However, "stripes" of side lobes separated by $\frac{1}{8}$ along the vT_r axis are visible. Finally, Fig. B.3 (d) depicts the array factor when $\mathbf{m}_2$ results from a random permutation of the vector $\mathbf{1}_8 \otimes [1, 2, \ldots, 8]^\mathsf{T}$. The depicted function has a unique maximum and the magnitude of the highest side lobe is significantly lower than in Fig. B.3 (c).

Due to the factorization (B.53), the constant volume property of the ambiguity function is fulfilled for the array factor as well. This effect is clearly visible in Fig. B.3 (a)–(d). In Fig. B.3 (a) the ambiguity volume is concentrated in eight lobes with unit maximum magnitude. Thus, the array factor depicted in Fig. B.3 (a) is ambiguous. In Fig. B.3 (b) the volume is mainly located in the wide main-lobe. In Fig. B.3 (c) the volume is concentrated in the main-lobe and in stripes of side-lobes. In Fig. B.3 (d) there is no large side-lobe and the main-lobe remains rather narrow. Instead, the ambiguity volume is distributed to the multiple small-magnitude side-lobes.

B.4.2 Necessary and Sufficient Condition for a Spatio-Temporal Aperture to be Ambiguous

The following lemma gives a necessary and sufficient condition for a spatio-temporal aperture to be ambiguous.

Lemma B.4.3: *A spatio-temporal aperture is ambiguous if, and only if, there exists $\boldsymbol{\vartheta} \in \mathcal{E}_\vartheta$, $\boldsymbol{\vartheta} \neq \mathbf{0}$, such that*

$$\left(\mathbf{a}_i - \mathbf{a}_{i+1}\right)^\mathsf{T} \boldsymbol{\vartheta} \equiv 0 \mod 1, \quad i = 1, \ldots, I - 1. \qquad (B.55)$$

Proof. The spatio-temporal array factor $\mathrm{AF}_\mathrm{n}(\boldsymbol{\vartheta}; \mathbf{A})$ has magnitude 1 if, and only if, the phases of the exponential terms in (B.54) satisfy

$$2\pi \mathbf{a}_1^\mathsf{T} \boldsymbol{\vartheta} \equiv 2\pi \mathbf{a}_2^\mathsf{T} \boldsymbol{\vartheta} \equiv \cdots \equiv 2\pi \mathbf{a}_I^\mathsf{T} \boldsymbol{\vartheta} \mod 2\pi. \qquad (B.56)$$

The total number of congruences in this system is the factorial of I. Solving (B.56) is equivalent to solving the $I - 1$ "neighboring" congruences (B.55). The latter set of congruences is always fulfilled for the "trivial solution" $\boldsymbol{\vartheta} = \mathbf{0}$. The array factor $\mathrm{AF}_\mathrm{n}(\boldsymbol{\vartheta}; \mathbf{A})$ is ambiguous if, and only if, (B.56) has a non-trivial solution ($\boldsymbol{\vartheta} \neq \mathbf{0}$) in $\mathcal{E}_\vartheta$. $\qquad \square$

B.4.3 Specific Examples (Continued)

In the following we define a class of spatio-temporal apertures for a SIMO-ULA system called modulo-type apertures and show that the elements in this class are ambiguous.

Definition B.4.4: *A modulo-type spatio-temporal aperture of a SIMO-ULA system is an aperture satisfying*

$$m_2(i) = (iK_a + K_b \mod M_2) + 1, \tag{B.57}$$

where $K_a, K_b \in \mathbb{Z}$ are relatively prime.

As an example the commonly used spatio-temporal aperture given in (B.35) is a modulo-type aperture with $K_a = 1$ and $K_b = -1$.

For a SIMO-ULA system (B.55) reads

$$-vT_r + (d_2(i) - d_2(i+1))\omega_2 \equiv 0 \mod 1, \text{ for all } i \in \{1, \dots, I-1\}. \tag{B.58}$$

It is easy to see that for a modulo-type aperture $m_2(i) - m_2(i+1) \in \{-K_a, M_2 - K_a\}$, for all $i \in \{1, \dots, I-1\}$. Therefore, by inserting (B.57) in (B.58) we obtain the congruences

$$vT_r + \tfrac{\omega_2}{2}K_a \equiv 0 \mod 1, \text{ and } \tfrac{\omega_2}{2}M_2 \equiv 0 \mod 1. \tag{B.59}$$

Solving for $(vT_r, \omega_2) \in \left(-\tfrac{1}{2}, \tfrac{1}{2}\right] \times (-1, 1]$ yields the system of equations

$$\omega_2 = \frac{2n_a}{M_2}, \quad n_a \in \mathbb{Z} \cap \left(-\tfrac{M_2}{2}, \tfrac{M_2}{2}\right], \quad \text{and}$$

$$vT_r = -K_a \frac{n_a}{M_2} + n_b, \quad n_b \in \left\{k \in \mathbb{Z} : vT_r \in \left(-\tfrac{1}{2}, \tfrac{1}{2}\right]\right\}. \tag{B.60}$$

It can be seen that for each n_a there exists a unique n_b satisfying (B.60) such that (B.56) holds. Therefore there exist in total M_2 different pairs $(vT_r, \omega_2) \in \left(-\tfrac{1}{2}, \tfrac{1}{2}\right] \times (-1, 1]$ such that (B.56) is fulfilled. Thus, any modulo-type spatio-temporal aperture of a SIMO-ULA system is ambiguous. As remarked in Subsection B.4.1 this effect is clearly visible in Fig. B.3 (a) where the array factor exhibit $M_2 = 8$ different lobes of unit magnitude at the positions $(vT_r, \omega_2) = (-n_a/8, n_a/4), n_a = -3, -2, \dots, +4$.

B.4.4 Component Apertures and Sub-Apertures

It is in general difficult to prove whether for a given spatio-temporal aperture the system of congruences (B.55) is fulfilled or not. However, in the following we give the definition of the two concepts of "component aperture" and "sub-aperture" and show two corollaries of Lemma B.4.3 which are useful for identifying ambiguous apertures.

Definition B.4.5 (Component aperture): *Let* $\mathbf{A}$ *be a spatio-temporal aperture matrix. Then the aperture matrix* $\tilde{\mathbf{A}}$ *of a component aperture is obtained by replacing one or two rows of* $\mathbf{A}$ *by the all-zero row.*

Definition B.4.6 (Sub-aperture): *Let* $\mathbf{A}$ *be spatio-temporal aperture matrix. Then the aperture matrix of a sub-aperture is obtained by erasing a number of columns in* $\mathbf{A}$.

Inserting Definition B.4.5 in Lemma B.4.3 yields the corollary:

Corollary B.4.7: *A spatio-temporal aperture with one ambiguous component aperture is ambiguous.*

Corollary B.4.8: *Any sub-aperture of an ambiguous aperture is ambiguous.*

Proof. The proof follows from the observation that if (B.56) is fulfilled then a subset of the congruences is fulfilled as well. Therefore, if (B.56) is fulfilled for $\mathbf{A}$, it is fulfilled for $\tilde{\mathbf{A}}$ too. □

As an example of Corollary B.4.7, a *sufficient* condition for an aperture of a MIMO-ULA system to be ambiguous is that either $\mathbf{m}_1$ or $\mathbf{m}_2$ yield an ambiguous array factor when used in a SIMO-ULA system. Therefore if a modulo-type aperture is used at either the transmitter or the receiver in a MIMO-ULA system, the corresponding array factor is ambiguous. It is worth noting that the most commonly used spatio-temporal apertures are indeed formed by a combination of a repetition scheme (as the one used in Fig. B.3(b)) at Array 1 and a modulo-type scheme at the Array 2. Since in this case the component aperture formed by the temporal aperture and the spatial aperture at Array 2 is ambiguous, the whole bi-spatio-temporal aperture is ambiguous.

We see by Corollary B.4.8 and the example given in Subsection B.4.3 that any aperture formed by leaving out sounding pulse of a modulo-type aperture is ambiguous. One such aperture was analyzed in [5].

B.5   *The Impact of the Spatio-Temporal Aperture on the Threshold Effect*

In the following we investigate the effect of the spatio-temporal aperture on the root mean-squared estimation error (RMSEE) of the joint Doppler frequency and spatial frequency estimator. We consider the one-path case ($L = 1$). To simplify the notation we drop the path index $\ell = 1$ in the sequel.

Generally the RMSEE of a nonlinear estimator exhibits the same typical behavior that we sketch here considering the parameter vector $\boldsymbol{\vartheta}$. Below a certain threshold $\gamma_{\mathrm{o},[\hat{\boldsymbol{\vartheta}}]_p}^{\mathrm{th}}$ in signal-to-noise ratio (SNR) the RMSEE of $[\hat{\boldsymbol{\vartheta}}]_p$

increases rapidly as the SNR decreases [25, 26]. This effect is commonly known as the *threshold effect*. The previous sections show that the spatio-temporal aperture determines the behavior of the array factor $\mathrm{AF_n}(\boldsymbol{\vartheta}; \mathbf{A})$ and therefore of the ambiguity function $\chi_0(\boldsymbol{\vartheta})$. As can be seen from the examples given in Section B.4.1, the magnitudes of the side-lobes of the array factor depend on the spatio-temporal aperture. Consequently the spatio-temporal aperture also affects the robustness of the estimators toward noise, since this robustness directly depends on the magnitudes of the side-lobes [25]. In the following, we use the normalized side-lobe level (NSL) associated with a spatio-temporal aperture as a figure of merit for noise robustness of the parameter estimators.

Definition B.5.1: The NSL associated with a spatio-temporal aperture matrix $\mathbf{A}$ *is defined as*

$$\mathrm{NSL}(\mathbf{A}) \triangleq \max_{\boldsymbol{\vartheta} \in \mathcal{L}} |\mathrm{AF_n}(\boldsymbol{\vartheta}; \mathbf{A})|, \tag{B.61}$$

where $\mathcal{L} \triangleq \left\{ \boldsymbol{\vartheta} \in \mathcal{E}_{\boldsymbol{\vartheta}} : \frac{\partial}{\partial \boldsymbol{\vartheta}} \mathrm{AF_n}(\boldsymbol{\vartheta}; \mathbf{A}) = \mathbf{0}, \boldsymbol{\vartheta} \neq \mathbf{0} \right\}$ *is the set of local maxima of* $|\mathrm{AF_n}(\boldsymbol{\vartheta}; \mathbf{A})|, \boldsymbol{\vartheta} \in \mathcal{E}_{\boldsymbol{\vartheta}}$.

If a spatio-temporal aperture is ambiguous there exists by definition at least one $\boldsymbol{\vartheta} \neq \mathbf{0}$ such that $|\mathrm{AF_n}(\boldsymbol{\vartheta}; \mathbf{A})| = 1$ and therefore NSL $= 1$. On the contrary, a spatio-temporal aperture with NSL less than one has a unique maximum. In that case the NSL coincides with the magnitude of the highest side-lobe of the normalized array factor. Generally, the NSL is hard to obtain analytically but it can however be computed numerically.

To study the relation between the NSL and γ_o^{th} in more detail, a method for computing γ_o^{th} is needed. Motivated by the observation that the estimators at hand all converge to the CRLB at high SNR, $\gamma_{o,[\hat{\boldsymbol{\vartheta}}]_p}^{\mathrm{th}}$ is defined in the following as the maximum γ_o such that the inequality

$$\mathrm{RMSEE}([\hat{\boldsymbol{\vartheta}}]_p) \leq 2\sqrt{\mathrm{CRLB}([\hat{\boldsymbol{\vartheta}}]_p)} \tag{B.62}$$

is fulfilled. The threshold γ_o^{th} of the joint estimator $\hat{\boldsymbol{\vartheta}}$ is defined as the maximum of the thresholds of the individual estimators $\hat{v}$, $\hat{\omega}_1$, and $\hat{\omega}_2$, i.e

$$\gamma_o^{\mathrm{th}} \triangleq \max\{\gamma_{o,\hat{v}}^{\mathrm{th}}, \gamma_{o,\hat{\omega}_1}^{\mathrm{th}}, \gamma_{o,\hat{\omega}_2}^{\mathrm{th}}\}. \tag{B.63}$$

Hence, γ_o^{th} can be determined if the RMSEE is known. In practice the RMSEE and $\hat{\gamma}_o^{\mathrm{th}}$ are estimated by means of Monte Carlo simulations.

B.5.1 Specific Examples (Continued)

Fig. B.4 reports the results of a Monte Carlo simulation comparing the RM-SEEs of $\hat{v}$, $\hat{\omega}_1$, and $\hat{\omega}_2$ using two different orthogonal spatio-temporal aperture
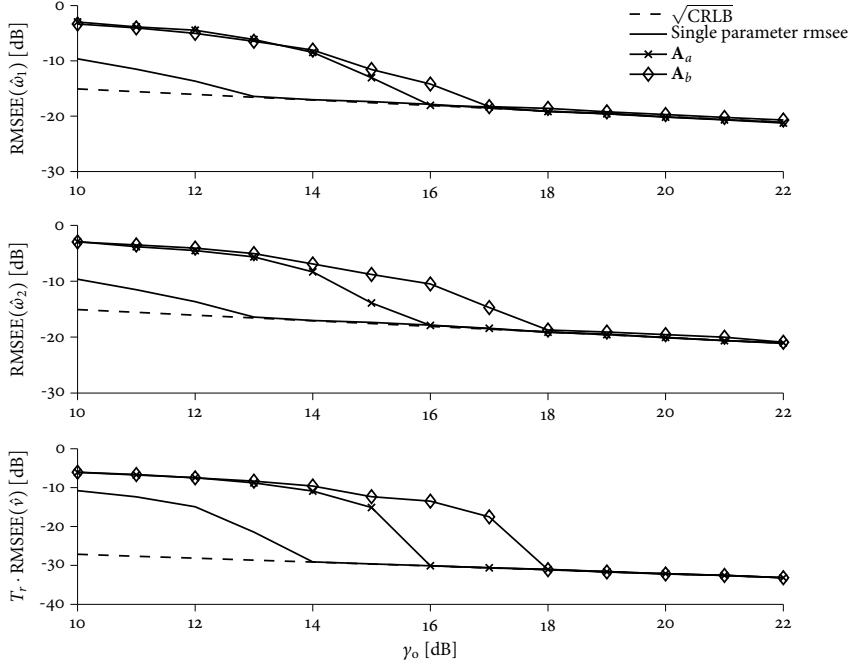
Fig. B.4: Simulated RMSEE-curves obtained from 1000 Monte Carlo runs using the two different orthogonal spatio-temporal apertures $\mathbf{A}_a$ (marked with ×) and $\mathbf{A}_b$ (marked with ◇). The dashed lines are the corresponding CRLBs obtained from (B.32). The solid curves without marks show the simulated RMSEE of the single-parameter maximum-likelihood estimator with all other parameters known. A MIMO-ULA type system with $M_1 = M_2 = 8$, and $I = 64$ is used and $\vartheta_1 = \mathbf{0}$. Isotropic sounding pulses are assumed (EF$(\vartheta) = 1$).

matrices $\mathbf{A}_a$ with NSL$(\mathbf{A}_a) = 0.50$ and $\mathbf{A}_b$ with NSL$(\mathbf{A}_b) = 0.63$ together with the corresponding CRLBs. The parameter setting used for this simulation is reported in the caption of the figure. For comparison we have included the simulated RMSEE of each single maximum likelihood estimator of v, ω_1, and ω_2 with the two other parameters known. These curves are lower bounds on the RMSEEs when all parameters are estimated jointly.

In the $\mathbf{A}_a$ case the threshold estimates $\hat{\gamma}^{\text{th}}_{\text{o},\hat{v}}$, $\hat{\gamma}^{\text{th}}_{\text{o},\hat{\omega}_1}$, and $\hat{\gamma}^{\text{th}}_{\text{o},\hat{\omega}_2}$ all take the value 16 dB, hence

$$\hat{\gamma}^{\text{th}}_{\text{o}} \triangleq \max\{\hat{\gamma}^{\text{th}}_{\text{o},\hat{v}}, \hat{\gamma}^{\text{th}}_{\text{o},\hat{\omega}_1}, \hat{\gamma}^{\text{th}}_{\text{o},\hat{\omega}_2}\} = 16 \text{ dB}; \tag{B.64}$$

for $\mathbf{A}_b$ the estimated threshold values are $\hat{\gamma}^{\text{th}}_{\text{o},\hat{v}} = \hat{\gamma}^{\text{th}}_{\text{o},\hat{\omega}_1} = 18$ dB, $\hat{\gamma}^{\text{th}}_{\text{o},\hat{\omega}_2} = 17$ dB and consequently $\hat{\gamma}^{\text{th}}_{\text{o}} = 18$ dB. Defining $\hat{\gamma}^{\text{th}}_{\text{o,single}}$ as the largest threshold estimate for the single-parameter estimators we see that $\hat{\gamma}^{\text{th}}_{\text{o}}$ exceeds $\hat{\gamma}^{\text{th}}_{\text{o,single}}$ by 2 dB and 4 dB in the $\mathbf{A}_a$ and $\mathbf{A}_b$ cases, respectively. The simulation results
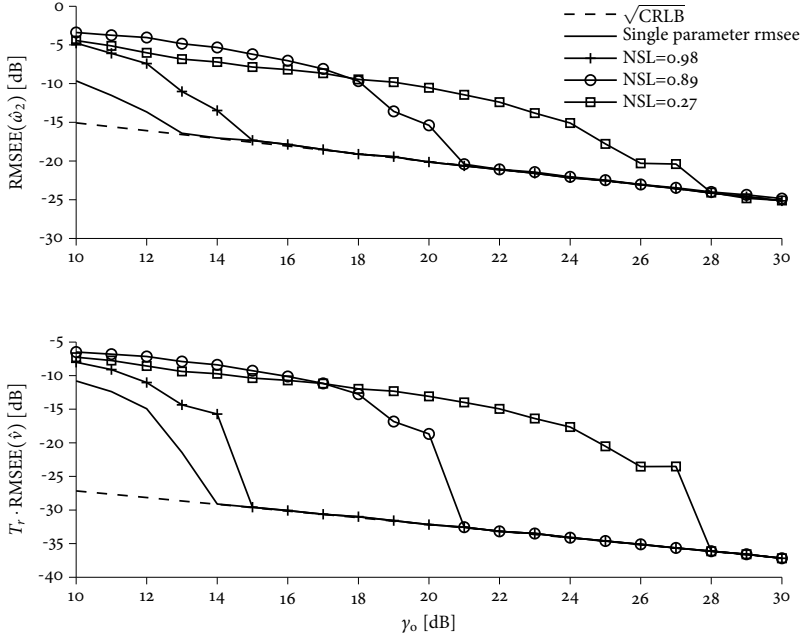
Fig. B.5: Simulated RMSEE-versus SNR for a SIMO-ULA system with settings $M_1 = 1$, $M_2 = 8$ and $I = 64$. The remaining settings are the same as those reported in the caption of Fig. B.4. The resulting RMSEEs of three spatio-temporal apertures with different NSLs are plotted. The dashed lines are the corresponding CRLBs. The solid curves without marks show the RMSEEs of the single-parameter maximum likelihood estimators when all other parameters are known.

given in Fig. B.4 suggest that one should select an orthogonal spatio-temporal aperture matrix that yields the lowest possible γ_o^{th}.

We now consider a SIMO-ULA system and assume that ω_1 is known. We consider three spatio-temporal apertures with NSL = $0.27, 0.89$, and 0.98, respectively. The simulated RMSEEs together with the corresponding CRLBs, and the simulated single-parameter RMSEEs are reported in Fig. B.5. As can be observed from the figure $\hat{\gamma}_o^{\text{th}}$ increases with the NSL. In the NSL = 0.27 case, $\hat{\gamma}_o^{\text{th}}$ exceeds $\hat{\gamma}_{o,\text{single}}^{\text{th}}$ by approximately 1 dB.

In the above investigation, a very large number of Monte Carlo runs is required to estimate the threshold position accurately. Therefore this approach is not feasible when a large number of spatio-temporal aperture matrices should be compared. Furthermore, the Monte Carlo simulations commonly underestimate γ_o^{th} due to the low outlier probability [27]. Hence the $\hat{\gamma}_o^{\text{th}}$ values obtained from Fig. B.4 and Fig. B.5 are too optimistic. Several methods for estimating the threshold value of an estimator are available in the literature. In [28, 29], Athley describes a method to approximate the RMSEE in the
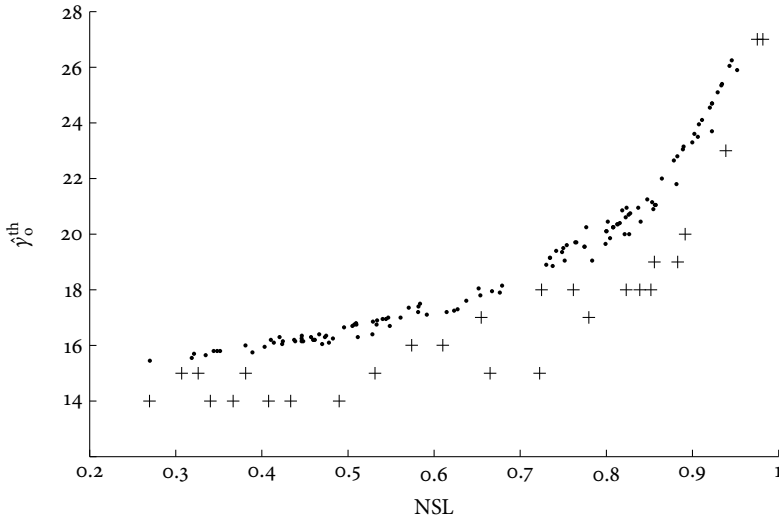
Fig. B.6: The estimated RMSEE threshold $\hat{\gamma}_o^{th}$ as a function of the NSL. The points marked by •
are obtained from the Athley's method, while the points marked with + are obtained from Monte
Carlo simulations. The simulation setting is described in the caption of Fig. B.5.

threshold region based on the magnitudes of the side-lobes of the ambiguity
function.

Fig. B.6 reports $\hat{\gamma}_o^{th}$ for different selections of **A** as a function of the
corresponding NSL. The parameter settings are the same as in Fig. B.5. The
points marked by "•" are obtained using Athley's method [28, eq. (20)]; the
points with mark "+" are obtained from Monte Carlo simulations with 1000
runs and varying γ_o in steps of 1 dB. It is apparent from the figure that
the values of $\hat{\gamma}_o^{th}$ obtained from the Monte Carlo simulations are maximally
4 dB lower than the $\hat{\gamma}_o^{th}$-values obtained using Athley's method. This is to be
expected due to the finite number of Monte Carlo runs and the uncertainty
caused by the 1 dB quantization of γ_o used in the simulation. As can be seen
for both methods, the obtained estimates $\hat{\gamma}_o^{th}$ exhibit an increasing trend with
respect to the NSL. Hence, the NSL can be used as a figure of merit to assess
the robustness of spatio-temporal aperture towards noise.

B.6 Conclusions

A novel model of wireless MIMO channel sounding systems was proposed.
This model is based on the concept of (bi-)spatio-temporal aperture and can
describe switched as well as parallel sounding systems. The proposed model
provides a description of the impact of spatio-temporal sounding on the

joint estimation of Doppler frequency, direction of arrival and direction of departure. The Fisher information matrix and the conditional Cramér-Rao lower bounds (CRLBs) on the estimator variances were derived. For the one-path case it was shown analytically that a spatio-temporal aperture fulfilling an orthogonality property yields the minimum CRLBs. It was also shown that the aperture which yields the minimum Bayesian CRLB (BCRLB) in the multipath case also fulfills this orthogonality criterion.

An ambiguity function for Doppler-bi-direction estimation was defined. The ambiguity function factorizes into an "element factor" multiplied by an "array factor." The necessary and sufficient condition for the array factor to be ambiguous was stated and a certain family of spatio-temporal apertures (the so-called modulo-type apertures), which includes the most commonly used apertures, were found to be ambiguous, i.e. to yield an ambiguous array factor.

Monte-Carlo simulations show that the normalized side-lobe level (NSL) is a sensible figure of merit for the identification of spatio-temporal apertures performing close to optimum in terms of root mean square estimation error among the class of spatio-temporal apertures exhibiting the orthogonality property.

As a general conclusion, when designing a spatio-temporal aperture for joint estimation of Doppler frequency, direction of departure and direction of arrival it is not advisable to optimize the temporal or spatial apertures separately. Joint optimization of the bi-spatio-temporal aperture should be performed instead.

B.I Derivation of the Conditional Fisher Information Matrix

The Fisher information matrix $\mathbf{F}(\boldsymbol{\theta})$ for joint estimation of the parameter vector $\boldsymbol{\theta} = [\boldsymbol{\theta}_1^\mathsf{T}, \ldots, \boldsymbol{\theta}_L^\mathsf{T}]^\mathsf{T}$ from an observation of $Y_1(t), \ldots, Y_I(t)$ can be written as

$$\mathbf{F}(\boldsymbol{\theta}) \triangleq \begin{bmatrix} \mathbf{F}_{\boldsymbol{\theta}_1 \boldsymbol{\theta}_1} & \cdots & \mathbf{F}_{\boldsymbol{\theta}_1 \boldsymbol{\theta}_L} \\ \vdots & \ddots & \vdots \\ \mathbf{F}_{\boldsymbol{\theta}_L \boldsymbol{\theta}_1} & \cdots & \mathbf{F}_{\boldsymbol{\theta}_L \boldsymbol{\theta}_L} \end{bmatrix}, \tag{B.65}$$

where we use the notation

$$\mathbf{F}_{\boldsymbol{\beta}\boldsymbol{\xi}} \triangleq -\mathsf{E}\left[\frac{\partial}{\partial \boldsymbol{\beta}} \Lambda(\boldsymbol{\theta}) \, \frac{\partial}{\partial \boldsymbol{\xi}^\mathsf{H}} \Lambda(\boldsymbol{\theta}) \right] \tag{B.66}$$

with the complex gradient defined as in [30, Appendix B]. We remark that in (B.66) the explicit mentioning of the dependence of $\boldsymbol{\theta}$ has been dropped to

simplify the notation. Using [2, Eq. (22)] $\mathbf{F}_{\boldsymbol{\theta}_\ell \boldsymbol{\theta}_{\ell'}}$ can be rewritten as

$$\mathbf{F}_{\boldsymbol{\theta}_\ell \boldsymbol{\theta}_{\ell'}} = \frac{2}{N_0} \Re \left\{ \int_{\mathcal{T}_0} \sum_{i=1}^{I} \frac{\partial s_i(t, \boldsymbol{\theta})}{\partial \boldsymbol{\theta}_\ell} \cdot \frac{\partial s_i^*(t, \boldsymbol{\theta})}{\partial \boldsymbol{\theta}_{\ell'}^{\mathsf{H}}} \, dt \right\}$$

$$= \frac{2}{N_0} \Re \left\{ \sum_{i=1}^{I} \int_{\mathcal{T}_{j(i)}} \frac{\partial s_i(t; \boldsymbol{\theta}_\ell)}{\partial \boldsymbol{\theta}_\ell} \cdot \frac{\partial s_i^*(t; \boldsymbol{\theta}_{\ell'})}{\partial \boldsymbol{\theta}_{\ell'}^{\mathsf{H}}} \, dt \right\}, \qquad \text{(B.67)}$$

where $s_i(t, \boldsymbol{\theta}) \triangleq s_{j(i),m_1(i),m_2(i)}(t; \boldsymbol{\theta})$ with $s_{j,m_1,m_2}(t; \boldsymbol{\theta})$ given in (B.5). Inserting (B.5) and (B.25) in (B.67) yields (B.24).

B.II Technical Lemmas

Lemma B.II.1 (Modified version of [21, Observation 7.1.2]): *Let $\beta \subset \{1, \ldots, n\}$ be an index set and $\mathbf{U}(\beta)$ and $\mathbf{V}(\beta)$ be the principal sub-matrices of the positive definite $n \times n$ matrices $\mathbf{U}$ and $\mathbf{V}$ formed by deleting the rows and columns complementary to those indexed by β. Then, we have*

$$\mathbf{U} \geq \mathbf{V} \Rightarrow \mathbf{U}(\beta) \geq \mathbf{V}(\beta). \qquad \text{(B.68)}$$

Proof. Let $\mathbf{x}$ be a vector with arbitrary entries in the components indicated by β and zero entries elsewhere. Let $\mathbf{x}(\beta)$ be the sub vector of $\mathbf{x}$ indicated by β. Thus $\mathbf{x}^{\mathsf{H}}\mathbf{U}\mathbf{x} = \mathbf{x}(\beta)^{\mathsf{H}}\mathbf{U}(\beta)\mathbf{x}(\beta)$ and $\mathbf{x}^{\mathsf{H}}\mathbf{V}\mathbf{x} = \mathbf{x}(\beta)^{\mathsf{H}}\mathbf{V}(\beta)\mathbf{x}(\beta)$. The lemma follows from insertion into $\mathbf{x}^{\mathsf{H}}\mathbf{U}\mathbf{x} \geq \mathbf{x}^{\mathsf{H}}\mathbf{V}\mathbf{x}$. □

We remark that for positive definite matrices $\mathbf{Q}$ and $\mathbf{R}$

$$\mathbf{Q}^{-1} \geq \mathbf{R}^{-1} \Leftrightarrow \mathbf{R} \geq \mathbf{Q}. \qquad \text{(B.69)}$$

A proof of (B.69) is given in [21, Theorem 7.7.4].

Lemma B.II.2: *Let $\mathbf{Q}$ and $\mathbf{R}$ be $n \times n$ positive definite matrices and let $\beta \subset \{1, \ldots, n\}$ be an index set. Then the implication*

$$\mathbf{R} \geq \mathbf{Q} \Rightarrow \left[(\mathbf{Q}(\beta))^{-1} \right]_{p,p} \geq \left[(\mathbf{R}(\beta))^{-1} \right]_{p,p}, \quad p = 1, \ldots, n \qquad \text{(B.70)}$$

holds.

Proof. From $\mathbf{R} \geq \mathbf{Q}$ and Lemma B.II.1 it follows that $\mathbf{R}(\beta) \geq \mathbf{Q}(\beta)$. Then by (B.69) we have $(\mathbf{Q}(\beta))^{-1} \geq (\mathbf{Q}(\beta))^{-1}$. Then Lemma B.II.2 follows by applying Lemma B.II.1. □

Lemma B.II.3: *A positive definite matrix $\mathbf{Q}$ fulfills $\left[\mathbf{Q}^{-1} \right]_{p,p} = 1/[\mathbf{Q}]_{p,p}$ for all p if, and only if, $\mathbf{Q}$ is diagonal.*

Proof. It is easily checked that if $\mathbf{Q}$ is diagonal, then $[\mathbf{Q}^{-1}]_{p,p} = 1/[\mathbf{Q}^{-1}]_{p,p}$ for all p.

We now prove the converse, i.e. if $[\mathbf{Q}^{-1}]_{p,p} = 1/[\mathbf{Q}^{-1}]_{p,p}$ for all p then $\mathbf{Q}$ is diagonal. Let $\mathbf{Q}_n = \mathbf{Q}$ be an $n \times n$ positive definite matrix and partition it as

$$\mathbf{Q}_n = \begin{bmatrix} \mathbf{Q}_{n-1} & \mathbf{j}_n \\ \mathbf{j}_n^{\mathsf{H}} & \eta_n \end{bmatrix}, \tag{B.71}$$

where η is a scalar, $\mathbf{j}_n$ is a vector, $\mathbf{Q}_{n-1}$ is the upper left $(n-1) \times (n-1)$ principal matrix of $\mathbf{Q}_n$. Inversion of $\mathbf{Q}_n$ yields

$$[\mathbf{Q}_n^{-1}]_{n,n} = \frac{1}{\eta_n + \mathbf{j}_n^{\mathsf{H}} \mathbf{Q}_{n-1}^{-1} \mathbf{j}_n}. \tag{B.72}$$

Assume that $[\mathbf{Q}_n^{-1}]_{p,p} = 1/[\mathbf{Q}_n]_{p,p}$ for all p and therefore in particular

$$[\mathbf{Q}_n^{-1}]_{n,n} = 1/[\mathbf{Q}_n]_{n,n} = 1/\eta_n. \tag{B.73}$$

Then (B.72) implies $\eta_n + \mathbf{j}_n^{\mathsf{H}} \mathbf{Q}_{n-1}^{-1} \mathbf{j}_n = \eta_n$ or $\mathbf{j}_n^{\mathsf{H}} \mathbf{Q}_{n-1}^{-1} \mathbf{j}_n = 0$. Since $\mathbf{Q}_n$ is positive definite so is $\mathbf{Q}_{n-1}^{-1}$. Thus $\mathbf{j}_n^{\mathsf{H}} \mathbf{Q}_{n-1}^{-1} \mathbf{j}_n = 0$ if, and only if, $\mathbf{j}_n = \mathbf{0}$. To complete the proof we repeat the argument for $\mathbf{Q}_{n-1}, \mathbf{Q}_{n-2}, \ldots, \mathbf{Q}_2$ to show that $\mathbf{j}_{n-1} = \mathbf{0}, \mathbf{j}_{n-2} = \mathbf{0}, \ldots, \mathbf{j}_2 = 0$ and thus $\mathbf{Q}_n$ is diagonal. $\square$

B.III   *Constant Volume Property of the Ambiguity Function*

In the following the ambiguity volume $V_{\mathrm{amb}} \triangleq \int_{\mathcal{E}} |\chi_0(\boldsymbol{\vartheta})|^2 \, d\boldsymbol{\vartheta}$ is derived. Making use of (B.49) some straightforward algebraic manipulations leads to

$$V_{\mathrm{amb}} = \int_{\mathcal{E}} \left| \frac{1}{IE} \sum_{i=1}^{I} \int \exp(j2\pi(vt + d_1(i)\omega_1 + d_2(i)\omega_2)) |p_i(t)|^2 dt \right|^2 d\boldsymbol{\vartheta}$$

$$= \frac{1}{(IE)^2} \int_{\mathcal{E}} \sum_{i=1}^{I} \int \exp(j2\pi(vt + d_1(i)\omega_1 + d_2(i)\omega_2)) |p_i(t)|^2 dt$$

$$\times \sum_{i'=1}^{I} \int \exp(-j2\pi(vt' + d_1(i')\omega_1 + d_2(i')\omega_2)) |p_{i'}(t')|^2 dt' \, d\boldsymbol{\vartheta}$$

$$= \frac{1}{(IE)^2} \sum_{i=1}^{I} \sum_{i'=1}^{I} z_{i,i'} \tag{B.74}$$

and

$$
\begin{aligned}
z_{i,i'} &\triangleq \iint |p_i(t)|^2 |p_{i'}(t')|^2 \\
&\quad \times \int_{\mathcal{E}} \exp(j2\pi((t-t')v+ \\
&\qquad\qquad (d_1(i)-d_1(i'))\omega_1 + (d_2(i)-d_2(i'))\omega_2))\mathrm{d}\vartheta \; \mathrm{d}t\mathrm{d}t' \\
&= \iint |p_i(t)|^2 |p_{i'}(t')|^2 \int_{-\infty}^{\infty} \exp(j2\pi(t-t')v)\,\mathrm{d}v\mathrm{d}t\mathrm{d}t' \\
&\quad \times \int_{-1}^{+1} \exp(j2\pi(d_1(i)-d_1(i'))\omega_1)\,\mathrm{d}\omega_1 \\
&\quad \times \int_{-1}^{+1} \exp(j2\pi(d_2(i)-d_2(i'))\omega_2)\,\mathrm{d}\omega_2 \\
&= 4 \cdot \mathrm{sinc}\left(2\pi(d_1(i)-d_1(i'))\right) \times \mathrm{sinc}\left(2\pi(d_2(i)-d_2(i'))\right) \\
&\quad \times \int |p_i(t)|^2 |p_{i'}(t)|^2 \mathrm{d}t.
\end{aligned}
\tag{B.75}
$$

The function $\mathrm{sinc}(\cdot)$ in (B.75) is defined as $\mathrm{sinc}(x) \triangleq \frac{\sin(x)}{x}, x \neq 0$ and $\mathrm{sinc}(0) \triangleq 1$. We notice that the integral term $\int |p_i(t)|^2 |p_{i'}(t)|^2 \mathrm{d}t$ in (B.75) vanishes for index values i, i' such that $t(i) \neq t(i')$. Similarly, $\mathrm{sinc}(2\pi(d_k(i) - d_k(i')))$ is zero for i, i' such that $2(d_k(i) - d_k(i'))$ is an integer. Thus, by selecting spatio-temporal array such that for any i, i' with $t(i) = t(i')$ at least one of the quantities $2(d_1(i) - d_1(i'))$ and $2(d_2(i) - d_2(i'))$ is an integer, the terms $z_{i,i'}, i \neq i'$ are zero. This condition holds for switched sounding systems where $i \neq i' \Leftrightarrow t(i) \neq t(i')$. The condition also holds for systems equipped with uniform linear arrays with half-wavelength inter-element spacing.

For a spatio-temporal array such that $z_{i,i'} = 0, i \neq i'$ the ambiguity volume reads

$$
V_{\mathrm{amb}} = \frac{4\sum_{i=1}^{I} z_{i,i}}{(IE)^2} = \frac{4\sum_{i=1}^{I} \int |p_i(t)|^4 \mathrm{d}t}{(IE)^2}.
\tag{B.76}
$$

Thus, for this class of spatio-temporal arrays, the ambiguity volume depends only on the second order moment E and fourth order moments $\int |p_i(t)|^4 \mathrm{d}t$, $i = 1, \ldots, I$ of the transmitted sounding pulses.

References

[1] S. Salous, P. Filippidis, R. Lewenz, I. Hawkins, N. Razavi-Ghods, and M. Abdallah, "Parallel receiver channel sounder for spatial and MIMO characterisation of the mobile radio channel," *IEE Proc. Commun.*, vol. 152, no. 6, pp. 912– 918, Dec. 2005.

[2] B. H. Fleury, M. Tschudin, R. Heddergott, D. Dahlhaus, and K. L. Pedersen, "Channel parameter estimation in mobile radio environments using the SAGE algorithm," *IEEE J. Sel. Areas Commun.*, vol. 17, no. 3, pp. 434–450, Mar. 1999.

[3] B. H. Fleury, P. Jourdan, and A. Stucki, "High-resolution channel parameter estimation for MIMO applications using the SAGE algorithm," in *Proc. Int. Zurich Seminar on Broadband Commun*, vol. 30, Feb. 2002, pp. 1–9.

[4] X. Yin, B. Fleury, P. Jourdan, and A. Stucki, "Doppler frequency estimation for channel sounding using switched multiple-element transmit and receive antennas," in *Proc. IEEE Global Telecommun. Conf. Globecom 2003*, vol. 4, Dec. 2003, pp. 2177–2181.

[5] T. Pedersen, C. Pedersen, X. Yin, B. H. Fleury, R. R. Pedersen, B. Bozinovska, A. Hviid, P. Jourdan, and A. Stucki, "Joint estimation of Doppler frequency and directions in channel sounding using switched Tx and Rx arrays," *Proc. IEEE Global Telecommun. Conf. (Globecom 2004)*, vol. 4, pp. 2354–2360, Dec. 2004.

[6] A. N. Mirkin and L. H. Sibul, "Cramér-rao bounds on angle estimation with a two-dimensional array," *IEEE Trans. Signal Process.*, vol. 39, no. 2, pp. 515–517, Feb. 1991.

[7] R. O. Nielsen, "Azimuth and elevation angle estimation with a three-dimensional array," *IEEE J. Ocean. Eng.*, vol. 19, no. 1, pp. 84–86, Jan. 1994.

[8] P. M. Woodward, *Probability and Information Theory, with Applications to Radar*, 2nd ed. Pergamon Press, 1964.

[9] M. J. D. Rendas and J. M. F. Moura, "Ambiguity in radar and sonar," *IEEE Trans. Signal Process.*, vol. 46, no. 2, pp. 294–305, Feb. 1998.

[10] H. L. V. Trees, *Detection, Estimation, and Modulation Theory.* John Wiley and Sons, 1971, vol. Part 3 : Radar-sonar Signal Processing and Gaussian Signals in Noise.

[11] G. San Antonio, D. R. Fuhrmann, and F. C. Robey, "Mimo radar ambiguity functions," *IEEE J. Sel. Topics Signal Process.*, vol. 1, no. 1, pp. 167–177, June 2007.

[12] P. J. Cullen, P. C. Fannin, and A. Molina, "Wide-band measurement and analysis techniques for the mobile radio channel," *IEEE Trans. Veh. Technol.*, vol. 42, no. 4, pp. 589–603, 1993.

[13] P. C. Fannin and A. Molina, "Analysis of mobile radio channel sounding measurements in inner Dublin at 1.808 GHz," *IEE Proc. Commun.*, vol. 143, no. 5, pp. 311–316, Oct. 1996.

[14] L. C. Godara and A. Cantoni, "Uniqueness and linear independence of steering vectors in array space," *The Journal of the Acoustical Society of America*, vol. 70, no. 2, pp. 467–475, Aug. 1981.

[15] J. T.-H. Lo and J. Stanley L. Marple, "Observability conditions for multiple signal direction finding and array sensor localization," *IEEE Trans. Signal Process.*, vol. 40, no. 11, pp. 2641–2650, Nov. 1992.

[16] K.-C. Tan, S. S. Goh, and E.-C. Tan, "A study of the rank-ambiguity issues in direction-of-arrival estimation," *IEEE Trans. Signal Process.*, vol. 44, no. 4, pp. 880 –887, 1996.

[17] H. V. Poor, *An Introduction to Signal Detection and Estimation.* New York, NY: Springer-Verlag, 1988.

[18] H. L. V. Trees, *Detection, Estimation, and Modulation Theory*. John Wiley and Sons, Inc., 1968, vol. Part 1 : Detection, Estimation and Linear Modulation Theory.

[19] W. J. Bangs, "Array processing with generalized beam-formers," Ph.D. dissertation, Yale University, New Haven, CT, 1971.

[20] L. L. Scharf, *Statistical Signal Processing: Detection, Estimation, and Time Series Analysis*. Addison Wesley, 1991.

[21] R. A. Horn and C. A. Johnson, *Matrix Analysis*. Cambridge University Press, 1985.

[22] A. Dogandžić and A. Nehorai, "Space-time fading channel estimation and symbol detection in unknown spatially correlated noise," Dept. Elect. Eng. Comput. Sci., Univ. Illinois, Chicago, Tech. Rep. Rep. UIC-EECS-00-9, Aug. 2000.

[23] ——, "Space-time fading channel estimation and symbol detection in unknown spatially correlated noise," *IEEE Trans. Signal Process.*, vol. 50, no. 3, pp. 457–474, Mar. 2002.

[24] C. Balanis, *Antenna Theory: Analysis and Design*, 2nd ed. John Wiley and Sons, 1997.

[25] R. J. McAulay and E. M. Hofstetter, "Barankin bounds on parameter estimation," *IEEE Trans. Inf. Theory*, vol. IT-17, no. 6, pp. 669–676, Nov. 1971.

[26] D. C. Rife and R. R. Boorstyn, "Single tone parameter estimation from discrete-time observations," *IEEE Trans. Inf. Theory*, vol. 20, no. 5, pp. 591–598, Sept. 1974.

[27] S. D. Howard and P. Lavoie, "Analysis of SNR threshold for differential Doppler frequency measurement in digital receivers," in *Proc. 2000 IEEE Int. Conf. on Acoustics, Speech, and Signal Processing, 2000.*, vol. 1, June 2000, pp. 289–292.

[28] F. Athley, "Performance analysis of DOA estimation in the threshold region," in *Proc. of IEEE Int. Conf. on Acoustics, Speech, and Signal Processing, 2002, ICASSP '02.*, vol. 3, May 2002, pp. 3017–3020.

[29] ——, "Threshold region performance of maximum likelihood direction of arrival estimators," *IEEE Trans. Signal Process.*, vol. 53, no. 4, pp. 1359–1373, Apr. 2005.

[30] S. S. Haykin, *Adaptive Filter Theory*. Prentice-Hall, Inc., 2002.

On the Impact of TDM in Estimation of MIMO Channel Capacity from Phase-Noise Impaired Measurements

Troels Pedersen, Attaphongse Taparugssanagorn, Juha Ylitalo, and Bernard H. Fleury

Abstract

Due to the significantly reduced cost and effort for system calibration time-division multiplexing (TDM) is a commonly used technique to switch between the transmit and receive antennas in multiple-input multiple-output (MIMO) radio channel sounding. Nonetheless, Baum *et al.* [1, 2] have shown that phase noise of the transmitter and receiver local oscillators, when it is assumed to be a white Gaussian random process, can cause up to around 100 % errors of the estimated channel capacity of a low-rank MIMO channel when using the standard channel matrix estimator. Experimental evidence shows that consecutive phase noise samples affecting measurement samples collected with real TDM-MIMO channel sounders are correlated. In addition the spatio-temporal aperture induced by the selected switching schemes has an impact on the ordering of the phase noise samples in the estimation of the channel matrix estimate. This paper investigates how both effects affect the channel capacity estimator based on the standard channel matrix estimator. We show by means of Monte Carlo simulations that by using an experimentally obtained ARMA model of phase noise the predicted error of the ergodic capacity estimate is reduced compared to the case where phase noise is white and Gaussian. We also show that the estimated ergodic capacity is highly influenced by the choice of the spatio-temporal aperture.

C.1   Introduction

To save hardware cost and alleviate the needed calibration procedures, most advanced multiple-input multiple-output (MIMO) radio channel sounders rely on a time-division multiplexing (TDM) technique. In such a system, which is represented schematically in Fig. C.1, a single sounding waveform generator is connected to a number of transmit antennas via a switch. Similarly, the output terminals of the receive array are sensed via another switch. Thereby channel observations are made via a spatio-temporal aperture [3].
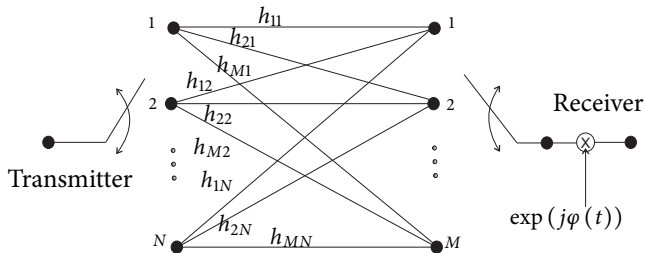

Fig. C.1: Model for TDM-MIMO channel sounding with phase noise.

It has been shown recently that the concatenated phase noise of the two oscillators in the transmitter and the receiver affects the estimation of MIMO channel capacity when using the standard channel matrix estimator to obtain a capacity estimate [1, 4]. For short we call this concatenated noise the phase noise of the sounding system. The effect of phase noise on MIMO capacity estimation is studied in [4] assuming that phase noise is a random walk process. Theoretical investigations reported in [1, 2] show that, provided phase noise is white and Gaussian, it leads to large measurement errors in terms of estimated channel capacity of a low-rank MIMO channel. In [2] a number of analytical results are given under the assumptions that the TDM, i.e. the spatio-temporal array [3], fulfills a separability condition and that the phase noise process is white. However, experimental studies [5] show that phase noise cannot be assumed white on the time-scale of a measurement period, which is the observation period critical for capacity estimation. In addition, the spatio-temporal aperture induced by the used switching schemes has an impact on the ordering of the phase noise samples in the estimation of the traditional channel matrix estimate. Both effects significantly affect the performance of capacity estimation based on this matrix estimator. Finally, it is worth mentioning that non-separable spatio-temporal arrays exist that are more efficient than separable spatio-temporal arrays, in the sense that they lead to better performance of bi-direction and Doppler frequency estimators [3, 6].

In this paper we analyze the combined impact of phase noise correlation and spatio-temporal aperture of a TDM-MIMO sounding system on the capacity estimation based on the traditional channel matrix estimator using the experimental phase noise model developed in [5]. We compare the performance of separable and non-separable spatio-temporal arrays for the purpose of capacity estimation.

C.2   System Model

We consider the TDM sounding system depicted schematically in Fig. C.1 with N transmit antennas and M receive antennas. As depicted in this figure the observed signal is modulated with a time varying phasor $\exp(j\varphi(t))$.

C.2.1   Phase Noise Model

In the model proposed in [5], which we adopt here, the phase noise $\varphi(t)$ is split into a non-stationary long-term component $\varphi_{\mathrm{L}}(t)$, and a wide-sense-stationary short-term component $\varphi_{\mathrm{S}}(t)$ such that

$$\varphi(t_k) = \varphi_{\mathrm{L}}(t_k) + \varphi_{\mathrm{S}}(t_k), \quad k = 1, 2, \ldots, \tag{C.1}$$
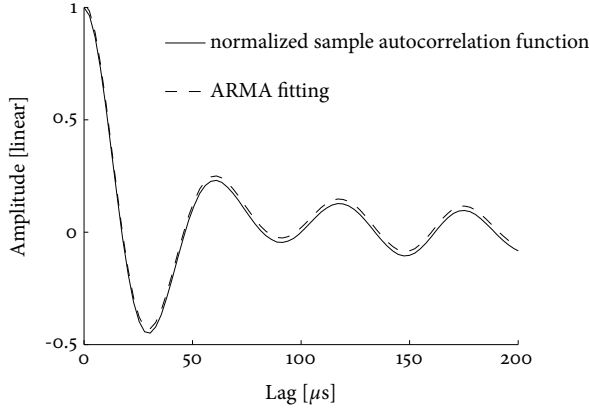
Fig. C.2: Normalized sample autocorrelation function and autocorrelation function of the ARMA process fitted to the short-term component of phase noise [5].

where t_k is the kth sample time instant. The short-term component is modelled as an auto-regressive moving-average (ARMA) process. The long-term component is modelled as an auto-regressive integrated moving average (ARIMA) process. We refer to [5] for the specifications of these two processes. On the scale of one measurement cycle, i.e. the period needed to sense all MN sub-channels of the MIMO system the long-term component of phase noise can be considered as constant. Without loss of generality we equate it to zero: $\varphi_L(t_k) = 0$. Fig. 2 depicts the normalized sample autocorrelation function of the short term component of a measured phase noise series, together with the normalized autocorrelation function of an ARMA process fitted to this component. The sampling period T of the measured phase noise is $T = 2.54\ \mu s$. It corresponds to twice the duration of a 127-chip long sequence with a chip rate of 100 MHz. The same sampling period is used in the selected phase noise model, i.e. $t_k = kT$ in (C.1).

C.2.2   Signal Model for TDM Sounding

The coefficient h_{mn} of the sub-channel consisting of the mth transmit array element, the propagation channel, and the nth receive array element is measured with the transmitter switch in position n and the receiver switch in position m (see Fig. C.1). At time t_k a measurement is acquired with the transmitter and receiver switches in position $n(k)$ and $m(k)$ respectively. The sequence $\{(t_k, m(k), n(k))\}$ defines the spatio-temporal array of the sounding system [3, 6]. The process of acquiring one measurement of the full $M \times N$ channel matrix $\mathbf{H}$, $[\mathbf{H}]_{mn} = h_{mn}$, is called a *measurement cycle*. The kth

measurement belongs to the cycle with index $i(k)$. A spatio-temporal array is *separable* if it fulfills [2]

$$t_k = i(k)T_c + [\mathbf{t}_{\text{Tx}}]_{n(k)} + [\mathbf{t}_{\text{Rx}}]_{m(k)}, \tag{C.2}$$

where $\mathbf{t}_{\text{Tx}}$ and $\mathbf{t}_{\text{Rx}}$ are vectors of dimensions N and M respectively, and $T_c = MNT$ is the cycle duration.

Four examples of spatio-temporal arrays [3] are reported in Fig. C.3. Array A is the traditionally used identity array [3, 6]. Array B is a cycle-dependent spatio-temporal array optimized for joint Doppler frequency and direction estimation [3, 6]. Array C is a modified version of Array A where the receiver switching scheme has been changed to achieve non-separability. Array D is a modified version of A, where the receiver switching sequence has been modified in such a way that for every transmit antenna, the receive antennas are switched in a different, randomly selected, order. Arrays B, C, and D are not separable.

The channel matrix $\mathbf{G}_i$ measured during cycle i is of the form [1]

$$\mathbf{G}_i = \mathbf{H} \circ \mathbf{exp}(j\Phi_i), \quad i = 1, \ldots, I, \tag{C.3}$$

where $[\Phi_{i(k)}]_{m(k)n(k)} = \varphi(t_k)$, $\mathbf{exp}(\cdot)$ is the element-wise exponential, $\circ$ denotes the Hadamard product, and I stands for the number of cycles. To simplify the notation we introduce the phase noise matrices

$$\Theta_i = \mathbf{exp}(j\Phi_i), \quad i = 1, \ldots, I. \tag{C.4}$$

It should be noticed that the ordering of the phase noise samples in Φ_i is determined by the spatio-temporal array. Thus the matrices Θ_i and $\mathbf{G}_i$ also depend on the spatio-temporal array.

C.2.3   Estimation of Capacity

When the channel is not known at the transmitter, but fully known at the receiver, its capacity at signal-to-noise ratio ρ reads [7]

$$C(\mathbf{H}\mathbf{H}^{\text{H}}) = \log_2 \det(\mathbf{I}_M + \tfrac{\rho}{N}\mathbf{H}\mathbf{H}^{\text{H}}), \tag{C.5}$$

where $\mathbf{H}^{\text{H}}$ denotes the Hermitian transpose of $\mathbf{H}$. A straightforward estimate of $C(\mathbf{H}\mathbf{H}^{\text{H}})$ is $C(\widehat{\mathbf{H}\mathbf{H}^{\text{H}}})$, where $\widehat{\mathbf{H}\mathbf{H}^{\text{H}}}$ is an estimate of $\mathbf{H}\mathbf{H}^{\text{H}}$. In the sequel we consider the standard estimate of $\mathbf{H}\mathbf{H}^{\text{H}}$ computed based on measurements of $\mathbf{H}$ obtained with the considered TDM-MIMO channel sounder under the assumption that channel noise is zero:

$$\widehat{\mathbf{H}\mathbf{H}^{\text{H}}} = \frac{1}{I}\sum_i \mathbf{G}_i\mathbf{G}_i^{\text{H}}. \tag{C.6}$$

In Section C.5 we comment further on the choice of the capacity estimator.

C.3 A Scenario When Capacity Estimation is Unaffected by Phase Noise

We consider the case where $I = 1$ and give the necessary and sufficient condition on the phase noise matrix such that $C(\mathbf{HH}^\mathsf{H}) = C(\mathbf{GG}^\mathsf{H})$ is fulfilled when $\mathbf{H}$ has rank one.

Theorem: Let $\mathbf{H} = \mathbf{ab}^\mathsf{T}$ where $\mathbf{a}$ and $\mathbf{b}$ are vectors with non-zero elements and let $\mathbf{G} = \mathbf{H} \circ \Theta$. Then

$$C(\mathbf{HH}^\mathsf{H}) = C(\mathbf{GG}^\mathsf{H}) \Leftrightarrow \Theta = \tilde{\mathbf{U}}\mathbf{1}_M\mathbf{1}_N^\mathsf{T}\tilde{\mathbf{V}}, \tag{C.7}$$

where $\tilde{\mathbf{U}}$ and $\tilde{\mathbf{V}}$ are unitary matrices and $\mathbf{1}_p$ is an all-one vector of dimension p.

Proof. For any matrix $\mathbf{H}$ we have the condition

$$C(\mathbf{HH}^\mathsf{H}) = C(\mathbf{GG}^\mathsf{H}) \Leftrightarrow \mathbf{G} = \mathbf{UHV}, \tag{C.8}$$

where $\mathbf{U}$ and $\mathbf{V}$ are unitary matrices. By the assumptions of the theorem the right-hand identity in (C.8) reads

$$\mathbf{ab}^\mathsf{T} \circ \Theta = \mathbf{UHV} \tag{C.9}$$
$$= \mathbf{Uab}^\mathsf{T}\mathbf{V}. \tag{C.10}$$

Using the identity $\mathbf{ab}^\mathsf{T} \circ \Theta = \mathrm{diag}(\mathbf{a})\Theta\,\mathrm{diag}(\mathbf{b})$ [1, Lemma 1], with $\mathrm{diag}(\cdot)$ denoting the diagonal matrix with diagonal elements equal to the elements of the vector given as an argument, in (C.10) yields

$$\mathrm{diag}(\mathbf{a})\Theta\,\mathrm{diag}(\mathbf{b}) = \mathbf{Uab}^\mathsf{T}\mathbf{V}. \tag{C.11}$$

Solving for Θ we obtain

$$\Theta = \mathrm{diag}(\mathbf{a})^{-1}\mathbf{Uab}^\mathsf{T}\mathbf{V}\,\mathrm{diag}(\mathbf{b})^{-1}. \tag{C.12}$$

Noticing that for a diagonal matrix $\mathbf{D}$ and a unitary matrix $\mathbf{S}$, there exists a unitary matrix $\tilde{\mathbf{S}}$ such that $\mathbf{SD} = \mathbf{D}\tilde{\mathbf{S}}$ we can recast (C.12) as

$$\Theta = \tilde{\mathbf{U}}\,\mathrm{diag}(\mathbf{a})^{-1}\mathbf{ab}^\mathsf{T}\,\mathrm{diag}(\mathbf{b})^{-1}\tilde{\mathbf{V}} \tag{C.13}$$
$$= \tilde{\mathbf{U}}\mathbf{1}_M\mathbf{1}_N^\mathsf{T}\tilde{\mathbf{V}}, \tag{C.14}$$

which is the sought identity. □

Example: We consider the case where the phasor $\exp(j\phi(t))$ can be assumed constant during the time needed to switch all receive antennas once. This is the case when the normalized autocorrelation function is assumed

close to unity for a time lag less that MT or, expressed in standard terminol-
ogy, when the coherence time of the short-term component of the phase noise
is larger than MT. Then $[\Theta]_{mn} = \theta_n$ holds for all receive antenna indices m.
We see that in this case

$$\Theta = \begin{bmatrix} \theta_1 \mathbf{1}_M & \theta_2 \mathbf{1}_M & \ldots & \theta_N \mathbf{1}_M \end{bmatrix} \tag{C.15}$$

$$= \mathbf{I}_M \mathbf{1}_M \mathbf{1}_N^{\mathrm{T}} \operatorname{diag}(\theta_1, \ldots, \theta_N) \tag{C.16}$$

and therefore, by Theorem 1, $C(\mathbf{H}\mathbf{H}^{\mathrm{H}}) = C(\mathbf{G}\mathbf{G}^{\mathrm{H}})$.

C.4 *Numerical Results*

Fig. C.4 reports the results of a Monte Carlo simulation of the ergodic capacity
estimate using the four spatio-temporal arrays defined in Fig. C.3 and the
experimental phase noise model described in Subsection C.2.1. In each Monte
Carlo run a rank-1 channel matrix $\mathbf{H}$ (i.e. a key-hole channel) with a single
non-zero eigenvalue of $\mathbf{H}\mathbf{H}^{\mathrm{H}}$ equal to M is generated. Phase noise is generated
according to the model given in [5]. The estimate of the ergodic capacity
resulting from one spatio-temporal array at a specific signal-to-noise ratio
is obtained by averaging over the capacity estimates computed from 100
Monte Carlo runs with this setting. The ergodic capacity estimates for the
case without phase noise and for the case with uncorrelated Gaussian phase
noise [1] are also given for comparison purpose.

As can be seen from Fig. C.4 all four simulation curves lie between the "No
phase noise" and "Uncorrelated phase noise" curves. Obviously, the lower the
curve is, the better the performance of the estimator is. We conclude that the
experimental phase noise model leads to a lower ergodic capacity estimate
compared to the uncorrelated phase noise case. The error reduction is a result
of the correlation among consecutive phase noise samples. Furthermore, the
performance of the ergodic capacity estimator is significantly affected by
the choice of the spatio-temporal array. Arrays A and B yield equal ergodic
capacity estimates, while the ergodic capacity estimate is slightly lower for
Array C. Among the tested arrays, Array D yields the highest ergodic capacity
estimate.

The reason for the gross difference in ergodic capacity estimate for Ar-
ray D compared to Arrays A, B, and C, is that the columns (and the rows) of
the phase noise matrix Θ_i are whitened due to the sample ordering induced
by Array D. It should be remarked that despite the similar performance of
the ergodic capacity estimators obtained with Arrays A, B and C, Array B is
superior in terms of higher accuracy and robustness of joint Doppler and bi-
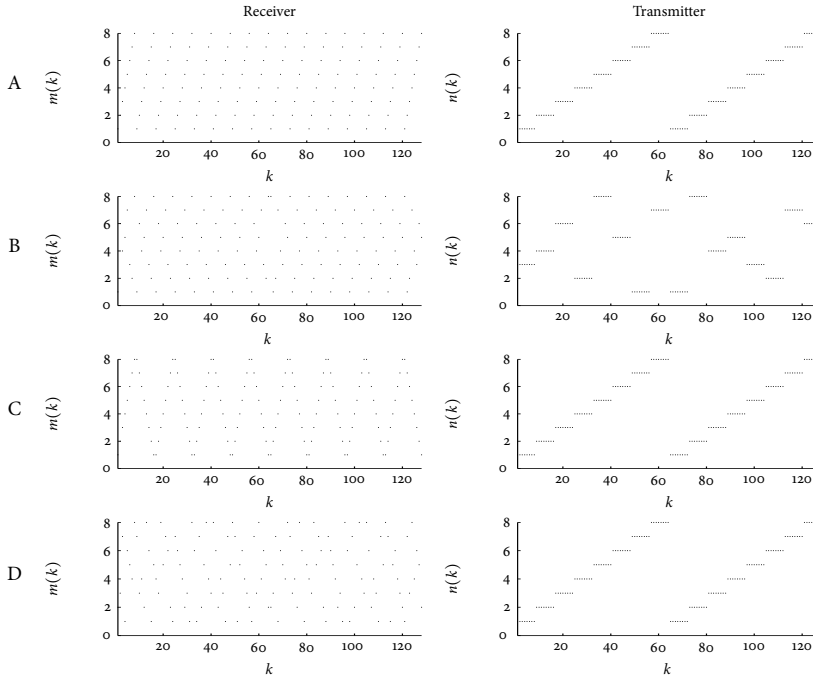direction estimates of path parameters [3, 6].

Fig. C.3: Four spatio-temporal arrays with M = N = 8, I = 2 and the timing scheme defined as $t_k = kT$, where the sampling T is 2.54 μs. Array A is the commonly used identity array [6]; Array B is a cycle-dependent and non-separable array [6]; Array C is a modified version of Array A where the receiver switching pattern is modified to achieve a non-separable array; Array D is a non-separable array.
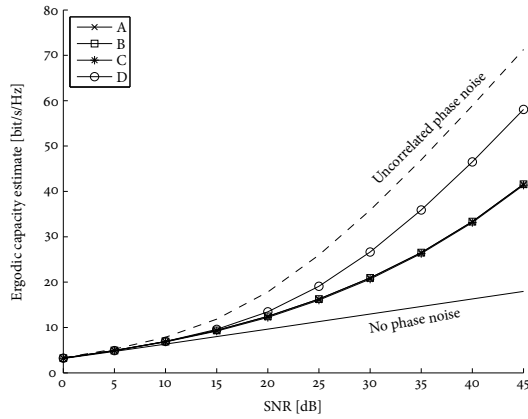

Fig. C.4: Ergodic capacity estimate versus signal-to-noise ratio for a rank-1 channel as described in the text. The spatio-temporal arrays marked A, B, C, and D are defined in Fig. C.3.

C.5   Discussion

The numerical results presented in the previous section have shown that short-term correlation of phase noise combined with appropriate choice of the spatio-temporal array aperture enable to significantly reduce the impact of phase noise on the capacity estimation based on the traditional channel matrix estimator. Another straightforward way to reduce this impact is to consider more than one cycle in (C.6), provided the channel can be assumed time-invariant over the duration of all the considered cycles [8]. The example in Section C.3 provides with some indication on an additional alternative: Select the bandwidth of the feedback loop in the phase-locked loop of the local oscillators in such a way that the resulting short-term phase noise exhibits a coherence time larger than MT. In this method, the selected bandwidth depends on both the number of elements in the receive array and the duration of the sounding sequence. Interestingly, the number of elements in the transmit array is not critical here.

However, the above approaches do not avoid the additional problem that, in practice, the measured matrices $\{\mathbf{G}_i\}$ are also impaired by additive noise, an effect which also impairs on the accuracy of the capacity estimator $C(\widehat{\mathbf{HH}^{\mathrm{H}}})$. This problem, and in fact the sensitivity to phase noise as well, is a consequence of the fact that the traditionally used estimator in (C.6) does not take into account these two noises. Estimators of $\mathbf{HH}^{\mathrm{H}}$ and $\mathbf{H}$ can be derived that exploit the statistical properties of these noises in order to mitigate their effects. Estimates $\hat{\mathbf{H}}$ constructed from estimates of the parameters of a parametric model of $\mathbf{H}$ seems to offer a promising solution. An example is the recently published phase noise compensated SAGE estimator for the estimation of path parameters [9]. This work shows that the effect of phase noise can be mitigated by taking its statistical property into consideration in the signal model underlying the derivation of the path parameter estimators. However, an open issue is how the mismatch between the physical world and the approximation of it provided the parametric model affects the capacity estimate.

C.6   Conclusions

This paper has presented some results on the impact of TDM-MIMO channel sounding on the estimation of MIMO channel capacity using the traditional channel matrix estimator. The necessary and sufficient condition on the phase noise matrix for the capacity estimate to be unaffected by phase noise is given. It is shown by means of Monte Carlo simulations that the choice of spatio-temporal array heavily impacts on the accuracy of the capacity estimator in

the presence of correlated phase noise. It was found that non-separable arrays exist that lead to the same capacity estimation error as separable arrays. As shown in [3, 6], the use of non-separable arrays leads to a lower mean square error and better ambiguity resolution abilities when used for estimation of Doppler frequency and bi-direction.

References

[1] D. S. Baum and H. Bölcskei, "Impact of phase noise on MIMO channel measurement accuracy," in *Proc. 2004 IEEE Vehicular Technology Conference*, vol. 3, Sept. 2004, pp. 1614–1618.

[2] D. S. Baum and H. Bölcskei, "Information-theoretic analysis of MIMO channel sounding," Sept. 2007, submitted to the IEEE Transactions on Information Theory. [Online]. Available: http://www.nari.ee.ethz.ch/commth/pubs/p/phase07

[3] T. Pedersen, C. Pedersen, X. Yin, and B. H. Fleury, "Optimisztion of spatio-temporal apertures in channel sounding," 2007, submitted to IEEE Transactions on Signal Processing.

[4] P. Almers, S. Wyne, F. Tufvesson, and A. Molisch, "Effect of random walk phase noise on MIMO measurements," in *Proc. 2005 IEEE Vehicular Technology Conference*, vol. 1, May 2005, pp. 141–145.

[5] A. Taparugssanagorn, J. Ylitalo, and B. H. Fleury, "Phase-noise in TDM and its impact on channel capacity," in *Proc. IEEE Global Communications Conference (Globecom 2007)*, November 2007, pp. 4559–4564.

[6] T. Pedersen, C. Pedersen, X. Yin, B. H. Fleury, R. R. Pedersen, B. Bozinovska, A. Hviid, P. Jourdan, and A. Stucki, "Joint estimation of Doppler frequency and directions in channel sounding using switched Tx and Rx arrays," *Proc. IEEE Global Telecommunications Conference (Globecom 2004)*, vol. 4, pp. 2354–2360, Dec. 2004.

[7] I. Telatar, "Capacity of multi-antenna Gaussian channels," *ETT – European Transactions on Telecommunications*, vol. 10, no. 6, pp. 585–597, 1999.

[8] A. Taparugssanagorn and J. Ylitalo, "Reducing the impact of phase noise in the MIMO capacity estimation." in *Proc. Wireless Personal Multimedia Communications*, Sept. 2005, pp. 527–531.

[9] A. Taparugssanagorn, X. Yin, J. Ylitalo, and B. H. Fleury, "Phase noise mitigation in channel parameter estimation for TDM-switched MIMO channel sounding." in *Asilomar Conference on Signals, Systems, and Computers*, Pacific Grove, CA, USA, Nov. 2007.

Estimation of MIMO Channel Capacity from Phase-Noise Impaired Measurements

Troels Pedersen, Xuefeng Yin, and Bernard H. Fleury

121

Abstract

Due to the significantly reduced cost and effort for system calibration time-division multiplexing (TDM) is a commonly used technique to switch between the transmit and receive antennas in multiple-input multiple-output (MIMO) radio channel sounding. Nonetheless, Baum *et al.* [1, 2] have shown that phase noise of the transmitter and receiver local oscillators, when it is assumed to be a white Gaussian random process, can cause large errors of the estimated channel capacity of a low-rank MIMO channel when the standard channel matrix estimator is used. Experimental evidence shows that consecutive phase noise samples affecting measurement samples collected with real TDM-MIMO channel sounders are correlated. In this contribution a capacity estimator that accounts for the phase noise correlation is proposed. The estimator is based on a linear minimum mean square error estimate of the MIMO channel matrix. It is shown by means of Monte Carlo simulations assuming a measurement-based phase noise model, that the MIMO channel capacity can be estimated accurately for signal-to-noise ratios up to about 35 dB.

D.1   Introduction

To save hardware cost and alleviate the needed calibration procedures, most advanced multiple-input multiple-output (MIMO) radio channel sounders rely on a time-division multiplexing (TDM) technique. In such a system, which is represented schematically in Fig. D.1, a single sounding waveform generator is connected to a number of transmit antennas via a switch. Similarly, the output terminals of the receive array are sensed via another switch. Thereby channel observations are made via a spatio-temporal aperture [3].

It has been shown recently that concatenated phase noise of the two oscillators in the transmitter and the receiver affects the estimation of MIMO channel capacity when using the standard channel matrix estimator to obtain a capacity estimate [1, 4]. For short we call this concatenated noise the phase
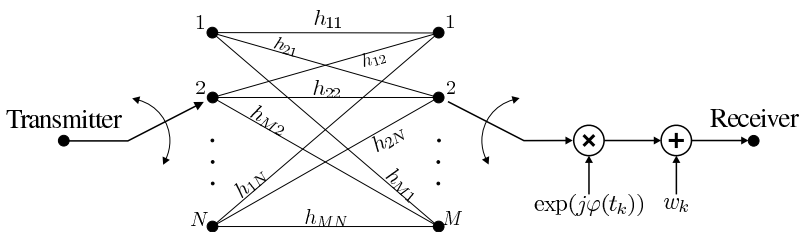

Fig. D.1: Model for TDM-MIMO channel sounding with phase noise.

noise of the sounding system. The effect of phase noise on MIMO capacity estimation is studied in [4] assuming that phase noise is a random walk process. Theoretical investigations reported in [1, 2] show that, provided phase noise is white and Gaussian, it leads to large measurement errors in terms of estimated channel capacity of a low-rank MIMO channel. In [2] analytical results are given under the assumptions that the TDM, i.e. the spatio-temporal array [3], fulfills a separability condition and that the phase noise process is white. However, experimental studies reported in [5] show that phase noise cannot be assumed to be white or a random walk on the time-scale of a measurement period [5, 6]. In addition, the spatio-temporal array induced by the used switching schemes [3] determines the ordering of the phase noise samples in the estimation of the standard channel matrix estimate. Both effects significantly affect the performance of capacity estimation based on this matrix estimator [7].

In this paper we propose an new method for estimation of the channel capacity from phase-noise impaired measurement data. The estimator relies on linear minimum mean-square-error (MMSE) estimation of the channel transfer matrix. The performance of the proposed estimator in terms of estimation accuracy is compared to standard estimators using the phase-noise model developed in [5].

D.2 Signal Model for Phase-Noise Impaired TDM-MIMO Sounding

We consider the TDM sounding system depicted schematically in Fig. D.1 with N transmit antennas and M receive antennas. To allow for measurements of the full $M \times N$ channel matrix $\mathbf{H}$, $[\mathbf{H}]_{mn} = h_{mn}$, the sounder is equipped with a switch at the transmitter and a switch at the receiver. The channel matrix $\mathbf{H}$ is assumed to be constant during one measurement run.[1] The coefficient h_{mn} of the sub-channel consisting of the nth transmit array element, the propagation channel, and the mth receive array element is measured with the transmitter switch in position n and the receiver switch in position m (see Fig. D.1). The receiver acquires K samples indexed by $k = 1, \ldots, K$. Sample k is obtained at time t_k with the transmitter switch in position $n(k) \in \{1, \ldots, N\}$ and receiver switch in position $m(k) \in \{1, \ldots, M\}$. Thus, at time instant t_k the system performs a measurement of the channel coefficient $h_{m(k)n(k)}$. The sequence $\{(t_k, m(k), n(k))\}$ defines the spatio-temporal array of the sounding system [3, 8]. We define the index set $\mathcal{K}_{mn}$ to be the set of sample

---

[1]The validity of this assumption depends on how rapidly the channel varies and on the duration of the measurement. Assuming a stationary channel is necessary for the definition of channel capacity given in Subsection D.3.1.

indices for which sub-channel (m, n) is measured, i.e.

$$\mathcal{K}_{mn} = \Big\{ k : (m(k), n(k)) = (m, n) \Big\}. \tag{D.1}$$

The cardinality of $\mathcal{K}_{mn}$, denoted by $\#\mathcal{K}_{mn}$, is equal to the number of samples acquired from sub-channel (m, n).

As depicted in Fig. D.1, the observed signal is modulated with a time-varying phasor $\exp(j\varphi(t_k))$ due to the phase noise in the oscillators of the sounding system. The kth sample is modeled as

$$g_k = h_{m(k)n(k)} \cdot \exp(j\varphi(t_k)) + w_k, \tag{D.2}$$

where $\{w_k\}$ is a white Gaussian noise process with sample variance σ_w^2. We define the measurement signal-to-noise ratio (SNR) as $\gamma = \sigma_h^2/\sigma_w^2$ where σ_h^2 is the variance of one channel coefficient. We consider the case where phase noise $\varphi(t)$ can be modeled as a wide-sense stationary process with mean zero and a known autocorrelation function $R_\varphi(\tau)$. This assumption hold true if the time-span during which measurements are acquired is sufficiently short. With the time-span considered in the following, this condition can be met by commercially available channel sounders [5].

We define a $K \times MN$ sounding matrix $\mathbf{S}$ that rearranges the vectorized channel matrix $\text{vec}(\mathbf{H})$ according to the order in which the sub-channels are measured:

$$\mathbf{S} \cdot \text{vec}(\mathbf{H}) = \begin{bmatrix} h_{m(1)n(1)} \\ \vdots \\ h_{m(k)n(k)} \\ \vdots \\ h_{m(K)n(K)} \end{bmatrix}, \tag{D.3}$$

i.e. the entries of row k of the sounding matrix are all zeros except for the entry corresponding to the entry $h_{m(k)n(k)}$ of the vectorized channel matrix $\text{vec}(\mathbf{H})$. As an example consider a sounding system with $M_1 = M_2 = 2$, and $K = 8$ using the identity sounding mode with $[n(1), \dots, n(8)] = [1, 1, 2, 2, 1, 1, 2, 2]$, $[m(1), \dots, m(8)] = [1, 2, 1, 2, 1, 2, 2, 1]$. In this case,

$$\mathbf{S} \cdot \text{vec}(\mathbf{H}) = \begin{bmatrix} 1 & & & \\ & 1 & & \\ & & 1 & \\ & & & 1 \\ 1 & & & \\ & 1 & & \\ & & 1 & \\ & & & 1 \end{bmatrix} \cdot \begin{bmatrix} h_{11} \\ h_{21} \\ h_{12} \\ h_{22} \end{bmatrix} = \begin{bmatrix} h_{11} \\ h_{21} \\ h_{12} \\ h_{22} \\ h_{11} \\ h_{21} \\ h_{12} \\ h_{22} \end{bmatrix}. \tag{D.4}$$

We can now, after defining the three vectors

$$\mathbf{g} \triangleq \begin{bmatrix} g_1 \\ \vdots \\ g_K \end{bmatrix}, \quad \boldsymbol{\varphi} \triangleq \begin{bmatrix} \varphi_1 \\ \vdots \\ \varphi_K \end{bmatrix}, \quad \text{and} \quad \mathbf{w} \triangleq \begin{bmatrix} w_1 \\ \vdots \\ w_K \end{bmatrix}, \tag{D.5}$$

recast (D.2) in the compact form

$$\mathbf{g} = [\mathbf{S} \cdot \text{vec}(\mathbf{H})] \circ \exp(j\boldsymbol{\varphi}) + \mathbf{w}, \tag{D.6}$$

where $\circ$ denotes the Hadamard (or element-wise) product and the exponential function is taken element-wise. Notice that if $t_1 < t_2 < \cdots < t_K$ then the entries of the vectors defined in (D.5) are ordered according to the temporal order.

In the case where each of the sub-channels is measured I times, the obtained measurements can be arranged in matrices $\{\mathbf{G}_i\}$ such that the entries fulfils $[\mathbf{G}_{i(k)}]_{m(k)n(k)} = g_k$ where $i(k) \in \{1, \ldots, I\}$ is a cycle-index assigned to sample k. There is a certain degree of freedom in the choice of $i(k)$: if the samples g_k and $g_{k'}$ are both acquired from the same sub-channel we are free to choose to assign the cycle indices as $i(k) = 1, i(k') = 2$ or $i(k) = 2, i(k') = 1$.

D.3   Estimation of Capacity

When the channel is not known at the transmitter, but fully known at the receiver, its capacity at SNR ρ reads [9]

$$C(\mathbf{H}\mathbf{H}^{\mathsf{H}}) = \log_2 \det(\mathbf{I}_M + \tfrac{\rho}{N}\mathbf{H}\mathbf{H}^{\mathsf{H}}), \tag{D.7}$$

where $\mathbf{H}^{\mathsf{H}}$ denotes the Hermitian transpose of $\mathbf{H}$. The problem considered here is to estimate the capacity $C(\mathbf{H}\mathbf{H}^{\mathsf{H}})$ from the noisy observation $\mathbf{g}$. It is important to distinguish between the SNR ρ in (D.7) at which we compute the capacity and the SNR γ during the measurement of $\mathbf{g}$. In general we wish to be able to compute capacities for other SNRs than the SNR prevailing during the measurement, i.e. for $\rho \neq \gamma$.

D.3.1   The Standard Capacity Estimator

The standard capacity estimator is defined as [1, 2, 7]

$$\hat{C}_{\text{std}} = C(\widehat{\mathbf{H}\mathbf{H}^{\mathsf{H}}}), \quad \text{with} \quad \widehat{\mathbf{H}\mathbf{H}^{\mathsf{H}}} = \frac{1}{I}\sum_{i=1}^{I} \mathbf{G}_i\mathbf{G}_i^{\mathsf{H}}, \tag{D.8}$$

where $\widehat{(\cdot)}$ denotes the estimate of the random element given as an argument.

We remark that the standard estimator can be applied only when I samples from each sub-channel are available. It is also worth mentioning that the standard estimator depends on the choice of $i(k)$. Therefore for the remainder of the paper we chose $i(k)$ according to the temporal ordering of the samples, i.e. the first sample of sub-channel (m, n) is in $\mathbf{G}_1$ and the second sample is in $\mathbf{G}_2$, etc.

D.3.2 Capacity Estimation by Averaging [6]

In [6] it is proposed to estimate the channel matrix by computing the average of $\mathbf{H}$ of the data acquired during the measurement:

$$\hat{\mathbf{H}}_{\text{avg}} = \frac{1}{I} \sum_{i=1}^{I} \mathbf{G}_i. \tag{D.9}$$

This estimator can be generalized to non-cycled sounding as:

$$[\hat{\mathbf{H}}_{\text{avg}}]_{mn} = \frac{1}{\#\mathcal{K}_{mn}} \sum_{k \in \mathcal{K}_{mn}} g_k. \tag{D.10}$$

The capacity estimate $\hat{C}_{\text{avg}}$ is then defined as $\hat{C}_{\text{avg}} \triangleq C(\hat{\mathbf{H}}_{\text{avg}} \hat{\mathbf{H}}_{\text{avg}}^{\mathsf{H}})$. This estimator leads to an estimation error lower than that of the standard estimator [6] and is independent of the choice of $i(k)$.

D.3.3 Capacity Estimator based on a Linear MMSE Channel Estimate

Neither of the above estimators exploit the knowledge of the phase noise autocorrelation $R_\varphi(\tau)$. In the following we develop a new estimator for $\mathbf{H}$ that takes this knowledge into account. The estimator relies on separate estimation of the moduli (magnitudes) and the arguments (phases) of the channel coefficients $\{h_{mn}\}$. Knowing the magnitude matrix $\mathbf{Z} \triangleq |\mathbf{H}|$ and the phase angle matrix $\mathbf{Y} \triangleq \angle\mathbf{H}$ we can recover the channel transfer matrix as

$$\mathbf{H} = \mathbf{Z} \circ \exp(j\mathbf{Y}). \tag{D.11}$$

Similarly, an estimate of $\mathbf{H}$ can be obtained from estimates of $\mathbf{Z}$ and $\mathbf{Y}$ as

$$\hat{\mathbf{H}} = \hat{\mathbf{Z}} \circ \exp(j\hat{\mathbf{Y}}). \tag{D.12}$$

We estimate the magnitude matrix $\mathbf{Z}$ by averaging the magnitudes of the acquired measurement data as

$$[\hat{\mathbf{Z}}]_{mn} = \frac{1}{\#\mathcal{K}_{mn}} \sum_{k \in \mathcal{K}_{mn}} |g_k|. \tag{D.13}$$

127

It is straightforward to show that $[\hat{\mathbf{Z}}]_{m,n}$ this is an asymptotically consistent estimator of $|h_{mn}|$ when the SNR γ tends to infinity.

The estimate of $\mathbf{Y}$ is less obvious. Using the definition of the phase operator $\angle_a$ provided in Appendix D.I, we define the vector $\mathbf{x} \triangleq [x_1, \ldots, x_K]^\mathsf{T}$ of phases

$$x_k \triangleq \angle_{a_{m(k)n(k)}} g_k, \tag{D.14}$$

where $\angle_{a_{m(k)n(k)}} g_k$ denotes the phase of g_k such that $\angle_{a_{m(k)n(k)}} g_k \in [\pi - a_{m(k)n(k)}, \pi + a_{m(k)n(k)})$ with the real number $a_{m(k)n(k)}$ defined in Appendix D.I. Thus, $\mathbf{x}$ is available for the estimation of the matrix of phases $\mathbf{Y}$ where element (m, n) of $\mathbf{Y}$ is defined as

$$y_{mn} \triangleq \angle_{a_{mn}} h_{mn}. \tag{D.15}$$

Introducing the vector $\mathbf{y} = \text{vec}(\mathbf{Y})$ we obtain the following expression for $\mathbf{x}$

$$\mathbf{x} = \mathbf{S}\mathbf{y} + \boldsymbol{\varphi} + \mathbf{v}, \tag{D.16}$$

which is valid when the measurement SNR γ is high. In (D.16), the vector $\mathbf{v} \triangleq [v_1, \ldots, v_K]^\mathsf{T}$ is a real-valued additive noise resulting from the additive noise $\mathbf{w}$. As shown in Appendix D.II, $\mathbf{v}$ can be approximated as $\mathbf{v} \sim \mathcal{N}(\mathbf{0}, \frac{1}{2\gamma}\mathbf{I})$.

The linear MMSE estimate of $\mathbf{y}$ from $\mathbf{x}$ is obtained as [10]

$$\hat{\mathbf{y}} = \mathbf{x}^\mathsf{T} \Sigma_{\mathbf{x}}^{-1} \Sigma_{\mathbf{xy}}, \tag{D.17}$$

where $\Sigma_{\mathbf{x}}$ denotes the covariance matrix of $\mathbf{x}$ and $\Sigma_{\mathbf{xy}}$ is the covariance matrix of $\mathbf{x}$ and $\mathbf{y}$. We assume that the phases of the channel coefficients are uncorrelated random variables with mean zero. This assumption is a "worst case" as in this case the estimator cannot exploit any correlation between the phases of the sub-channels. We further assume that each element of $\mathbf{y}$ has variance $\frac{\pi^2}{3}$ corresponding to the variance of a random variable uniformly distributed on the interval $[-\pi, \pi)$. Monte Carlo simulations of the mean square estimation error show that this assumption is indeed appropriate. Under these assumptions, $E(\mathbf{y}) = \mathbf{0}$ and $\Sigma_{\mathbf{y}} = \frac{\pi^2}{3}\mathbf{I}$. Hence, $\Sigma_{\mathbf{xy}}$ reads

$$\Sigma_{\mathbf{xy}} = E(\mathbf{x}\mathbf{y}^\mathsf{T}) = \mathbf{S}E(\mathbf{y}\mathbf{y}^\mathsf{T}) = \mathbf{S}\Sigma_{\mathbf{y}} = \frac{\pi^2}{3}\mathbf{S}. \tag{D.18}$$

where we made use of the fact that $\boldsymbol{\varphi}$ and $\mathbf{v}$ have zero-mean and therefore by (D.16), $E(\mathbf{x}) = \mathbf{0}$. Using (D.16) and (D.18) the covariance matrix of $\mathbf{x}$ can be derived as

$$\Sigma_{\mathbf{x}} = \frac{\pi^2}{3}\mathbf{S}\mathbf{S}^\mathsf{T} + \Sigma_{\boldsymbol{\varphi}} + \frac{1}{2\gamma}\mathbf{I}, \tag{D.19}$$

Setting	Value
M	8
N	8
I	2
K	128
t_k	kT
Sample time T	2.54 μs
Monte Carlo Runs	100
rank($\mathbf{H}$)	1
$\gamma \triangleq \sigma_h^2/\sigma_w^2$	20 dB[†]
ρ	35 dB[†]

[†]When no other values are given.

where $\Sigma_{\boldsymbol{\varphi}}$ is the known covariance matrix of $\boldsymbol{\varphi}$ defined as

$$[\Sigma_{\boldsymbol{\varphi}}]_{k\ell} \triangleq R_{\varphi}(t_k - t_\ell). \tag{D.20}$$

Finally, we propose to use the capacity estimator:

$$\hat{C}_{\text{MMSE}} = C(\hat{\mathbf{H}}\hat{\mathbf{H}}^{\mathsf{H}}), \tag{D.21}$$

where $\hat{\mathbf{H}}$ is given in (D.12) with $\hat{\mathbf{Z}}$ obtained from (D.13), and $\hat{\mathbf{Y}}$ obtained from (D.17) as $\hat{\mathbf{Y}} = \text{vec}^{-1}(\hat{\mathbf{y}})$.

D.4   Numerical Results

We now compare the proposed estimator and the estimators reported in Sub-sections D.3.1 and D.3.2 by means of Monte Carlo simulations. The simulation settings are reported in Table. D.1. On the time-scale used in the simulations presented in this contribution, the phase noise process can be modeled as an auto-regressive moving-average (ARMA) process of order (7,6) [5, 7]:

$$\varphi_k = \sum_{p=1}^{7} \phi_p \varphi_{k-p} + \sum_{q=1}^{6} \theta_q d_{k-q} + d_k, \quad \varphi_k = \varphi(kT) \tag{D.22}$$

where the driving process $\{d_k\}$ is a white Gaussian process with sample variance σ_d^2 and T denotes the sample time. The phase noise process was measured using a commercially available sounder as described in [5]. Fig. D.3

depicts the sample autocorrelation function of the measured phase noise series together with the autocorrelation function and the coefficients of the fitted ARMA process [5].[2] The sample time T = 2.54 μs corresponds to twice the duration of a 127-chip long sequence with a chip rate of 100 MHz.

In each Monte Carlo run a rank-1 channel matrix **H** (i.e. a key-hole channel) is generated.[3] Then phase noise is generated according to the above model. The average capacity estimates are obtained by averaging over the capacity estimates computed from 100 Monte Carlo runs.

Two different spatio-temporal arrays named Array A and Array B are considered. The two arrays defined by $m(k)$ and $n(k)$ are given in Fig. D.2. Array A is the commonly used identity array [3, 8] and Array B is a non-separable spatio-temporal array optimized for high accuracy and robustness of joint Doppler frequency and direction estimation [3, 8]. Array A is *separable* in the sense that it fulfills the condition [2]

$$t_k = i(k) T_c + [\mathbf{t}_{\mathrm{Tx}}]_{n(k)} + [\mathbf{t}_{\mathrm{Rx}}]_{m(k)}, \tag{D.23}$$

where $\mathbf{t}_{\mathrm{Tx}}$ and $\mathbf{t}_{\mathrm{Rx}}$ are vectors of dimensions N and M respectively and $T_c = MNT$.

Fig. D.4 reports the averaged estimated capacities obtained with the three estimators when Array A and Array B given in Fig. D.2 are used. The resulting capacity estimates are plotted as functions of the SNR ρ as in (D.7). Fig. D.4(a) reports the estimates obtained using Array A. As can be seen from the figure, all three estimators overestimate the capacity for ρ > 18 dB. It can be observed that in this scenario, the estimators $\hat{C}_{\mathrm{avg}}$ and $\hat{C}_{\mathrm{MMSE}}$ show the same accuracy, while the standard estimator $\hat{C}_{\mathrm{std}}$ is less accurate. Fig. D.4(b) reports the estimates using Array B. It can be observed that the estimators $\hat{C}_{\mathrm{std}}$ and $\hat{C}_{\mathrm{std}}$ perform significantly worse compared to Fig. D.4(a) as also reported in [7], while the estimation accuracy of the proposed estimator $\hat{C}_{\mathrm{MMSE}}$ improves drastically. In Fig. D.4(b), the capacity estimates diverge significantly from the true capacity at about 13 dB for estimators $\hat{C}_{\mathrm{std}}$ and $\hat{C}_{\mathrm{avg}}$, and at about 35 dB for the proposed estimator $\hat{C}_{\mathrm{MMSE}}$. In practice, MIMO communication systems seldom operate at SNRs as high as 35 dB. Thus, the proposed capacity estimator can be seen to return valid estimates at SNRs considered in practice.

In Fig. D.5 the capacity estimates and the mean-square channel estimation error obtained with Array B are reported versus the measurement SNR γ for

---

[2]The parameter values reported in [5] differ from the values in Fig. D.3 even-though the same measurement data was used. This discrepancy is due to an unfortunate misprint in [5].

[3]The impact of phase noise to estimation of capacity is most significant for low rank channels [1, 2]. Thus, despite the fact that a key-hole channels are rare under realistic propagation conditions, the low rank channel is useful for assessing the robustness of a capacity estimator towards phase noise.
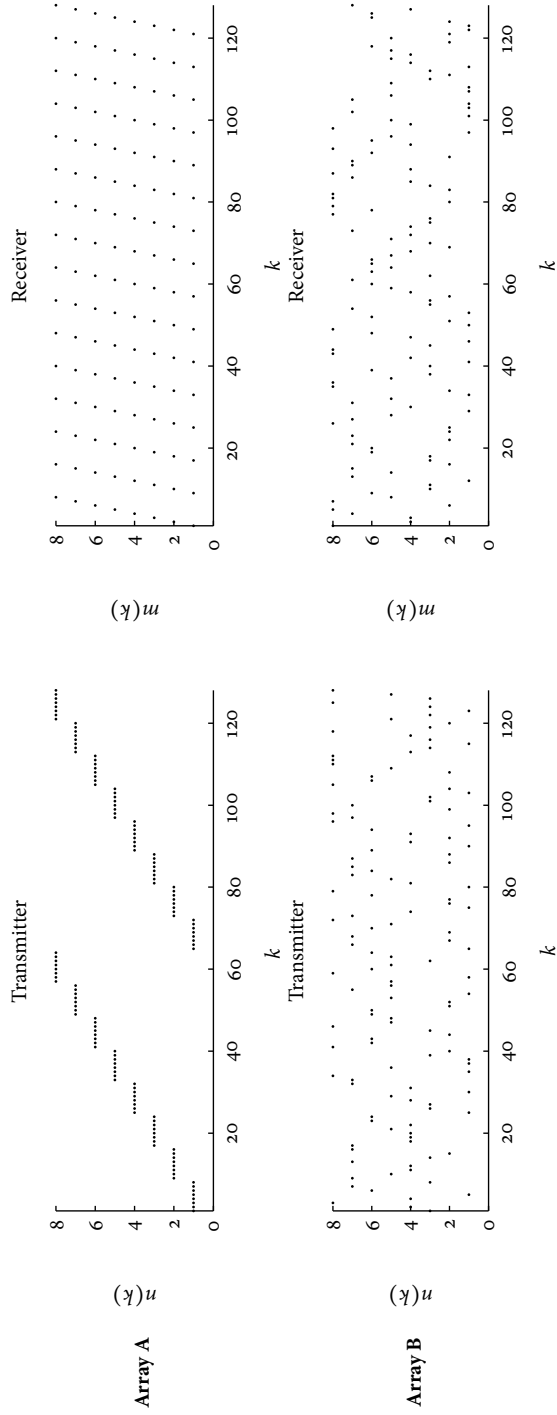
Fig. D.2: *Spatio-temporal arrays used in the simulations. Array A (upper panels) is the commonly used separable identity array [8]; Array B (lower panels) is a non-separable randomly selected array.*

k	1	2	3	4	5	6	7
ϕ_k	−0.239	−0.353	−1.085	0.442	0.508	0.227	−0.212
θ_k	1.340	1.314	0.431	0.260	0.295	0.238	—

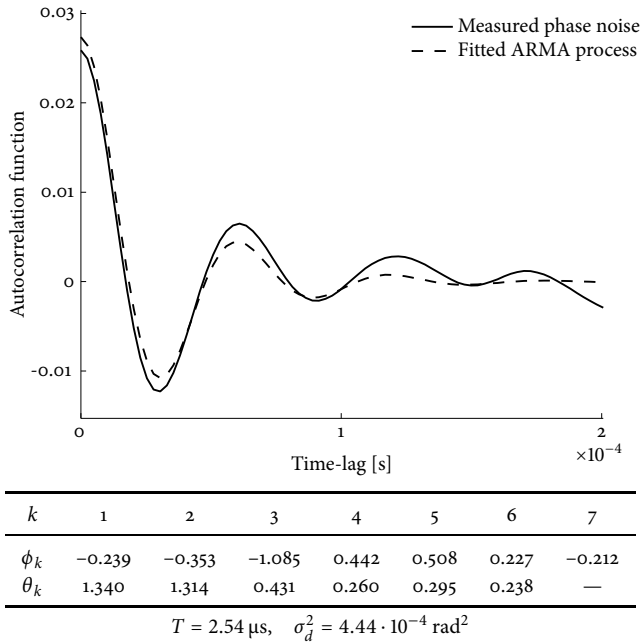$$T = 2.54\,\mu s, \quad \sigma_d^2 = 4.44 \cdot 10^{-4}\,\text{rad}^2$$

Fig. D.3: Sample autocorrelation function (solid line) and autocorrelation function of the ARMA process fitted to the short-term component of phase noise (broken line) [5]. The table reports the parameters of the fitted ARMA process.

all three estimators. The mean square error of the channel matrix estimates is computed by averaging the Frobenius norm of the error matrices $\mathbf{H} - \hat{\mathbf{H}}$ generated in the Monte Carlo runs. It is apparent that the proposed MMSE estimator yields a capacity estimation error lower than those obtained with the other estimators and that it approaches the exact capacity for γ higher than about 20 dB. Furthermore, it can be seen that the proposed estimator yields a five times lower mean square error than that achieved with the averaging approach (D.9) for $\gamma > 20$ dB. This improvement results because the MMSE estimator exploits the known autocorrelation of the phase noise.

D.5 Conclusions

This paper has presented a new estimator for the MIMO channel capacity for the case where the available channel measurements are impaired by both phase noise and additive noise. The proposed estimator relies on separate estimation of the magnitudes and phases of the channel coefficients and exploits knowledge of the phases noise autocorrelation function. This autocorrelation function can be obtained by calibration measurements of the
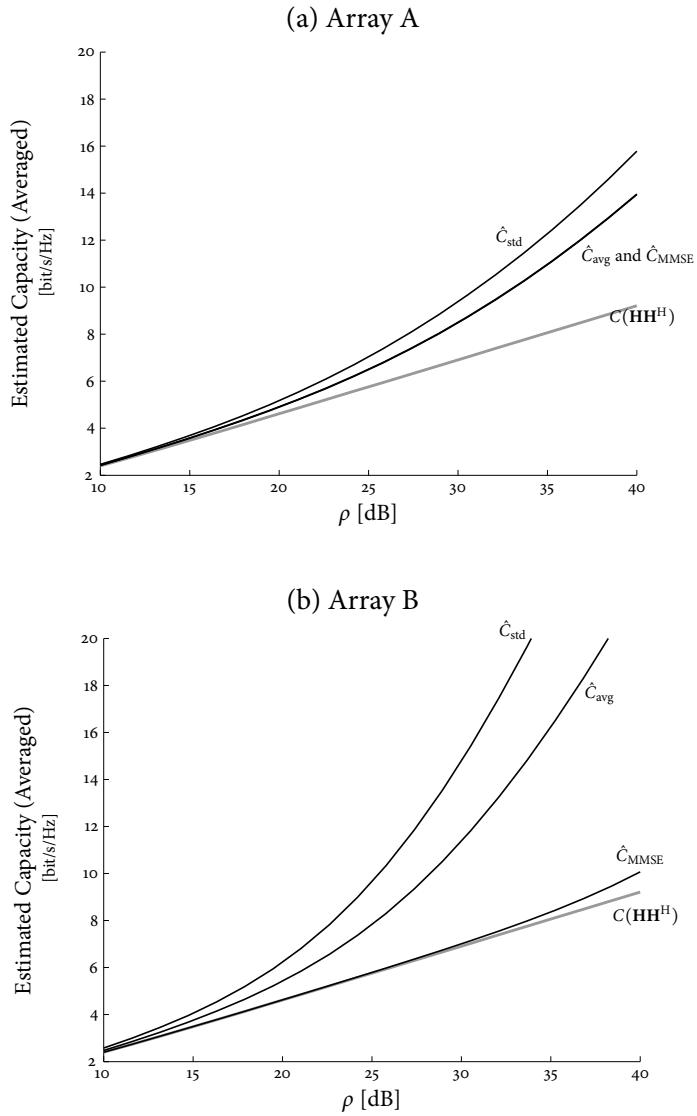
(a) Array A

(b) Array B

Fig. D.4: *Averaged capacity estimates simulated using the settings listed in Fig. D.2. Panel (a) reports the results when Array A is used; In panel (b), Array B is used.*
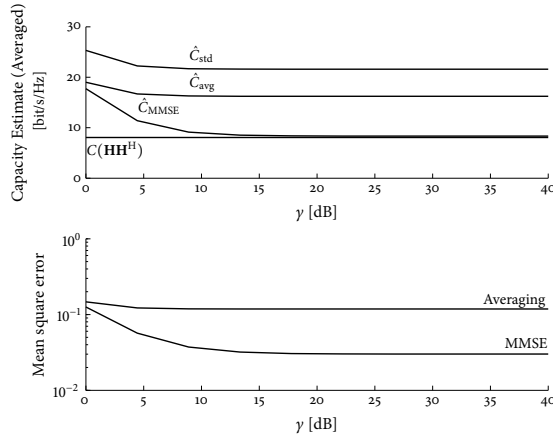
*Fig. D.5: Averaged capacity estimates and mean square error of the channel matrix estimates
versus SNR γ. Array B is used. Upper panel: Estimated capacity with ρ = 35 dB. Lower panel:
Mean square error of the channel matrix estimates.*

channel sounder. The proposed capacity estimator was compared to conventional methods using two different spatio-temporal arrays. It was found by simulation that the accuracy of the proposed capacity estimator is higher when the measurement data is acquired using a non-separable array than when using a separable identity array. Interestingly, the opposite effect applies when the standard capacity estimator is applied: here the separable array leads to the best performance. In conclusion, the simulation results show that the proposed estimator leads to a significant improvement in the estimation of channel capacity from phase-noise impaired measurement data compared to the conventional estimators.

D.I   Definition of the Angle Operator

The angle of a complex number is a real number that takes a value on an interval of length 2π, e.g the interval $[a - \pi, a + \pi)$ where a is a real number. We define the mapping

$$\angle_a : \mathbb{C} \to [a - \pi, a + \pi) \quad \text{s.t.} \quad c = |c| \exp(j\angle_a c). \qquad (D.24)$$

Notice that a can be any real number. For example it is customary to select $a = 0$. However, this causes problems when considering angles between pairs of complex numbers. As an example the numbers $\exp(j(\pi - \frac{\pi}{8}))$ and $\exp(j(\pi + \frac{\pi}{8}))$, differ in angle by $\frac{\pi}{4}$, whereas $\angle_0 \exp(j(\pi - \frac{\pi}{8})) - \angle_0 \exp(j(\pi + \frac{\pi}{8})) = \frac{7\pi}{4}$.

We assume that the variance of the phase noise components is sufficiently small such that the phases of the samples taken from sub-channel (m, n) all
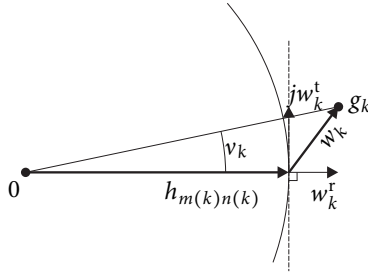
Fig. D.6: The noise projection in the complex plane used to compute an approximation of **v** *in (D.16).*

lie in the interval $\left[\angle_0 h_{mn} - \frac{\pi}{2}, \angle_0 h_{mn} + \frac{\pi}{2} \right]$ with high probability. In this case we can define an angle mapping $\angle_{a_{mn}}$ where the value of a_{mn} is defined as the angle of the geometric mean of the set of samples taken from a specific sub-channel (m, n):

$$a_{mn} = \angle_0 \left[\prod_{k \in \mathcal{K}_{mn}} \left(\frac{g_k}{|g_k|} \right)^{\frac{1}{\# \mathcal{K}_{mn}}} \right]. \tag{D.25}$$

For phase noise processes with sufficiently small sample variance, this per-sub-channel definition of the angle operator enables computation of phase differences between phases of measurements acquired from the same sub-channel by subtraction of the phases.

D.II The Additive Noise in (D.16)

The kth noise sample v_k in (D.16) denotes the phase contribution due to the additive complex noise sample w_k. As illustrated in Fig. D.6, w_k can be decomposed into the radial component w_k^{r} and the tangential component $j w_k^{\mathrm{t}}$. When $|w_k^{\mathrm{r}}|$ is sufficiently small compared to $|h_{m(k)n(k)}|$ we can use the approximation $|h_{m(k)n(k)}| v_k \approx w_k^{\mathrm{t}}$. Since w_k is a zero-mean circular symmetric complex Gaussian random variable, the tangential component is Gaussian distributed with variance $\sigma_w^2/2$. Then, when the above approximation is valid, $v_k \sim \mathcal{N}(0, \frac{1}{2\gamma})$. Thus the covariance matrix of **v** is $\frac{1}{2\gamma}\mathbf{I}$.

References

[1] D. S. Baum and H. Bölcskei, "Impact of phase noise on MIMO channel measurement accuracy," in *Proc. 2004 IEEE Vehicular Technology Conf.*, vol. 3, Sept. 2004, pp. 1614–1618.

[2] D. S. Baum and H. Bölcskei, "Information-theoretic analysis of MIMO channel sounding," Sept. 2007, submitted to the IEEE Tran. on Inf. Theory.

[3] T. Pedersen, C. Pedersen, X. Yin, and B. H. Fleury, "Optimization of spatio-temporal apertures in channel sounding," 2008, accepted for publication in IEEE Tran. on Signal Process.

[4] P. Almers, S. Wyne, F. Tufvesson, and A. Molisch, "Effect of random walk phase noise on MIMO measurements," in *Proc. 2005 IEEE Vehicular Technology Conf.*, vol. 1, May 2005, pp. 141–145.

[5] A. Taparugssanagorn, J. Ylitalo, and B. H. Fleury, "Phase-noise in TDM and its impact on channel capacity," in *Proc. IEEE Global Commun. Conf. (Globecom)*, Nov. 2007, pp. 4559–4564.

[6] A. Taparugssanagorn and J. Ylitalo, "Reducing the impact of phase noise in the MIMO capacity estimation." in *Proc. Wireless Personal Multimedia Commun.*, Sept. 2005, pp. 527–531.

[7] T. Pedersen, A. Taparugssanagorn, J. Ylitalo, and B. H. Fleury, "On the impact of TDM in estimation of MIMO channel capacity from phase-noise impaired measurements," in *Proc. 2008 Int. Zürich Seminar on Commun.*, Mar. 2008, pp. 128–131.

[8] T. Pedersen, C. Pedersen, X. Yin, B. H. Fleury, R. R. Pedersen, B. Bozinovska, A. Hviid, P. Jourdan, and A. Stucki, "Joint estimation of Doppler frequency and directions in channel sounding using switched Tx and Rx arrays," *Proc. IEEE Global Telecommun. Conf. (Globecom)*, vol. 4, pp. 2354–2360, Dec. 2004.

[9] I. Telatar, "Capacity of multi-antenna Gaussian channels," *European Tran. on Telecommun.*, vol. 10, no. 6, pp. 585–597, 1999.

[10] S. M. Kay, *Fundamentals of Statistical Signal Processing: Estimation Theory*. Prentice Hall, 1993.

Parametric Characterization and Estimation of Bi-Azimuth Dispersion of Path Components

Xuefeng Yin, Troels Pedersen, Nicolai Czink, and Bernard H. Fleury

Abstract

In this contribution, we derive a probability distribution suitable for characterizing bi-azimuth (azimuth of arrival and azimuth of departure) direction dispersion of individual path components in the response of the propagation channel. This distribution belongs to the family of generalized von-Mises-Fisher distributions. The elements in this family maximize the entropy under the constraint that the expectations and correlation matrix of the directions are known. The probability density function (pdf) of the proposed distribution is used to describe the bi-azimuth power spectrum of individual path components. An estimator of the parameters of the pdf is derived and applied to characterize the spreads in both azimuth of departure and azimuth of arrival, as well as the correlation between both azimuths of individual path components. Preliminary results from an experimental investigation demonstrate the applicability of the proposed characterization in real environments.

E.1   Introduction

Due to the heterogeneity of the propagation environment, the received signal at the receiver (Rx) of a radio communication system is the superposition of a number of components. Each individual component, which we call "path component", is contributed by an electromagnetic wave propagating along a path from the transmitter (Tx) to the Rx. Along this path, the wave interacts with a certain number of objects referred to as scatterers. Due to the geometrical and electromagnetic properties of the scatterers, the individual path components may be dispersive in delay, direction of departure (DoD), direction of arrival (DoA), polarizations, as well as in Doppler frequency when the environment is time-variant.

Path components can be observed in the response of the channel and any characterizing function derived from this response. As an example, in Fig. E.1 we show two estimated power spectra with respect to azimuth of departure (AoD) and azimuth of arrival (AoA) at specific delays calculated from measurement data using the Bartlett beamformer [2]. In the sequel, we refer to these spectra as (bi-azimuth) Bartlett spectra. A certain number of spots can be observed. Each spot corresponds to either one or more specific path components. It can be observed from Fig. E.1 (a) and (b) that the path components are spread in AoA and AoD. Moreover, they appear tilted. Both effects are due to the geometrical and electromagnetic properties of the scatterers along the paths, as well as the response – in particular the limited resolution – of the measurement equipment.
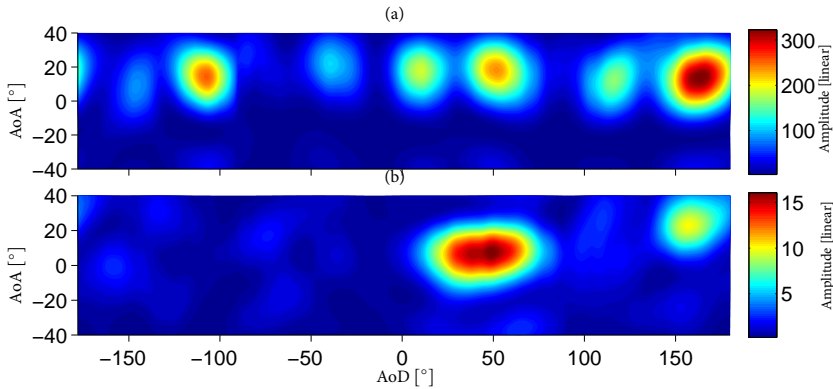
Fig. E.1: Examples of two bi-azimuth Bartlett spectra calculated at specific relative delays (78 ns, 133 ns) from the correlator output of the channel sounder [1] in (a) an office; (b) a big hall. In the calculation, the responses of the Tx and Rx arrays in vertical-polarization only are considered. The details of the measurement campaign and measurement setup are provided in Section E.5.

Recently, estimation of the characteristics of individual path components have gained much attention. The conventional approach consists in estimating the channel response and any characterizing functions derived from this response. An example of the characterizing function is the power spectrum and a traditional estimate of it is the Bartlett spectrum. However, due to the response of the measurement equipment, the path components are blurred and consequently, their spreads are artificially increased. In recent years, several model-based estimation techniques have been proposed to estimate the nominal azimuth and azimuth dispersion of the path components at one side of the link [3] [4] [5]. These techniques are based on the assumption that the azimuth power spectra of individual path components exhibit a shape which is close to that of the probability density function (pdf) of a certain distribution, like the uniform distribution [4], the (truncated) Gaussian distribution [3] [4] and the von-Mises distribution [5].

In this contribution, we propose an entropy-maximizing bi-direction (i.e. DoD and DoA) distribution to characterize bi-direction dispersion by means of the mean directions and correlation matrix between both directions. Such distributions have been derived in [6] and are called generalized von-Mises-Fisher distributions. We consider the case of horizontal-only propagation. The von-Mises-Fisher distribution is described by three free parameters (two vector parameters and one matrix parameter) that we identify. To do so, we assume that in the case where the path components are slightly dispersive the bi-azimuth distribution is close to a two-dimensional (2-D) truncated Gaussian distribution. Furthermore, we derive a maximum likelihood estimator for the

parameters of the pdf of the von-Mises Fisher distribution. This estimator is applicable in time-variant environments, i.e. when fast-fading occurs [7].

The organization of this contribution is as follows. In Section E.2, we derive the pdf of the bi-variate von-Mises-Fisher distribution. Section E.3 presents the signal model describing bi-azimuth dispersion of path components. The maximum likelihood estimator of the parameters of the pdf is derived in Section E.4. Section E.5 presents the result of the experimental investigation. Finally concluding remarks are made in Section E.6.

E.2 Von-Mises-Fisher Distribution

Following the nomenclature in [8], we use a unit vector $\boldsymbol{\Omega}$ to characterize a direction. In the considered case of horizontal-only propagation, the vector $\boldsymbol{\Omega}$ has its initial point anchored at the origin O of a coordinate system specified in the region surrounding the array of interest, and terminal point located on a unit circle $\mathbb{S}_1$ centered at O. The vector $\boldsymbol{\Omega}$ is uniquely determined by its azimuth ϕ. The one-to-one relation between $\boldsymbol{\Omega}$ and ϕ is

$$\boldsymbol{\Omega} = \mathbf{e}(\phi) \doteq \left[\cos(\phi), \sin(\phi)\right]^{\mathrm{T}} \tag{E.1}$$

with $[\cdot]^{\mathrm{T}}$ denoting transposition.

Among all probability distributions on $\mathbb{S}_1$, the von-Mises distribution appears to be a natural candidate to describe direction dispersion by individual path components, provided the characterization of direction dispersion is only by means of the mean direction $\mathrm{E}[\boldsymbol{\Omega}]$ [8]. The von-Mises distribution shares the same virtue as the Gaussian distribution, namely it maximizes the entropy among the family of probability distributions on the circle with the constraint that the second central moment is fixed. Notice that the second central moment of a circular distribution is the direction spread [8]. It is uniquely determined by the norm of the mean direction. Indeed, if $\sigma_{\boldsymbol{\Omega}}$ denotes the direction spread, then $\sigma_{\boldsymbol{\Omega}} = \sqrt{1 - \|\mathrm{E}[\boldsymbol{\Omega}]\|^2}$ [8]. The pdf of the von-Mises distribution reads [6, Sect. 2.1]

$$f(\boldsymbol{\Omega}) = \frac{1}{2\pi I_0(\kappa)} \exp\{\kappa \bar{\boldsymbol{\Omega}}^{\mathrm{T}} \boldsymbol{\Omega}\},$$

where $I_n(\cdot)$ is the modified Bessel function of the first kind and order n, $\kappa \geq 0$ is called the concentration parameter, and $\bar{\boldsymbol{\Omega}} \doteq \mathbf{e}(\bar{\phi})$ denotes a unit vector with azimuth $\bar{\phi}$ equal to the azimuth of $\mathrm{E}[\boldsymbol{\Omega}]$. The azimuth distribution induced by the von-Mises distribution via the mapping (E.1) has the pdf [9, P. 36]

$$f(\phi) = \frac{1}{2\pi I_0(\kappa)} \exp\{\kappa \cos(\phi - \bar{\phi})\}. \tag{E.2}$$

By a generalization of terminology, the azimuth probability distribution with the pdf (E.2) is referred to the von-Mises distribution as well.

Note that throughout the paper, azimuth variables are within the range $[-\pi, \pi)$. Addition and subtraction of azimuth variables are defined in such a way that the resulting angle lies in the range $[-\pi, \pi)$. When κ is large, typically $\kappa > 7$,

$$(\phi - \bar{\phi})^2 \approx \|\boldsymbol{\Omega} - \bar{\boldsymbol{\Omega}}\|^2 \qquad (\text{E.3})$$

holds, which leads to the approximation $\cos(\phi - \bar{\phi}) \approx 1 - \frac{1}{2}(\phi - \bar{\phi})^2$. Inserting this approximation in (E.2) yields the Gaussian pdf $f_G(\phi) = \frac{\sqrt{\kappa}}{\sqrt{2\pi}} \exp\{-\frac{\kappa}{2}(\phi - \bar{\phi})^2\}$ [9, P. 37].

In the sequel, we derive a bivariate pdf of the DoA $\boldsymbol{\Omega}_1$ and the DoD $\boldsymbol{\Omega}_2$ for horizontal-only propagation. The symbols with subscript 1 and 2 are with respect to the Tx array and the Rx array respectively. It is shown in [6] that the maximum entropy bi-direction distribution when the expectations $E[\boldsymbol{\Omega}_1]$ and $E[\boldsymbol{\Omega}_2]$ and the correlation matrix $E[\boldsymbol{\Omega}_1 \boldsymbol{\Omega}_2^T]$ are specified has a pdf of the form

$$f(\boldsymbol{\Omega}_1, \boldsymbol{\Omega}_2) = C \cdot \exp\{\mathbf{a}_1^T \boldsymbol{\Omega}_1 + \mathbf{a}_2^T \boldsymbol{\Omega}_2 + \boldsymbol{\Omega}_1^T \mathbf{A} \boldsymbol{\Omega}_2\}, \qquad (\text{E.4})$$

where C denotes a normalization factor, $\mathbf{a}_1, \mathbf{a}_2 \in \mathbb{R}^{2 \times 1}$ and $\mathbf{A} \in \mathbb{R}^{2 \times 2}$. Following [6] we refer to this distribution as the generalized von-Mises-Fisher distribution.

The parameters $\mathbf{a}_1$, $\mathbf{a}_2$ and $\mathbf{A}$ in (E.4) are free parameters, the specification of which depends on the particular problem at hand. To find the appropriate expressions of $\mathbf{a}_1$, $\mathbf{a}_2$ and $\mathbf{A}$ for our particular application, i.e. the characterization of bi-azimuth dispersion, we postulate that, for slightly distributed path components, the bi-azimuth pdf induced by (E.4) via the mapping (E.1) should be close to the truncated pdf of a 2-D Gaussian distribution:

$$f_G(\phi_1, \phi_2) \propto \exp\left\{-\frac{1}{2(1-\rho^2)} \cdot \left[\left(\frac{\phi_1 - \bar{\phi}_1}{\sigma_1}\right)^2 \right. \right.$$
$$\left. \left. + \left(\frac{\phi_2 - \bar{\phi}_2}{\sigma_2}\right)^2 - \frac{2\rho(\phi_1 - \bar{\phi}_1)(\phi_2 - \bar{\phi}_2)}{\sigma_1 \sigma_2}\right]\right\}. \quad (\text{E.5})$$

Notice that the traditional meaning of the parameters σ_1, σ_2 and ρ as second-order central moments of a bivariate Gaussian distribution does not hold any more for the pdf (E.5) due to the fact that the azimuth ranges are bounded.

In the case where the path components are slightly dispersive, the approximation in (E.3) is valid for both AoA and AoD. In addition, the approximation

$$(\phi_1 - \bar{\phi}_1)(\phi_2 - \bar{\phi}_2) \approx (\boldsymbol{\Omega}_1 - \bar{\boldsymbol{\Omega}}_1)^T \mathbf{R}(\boldsymbol{\Omega}_2 - \bar{\boldsymbol{\Omega}}_2) \qquad (\text{E.6})$$

holds where

$$\mathbf{R} \doteq \mathbf{B}(\bar{\phi}_1)\mathbf{B}(\bar{\phi}_2)^{\mathrm{T}} = \begin{bmatrix} \cos(\bar{\phi}_1 - \bar{\phi}_2) & -\sin(\bar{\phi}_1 - \bar{\phi}_2) \\ \sin(\bar{\phi}_1 - \bar{\phi}_2) & \cos(\bar{\phi}_1 - \bar{\phi}_2) \end{bmatrix}.$$

The matrix $\mathbf{B}(\bar{\phi})$ is the orthonormal matrix that rotates the vector $\mathbf{e}(\bar{\phi})$ to $[0,1]^{\mathrm{T}}$. Hence, $\mathbf{B}(\bar{\phi}) \doteq [\mathbf{e}^{\perp}(\bar{\phi}) \quad \mathbf{e}(\bar{\phi})]$ with $\mathbf{e}^{\perp}(\bar{\phi}) = \mathbf{e}(\bar{\phi} + \pi/2)$ denoting the unit vector portside orthogonal to $\mathbf{e}(\bar{\phi})$. The right-hand-side of (E.6) is rotational invariant, i.e. it does not change when for any specific index $i \in \{1, 2\}$, $\mathbf{\Omega}_i$, $\bar{\mathbf{\Omega}}_i$ and $\mathbf{e}(\bar{\phi}_i)$ are rotated by an identical arbitrary azimuth.

Inserting (E.3) and (E.6) into (E.5) and identifying (E.4) and (E.5), we obtain after some straightforward algebraic manipulations

$$\mathbf{a}_i \approx \frac{\kappa_i}{1 - \rho^2}\Big(1 - \rho\sqrt{\frac{\kappa_j}{\kappa_i}}\Big)\bar{\mathbf{\Omega}}_i, \quad i, j \in \{1, 2\}, \ i \neq j$$

$$\mathbf{A} \approx \frac{\rho\sqrt{\kappa_1\kappa_2}}{1 - \rho^2}\mathbf{R}$$

with the definitions $\kappa_i \doteq \sigma_i^{-2}$, $i = 1, 2$. Inserting the right-hand-sides in (E.4) yields the sought pdf:

$$f(\mathbf{\Omega}_1, \mathbf{\Omega}_2) = C \cdot \exp\Big\{ \frac{\kappa_1 - \rho\sqrt{\kappa_1\kappa_2}}{1 - \rho^2}\bar{\mathbf{\Omega}}_1^{\mathrm{T}}\mathbf{\Omega}_1 +$$

$$\frac{\kappa_2 - \rho\sqrt{\kappa_1\kappa_2}}{1 - \rho^2}\bar{\mathbf{\Omega}}_2^{\mathrm{T}}\mathbf{\Omega}_2 + \frac{\rho\sqrt{\kappa_1\kappa_2}}{1 - \rho^2}\mathbf{\Omega}_1^{\mathrm{T}}\mathbf{R}\mathbf{\Omega}_2 \Big\}. \quad (\text{E.7})$$

The normalization constant C can be computed from the expression derived in [10, P. 167] for the general form (E.7):

$$C = \Big[4\pi^2 \sum_{m=0}^{\infty} m \cdot I_m\Big(\frac{\kappa_1 - \rho\sqrt{\kappa_1\kappa_2}}{1 - \rho^2}\Big) \cdot I_m\Big(\frac{\rho\sqrt{\kappa_1\kappa_2}}{1 - \rho^2}\Big) I_m\Big(\frac{\kappa_2 - \rho\sqrt{\kappa_1\kappa_2}}{1 - \rho^2}\Big) \Big]^{-1}.$$

From (E.7) the joint pdf of ϕ_1 and ϕ_2 is calculated to be

$$f(\phi_1, \phi_2) = C \cdot \exp\Big\{ \Big(\frac{\kappa_1 - \rho\sqrt{\kappa_1\kappa_2}}{1 - \rho^2}\Big)\cos(\phi_1 - \bar{\phi}_1)$$

$$+ \Big(\frac{\kappa_2 - \rho\sqrt{\kappa_1\kappa_2}}{1 - \rho^2}\Big)\cos(\phi_2 - \bar{\phi}_2)$$

$$+ \frac{\rho\sqrt{\kappa_1\kappa_2}}{1 - \rho^2}\cos[(\phi_1 - \bar{\phi}_1) - (\phi_2 - \bar{\phi}_2)] \Big\}. \quad (\text{E.8})$$
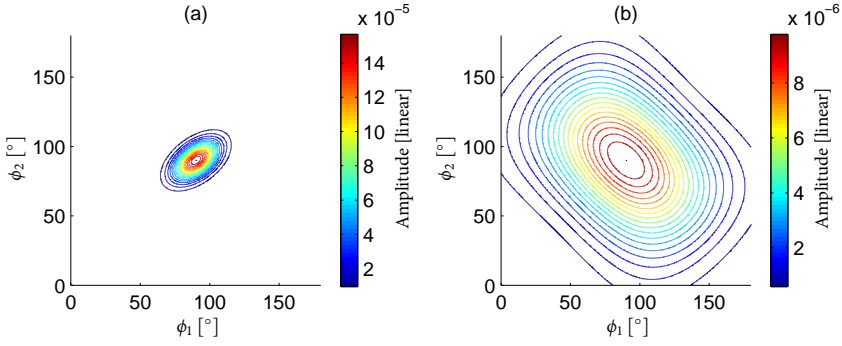
Fig. E.2: *Contour plots of the bi-azimuth pdf (E.8) with parameter settings $\bar{\phi}_1 = \bar{\phi}_2 = 90°$ and (a) $(\kappa_1, \kappa_2, \rho) = (30, 40, 0.5)$, (b) $(\kappa_1, \kappa_2, \rho) = (2, 2, -0.5)$.*

Fig. E.2 illustrates the contour plots of (E.8) for two different settings of the parameters κ_1, κ_2 and ρ. It can be observed that when κ_1 and κ_2 are large, the contour lines are close to tilted ellipses. This is consistent with the fact that the pdf (E.8) is close to a bivariate normal pdf in this case. When both κ_1 and κ_2 are small, the contour lines are still close to ellipses in a range enclosing $(\bar{\phi}_1, \bar{\phi}_2)$. This observation indicates that in this region the pdf (E.8) can be approximated by a bivariate normal pdf as well.

E.3 Signal Model for Bi-azimuth Dispersion by Path Components in MIMO Channel Sounding

We consider horizontal-only propagation and narrow-band transmission. The latter condition implies that the product of the signal bandwidth times the channel delay spread is much smaller than one. Following the nomenclature in [8], the continuous-time output signal of the Rx array reads

$$\mathbf{Y}(t) = \mathbf{H}(t)\mathbf{s}(t) + \mathbf{W}(t)$$
$$= \left[\iint \mathbf{c}_2(\phi_2)\mathbf{c}_1(\phi_1)^{\mathrm{T}} h(t; \phi_1, \phi_2) \mathrm{d}\phi_1 \mathrm{d}\phi_2 \right] \mathbf{s}(t) + \mathbf{W}(t). \qquad (E.9)$$

The M_2-D complex vector $\mathbf{Y}(t) \in \mathbb{C}^{M_2 \times 1}$ contains the output signals of the Rx array observed at time instance t. The matrix $\mathbf{H}(t) \in \mathbb{C}^{M_2 \times M_1}$ represents the time-variant transfer matrix of the MIMO system. The M_1-D vector $\mathbf{s}(t) \in \mathbb{C}^{M_1 \times 1}$ denotes the complex envelope of the transmitted signal. The function $h(t; \phi_1, \phi_2)$ is referred to as the (time-variant) bi-azimuth spread function of the propagation channel [8]. In a scenario where the electromagnetic energy

144

propagates from the Tx to the Rx via D paths, $h(t; \phi_1, \phi_2)$ can be decomposed
as

$$h(t; \phi_1, \phi_2) = \sum_{d=1}^{D} h_d(t; \phi_1, \phi_2). \qquad (E.10)$$

The summand $h_d(t; \phi_1, \phi_2)$ denotes the dth path component in $h(t; \phi_1, \phi_2)$.
The noise component $\mathbf{W}(t) \in \mathbb{C}^{M_2 \times 1}$ in (E.9) is a vector-valued circularly
symmetric, spatially and temporally white Gaussian process with component
spectral height σ_w^2. Finally, the complex vectors

$$\mathbf{c}_i(\phi) \doteq [c_{i,1}(\phi), \dots, c_{i,m_i}(\phi), \dots, c_{i,M_i}(\phi)]^{\mathsf{T}} \in \mathbb{C}^{M_i \times 1}, \quad i = 1, 2$$

are the responses of the Tx array ($i = 1$) and the Rx array ($i = 2$).

Moreover, we make the following assumptions regarding the properties
of some components in (E.9):

a. The channel is sounded during N non-overlapping intervals of dura-
tion T. Thus, the overall sounding period is of the form $\bigcup_{n=1}^{N}[t_n, t_n + T]$
where t_n denotes the beginning of the nth interval and $t_{n+1} > t_n + T$,
$n = 1, \dots, N$.

b. The sounding signal $\mathbf{s}(t)$ is known to the Rx. Its components are or-
thonormal[1], i.e.

$$\int_{t_n}^{t_n + T} \mathbf{s}(t)\mathbf{s}(t)^{\mathsf{H}} dt = \mathbf{I}_{M_1}, \quad n \in [1, \dots, N]$$

. Here, $\mathbf{I}_{(\cdot)}$ denotes an identity matrix of dimension given as an index.

c. The transfer matrix $\mathbf{H}(t)$ fluctuates over the overall sounding period,
but it is constant within individual observation intervals:

$$\mathbf{H}(t) = \mathbf{H}(t_n) \doteq \mathbf{H}_n, \quad t \in [t_n, t_n + T).$$

Similarly, the bi-azimuth spread function $h_d(t; \phi_1, \phi_2)$ arising in (E.10)
is constant within individual observation intervals:

$$h_d(t; \phi_1, \phi_2) = h_d(t_n; \phi_1, \phi_2) \doteq h_{d,n}(\phi_1, \phi_2), \quad t \in [t_n, t_n + T).$$

The processes $h_{d,n}(\phi_1, \phi_2), n \in [1, \dots, N], d \in [1, \dots, D]$ are uncor-
related complex (zero-mean) orthogonal stochastic measures, i.e.

$$\mathrm{E}[h_{d,n}^*(\phi_1, \phi_2) h_{d',n'}(\phi_1', \phi_2')] =$$
$$P_d(\phi_1, \phi_2)\delta_{nn'}\delta_{dd'}\delta(\phi_1 - \phi_1')\delta(\phi_2 - \phi_2'), \quad (E.11)$$

---

[1]The orthogonality of the signal components can be obtained by using different sounding
techniques, such as time-division [11] and frequency-division multiplexing. It can be also
nearly achieved by using different pseudo-noise (PN) sequences or differently-shifted versions
of the same PN sequence as the components of the sounding signal $\mathbf{s}(t)$.

where $(\cdot)^*$ denotes the complex conjugate, $\delta_{(\cdot)}$ and $\delta(\cdot)$ represent the
Kronecker delta and the Dirac delta function respectively, and $P_d(\phi_1,
\phi_2) \doteq \mathrm{E}[|h_{d,n}(\phi_1, \phi_2)|^2]$ is the bi-azimuth power spectrum of the dth
path component. Thus, identity (E.11) implies that the spread functions
of different individual path components or at different observation
intervals are uncorrelated. This scenario is referred to as the *incoherent-
distributed-source* case in the literature (see e.g. [12]).

d. The spectrum $P_d(\phi_1, \phi_2)$ describes the manner the average power of
the dth path component is distributed with respect to both AoD and
AoA. We assume $P_d(\phi_1, \phi_2) = P_d \cdot f_d(\phi_1, \phi_2)$ with P_d representing the
total average power of the dth path component and $f_d(\phi_1, \phi_2)$ being of
the form (E.8) with path-specific parameters

$$\boldsymbol{\theta}_d \doteq [\bar{\phi}_{d,1}, \bar{\phi}_{d,2}, \kappa_{d,1}, \kappa_{d,2}, \rho_d].$$

E.4   Maximum Likelihood Estimation

Let $\boldsymbol{\theta}$ denote a vector containing the model parameters in (E.9)

$$\boldsymbol{\theta} \doteq [\sigma_w^2, P_1, P_2, \ldots, P_D, \boldsymbol{\theta}_1, \boldsymbol{\theta}_2, \ldots, \boldsymbol{\theta}_D].$$

Under the assumption that the components of $\mathbf{s}(t)$ are orthonormal, the $M_2 \times
M_1$ matrices

$$\widehat{\mathbf{H}}_n \doteq \int_{t_n}^{t_n+T} \mathbf{y}(t)\mathbf{s}(t)^{\mathrm{H}}\mathrm{d}t, \quad n = 1, \ldots, N \tag{E.12}$$

form a sufficient statistic for the estimation of $\boldsymbol{\theta}$. It can be shown that $\widehat{\mathbf{H}}_n = \mathbf{H} +
\mathbf{N}_n$ where $\mathbf{N}_n \in \mathbb{C}^{M_2 \times M_1}$, $n = 1, \ldots, N$ is a sequence of independent random
matrices the entries of which are independent circularly symmetric Gaussian
random variables with variance σ_w^2.

The maximum likelihood estimate of $\boldsymbol{\theta}$ based on the observation $\mathbf{Y}(t) =
\mathbf{y}(t)$ during the sounding interval $\bigcup_{n=1}^{N}[t_n, t_n + T)$ is a solution of [2]:

$$\hat{\boldsymbol{\theta}} \doteq \arg\max_{\boldsymbol{\theta}}\{-\ln[|\boldsymbol{\Sigma}|] - \mathrm{tr}[(\boldsymbol{\Sigma})^{-1}\hat{\boldsymbol{\Sigma}}]\} \tag{E.13}$$

with $\mathrm{tr}[\cdot]$ representing the trace of the matrix given as an argument and

$$\boldsymbol{\Sigma} \doteq \mathrm{E}[\mathrm{vec}[\widehat{\mathbf{H}}_n] \cdot \mathrm{vec}[\widehat{\mathbf{H}}_n]^{\mathrm{H}}]$$
$$= \sum_{d=1}^{D} P_d \iint [\mathbf{c}_1(\phi_1)\mathbf{c}_1^{\mathrm{H}}(\phi_1)] \otimes [\mathbf{c}_2(\phi_2)\mathbf{c}_2^{\mathrm{H}}(\phi_2)] f_d(\phi_1, \phi_2)\mathrm{d}\phi_1\mathrm{d}\phi_2 + \sigma_w^2\mathbf{I}_{M_2 M_1},$$
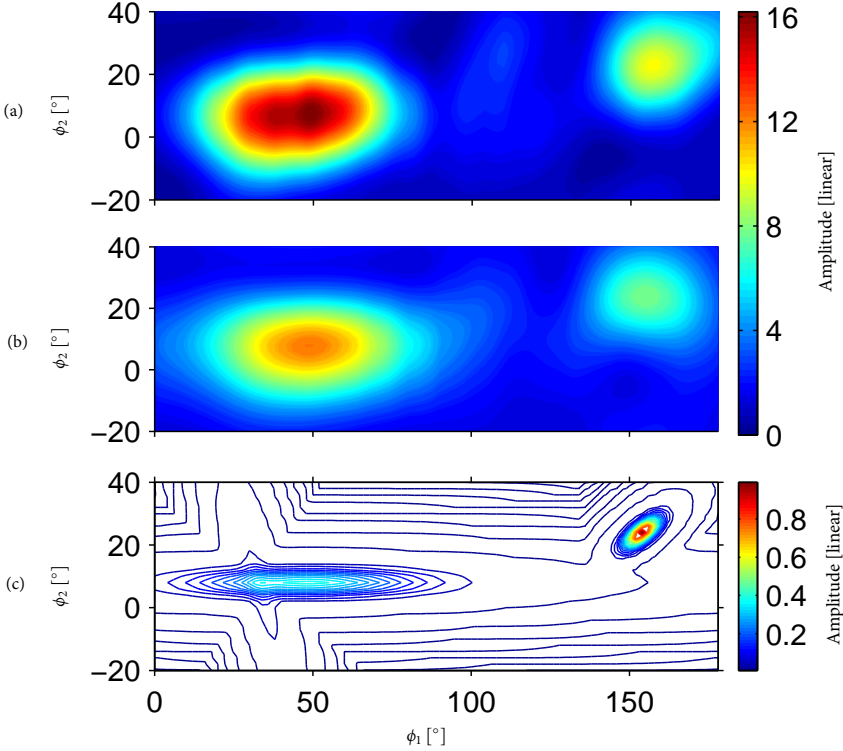$$\tag{E.14}$$

Fig. E.3: (a): Bi-azimuth Bartlett spectrum calculated from the received signal as is; (b): Bi-azimuth Bartlett spectrum calculated from the matrix $\boldsymbol{\Sigma}$ in (E.14) parameterized with the estimate $\hat{\boldsymbol{\theta}}$; (c): Contour lines of the estimated bi-azimuth power spectrum using the proposed characterization by means of the von-Mises-Fisher pdf (E.8).

where the operator vec[·] stacks the columns of the given matrix into a vector and ⊗ denotes the Kronecker product. In (E.13) the matrix

$$\hat{\boldsymbol{\Sigma}} = \frac{1}{N} \sum_{n=1}^{N} \text{vec}[\widehat{\mathbf{H}}_n]\text{vec}[\widehat{\mathbf{H}}_n]^{\text{H}}$$

is an estimate of $\boldsymbol{\Sigma}$ computed from the observation $\mathbf{y}(t)$ over $\bigcup_{n=1}^{N}[t_n, t_n + T)$.

Calculation of $\hat{\boldsymbol{\theta}}$ requires $(5D+1)$-D maximization operations. The SAGE algorithm described in [13] can be used to compute a low-complexity approximation of the maximum likelihood estimator in (E.13).

E.5 Preliminary Experimental Investigation

In this section, we assess the applicability of the characterization by means of the von-Mises-Fisher pdf (E.8) in a real environment. The measurement data

were obtained with the MIMO wideband radio channel sounder Elektrobit Propsound CS [1]. The measurement campaign was conducted in a big hall at a center frequency of 5.2 GHz with bandwidth 100 MHz. The Tx and Rx were both equipped with two similar 9-element circular arrays. The polarization direction of the elements is 45° slanted with respect to the vertical. The positions of the Rx and Tx were kept fixed. The hall was crowded with people moving around during the measurement runs. This introduced time variations of the channel response. The equipment collects wideband measurement data. However, the narrowband model developed in Sect. E.3 can still be applied by considering the correlator output of the channel sounder at some specific relative delay.

We specifically selected a propagation scenario and for that scenario, a relative delay at which only few path components can be observed. The Bartlett spectrum shown in Fig. E.1 (b) corresponds to such a situation with two or, possibly, three path components. Portion of this Bartlett spectrum including the path components is reproduced in Fig. E.3 (a).

The SAGE algorithm is used to estimate the parameters of the path components. In this preliminary study, we assume that the number of path components is known in advance. In the considered case, this number equals 3, which coincides with the amount of the path components that can be visually identified from the Bartlett spectrum shown in Fig. E.1 (b). We consider vertical polarization only, i.e. the vectors $\mathbf{c}_i(\phi)$, $i = 1, 2$ used in the calculation of $\boldsymbol{\Sigma}$ in (E.14) are the array responses for vertical polarization. The initial estimates of the parameters of the individual path components are computed using a combination of the successive interference cancelation method described in [13] and an estimator derived based on the generalized array manifold model [14]. At each iteration of the SAGE algorithm, the parameter estimates of one path component and the estimate of the noise spectral height σ_w^2 are updated. The admissible hidden data is selected to be the sum of the path component, of which the parameters are estimated, and an M_2-D noise vector with statistical properties identical to those of $\mathbf{W}(t)$ weighted by $1/\sqrt{3}$. The definition and meaning of the weighting factor are given in [13].

The obtained parameter estimates are reported in Table E.1. Estimates $\hat{\sigma}_{d,i} = \sqrt{1/\hat{\kappa}_{d,i}}$, $d = 1, 2, 3$, $i = 1, 2$ of the azimuth spreads of the path components expressed in degree are also provided. Fig. E.3 (c) depicts the estimated bi-azimuth power spectrum

$$\hat{P}(\phi_1, \phi_2) = \sum_{d=1}^{3} \hat{P}_d \hat{f}_d(\phi_1, \phi_2), \qquad (E.15)$$

where $\hat{f}_d(\phi_1, \phi_2)$ denotes the pdf $f(\phi_1, \phi_2)$ in (E.8) parameterized with the

Table E.1: *Parameter estimates in the experimental investigation.*

d	$\hat{\hat{\phi}}_{d,1}$	$\hat{\hat{\phi}}_{d,2}$	$\hat{\kappa}_{d,1}$	$\hat{\sigma}_{d,1}$	$\hat{\kappa}_{d,2}$	$\hat{\sigma}_{d,2}$	$\hat{\rho}_d$	$\hat{P}_d/\widehat{\sigma_w^2}$
1	48°	8°	6.29	22.9°	480	2.6°	0.02	15.5 dB
2	34°	4°	153.75	4.6°	18.36	13.4°	−0.83	4.69 dB
3	154°	24°	233.02	3.8°	320	3.2°	0.70	11.1 dB

estimate $\hat{\boldsymbol{\theta}}_d$. From Fig. E.3 (c), we observe that the path components are significantly more concentrated than the corresponding components in the Bartlett spectrum shown in Fig. E.3 (a). Moreover, the third path component in Fig. E.3 (c) appears to be stronger than the first component even though $\hat{P}_3 < \hat{P}_1$. This is because the power spectrum of the third path component is more concentrated than the spectrum of the first component.

Fig. E.3 (b) depicts the Bartlett spectrum calculated from the reconstructed signal with the bi-azimuth power spectrum (E.15). Notice that the spectral height estimate $\widehat{\sigma_w^2}$ is also considered in the calculation. The blurring effect due to the limited resolution in azimuth of the used arrays is clearly demonstrated. As a result, the path components in the Bartlett spectrum exhibit significantly larger spreads compared to the spreads of the estimated components. Notice that the Bartlett spectrum shown in Fig. E.3 (b) looks similar to the spectrum in Fig. E.3 (a). Furthermore, it is observed that the magnitude of the path components depicted in Fig. E.3 (b) is lower than that observed in Fig. E.3 (a). This is consistent with an analytical result not reported here, which shows that the power estimate of a path component is reduced, compared to the true value, by a certain amount depending on the residual interference. This interference results since the path components are not estimated exactly due to either model mismatch or errors in the parameter estimation.

Calculations show that the ratio of the maximum of the Bartlett spectrum computed from the reconstructed signal with $\widehat{\sigma_w^2} = 0$ to the maximum of the Bartlett spectrum calculated from the received signal, is equal to 68.7%. Experimental investigations also show that this number reduces to 37.7% when the ISIS algorithm [11] derived based on the specular-scatterer model is applied to the same measurement data. This observation, together with the conclusions drawn from Fig. E.3, demonstrate that the von-Mises-Fisher pdf (E.8) provides an appropriate characterization of bi-azimuth dispersion by individual path components.

E.6   Conclusions

In this contribution, we proposed a bi-variate generalized von-Mises-Fisher probability density function (pdf) suitable for characterizing bi-azimuth (azimuth of arrival and azimuth of departure) dispersion of individual path components. We also derived an estimator of the parameters of the pdf. Preliminary experimental results demonstrated the applicability of the proposed characterizing method in real situations. These results also made evident that the path components are noticeably more concentrated in the bi-azimuth plane compared to their corresponding footprints in the Bartlett spectrum.

References

[1] E. Bonek, N. Czink, V. M. Holappa, M. Alatossava, L. Hentilä, J. Nuutinen, and A. Pal, "Indoor MIMO measurements at 2.55 and 5.25 GHz - a comparison of temporal and angular characteristics," in *Proceedings of the 15th IST Mobile Summit*, 2006.

[2] H. Krim and M. Viberg, "Two decades of array signal processing research: the parametric approach," *IEEE Trans. Signal Processing*, vol. 13, pp. 67–94, July 1996.

[3] T. Trump and B. Ottersten, "Estimation of nominal direction of arrival and angular spread using an array of sensors," *Signal Processing*, vol. 50, pp. 57–69, Apr. 1996.

[4] O. Besson and P. Stoica, "Decoupled estimation of DoA and angular spread for spatially distributed sources," *IEEE Trans. Signal Processing*, vol. 49, pp. 1872–1882, 1999.

[5] C. B. Ribeiro, E. Ollila, and V. Koivunen, "Stochastic maximum likelihood method for propagation parameter estimation," in *Proceedings of the 15th IEEE International Symposium on Personal, Indoor and Mobile Radio Communications (PIMRC)*, vol. 3, Sept. 5-8 2004, pp. 1839 – 1843.

[6] K. V. Mardia, "Statistics of directional data," *Journal of the Royal Statistical Society. Series B (Methodological)*, vol. 37, pp. 349–393, 1975.

[7] M. Bengtsson and B. Ottersten, "Low-complexity estimators for distributed sources," *IEEE Trans. Signal Processing*, vol. 48, no. 8, pp. 2185–2194, Aug. 2000.

[8] B. H. Fleury, "First- and second-order characterization of direction dispersion and space selectivity in the radio channel," *IEEE Trans. Information Theory*, no. 6, pp. 2027–2044, Sept. 2000.

[9] K. V. Mardia and P. E. Jupp, *Directional Statistics*.   John Wiley and Sons, Ltd., 2000.

[10] P. E. Jupp and K. V. Mardia, "A general correlation coefficient for directional data and related regression problems," *Biometrika*, vol. 67, pp. 163–173, 1980.

[11] B. H. Fleury, P. Jourdan, and A. Stucki, "High-resolution channel parameter estimation for MIMO applications using the SAGE algorithm," in *Proceedings of International Zurich Seminar on Broadband Communications*, vol. 30, Zurich, Switzerland, Feb. 2002, pp. 1–9.

[12] S. Shahbazpanahi, S. Valaee, and M. Bastani, "Distributed source localization using ESPRIT algorithm," *IEEE Transactions on Signal Processing*, vol. 49, no. 10, pp. 2169–2178, 2001.

[13] B. H. Fleury, M. Tschudin, R. Heddergott, D. Dahlhaus, and K. L. Pedersen, "Channel parameter estimation in mobile radio environments using the SAGE algorithm," *IEEE Journal on Selected Areas in Communications*, vol. 17, no. 3, pp. 434–450, Mar. 1999.

[14] D. Asztély, B. Ottersten, and A. L. Swindlehurst, "A generalized array manifold model for local scattering in wireless communications," in *Proceedings of IEEE International Conference on Acoustics, Speech and Signal Processing (ICASSP)*, 1997.

Parametric Characterization and Estimation of Bi-Azimuth and Delay Dispersion of Individual Path Components

Xuefeng Yin, Troels Pedersen, Nicolai Czink, and Bernard H. Fleury

153

Abstract

In this contribution, we derive a distribution that is suitable for characterizing biazimuth (azimuth of arrival and azimuth of departure) and delay dispersion of individual path components in the response of the radio channel. This distribution maximizes the entropy under the constraint that its first and second moments are specified. We propose to use the density function of the derived distribution to characterize the shape of the biazimuth-delay power spectrum of individual path components. The applicability of this characterization in real conditions is assessed using measurement data.

F.1 Introduction

Due to the heterogeneity of the propagation environment, the response of the radio channel is the superposition of a certain number of components. Each component, which we call a "path component", is contributed by an electromagnetic wave propagating along a path from the transmitter (Tx) to the receiver (Rx). Along this path, the wave interacts with a certain number of objects called scatterers. Due to the geometrical and electromagnetic properties of the scatterers, a propagation path may be dispersive in delay, direction of departure, direction of arrival, polarizations, as well as in Doppler frequency when the environment is time-variant. As a consequence, an individual path component may be spread or dispersed in these dispersion dimensions.

Recently, estimation of dispersive characteristics of individual path components has gained much attention. Conventional methods rely on estimation of the channel response and any characterizing functions derived from this response. An example of a characterizing function is the power spectrum. A traditional estimate of the power spectrum is the Bartlett spectrum, i.e. the spectrum calculated using the Bartlett beamformer [1]. However, due to the ambiguity function of the measurement equipment, the path components in the Bartlett spectrum are blurred and consequently, their spreads are artificially increased. In recent years, several methods based on parametric models have been proposed to estimate the nominal azimuth and azimuth spread of path components at one side of the link [2], [3], [4]. These estimators make use of the assumption that the azimuth power spectrum of individual path components exhibits a shape close to the density function of a distribution, like the uniform distribution within a certain interval [3], the (truncated) Gaussian distribution [2], [3] and the von-Mises distribution [4].

Recently, the density function of a bivariate von-Mises-Fisher distribution has been proposed to characterize the shape of the biazimuth (azimuth of departure (AoD) and azimuth of arrival (AoA)) power spectrum of individ-

ual path components [5]. The von-Mises-Fisher distribution maximizes the entropy under the constraint that its first and second moments are specified. In [5], the proposed characterization method is assessed in real conditions using measurement data.

In this contribution, we derive an entropy-maximizing distribution suitable for characterizing biazimuth-delay dispersion of individual path components. More specifically, the density function of this distribution is used to characterize the shape of the biazimuth-delay power spectrum of individual path components. The density function is parameterized by some free parameters. To identify these parameters, we postulate that in the case where a path component is slightly dispersed, the proposed density function is close to a truncated multivariate Gaussian density function. Experimental investigations assess the applicability of the proposed characterization in real situations.

The organization of this contribution is as follows. In Section F.2, we derive the entropy-maximizing biazimuth-delay density function. In Section F.3, the signal model is presented. Section F.4 shows the results and discussions of the experimental investigations. Finally concluding remarks are stated in Section F.5.

F.2   Entropy-Maximizing Biazimuth-Delay Density Function

Following the nomenclature in [6], we use a unit vector $\boldsymbol{\Omega}$ to characterize a direction. This vector has its initial point anchored at the origin O of a coordinate system specified in the region surrounding the array of interest, and terminal point located on a unit sphere $\mathbb{S}_2$ centered at O. In the case of horizontal-only propagation, the terminal point of $\boldsymbol{\Omega}$ is located on a unit circle $\mathbb{S}_1$. The one-to-one relation between $\boldsymbol{\Omega}$ and the azimuth ϕ is in this case

$$\boldsymbol{\Omega} = \mathbf{e}(\phi) \doteq \left[\cos(\phi), \sin(\phi)\right]^{\mathsf{T}} \tag{F.1}$$

with $[\cdot]^{\mathsf{T}}$ denoting transposition.

Among all distributions on $\mathbb{S}_1$, the von-Mises distribution maximizes the entropy provided the first moment

$$\boldsymbol{\mu_\Omega} \doteq \int \boldsymbol{\Omega} f(\boldsymbol{\Omega}) \mathrm{d}\boldsymbol{\Omega}$$

is specified [6], [7]. Here, $f(\boldsymbol{\Omega})$ denotes the density function of any distribution on $\mathbb{S}_1$. Notice that $\int f(\boldsymbol{\Omega}) \mathrm{d}\boldsymbol{\Omega} = 1$. The density function of the von-Mises distribution is given by [8, P. 36]

$$f(\boldsymbol{\Omega}) = \frac{1}{2\pi I_0(\kappa)} \exp\{\kappa \bar{\boldsymbol{\Omega}}^{\mathsf{T}} \boldsymbol{\Omega}\} \tag{F.2}$$

with $I_0(\cdot)$ denoting the modified Bessel function of the first kind and order 0, $\kappa \geq 0$ being the concentration parameter, and $\bar{\boldsymbol{\Omega}} \in \mathbb{S}_1$. For $\kappa > 0$, $\bar{\boldsymbol{\Omega}}$ is the mode of $f(\boldsymbol{\Omega})$ and $\bar{\boldsymbol{\Omega}} = \|\boldsymbol{\mu}_{\boldsymbol{\Omega}}\|^{-1}\boldsymbol{\mu}_{\boldsymbol{\Omega}}$ holds. Here, $\|\cdot\|$ denotes the Euclidean norm. It is shown in [6] that the root second central moment of a distribution on $\mathbb{S}_1$, i.e. the direction spread $\sigma_{\boldsymbol{\Omega}}$, is uniquely determined by the norm of the first moment: $\sigma_{\boldsymbol{\Omega}} = \sqrt{1 - \|\boldsymbol{\mu}_{\boldsymbol{\Omega}}\|^2}$. It follows from this result that the von-Mises distribution also maximizes the entropy under the constraint that the mode, provided that it exists, and the direction spread are specified. In [9], the von-Mises density function has been used to characterize the shape of the azimuth power spectrum of individual path components.

Among all distributions on $\mathbb{S}_1 \times \mathbb{S}_1$, the generalized von-Mises-Fisher distribution [7] maximizes the entropy under the constraints that the first moments

$$\boldsymbol{\mu}_{\boldsymbol{\Omega}_i} \doteq \int \boldsymbol{\Omega}_i f(\boldsymbol{\Omega}_1, \boldsymbol{\Omega}_2) \mathrm{d}\boldsymbol{\Omega}_1 \mathrm{d}\boldsymbol{\Omega}_2, \quad i = 1, 2 \tag{F.3}$$

and second moments in the matrix

$$\boldsymbol{\Sigma}_{\boldsymbol{\Omega}_1\boldsymbol{\Omega}_2} \doteq \int \boldsymbol{\Omega}_1 \boldsymbol{\Omega}_2^{\mathsf{T}} f(\boldsymbol{\Omega}_1, \boldsymbol{\Omega}_2) \mathrm{d}\boldsymbol{\Omega}_1 \mathrm{d}\boldsymbol{\Omega}_2 \tag{F.4}$$

are specified. In (F.3) and (F.4), $f(\boldsymbol{\Omega}_1, \boldsymbol{\Omega}_2)$ is the density function of any distribution on $\mathbb{S}_1 \times \mathbb{S}_1$. The density function of the generalized von-Mises-Fisher distribution is of the form [7]

$$f(\boldsymbol{\Omega}_1, \boldsymbol{\Omega}_2) = C \cdot \exp\{\mathbf{a}_1^{\mathsf{T}}\boldsymbol{\Omega}_1 + \mathbf{a}_2^{\mathsf{T}}\boldsymbol{\Omega}_2 + \boldsymbol{\Omega}_1^{\mathsf{T}}\mathbf{A}\boldsymbol{\Omega}_2\}, \tag{F.5}$$

where C denotes a normalization constant, while $\mathbf{a}_1$, $\mathbf{a}_2 \in \mathbb{R}^{2 \times 1}$ and $\mathbf{A} \in \mathbb{R}^{2 \times 2}$ are free parameters. This density function has been proposed in [5] to characterize the shape of the biazimuth power spectrum of individual path components. In this case, $\boldsymbol{\Omega}_1, \boldsymbol{\Omega}_2$ are written to be $\boldsymbol{\Omega}_i = \mathbf{e}(\phi_i)$, $i = 1, 2$ with ϕ_1 and ϕ_2 denoting the AoD and AoA respectively. The expressions of the free parameters $\mathbf{a}_1$, $\mathbf{a}_2$ and $\mathbf{A}$ are identified in [5]. Experimental investigations reported in this reference showed that this density function can be used to characterize the shape of the biazimuth power spectrum of individual path components.

Following the same approach as used in [5], we derive in the sequel a distribution suitable to describe dispersion of individual path components in $\boldsymbol{\Omega}_1$, $\boldsymbol{\Omega}_2$ and propagation delay τ. More specifically, the density function of the sought distribution characterizes the shape of the biazimuth-delay power spectrum of individual path components.

We define the parameter vector $\boldsymbol{\psi} \doteq [\boldsymbol{\Omega}_1^{\mathsf{T}}, \boldsymbol{\Omega}_2^{\mathsf{T}}, \tau]^{\mathsf{T}}$. The density function $f(\boldsymbol{\psi})$ of the distribution maximizing the entropy with its first moment

$$\boldsymbol{\mu}_{\boldsymbol{\psi}} \doteq \int \boldsymbol{\psi} f(\boldsymbol{\psi}) \mathrm{d}\boldsymbol{\psi}$$

and second moments in the matrix

$$\mathbf{\Sigma}_\psi \doteq \int \psi\psi^\mathsf{T} f(\psi)\mathrm{d}\psi$$

specified, is of the form [7]

$$f(\psi) \propto \exp\{\mathbf{b}^\mathsf{T}\psi + \psi^\mathsf{T}\mathbf{B}\psi\}, \tag{F.6}$$

where $\mathbf{b} \in \mathbb{R}^{5\times1}$ and $\mathbf{B} \in \mathbb{R}^{5\times5}$ are free parameters.

The biazimuth-delay distribution induced by the above entropy-maximizing distribution via the mapping $[\phi_1, \phi_2, \tau] \mapsto [\mathbf{e}(\phi_1)^\mathsf{T}, \mathbf{e}(\phi_2)^\mathsf{T}, \tau]$ has density function

$$f(\phi_1, \phi_2, \tau) = f(\psi)|_{\psi=[\mathbf{e}(\phi_1)^\mathsf{T}, \mathbf{e}(\phi_2)^\mathsf{T}, \tau]^\mathsf{T}}. \tag{F.7}$$

To identify the expressions of the vector $\mathbf{b}$ and the matrix $\mathbf{B}$, we assume that in the case where dispersion of individual path components is small, the density function in (F.7) is close to a truncated multivariate Gaussian density function. Define the parameter vector $\boldsymbol{\omega} \doteq [\phi_1, \phi_2, \tau]^\mathsf{T}$. The truncated Gaussian density function is of the form

$$f_\mathrm{G}(\boldsymbol{\omega}) \propto \frac{1}{\det(\mathbf{\Sigma}_{\boldsymbol{\omega}})^{1/2}} \exp\{-\frac{1}{2}(\boldsymbol{\omega} - \boldsymbol{\mu}_{\boldsymbol{\omega}})^\mathsf{T}\mathbf{\Sigma}_{\boldsymbol{\omega}}^{-1}(\boldsymbol{\omega} - \boldsymbol{\mu}_{\boldsymbol{\omega}})\}, \tag{F.8}$$

with $\boldsymbol{\mu}_{\boldsymbol{\omega}} \doteq [\bar\phi_1, \bar\phi_2, \bar\tau]^\mathsf{T}$ denoting the mode of $f_\mathrm{G}(\boldsymbol{\omega})$ and

$$\mathbf{\Sigma}_{\boldsymbol{\omega}} \doteq \begin{bmatrix} \sigma_{\phi_1}^2 & \rho_{\phi_1\phi_2}\sigma_{\phi_1}\sigma_{\phi_2} & \rho_{\phi_1\tau}\sigma_{\phi_1}\sigma_\tau \\ \rho_{\phi_1\phi_2}\sigma_{\phi_1}\sigma_{\phi_2} & \sigma_{\phi_2}^2 & \rho_{\phi_2\tau}\sigma_{\phi_2}\sigma_\tau \\ \rho_{\phi_1\tau}\sigma_{\phi_1}\sigma_\tau & \rho_{\phi_2\tau}\sigma_{\phi_2}\sigma_\tau & \sigma_\tau^2 \end{bmatrix}. \tag{F.9}$$

Notice that strictly speaking, the traditional meaning of σ_{ϕ_1}, σ_{ϕ_2}, $\rho_{\phi_1\phi_2}$, $\rho_{\phi_1\tau}$ and $\rho_{\phi_2\tau}$ as second-order central moments of a 3-variate Gaussian distribution does not apply anymore to (F.8), due to the fact that the azimuth ranges are bounded. However, these parameters provide good approximations of these moments when σ_{ϕ_1}, σ_{ϕ_2} are small. For notational convenience, we use ρ_1, ρ_2 and ρ_{12} to denote $\rho_{\phi_1\tau}$, $\rho_{\phi_2\tau}$ and $\rho_{\phi_1\phi_2}$ respectively.

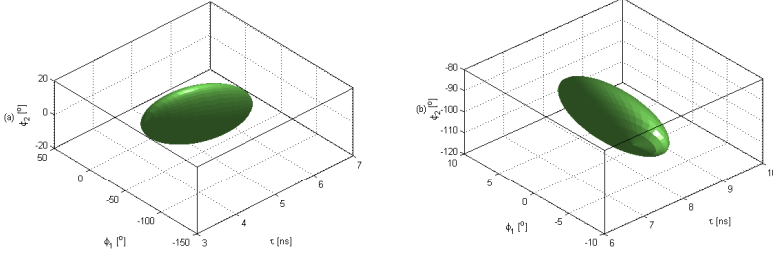In the case where dispersion of a path component is sufficiently small, the following approximations hold:

$$(\phi_1 - \bar\phi_1)(\phi_2 - \bar\phi_2) \approx [\mathbf{e}(\phi_1) - \mathbf{e}(\bar\phi_1)]^\mathsf{T}\mathbf{R}[\mathbf{e}(\phi_2) - \mathbf{e}(\bar\phi_2)] \tag{F.10}$$

$$(\phi_i - \bar\phi_i)(\tau - \bar\tau) \approx [\mathbf{e}(\phi_i) - \mathbf{e}(\bar\phi_i)]^\mathsf{T}\mathbf{e}(\bar\phi_i + \pi/2)(\tau - \bar\tau) \tag{F.11}$$

$$(\phi_i - \bar\phi_i)^2 \approx \|\mathbf{e}(\phi_i) - \mathbf{e}(\bar\phi_i)\|^2 \tag{F.12}$$

with $i \in \{1, 2\}$ and

$$\mathbf{R} \doteq \begin{bmatrix} \cos(\bar\phi_1 - \bar\phi_2) & -\sin(\bar\phi_1 - \bar\phi_2) \\ \sin(\bar\phi_1 - \bar\phi_2) & \cos(\bar\phi_1 - \bar\phi_2) \end{bmatrix}.$$

	$\bar{\tau}[\text{ns}]$	$\bar{\phi}_1[°]$	$\bar{\phi}_2[°]$	$\sigma_\tau[\text{ns}]$	κ_1	$\sigma_{\phi_1}[°]$	κ_2	$\sigma_{\phi_2}[°]$	ρ_{12}	ρ_1	ρ_2
(a)	5	−40	0	1	5	25.6	10	18.1	−0.4	−0.3	−0.3
(b)	8	0	−100	0.5	50	8.1	30	10.5	−0.5	0.6	−0.2

Fig. F.1: 3 dB-spread surfaces calculated using the density function (F.13) with parameter settings given above.

The motivation for selecting the matrix **R** and the meaning of this matrix are described in [5]. Notice that subtraction of azimuth variables arising in the right-hand side in (F.8) and the left-hand sides in (F.10)–(F.12) is defined in such a way that the resulting angle lies in the range $[-\pi, \pi)$.

Inserting (F.10), (F.11) and (F.12) into (F.8) and identifying (F.7) and (F.8), yields for (F.7)

$$
\begin{aligned}
f(\phi_1, \phi_2, \tau) = D \cdot \exp\{ & \alpha_1 \cos(\phi_1 - \bar{\phi}_1) + \alpha_2 \cos(\phi_2 - \bar{\phi}_2) \\
& + (\tau - \bar{\tau})[\alpha_3 \sin(\phi_1 - \bar{\phi}_1) + \alpha_4 \sin(\phi_2 - \bar{\phi}_2)] \\
& + \alpha_5 (\tau - \bar{\tau})^2 + \alpha_6 \cos[(\phi_1 - \bar{\phi}_1) - (\phi_2 - \bar{\phi}_2)]\}, \quad \text{(F.13)}
\end{aligned}
$$

where D is a normalization factor, while $\alpha_1, \ldots, \alpha_6$ are given by

$$
\alpha_1 = \frac{1}{a}\left[\kappa_1(\rho_2^2 - 1) + \sqrt{\kappa_1\kappa_2}(\rho_{12} - \rho_1\rho_2)\right],
$$

$$
\alpha_2 = \frac{1}{a}\left[\kappa_2(\rho_1^2 - 1) + \sqrt{\kappa_1\kappa_2}(\rho_{12} - \rho_1\rho_2)\right],
$$

$$
\alpha_3 = \sqrt{\kappa_1}(\rho_{12}\rho_2 - \rho_1)/(a\sigma_\tau),
$$

$$
\alpha_4 = \sqrt{\kappa_2}(\rho_{12}\rho_1 - \rho_2)/(a\sigma_\tau),
$$

$$
\alpha_5 = \frac{1}{2a} \cdot \frac{1 - \rho_{12}^2}{\sigma_\tau^2},
$$

$$
\alpha_6 = \frac{\sqrt{\kappa_1\kappa_2}(\rho_1\rho_2 - \rho_{12})}{a}
$$

with $\kappa_i = 1/\sigma_{\phi_i}^2$, $i = 1,2$ denoting the concentration parameters in AoD and AoA respectively and $a = \rho_2^2 + \rho_{12}^2 + \rho_1^2 - 2\rho_{12}\rho_1\rho_2 - 1$.

Fig. F.1 depicts the 3 dB-spread surface

$$\left\{ (\phi_1, \phi_2, \tau) : f(\phi_1, \phi_2, \tau) = \frac{1}{2} f(\bar{\phi}_1, \bar{\phi}_2, \bar{\tau}) \right\} \tag{F.14}$$

computed using the density function (F.13) for the two parameter settings also reported in this figure. We observe that these surfaces are close to ellipsoids when κ_1 and κ_2 are large. This is reasonable as the density function (F.13) is close to the density function of a truncated multivariate Gaussian distribution (F.8) in the case of small dispersion. Notice that the 3 dB-spread surface of the multivariate Gaussian distribution is an ellipsoid.

F.3 Signal Model

We consider the case where the path components are dispersed in biazimuth and delay. Following the nomenclature in [6], the continuous-time (complex baseband representation of the) output signal of the Rx array reads

$$\mathbf{Y}(t) = \int_{-\pi}^{+\pi} \int_{-\pi}^{+\pi} \int_{-\infty}^{+\infty} \mathbf{c}_2(\phi_2)\mathbf{c}_1(\phi_1)^\mathsf{T} \mathbf{s}(t - \tau) h(t; \phi_1, \phi_2, \tau) \, \mathrm{d}\phi_1 \mathrm{d}\phi_2 \mathrm{d}\tau + \mathbf{W}(t). \tag{F.15}$$

In (F.15), $\mathbf{Y}(t) \in \mathbb{C}^{M_2 \times 1}$ contains the output signals of the Rx array elements observed at time instance t, $\mathbf{s}(t) \in \mathbb{C}^{M_1 \times 1}$ denotes the complex baseband representation of the transmitted signal, and the function $h(t; \phi_1, \phi_2, \tau)$ is referred to as the (time-variant) biazimuth-delay spread function of the propagation channel. In a scenario where the electromagnetic energy propagates from the Tx to the Rx via D paths, $h(t; \phi_1, \phi_2, \tau)$ can be decomposed as

$$h(t; \phi_1, \phi_2, \tau) = \sum_{d=1}^{D} h_d(t; \phi_1, \phi_2, \tau). \tag{F.16}$$

The summand $h_d(t; \phi_1, \phi_2, \tau)$ denotes the dth path component. The noise vector $\mathbf{W}(t) \in \mathbb{C}^{M_2 \times 1}$ in (F.15) is a circularly symmetric, spatially and temporally white complex Gaussian process with component spectral height σ_w^2. Finally, $\mathbf{c}_i(\phi) \doteq [c_{i,1}(\phi), \ldots, c_{i,m_i}(\phi), \ldots, c_{i,M_i}(\phi)]^\mathsf{T} \in \mathbb{C}^{M_i \times 1}$, $i = 1,2$ are the responses of the Tx array and the Rx array respectively.

We assume that the biazimuth-delay spread functions $h_d(t; \phi_1, \phi_2, \tau)$, $d \in \{1, \ldots, D\}$ are uncorrelated complex (zero-mean) orthogonal stochastic

measures, i.e.

$$E[h_d(t;\phi_1,\phi_2,\tau)^*h_{d'}(t';\phi_1',\phi_2',\tau')] =$$
$$P_d(\phi_1,\phi_2,\tau)\delta_{dd'}\delta_{tt'}\delta(\phi_1-\phi_1')\delta(\phi_2-\phi_2')\delta(\tau-\tau'), \quad \text{(F.17)}$$

where $(\cdot)^*$ denotes complex conjugate, $\delta_{..}$ and $\delta(\cdot)$ represent the Kronecker delta and Dirac delta function respectively, t and t' are discrete time instants at which the spread function are sampled, and

$$P_d(\phi_1,\phi_2,\tau) \doteq E[|h_d(t;\phi_1,\phi_2,\tau)|^2]$$

is the biazimuth-delay power spectrum of the dth path component. Identity (F.17) implies that the spread functions of different individual path components or at different observation instants are uncorrelated. With the above assumptions, $h(t;\phi_1,\phi_2,\tau)$ is also an uncorrelated complex zero-mean stochastic measure specified by

$$E[h(t;\phi_1,\phi_2,\tau)^*h(t';\phi_1',\phi_2',\tau')] =$$
$$P(\phi_1,\phi_2,\tau)\delta_{tt'}\delta(\phi_1-\phi_1')\delta(\phi_2-\phi_2')\delta(\tau-\tau') \quad \text{(F.18)}$$

with $P(\phi_1,\phi_2,\tau) = \sum_{d=1}^{D} P_d(\phi_1,\phi_2,\tau)$.

The biazimuth-delay spectrum $P_d(\phi_1,\phi_2,\tau)$ describes the manner the average power of the dth path component is distributed with respect to AoD, AoA and delay. We assume that

$$P_d(\phi_1,\phi_2,\tau) = P_d \cdot f(\phi_1,\phi_2,\tau;\boldsymbol{\theta}_d),$$

where P_d represents the total average power of the dth path component and $f(\phi_1,\phi_2,\tau;\boldsymbol{\theta}_d)$ is the density function (F.13) with path-specific parameters

$$\boldsymbol{\theta}_d \doteq [\bar{\phi}_{1,d}, \bar{\phi}_{2,d}, \bar{\tau}_d, \kappa_{1,d}, \kappa_{2,d}, \sigma_{\tau_d}, \rho_{1,d}, \rho_{2,d}, \rho_{12,d}].$$

Clearly, the center of gravity of $P_d(\phi_1,\phi_2,\tau)$ coincides with $(\bar{\phi}_{1,d}, \bar{\phi}_{2,d}, \bar{\tau}_d)$, i.e. the location at which the density function $f(\phi_1,\phi_2,\tau;\boldsymbol{\theta}_d)$ exhibits its maximum. The shape of $P_d(\phi_1,\phi_2,\tau)$ is determined jointly by $\kappa_{1,d}$, $\kappa_{2,d}$, σ_{τ_d}, $\rho_{1,d}$, $\rho_{2,d}$, and $\rho_{12,d}$.

Let $\boldsymbol{\theta}$ denote a vector containing the model parameters in (F.15)

$$\boldsymbol{\theta} \doteq [\sigma_w^2, P_1, P_2, \dots, P_D, \boldsymbol{\theta}_1, \boldsymbol{\theta}_2, \dots, \boldsymbol{\theta}_D].$$

A stochastic maximum likelihood estimator of $\boldsymbol{\theta}$ can be easily derived [10] for the case where the spread functions of the path components are Gaussian. Due

Table F.1: Setting of the measurement equipment.

Carrier frequency	5.25 GHz
Bandwidth	200 MHz
Chip frequency	100 MHz
Code length	255 Chips
Tx array height	1.53 m
Rx array height	0.82 m

to the property expressed in (F.17), the spread functions of distinct path components or at different time instants are independent. The SAGE algorithm [11] can be easily implemented as a low-complexity approximation of the maximum likelihood estimator. Due to the space limitation, the descriptions of the maximum likelihood estimator and the SAGE algorithm are omitted in this paper.

F.4   Experimental Investigations

The measurement data were collected using the MIMO wideband radio channel sounder Elektrobit Propsound CS [12] [13]. The setting of the equipment is reported in Table F.1. The Tx and Rx were both equipped with two identical 50-element dual-polarized omni-directional arrays (See Fig. F.2). The polarization direction of the elements is ±45° slanted with respect to the vertical.

The measurement experiment was conducted in a big hall. During the measurement procedure, the hall was crowded with people moving around. These movements introduced time variations of the channel response. The positions of the Rx and Tx were kept fixed during the measurement procedure. Fig. F.3 (a) and Fig. F.3 (b) show a photograph of the surroundings of the Tx and the Rx respectively. Fig. F.4 depicts the map of the premises. We notice that the Rx position is in the hall and the Tx is located at the entrance of a corridor. The data of 900 measurement cycles were collected within a period of 60 s. A measurement cycle refers to the interval within which all 50×50 subchannels are sounded once.

In order to maintain low computational complexity, the measurement data collected using two identical subarrays of the Tx and Rx arrays are considered. Each subarray consists of 9 dual-polarized elements uniformly spaced on a cylinder (See Fig. F.2). Fig. F.5 depicts the estimated delay power spectrum obtained by averaging the squared responses of the 81 subchannels of the 9×9 MIMO system. Again, to limit the computational effort the

Ring of 9-element
subarray used for
the estimation of
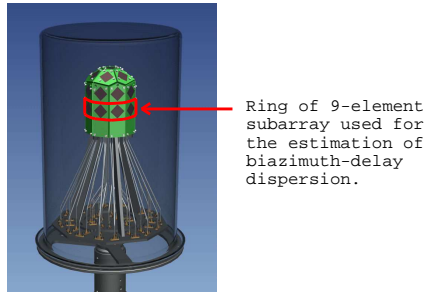biazimuth-delay
dispersion.

Fig. F.2: Illustration of the antenna arrays used in the Tx and the Rx of the channel sounder.

(a) Surroundings of the Tx.   (b) Surroundings of the Rx.

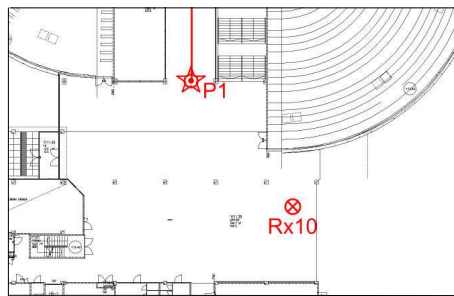*Fig. F.3: Photographs of the premises where the measurement experiment was conducted.*

Fig. F.4: Map of the premises where the measurement experiment was conducted. The Tx and Rx locations are marked with "P1" and "Rx10" respectively.
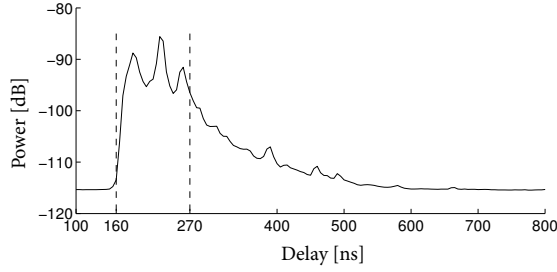
Fig. F.5: Estimated delay power spectrum.

observation samples collected from delay 160 ns to delay 270 ns are considered
in the estimation process.

   In the SAGE algorithm, the dynamic range for the path power estimates
is set to be 30 dB with respect to the maximum power estimate. The Bartlett
beamformer [1] is used to initialize the path parameter estimates. The param-
eters that the Bartlett beamformer is incapable to estimate are set to certain
predefined values. So, the estimates of the concentration parameters $\kappa_{1,d}, \kappa_{2,d}$,
$d = 1, \ldots, D$ are set to 50 and the estimates of the coefficients $\rho_{1,d}, \rho_{2,d}, \rho_{12,d}$,
$d = 1, \ldots, D$ equal 0. With this setting it is assumed a priori that the path
components are close to being specular and that no dependency occurs across
the considered dispersion dimensions.

   After 10 SAGE iteration cycles, the parameter estimates of 20 path compo-
nents are obtained. Table F.4 reports the values of these estimates. The mean
of the delay spread estimates of these components is 5.0 ns. The AoD spread
estimates range from 4.4° to 16.2° with a mean equal to 9.0°. The AoA spread
estimates range from 3.2° to 8.8° with a mean 5.0°. The difference between the
AoA and AoD spread estimates can be attributed to the different structures
of the environments surrounding the Tx and the Rx. From these results we
observe that in a closed environment, e.g. in a corridor where the Tx is located,
path components exhibit larger angular spreads than in an open environment,
like the hall where the Rx is located.

   Fig. F.6 depicts Bartlett($\hat{\Sigma}$), Bartlett($\Sigma(\hat{\theta})$) and the estimated power spec-
trum $\hat{P}(\phi_1, \phi_2, \tau)$. The notations "Bartlett($\hat{\Sigma}$)" and "Bartlett($\Sigma(\hat{\theta})$)" denote
the Bartlett spectrum calculated from respectively the sample covariance
matrix and the covariance matrix computed based on the parameter estimate
$\hat{\theta}$. The estimated power spectrum $\hat{P}(\phi_1, \phi_2, \tau)$ is given by

$$\hat{P}(\phi_1, \phi_2, \tau) = \sum_{d=1}^{20} \hat{P}_d \cdot f(\phi_1, \phi_2, \tau; \hat{\theta}_d), \tag{F.19}$$

where $\hat{\theta}_d$ denotes the estimate of the path-specific parameter θ_d. Note that

d	$\bar{\tau}_d$ ns	$\bar{\phi}_{1,d}$ [°]	$\bar{\phi}_{2,d}$ [°]	σ_{τ_d} ns	$\kappa_{1,d}$	$\sigma_{1,d}$ [°]	$\kappa_{2,d}$	$\sigma_{2,d}$ [°]	$\rho_{1,d}$	$\rho_{2,d}$	$\rho_{12,d}$	$P_d[10^{-7}]$	P_d [dB]
1	210	40	146	4.7	56.3	7.6	203.8	4.0	0.1	0.0	0.1	3.8	0
2	170	50	28	4.4	22.5	12.1	265.0	3.5	0.5	0.0	−0.3	3.5	−0
3	210	124	146	4.7	37.5	9.4	320.0	3.2	−0.3	0.0	−0.1	3.1	−1
4	170	126	26	4.9	95.0	5.9	176.3	4.3	−0.3	−0.2	0.4	1.8	−3
5	165	120	20	9.4	33.8	9.9	111.3	5.4	0.7	−0.4	−0.6	1.0	−6
6	170	−50	26	4.3	43.8	8.7	321.3	3.2	−0.3	−0.1	0.4	0.7	−7
7	210	−130	148	4.0	103.8	5.6	147.5	4.7	0.4	0.1	0.0	0.7	−7
8	245	136	138	4.2	57.5	7.6	90.0	6.0	0.3	0.0	−0.5	0.6	−8
9	245	74	136	4.2	36.3	9.5	290.0	3.4	0.4	0.2	−0.7	0.6	−8
10	175	176	26	5.9	116.3	5.3	210.0	4.0	−0.4	−0.8	0.5	0.5	−9
11	245	36	6	5.8	35.0	9.7	65.0	7.1	0.0	−0.8	0.4	0.5	−9
12	245	14	138	3.7	170.0	4.4	260.0	3.6	0.3	−0.3	0.7	0.3	−11
13	200	56	32	4.5	96.3	5.8	107.5	5.5	0.2	−0.4	−0.1	0.3	−11
14	250	168	30	4.8	16.3	14.2	52.5	7.9	0.5	0.2	0.9	0.3	−12
15	175	−134	22	6.4	71.3	6.8	163.8	4.5	0.2	−0.1	−0.8	0.2	−12
16	210	−38	146	5.7	12.5	16.2	73.8	6.7	0.2	0.0	0.3	0.2	−14
17	210	−178	148	4.2	13.8	15.5	66.3	7.0	−0.1	0.1	−0.1	0.1	−15
18	195	50	150	2.9	56.3	7.6	298.8	3.3	−0.1	−0.1	−0.2	0.1	−16
19	170	50	0	3.2	30.0	10.5	157.5	4.6	0.3	0.2	0.4	0.1	−16
20	210	110	110	7.9	52.5	7.9	42.5	8.8	−0.5	0.6	−0.3	0.05	−19
Mean				5.0	57.8	9.0	171.1	5.0	0.1	−0.10	0.0	0.0	

Table F.2: Estimates of the parameters of individual path components.
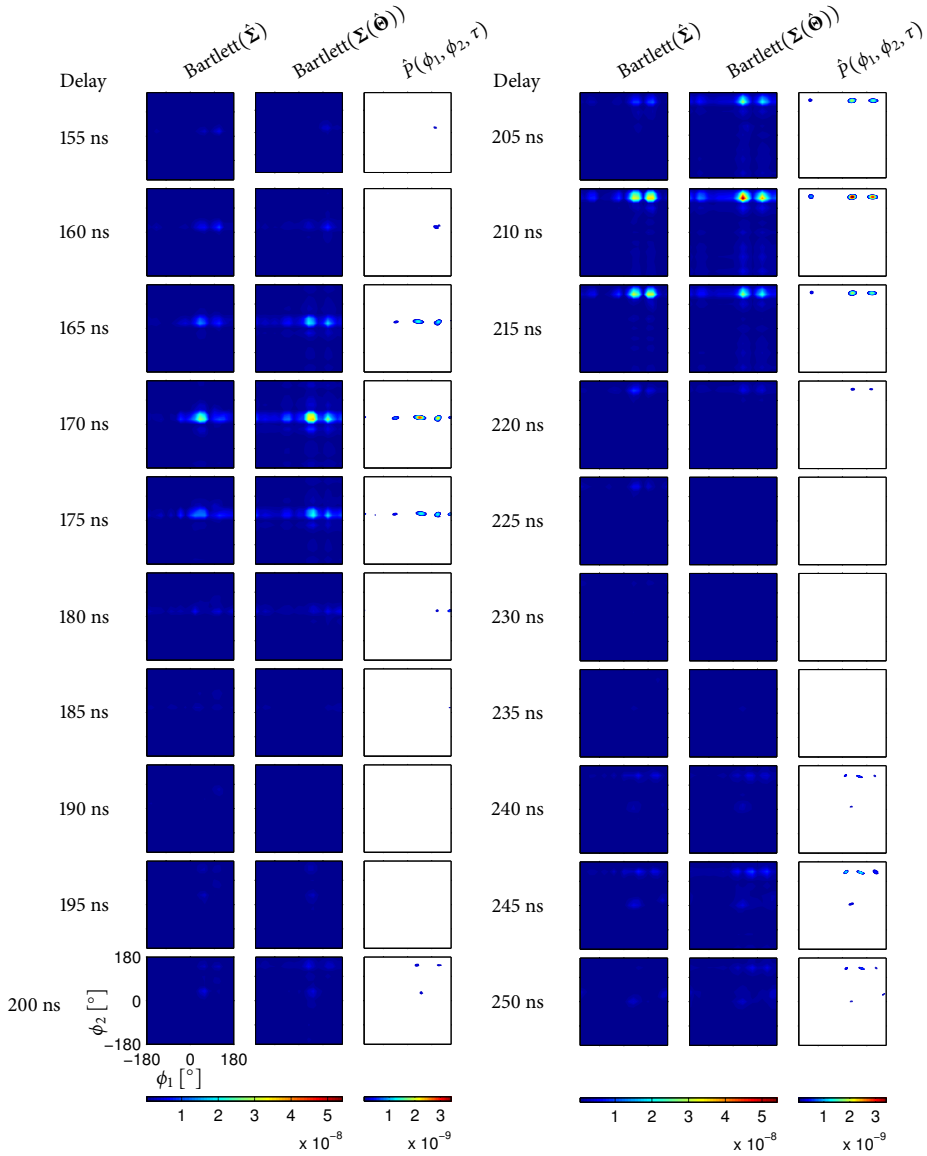
165

Fig. F.6: *Estimated biazimuth-delay power spectrum.*

although the biazimuth power spectra are plotted versus delay in Fig. F.6, the power spectrum of individual path components is estimated in AoA, AoD and delay jointly.

From Fig. F.6 we observe that the estimated power spectra of individual path components are more concentrated than the corresponding footprints observed in $\mathrm{Bartlett}(\boldsymbol{\Sigma}(\hat{\boldsymbol{\theta}}))$. The blurring effect observed in $\mathrm{Bartlett}(\boldsymbol{\Sigma}(\hat{\boldsymbol{\theta}}))$ is due to the product of the ambiguity functions of the Tx and Rx array responses in azimuth. $\mathrm{Bartlett}(\hat{\boldsymbol{\Sigma}})$ and $\mathrm{Bartlett}(\boldsymbol{\Sigma}(\hat{\boldsymbol{\theta}}))$ are observed to be similar. In the following, the ratio $\mathrm{tr}[\boldsymbol{\Sigma}_S(\hat{\boldsymbol{\theta}})]/\mathrm{tr}[\hat{\boldsymbol{\Sigma}}]$ is calculated, which can be conceived as the fraction of the signal power extracted from the sample covariance matrix. Here, $\mathrm{tr}[\cdot]$ denotes the trace of the matrix given as an argument. The signal-only covariance matrix $\boldsymbol{\Sigma}_S(\hat{\boldsymbol{\theta}})$ is calculated using the parameter estimate $\hat{\boldsymbol{\theta}}$ with the noise variance estimate $\hat{\sigma}_w^2$ set to zero. This ratio equals 87.6 % for the considered case.

Although $\mathrm{Bartlett}(\hat{\boldsymbol{\Sigma}})$ and $\mathrm{Bartlett}(\boldsymbol{\Sigma}(\hat{\boldsymbol{\theta}}))$ in Fig. F.6 are observed to be similar, their significant global and local maxima slightly differ. This difference might be due to the fact that in the parameter estimation process, the assumption of horizontal-only propagation is used. However, from the photographs shown in Fig. F.3 we see that this assumption may not hold for all propagation paths. This inconsistency may introduce estimation errors as shown by further simulation studies. Another reason which might lead to this effect is that the derived density function (F.13) only provides an approximation to the shape of the effective power spectrum of individual path components. Estimation errors might result in the case where the difference is significant.

Fig. F.7 depicts the estimated 3 dB-spread surfaces (F.14) with the true path component parameters replaced by their estimates. The color of the surfaces codes the path power estimates according to the included color scale. We observe that some of the surfaces are not symmetric with respect to the axes of the delay, the AoD and the AoA. This effect indicates dependency of dispersion of individual path components across different dispersion dimensions. Some recent published works, e.g. [9], assume that dispersion of individual propagation paths in different dimensions (e.g. in delay and in AoA) is independent. Clearly, this assumption does not hold for some of the estimated path components in the investigated propagation environment. Further investigations are necessary in order to assess whether this observation is valid for all types of environments or not.
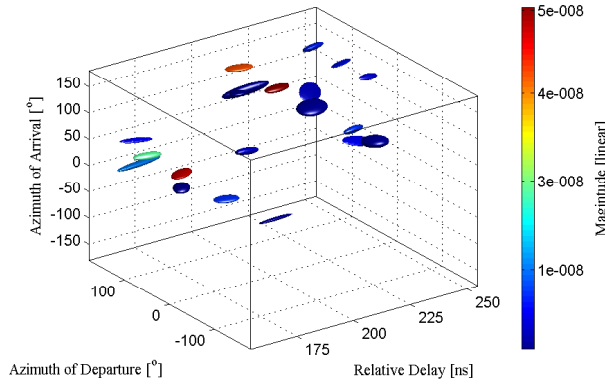
*Fig. F.7: Estimated 3 dB-spread surfaces of individual dispersed path components. The color of the
surfaces codes the path power estimates according to the color scale reported on the right.*

F.5   Conclusions

In this contribution, we derived a distribution which is suitable for charac-
terizing biazimuth (azimuth of arrival and azimuth of departure) and delay
dispersion of individual path components in the response of the propagation
channel. This distribution maximizes the entropy under the constraint that
its first and second moments are specified. The density function of the dis-
tribution characterizes the shape of the biazimuth-delay power spectrum of
individual path components.

Preliminary experimental investigations were conducted to assess the
applicability of the proposed characterization in real situations. From the
obtained results we observed that dispersion of the path components in both
azimuths and delay is much smaller than that one might infer from the
corresponding footprints in the Bartlett spectrum. Moreover, the estimated
power spectra of some path components are not symmetric with respect to
the axes of the delay, the azimuth of arrival and the azimuth of departure. This
indicates dependency across different dispersion dimensions. The results also
show that the characterization method should include dispersion in elevation.

References

[1] M. Bartlett, "Smoothing periodograms from time series with continuous
spectra," *Nature*, vol. 161, 1948.

[2] T. Trump and B. Ottersten, "Estimation of nominal direction of arrival and angular spread using an array of sensors," *Signal Processing*, vol. 50, pp. 57–69, Apr. 1996.

[3] O. Besson and P. Stoica, "Decoupled estimation of DoA and angular spread for spatially distributed sources," *IEEE Trans. Signal Processing*, vol. 49, pp. 1872–1882, 1999.

[4] C. B. Ribeiro, E. Ollila, and V. Koivunen, "Stochastic maximum likelihood method for propagation parameter estimation," in *Proceedings of the 15th IEEE International Symposium on Personal, Indoor and Mobile Radio Communications (PIMRC)*, vol. 3, Sept. 5-8 2004.

[5] X. Yin, T. Pedersen, N. Czink, and B. H. Fleury, "Parametric characterization and estimation of bi-azimuth dispersion of path components," in *Proceedings of the 7th IEEE International Workshop on Signal Processing Advances for Wireless Communications (SPAWC)*, Nice, France, July 2006.

[6] B. H. Fleury, "First- and second-order characterization of direction dispersion and space selectivity in the radio channel," *IEEE Trans. Information Theory*, no. 6, pp. 2027–2044, Sept. 2000.

[7] K. V. Mardia, "Statistics of directional data," *Journal of the Royal Statistical Society. Series B (Methodological)*, vol. 37, pp. 349–393, 1975.

[8] K. V. Mardia and P. E. Jupp, *Directional Statistics*. John Wiley and Sons, Ltd., 2000.

[9] C. B. Ribeiro, A. Richter, and V. Koivunen, "Stochastic maximum likelihood estimation of angle- and delay-domain propagation parameters," in *Proceedings of the 16th IEEE International Symposium on Personal, Indoor and Mobile Radio Communications (PIMRC)*, Berlin, Germany, 2005.

[10] H. Krim and M. Viberg, "Two decades of array signal processing research: the parametric approach," *IEEE Trans. Signal Processing*, vol. 13, pp. 67–94, July 1996.

[11] B. H. Fleury, M. Tschudin, R. Heddergott, D. Dahlhaus, and K. L. Pedersen, "Channel parameter estimation in mobile radio environments using the SAGE algorithm," *IEEE Journal on Selected Areas in Communications*, vol. 17, no. 3, pp. 434–450, Mar. 1999.

[12] N. Czink, E. Bonek, X. Yin, and B. H. Fleury, "Cluster angular spreads in a MIMO indoor propagation environment," in *Proceedings of the 16th IEEE International Symposium on Personal, Indoor and Mobile Radio Communications (PIMRC)*, Berlin, Germany, 2005.

[13] E. Bonek, N. Czink, V. M. Holappa, M. Alatossava, L. Hentilä, J. Nuutinen, and A. Pal, "Indoor MIMO measurements at 2.55 and 5.25 GHz - a comparison of temporal and angular characteristics," in *Proceedings of the 15th IST Mobile Summit*, 2006.

A SAGE Algorithm for Estimation of the Direction Power Spectrum of Individual Path Components

Xuefeng Yin, Lingfeng Liu, Daniel K. Nielsen, Troels Pedersen, and Bernard H. Fleury

Abstract

In this contribution, the Fisher-Bingham-5 (FB5) probability density function (pdf) is used to model the shape of the direction power spectral density function (psdf) of individual path components in the radio channel. The FB5 distribution is selected because, among all direction distributions, it maximizes the entropy under the constraints that the first and second distribution moments are specified. A SAGE (Space-Alternating Generalized Expectation-maximization) algorithm is derived based on this model for estimation of the parameters characterizing the direction psdf of each path component in a multi-path scenario. The performance of the SAGE algorithm is evaluated using measurement data. Preliminary results show that the estimated direction psdfs of individual path components exhibit different ovalnesses and tilt angles. These density functions are noticeably more concentrated than the corresponding footprints in the Bartlett spectrum.

G.1 Introduction

Due to the heterogeneity of the propagation environment, the response of the radio channel can be viewed as the superposition of a certain number of components. Each component, which we refer to as "path component", is contributed by an electromagnetic wave propagating along a path from the transmitter (Tx) to the receiver (Rx). Along this path, the wave interacts with a certain number of objects called scatterers. Due to the geometrical extent and the nonhomogeneous electromagnetic properties of the scatterers, a path may be dispersive in delay, direction of departure, direction of arrival, polarizations, as well as in Doppler frequency when the environment is time-variant. As a consequence, an individual path component may be spread in these dispersion dimensions. Modeling of these dispersion phenomena is required for the design and optimization of mobile communication systems and thus, experimental knowledge of the dispersive characteristics of path components is necessary.

In recent years, estimation of the dispersive characteristics of individual path components in multiple dimensions has attracted much attention. Some of the techniques are derived using the assumption that the normalized power spectral density function (psdf) of individual path components can be described using a certain probability density function (pdf). In [1], the product of the von-Mises pdf and the exponential pdf is used to model the normalized delay–Azimuth-of-Arrival (AoA) psdf. In [2] and [3], the von–Mises–Fisher and Fisher–Bingham–5 (FB$_5$) pdfs are used to characterize the normalized AoA–Azimuth-of-Departure (AoD) psdf and direction (azimuth

and elevation) psdf respectively. The normalized delay–AoA–AoD psdf is characterized using a 3-variate pdf derived in [4].

In this contribution, we derive a SAGE algorithm to estimate the direction (azimuth and elevation) power spectrum of individual path components. The normalized direction psdf is modeled using the FB_5 pdf as described in [3]. The SAGE algorithm is applied to measurement data to estimate the direction power spectra of multiple dispersive path components.

This contribution is organized as follows. In Section G.2, a signal model for channel sounding is presented and characterization of the normalized direction psdf using the FB_5 pdf is introduced. In Section G.3, the estimators of the model parameters are derived within the SAGE framework. Section G.4 shows the experimental results. Finally concluding remarks are provided in Section G.5.

G.2   Signal Model

In this contribution, we focus on the dispersive characteristics of individual path components in direction of arrival (DoA). The channel sounding system considered has a SIMO (single-input multiple-ouput) configuration with a single Tx antenna and a M-element Rx antenna array. The signal model, the characterization method, and the estimation method derived here can be easily modified to handle a MISO (multiple-input single-ouput) channel sounding configuration where dispersion in direction of departure (DoD) is of interest.

We consider narrow-band transmission, which implies that the product of the signal bandwidth times the channel delay spread is much smaller than one. Following the nomenclature in [5], the continuous-time output signal of the Rx array of the SIMO system reads

$$\mathbf{Y}(t) = \mathbf{H}(t)u(t) + \mathbf{W}(t) \in \mathbb{C}^M$$
$$= \left[\int_{\mathbb{S}_2} \mathbf{c}(\mathbf{\Omega})h(t;\mathbf{\Omega})\mathrm{d}\mathbf{\Omega} \right] u(t) + \mathbf{W}(t). \qquad (G.1)$$

The complex vector $\mathbf{Y}(t)$ contains the output signals of the Rx array observed at time instance t. The scalar function $u(t)$ denotes the complex envelope of the transmitted sounding signal at time t. The vector $\mathbf{H}(t)$ represents the time-variant response of the SIMO system. We assume that $u(t)$ is known to the Rx and that $\int_0^T u(t)u(t)^* \mathrm{d}t = 1$, where $[\cdot]^*$ denotes complex conjugate and T represents the duration of observation interval. The function $h(t;\mathbf{\Omega})$ is the (time-variant) DoA spread function of the propagation channel [5]. Here, $\mathbf{\Omega}$ denotes the DoA, which is defined to be a unit vector with initial point

anchored at the origin $\mathcal{O}$ of a coordinate system located in the vicinity of the Rx array. The end point of $\mathbf{\Omega}$ lies on a unit sphere $\mathbb{S}_2$ centered at $\mathcal{O}$. The DoA $\mathbf{\Omega}$ is uniquely determined by the spherical coordinates $(\phi, \theta) \in [-\pi, \pi) \times [0, \pi]$ of its end point according to the relation

$$\mathbf{\Omega} = \begin{bmatrix} \cos(\phi)\sin(\theta) \\ \sin(\phi)\sin(\theta) \\ \cos(\theta) \end{bmatrix}. \tag{G.2}$$

The angles ϕ and θ are referred to as the AoA and elevation of arrival (EoA) respectively. The noise $\mathbf{W}(t)$ in (G.1) is a vector-valued, circularly symmetric, spatially and temporally white Gaussian process with component spectral height σ_w^2. We assume that σ_w^2 can be measured and therefore is known in advance. In (G.1) the complex vector

$$\mathbf{c}(\mathbf{\Omega}) \doteq [c_1(\mathbf{\Omega}), c_2(\mathbf{\Omega}), \ldots, c_M(\mathbf{\Omega})]^{\mathsf{T}} \tag{G.3}$$

with $[\cdot]^{\mathsf{T}}$ denoting transposition is the responses of the Rx array. In a scenario where the electromagnetic energy propagates from the Tx to the Rx via D paths, the DoA spread function $h(t; \mathbf{\Omega})$ can be decomposed as

$$h(t; \mathbf{\Omega}) = \sum_{d=1}^{D} h_d(t; \mathbf{\Omega}). \tag{G.4}$$

The summand $h_d(t; \mathbf{\Omega})$ denotes the dth path component in $h(t; \mathbf{\Omega})$.

We assume that the transfer vector $\mathbf{H}(t)$ fluctuates over the overall sounding period, but remains constant within individual observation intervals:

$$\mathbf{H}(t) \doteq \mathbf{H}_n, \quad t \in [t_n, t_n + T) \text{ and } n \in [1, \ldots, N]. \tag{G.5}$$

Here, t_n denotes the time instance at which the nth observation interval starts and N represents the number of observation intervals. Similarly, the spread functions $h_d(t; \mathbf{\Omega})$, $d = 1, \ldots, D$ arising in (G.4) are constant within individual observation intervals:

$$h_d(t; \mathbf{\Omega}) = h_d(t_n; \mathbf{\Omega}) \doteq h_{d,n}(\mathbf{\Omega}), \quad t \in [t_n, t_n + T). \tag{G.6}$$

The processes $h_{d,n}(\mathbf{\Omega})$, $n \in [1, \ldots, N]$, $d \in [1, \ldots, D]$ are assumed to be uncorrelated complex (zero-mean) orthogonal stochastic measures, i.e.

$$\mathrm{E}[h_{d,n}^*(\mathbf{\Omega})h_{d',n'}(\mathbf{\Omega}')] = P_d(\mathbf{\Omega})\delta_{nn'}\delta_{dd'}\delta(\mathbf{\Omega} - \mathbf{\Omega}'). \tag{G.7}$$

Here, $\delta_{(\cdot)}$ and $\delta(\cdot)$ represent the Kronecker delta and the Dirac delta function respectively, and $P_d(\mathbf{\Omega}) \doteq \mathrm{E}[|h_{d,n}(\mathbf{\Omega})|^2]$ denotes the direction psdf of

the dth path component. Identity (G.7) implies that the spread functions of distinct individual path components or at different observation intervals are uncorrelated. This scenario is referred to as the *uncorrelated scattering* case in the literature (see e.g. [5]).

The direction psdf $P_d(\Omega)$ describes the manner the average power of the dth path component is distributed on the unit sphere $\mathbb{S}_2$. It can be written as

$$P_d(\Omega) = P_d \cdot f_d(\Omega) \tag{G.8}$$

with P_d representing the average power of the dth path component and $f_d(\Omega)$ being a normalized direction psdf.

In this contribution, we assume that $f_d(\Omega)$ coincides with the FB_5 pdf [6]. Among all distributions on the unit sphere $\mathbb{S}_2$, the FB_5 distribution [6] maximizes the entropy under the constraints that the distribution first and second moments are specified. The first moment of the distribution is parameterized by the nominal direction, while the second moments are characterized by parameters describing the concentration and the ovalness of the spreads of $f_d(\Omega)$ on $\mathbb{S}_2$. The pdf $f_{FB_5}(\Omega)$ reads

$$f_{FB_5}(\Omega) = C(\kappa, \eta)^{-1} \exp\{\kappa \gamma_1^\mathsf{T}\Omega + \kappa \cdot \eta[(\gamma_2^\mathsf{T}\Omega)^2 - (\gamma_3^\mathsf{T}\Omega)^2]\}, \tag{G.9}$$

where $\kappa \geq 0$ represents the concentration parameter and $\eta \in [0, 1/2)$ is an ovalness factor. In (G.9), $C(\kappa, \eta)$ denotes a normalization constant depending on κ and η, γ_1, γ_2, and $\gamma_3 \in \mathbb{R}^3$ are unit vectors. The matrix $\Gamma \doteq [\gamma_1, \gamma_2, \gamma_3]$ is uniquely determined by three angular parameters $\bar{\theta}$, $\bar{\phi}$ and α according to

$$\Gamma = \begin{bmatrix} \sin(\bar{\theta})\cos(\bar{\phi}) & -\sin(\bar{\phi}) & \cos(\bar{\theta})\cos(\bar{\phi}) \\ \sin(\bar{\theta})\sin(\bar{\phi}) & \cos(\bar{\phi}) & \cos(\bar{\theta})\sin(\bar{\phi}) \\ \cos(\bar{\theta}) & 0 & -\sin(\bar{\theta}) \end{bmatrix} \cdot \begin{bmatrix} 1 & 0 & 0 \\ 0 & \cos(\alpha) & -\sin(\alpha) \\ 0 & \sin(\alpha) & \cos(\alpha) \end{bmatrix}. \tag{G.10}$$

In (G.10), $\bar{\phi}$ and $\bar{\theta}$ coincide with respectively the azimuth and the elevation of the nominal direction. The angle α describes how the pdf is tilted on $\mathbb{S}_2$. A detailed description of the meanings of γ_1, γ_2 and γ_3 can be found in [6]. Note that when η equals 0, the FB_5 pdf does not depend on the values of α and the equal-value contours of $f_{FB_5}(\Omega)$ are circles. For $\eta \in (0, 1/2)$, the equal-density contours of the pdf exhibit the ovalness, which becomes significant as η increases. The equal-value contours resemble ellipses when κ is small. Fig. G.1 depicts the FB_5 pdf for the parameter setting reported in the caption of this figure.

The parameters of $f_d(\Omega)$ are concatenated in $\tilde{\theta}_d \doteq [\bar{\phi}_d, \bar{\theta}_d, \kappa_d, \eta_d, \alpha_d]$. We use a vector θ to represent all unknown model parameters in (G.1), i.e.

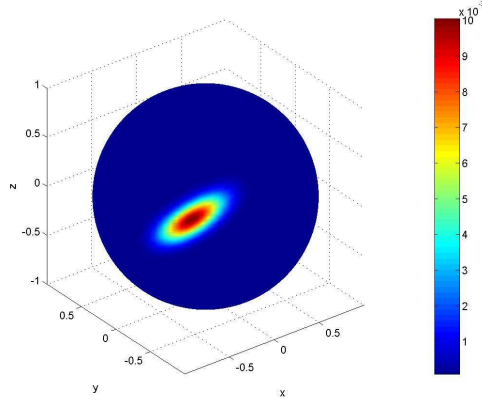$$\theta \doteq [P_1, P_2, \ldots, P_D, \tilde{\theta}_1, \tilde{\theta}_2, \ldots, \tilde{\theta}_D]. \tag{G.11}$$

Fig. G.1: The FB₅ pdf with $\bar{\phi} = 135°$, $\bar{\theta} = 18°$, $\alpha = 144°$, $\kappa = 80$ and $\eta = 0.375$. The color bar to the right of the plot shows the magnitude expressed in linear scale.

G.3   Estimation of the Model Parameters

In a scenario with multiple path components, as depicted by (G.1), the problem at hand is to estimate the parameter vector $\boldsymbol{\theta}$. Maximum likelihood estimation of $\boldsymbol{\theta}$ requires to solve a $6D$ dimensional non-linear optimization problem. The high computational complexity involved prohibits the implementation of the maximum likelihood estimation in practise. In the sequel, we derive a SAGE algorithm [7] as an approximation of the maximum likelihood estimator of $\boldsymbol{\theta}$.

G.3.1   Admissible hidden data

We choose the subsets of parameters updated at the different iterations of the SAGE algorithm to be the sets including the parameters characterizing individual path components. Hence, in Iteration $i = 1, 2, \ldots$, the parameter subset $\boldsymbol{\theta}_d \doteq [P_d, \tilde{\boldsymbol{\theta}}_d]$ with $d = [(i-1) \mod D] + 1$ is updated.

We define the admissible hidden data associated with $\boldsymbol{\theta}_d$ as

$$\mathbf{X}_d(t) \doteq \mathbf{H}_d(t)u(t) + \mathbf{W}(t)$$
$$= \left[\int_{\mathbb{S}_2} \mathbf{c}(\boldsymbol{\Omega})h_d(t;\boldsymbol{\Omega})\mathrm{d}\boldsymbol{\Omega} \right]u(t) + \mathbf{W}(t). \qquad \text{(G.12)}$$

It follows from the properties of $h_d(t;\boldsymbol{\Omega})$ that $\mathbf{H}_d(t)$ is constant within indi-

vidual observation intervals, i.e.

$$\mathbf{H}_d(t) \doteq \mathbf{H}_{d,n} = \int_{\mathbb{S}_2} \mathbf{c}(\mathbf{\Omega}) h_{d,n}(\mathbf{\Omega}) \mathrm{d}\mathbf{\Omega}. \tag{G.13}$$

The output of a correlator

$$\tilde{\mathbf{H}}_{d,n} \doteq \int_{t_n}^{t_n+T} \mathbf{x}_d(t) u(t)^* \mathrm{d}t, \quad n = 1, \dots, N \tag{G.14}$$

when the input is the observation $\mathbf{X}_d(t) = \mathbf{x}_d(t)$ can be written as

$$\tilde{\mathbf{H}}_{d,n} = \mathbf{H}_{d,n} + \mathbf{N}_n, \tag{G.15}$$

where $\mathbf{N}_n \in \mathbb{C}^M$, $n = 1, \dots, N$ is a sequence of N independent random vectors, the entries of which are independent circularly symmetric Gaussian random variables with variance σ_w^2. Invoking the central limit theorem, the elements of $\tilde{\mathbf{H}}_{d,n}$ in (G.12) are assumed to be Gaussian random variables. The vectors $\tilde{\mathbf{H}}_{d,1}, \dots, \tilde{\mathbf{H}}_{d,N}$ form a sufficient statistic for the estimation of $\boldsymbol{\theta}_d$.

G.3.2 *Expectation Step*

In the Expectation (E-) step of Iteration i, we compute the expectation of the likelihood of $\boldsymbol{\theta}_d$ conditioned on the observation $\mathbf{Y}(t) = \mathbf{y}(t)$ and assuming that $\boldsymbol{\theta} = \widehat{\boldsymbol{\theta}}^{[i-1]}$:

$$Q(\boldsymbol{\theta}_d | \widehat{\boldsymbol{\theta}}^{[i-1]}) \doteq \mathrm{E}\big[\Lambda(\mathbf{\Omega}_d; \mathbf{x}_d) | \mathbf{Y}(t) = \mathbf{y}(t), \widehat{\boldsymbol{\theta}}^{[i-1]})\big]. \tag{G.16}$$

Here, $\widehat{\boldsymbol{\theta}}^{[i-1]}$ denotes the parameter estimates obtained in the $(i-1)$th iteration and $\Lambda(\mathbf{\Omega}_d; \mathbf{x}_d)$ represents the log-likelihood function of $\mathbf{\Omega}_d$ given an observation $\mathbf{X}_d(t) = \mathbf{x}_d(t)$. It can be shown that (G.16) is of the form

$$Q(\boldsymbol{\theta}_d | \widehat{\boldsymbol{\theta}}^{[i-1]}) = -\ln|\mathbf{\Sigma}_{\tilde{\mathbf{H}}_d}(\boldsymbol{\theta}_d)| - \mathrm{tr}\big[(\mathbf{\Sigma}_{\tilde{\mathbf{H}}_d}(\boldsymbol{\theta}_d))^{-1} \cdot \widehat{\mathbf{\Sigma}}_{\tilde{\mathbf{H}}_d}(\widehat{\boldsymbol{\theta}}^{[i-1]})\big], \tag{G.17}$$

where $\mathrm{tr}[\cdot]$ is the trace of the matrix given as an argument and $\mathbf{\Sigma}_{\tilde{\mathbf{H}}_d}(\boldsymbol{\theta}_d)$ is the covariance matrix of $\tilde{\mathbf{H}}_{d,n}$:

$$\mathbf{\Sigma}_{\tilde{\mathbf{H}}_d}(\boldsymbol{\theta}_d) = P_d \int_{\mathbb{S}_2} \mathbf{c}(\mathbf{\Omega}) \mathbf{c}(\mathbf{\Omega})^{\mathrm{H}} f_d(\mathbf{\Omega}) \mathrm{d}\mathbf{\Omega} + \sigma_w^2 \mathbf{I}_M \tag{G.18}$$

with $[\cdot]^{\mathrm{H}}$ denoting the Hermitian operator. In (G.17), $\widehat{\mathbf{\Sigma}}_{\tilde{\mathbf{H}}_d}(\boldsymbol{\theta})$ is the conditional covariance matrix of $\tilde{\mathbf{H}}_{d,n}$ given the observation $\mathbf{y}(t)$ for $\boldsymbol{\theta}$. It can be shown that $\widehat{\mathbf{\Sigma}}_{\tilde{\mathbf{H}}_d}(\widehat{\boldsymbol{\theta}}^{[i]})$ is calculated as

$$\widehat{\mathbf{\Sigma}}_{\tilde{\mathbf{H}}_d}(\widehat{\boldsymbol{\theta}}^{[i]}) = \mathbf{\Sigma}_{\tilde{\mathbf{H}}_d}(\widehat{\boldsymbol{\theta}}_d^{[i]}) + \mathbf{\Sigma}_{\tilde{\mathbf{H}}_d}(\widehat{\boldsymbol{\theta}}_d^{[i]})\big[\mathbf{\Sigma}_{\tilde{\mathbf{H}}}(\widehat{\boldsymbol{\theta}}^{[i]})\big]^{-1}\big(\widehat{\mathbf{\Sigma}}_{\tilde{\mathbf{H}}} - \mathbf{\Sigma}_{\tilde{\mathbf{H}}_d}(\widehat{\boldsymbol{\theta}}_d^{[i]})\big)$$
$$\cdot \big[\mathbf{\Sigma}_{\tilde{\mathbf{H}}}(\widehat{\boldsymbol{\theta}}^{[i]})\big]^{-1}\mathbf{\Sigma}_{\tilde{\mathbf{H}}_d}(\widehat{\boldsymbol{\theta}}_d^{[i]}), \tag{G.19}$$

where

$$\boldsymbol{\Sigma}_{\tilde{\mathbf{H}}}(\widehat{\boldsymbol{\theta}}^{[i]}) = \sum_{d=1}^{D} \boldsymbol{\Sigma}_{\tilde{\mathbf{H}}_d}(\widehat{\boldsymbol{\theta}}_d^{[i]}) + \sigma_w^2 \mathbf{I}_M, \tag{G.20}$$

and

$$\widehat{\boldsymbol{\Sigma}}_{\tilde{\mathbf{H}}} = \frac{1}{N} \sum_{n=1}^{N} \tilde{\mathbf{H}}_n \tilde{\mathbf{H}}_n^{\mathrm{H}} \tag{G.21}$$

with $\tilde{\mathbf{H}}_n \doteq \int_{t_n}^{t_n+T} \mathbf{y}(t)u(t)^* \mathrm{d}t$, $n = 1, \dots, N$.

G.3.3 Maximization Step

In the M-step, the estimate $\widehat{\boldsymbol{\theta}}_d^{[i]}$ is calculated as

$$\widehat{\boldsymbol{\theta}}_d^{[i]} = \arg\max_{\boldsymbol{\theta}_d} Q(\boldsymbol{\theta}_d|\widehat{\boldsymbol{\theta}}^{[i-1]}). \tag{G.22}$$

By applying a coordinate-wise updating procedure similar to the one used in [8], the required multiple-dimensional maximization can be reduced to multiple one-dimensional maximization problems. This coordinate-wise updating still remains within the SAGE framework with the admissible data given in (G.12).

G.3.4 Initialization Step

In the initialization step, the nominal AoAs and EoAs of the path components are estimated using a SAGE algorithm derived based on the specular-path model [8]. The parameters which cannot be estimated using this method are set equal certain predefined values. More specifically, the estimates of the concentration parameters κ_d, $d = 1, \dots, D$ are set equal to 100 and the ovalness parameters are set equal to zero. With this setting it is assumed a priori that the path components are close to specular path components. This initialization procedure has proved to work well for measurement data in the experimental scenarios in which it was tested.

G.4 Experimental Investigations

The measurement data were collected using the Elektrobit Propsound CS switched channel sounder [2] in an office building. The sounder was used in a MISO (multiple-input single-output) configuration where the Rx has a single antenna and the Tx is equipped with a 50-element omnidirectional antenna

(a) Surroundings of the Tx.   (b) Surroundings of the Rx.
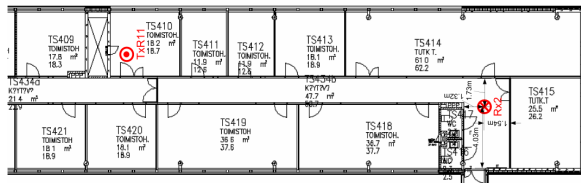

(c) Map of the premises.

Fig. G.2: Photographs and map of the premises where the measurement experiment was conducted.

array. A detailed description of the sounder, the array and the measurement settings can be found in [2]. During the measurement, the Rx was located in a corridor and the Tx was placed in an office room. Two photographs and the map shown in Fig. G.2 depict the surroundings of the Rx and Tx. The locations of the Tx and the Rx are marked with the symbols ⊙ and ⊗ respectively on the map. During the measurement period, both Tx and Rx were fixed. People were moving in the office where the Tx was located. These movements created the randomness of the radio channel. Due to this fact, the uncorrelated scattering condition as depicted in (G.7) is considered to be valid.

The data obtained from 50 consecutive measurement cycles covering a period of 3.3 seconds are considered. A measurement cycle is referred to as the interval within which all 50 subchannels are sounded once. In this preliminary study, we investigate dispersion of individual path components in direction of departure and neglect dispersion in other dimensions. To this aim, we consider the output of the Rx antenna within the relative delay bin 160-170 ns. The narrow-band signal model (G.1) is applicable in the considered scenario for this delay bin. The parameter estimators derived based on

Table G.1: *The estimates of the parameters obtained using the SAGE algorithm.*

d	$\bar{\phi}_d\,[°]$	$\hat{\bar{\theta}}_d\,[°]$	$\hat{\kappa}_d$	$\hat{\eta}_d$	$\hat{\alpha}_d\,[°]$	$\hat{P}_d[10^{-10}]$	$\hat{P}_d/\hat{P}_1\,[\text{dB}]$
1	−84	4	140	0.33	59.3	7.10	0
2	114	−4	160	0.49	15.8	5.72	−1
3	44	−10	923	0.00	26.5	5.19	−1
4	−24	8	923	0.17	144.0	4.10	−2

the SAGE algorithm can be easily modified to estimate the parameters of the DoD psdfs of individual path components.

The SAGE algorithm is applied while assuming that the number of the path components is known and equals 4 in the considered scenario. Totally 10 SAGE iteration cycles are performed. Here, an iteration cycle is referred to as the procedure in which the estimates of all elements in $\boldsymbol{\theta}$ are updated once. In the M-step we select the quantization step to coincide with the resolution of the calibration measurements, i.e. be 2° in both azimuth and elevation.

Fig. G.3 depicts the estimation results returned by the SAGE algorithm. The parameter estimates are reported in Table G.1. The notation Bartlett($\cdot$) arising in the captions of Fig. G.3(a) and Fig. G.3(b) denotes the power spectrum estimate obtained with Bartlett beamformer [9] using the covariance matrix given as an argument. Fig. G.3(c) demonstrates the azimuth-elevation psdf corresponding to the estimate of the direction psdf $\hat{P}(\boldsymbol{\Omega})$ of the radio channel. It can be observed that the azimuth-elevation psdfs of individual path components estimated using the SAGE algorithm are noticeably more concentrated than the corresponding footprints visible in Bartlett($\boldsymbol{\Sigma}_{\tilde{\mathbf{H}}}(\widehat{\boldsymbol{\theta}})$). These psdfs differ in concentration, ovalness and tilt angle. The "blurring" effect arising in the Bartlett spectrum is due to the response of the Rx array.

The footprints of the path components shown in Bartlett($\boldsymbol{\Sigma}_{\tilde{\mathbf{H}}}(\widehat{\boldsymbol{\theta}})$) and Bartlett($\widehat{\boldsymbol{\Sigma}}_{\tilde{\mathbf{H}}}$) are observed to be similar. This implies that the reconstructed covariance matrix computed using the parameter estimates is close to the sample covariance matrix. We also observe some differences in the shapes and the (local) maxima of the corresponding footprints. These differences are supposed to be caused by discrepancies between the "true" normalized psdfs of individual path components and the FB_5 pdf. Another possible reason for the difference is that dispersion in other dimensions, e.g. in delay, is not considered.

(a) Bartlett($\widehat{\boldsymbol{\Sigma}}_{\hat{\mathbf{H}}}$)

(b) Bartlett($\boldsymbol{\Sigma}_{\hat{\mathbf{H}}}(\widehat{\boldsymbol{\theta}})$)

(c) Azimuth-Elevation psdfs of path components corresponding to $\hat{P}(\boldsymbol{\Omega})$
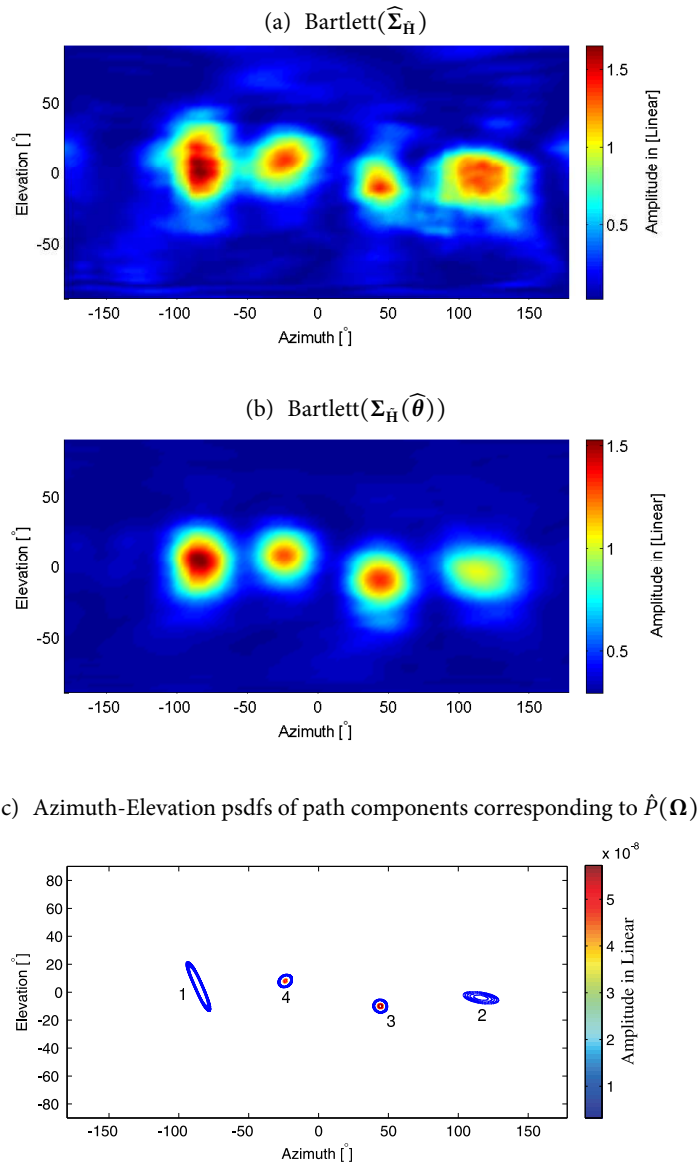
*Fig. G.3: Estimates of the azimuth-elevation psdf within the delay bin 160-170 ns. The estimates
of the parameters are shown in Table G.1. The indices of the path components reported in Table
G.1 are consistent with those given in Figure G.3(c).*

G.5   Conclusions

In this contribution, we derived a SAGE algorithm for estimation of the parameters characterizing the direction power spectral density function (psdf) of individual path components in a radio propagation channel. The Fisher-Bingham-5 probability density function (pdf) was used to describe the normalized direction psdf of individual path components. The performance of the SAGE algorithm was evaluated using measurement data. From the results we observed that the Bartlett spectrum computed with the signal covariance matrix calculated using the SAGE estimates is similar to the Bartlett spectrum computed with the sample covariance matrix. The estimated psdfs of individual path components exhibit different ovalness and tilt angle. Moreover they are more concentrated than the corresponding footprints in the Bartlett spectrum. These results indicated that dispersive path components exist in real propagation channels. In such a case, the conventional algorithms derived based on the specular-path model are inappropriate for estimation of the parameters of these path components. As shown in [10], the mismatch between the specular-path model and the "true" dispersive feature of path components results in significant errors of estimation of the path parameters with large probabilities of occurrence.

References

[1] C. B. Ribeiro, A. Richter, and V. Koivunen, "Stochastic maximum likelihood estimation of angle- and delay-domain propagation parameters," in *Proceedings of the 16th IEEE International Symposium on Personal, Indoor and Mobile Radio Communications (PIMRC)*, vol. 1, Berlin, Germany, 2005, pp. 624 – 628.

[2] X. Yin, T. Pedersen, N. Czink, and B. H. Fleury, "Parametric characterization and estimation of bi-azimuth dispersion of path components," in *Proceedings of the 7th IEEE International Workshop on Signal Processing Advances for Wireless Communications (SPAWC)*, Nice, France, July 2006.

[3] X. Yin, L. Liu, D. Nielsen, N. Czink, and B. H. Fleury, "Characterization of the azimuth-elevation power spectrum of individual path components," in *Proceedings of the International ITG/IEEE Workshop on Smart Antennas (WSA)*, Vienna, Austria, Feb. 2007.

[4] X. Yin, T. Pedersen, N. Czink, and B. H. Fleury, "Parametric characterization and estimation of bi-azimuth and delay dispersion of path components," in *Proceedings of The First European Conference on Antennas and Progation (EuCAP)*, Acropolis, Nice, France, November 2006.

[5] B. H. Fleury, "First- and second-order characterization of direction dispersion and space selectivity in the radio channel," *IEEE Trans. Information Theory*, no. 6, pp. 2027–2044, Sept. 2000.

[6] J. T. Kent, "The Fisher-Bingham distribution on the sphere," *Journal of the Royal Statistical Society, Serieal B (Methodological)*, vol. 44, pp. 71–80, 1982.

[7] J. A. Fessler and A. O. Hero, "Space-alternating generalized expectation-maximization algorithm," *IEEE Trans. on Signal Processing*, vol. 42, no. 10, pp. 2664–2677, Oct. 1994.

[8] B. H. Fleury, M. Tschudin, R. Heddergott, D. Dahlhaus, and K. L. Pedersen, "Channel parameter estimation in mobile radio environments using the SAGE algorithm," *IEEE Journal on Selected Areas in Communications*, vol. 17, no. 3, pp. 434–450, Mar. 1999.

[9] M. Bartlett, "Smoothing periodograms from time series with continuous spectra," *Nature*, vol. 161, 1948.

[10] M. Bengtsson and B. Völcker, "On the estimation of azimuth distributions and azimuth spectra," in *Proceedings of the 54th IEEE Vehicular Technology Conference (VTC-Fall)*, vol. 3, no. 12, 2001, pp. 1612–1615.

A SAGE Algorithm for Estimation of the Direction Power Spectrum of Individual Path Components

Xuefeng Yin, Lingfeng Liu, Troels Pedersen, Daniel K., Nielsen, and Bernard H. Fleury

Abstract

In this contribution, a multi-variate probability density function (pdf) is derived and used to describe the normalized direction–(i.e. azimuth and elevation)–delay power spectral density of individual dispersed components in the response of the propagation channel. This pdf maximizes the entropy under the constraint that its first and second moments are specified. We use a SAGE algorithm, as an approximation of the maximum-likelihood method, to estimate the parameters of the component direction–delay power spectral densities from measurement data. The experimental results show that the proposed pdf and the SAGE algorithm form altogether an effective tool to characterize direction-delay dispersion in the propagation channel.

H.1   Introduction

Due to the heterogeneity of the propagation environment, the received signal at the receiver (Rx) of a radio communication system can be modelled as the superposition of a number of components originating from waves propagating along specific propagation paths. Each component may be dispersive in delay, direction of departure (DoD), direction of arrival (DoA), Doppler frequency and polarization. Dispersion of individual components in these dimensions significantly influences the performance of communication systems using MIMO (multiple-input multiple-output) techniques [1].

In conventional parametric models for the MIMO wideband propagation channel, such as [2, Chapter 3], [3] and [4], dispersion of individual components is modeled using a cluster of multiple specular components estimated from measurement data. The cluster parameters, such as the nominal direction and direction spread, can be calculated for each cluster from the parameter estimates of the specular components assigned to this cluster. However, as shown in [5], the extracted dispersion parameters (e.g. azimuth) of the specular components do not accurately characterize the true dispersive behavior of the original component when this component is dispersed. This phenomenon limits the reliability of channel models derived based on specular components estimated from measurement data collected in real environments. Therefore, in order to design more realistic channel models we need appropriate parametric models characterizing dispersion of individual components, as well as efficient estimators of the parameters entering these models.

In recent years, various algorithms have been proposed for the estimation of the dispersive characteristics of individual components in the channel response [1, 6–8]. These algorithms estimate the parameters describing the

power spectral density (psd) of individual components. In real environments, a component psd can be irregular due to the heterogenous physical and electromagnetic properties of the scatterers with which the waves generating this component interact. The center of gravity and spreads of a component psd are considered as the characteristic dispersion parameters. The algorithms proposed in these contributions estimate these parameters by approximating the component psd with a certain probability density function (pdf), e.g. in azimuth–of–arrival (AoA) [6–8] and in AoA and azimuth of departure (AoD) [1]. The values of the parameter estimates obtained by using these algorithms depend on the underlying pdfs. However, no rationale behind the selection of the pdfs is given in these contributions. Furthermore, the performance of these algorithms has not been investigated using measurement data.

In order to obtain accurate estimates of the dispersion parameters, a rationale relying on the maximum-entropy (ME) principle [9] is proposed in [10–12] for the selection/derivation of the pdfs characterizing component psds. This rationale utilizes the assumptions that each component psd has fixed center of gravity and spreads, and moreover, no information is available for any other properties, such as the exact shape and number of local maxima, of the component psd. The center of gravity and the spreads of a component psd are described by the first and second moments of a pdf. Thus, using the ME principle we derive a pdf which satisfies the constraint of fixed first and second moments, while maximizes the entropy of any other constraint. The estimates of the dispersion parameters obtained by modeling the component psd with this entropy-maximizing pdf provide the "safest" results in the sense that, they are more accurate than the estimates computed using a pdf subject to any constraint that is invalid in real situations. Based on this rationale, a bivariate von-Mises-Fisher pdf and a Fisher-Bingham-5 (FB_5) pdf are derived for modeling the component psd in AoA and AoD [10] and in elevation and azimuth [11, 12] respectively. Experimental investigations using measurement data demonstrate that these characterizations are applicable in real environments.

In this contribution, we consider a single-input multiple-output (SIMO) scenario where the propagation channel is dispersive in DoA (i.e. azimuth and elevation of arrival) and delay. We propose to characterize the component DoA–delay psd by a multi-variate pdf. The applicability of this characterization method is evaluated using measurement data. With proper modifications, the characterization method can be used to describe dispersion of individual components in DoD (i.e. azimuth and elevation of departure) and delay in a multiple-input single-output (MISO) scenario.

The organization of this contribution is as follows. In Section H.2, the signal model for SIMO channel sounding is presented. Section H.3 introduces

the derived pdf characterizing the shape of the component DoA–delay psd. In Section H.4, the SAGE estimators of the parameters of the psd are briefly described. Section H.5 presents the results from experimental investigations. Finally, concluding remarks are addressed in Section H.6.

H.2 Signal Model and Assumptions

In this section, we introduce the signal model for SIMO channel sounding and state our assumptions on dispersion in DoA and delay in the propagation channel.

H.2.1 Signal Model for SIMO Channel Sounding

The channel sounder considered here has a single antenna in the Tx and M antennas in the Rx. We focus on a scenario where the propagation channel is dispersive in delay $\tau \in \mathbb{R}$ and DoA Ω. Here, Ω is defined to be a unit vector with initial point anchored at the origin $\mathcal{O}$ of a coordinate system located in the vicinity of the Rx array. The end point of Ω lies on a unit sphere $\mathbb{S}_2$ centered at $\mathcal{O}$ [13]. The DoA Ω is uniquely specified by the azimuth of arrival $\phi \in [-\pi, +\pi)$ and the elevation of arrival $\theta \in [0, \pi]$ according to

$$\Omega = \mathbf{e}(\phi, \theta) \doteq \begin{bmatrix} \cos(\phi)\sin(\theta) \\ \sin(\phi)\sin(\theta) \\ \cos(\theta) \end{bmatrix}. \tag{H.1}$$

Following the nomenclature in [13], in one measurement period the continuous-time (complex baseband representation of the) output signal of the mth Rx antenna reads

$$Y_m(t) = \int_{-\infty}^{+\infty} \int_{\mathbb{S}_2} c_m(\Omega)u(t-\tau)H(\Omega, \tau)\mathrm{d}\Omega\mathrm{d}\tau + W_m(t), \tag{H.2}$$

where $c_m(\Omega)$ denotes the response of the mth Rx antenna, $u(t)$ represents the transmitted signal, and $H(\Omega, \tau)$ is referred to as the DoA-delay spread function of the propagation channel. The noise component $W_m(t)$ in (H.2) is a circularly symmetric, spatially and temporally white complex Gaussian process with spectral height σ_w^2.

In a scenario with D components, $H(\Omega, \tau)$ can be decomposed as

$$H(\Omega, \tau) = \sum_{d=1}^{D} H_d(\Omega, \tau), \tag{H.3}$$

189

where the summand $H_d(\mathbf{\Omega}, \tau)$ represents the DoA-delay spread function of the dth component.

Replacing $H(\mathbf{\Omega}, \tau)$ in (H.2) with the sum in (H.3), $Y_m(t)$ can be recast as

$$Y_m(t) = \sum_{d=1}^{D} S_{d,m}(t) + W_m(t), \tag{H.4}$$

where $S_{d,m}(t)$ is the dth component in the received signal, i.e.

$$S_{d,m}(t) = \int_{-\infty}^{+\infty} \int_{\mathbb{S}_2} c_m(\mathbf{\Omega})u(t-\tau)H_d(\mathbf{\Omega}, \tau)\, \mathrm{d}\mathbf{\Omega}\mathrm{d}\tau. \tag{H.5}$$

H.2.2 Assumptions for the DoA-Delay Spread Functions

We assume that the component spread function $H_d(\mathbf{\Omega}, \tau), d \in \{1, \ldots, D\}$ are uncorrelated complex (zero-mean) orthogonal stochastic measures, i.e.

$$\mathrm{E}[H_d(\mathbf{\Omega}, \tau)^* H_{d'}(\mathbf{\Omega}', \tau')] = P_d(\mathbf{\Omega}, \tau)\delta_{dd'}\delta(\mathbf{\Omega} - \mathbf{\Omega}')\delta(\tau - \tau'), \tag{H.6}$$

where $(\cdot)^*$ denotes complex conjugation, $\delta_{..}$ and $\delta(\cdot)$ represent the Kronecker delta and the Dirac delta function respectively, while

$$P_d(\mathbf{\Omega}, \tau) = \mathrm{E}[|H_d(\mathbf{\Omega}, \tau)|^2] \tag{H.7}$$

is the DoA–delay power spectrum of the dth component. Identity (H.6) implies that the DoA-delay spread functions of different components are uncorrelated.

Invoking (H.3), (H.6) and (H.7), we can easily show that the spread function $H(\mathbf{\Omega}, \tau)$ of the propagation channel is a complex zero-mean orthogonal stochastic measure, i.e.

$$\mathrm{E}[H(\mathbf{\Omega}, \tau)^* H(\mathbf{\Omega}', \tau')] = P(\mathbf{\Omega}, \tau)\delta(\mathbf{\Omega} - \mathbf{\Omega}')\delta(\tau - \tau'), \tag{H.8}$$

where

$$P(\mathbf{\Omega}, \tau) = \sum_{d=1}^{D} P_d(\mathbf{\Omega}, \tau) \tag{H.9}$$

is the DoA-delay power spectrum of the propagation channel. The component power spectrum $P_d(\mathbf{\Omega}, \tau)$ can be written as

$$P_d(\mathbf{\Omega}, \tau) = P_d \cdot f_d(\mathbf{\Omega}, \tau), \tag{H.10}$$

with P_d and $f_d(\mathbf{\Omega}, \tau)$ representing respectively, the total average power and the (normalized) direction–delay power spectral density (psd) of the dth component.

H.3   The Direction-Delay Power Spectral Density

In this subsection, we use the Maximum Entropy (ME) rationale proposed in [10, 11] to derive a pdf for modeling the component DoA-delay psd $f_d(\mathbf{\Omega}, \tau)$. We make the assumption that each component psd has its fixed center of gravity and spreads in DoA and in delay. These parameters are represented by the first and the second moments of the pdf. The sought pdf maximizes the entropy under the constraint that its first and second moments are specified.

An ME pdf $f_{\mathrm{ME}}(\mathbf{\Omega}, \tau)$ of the direction variable $\mathbf{\Omega}$ and the delay variable τ under the constraint that its first and second moments are specified, has the form [14]

$$f_{\mathrm{ME}}(\mathbf{\Omega}, \tau) \propto \exp\left\{ \begin{bmatrix} \mathbf{\Omega} - \bar{\mathbf{\Omega}} \\ \tau - \bar{\tau} \end{bmatrix}^{\mathsf{T}} \begin{bmatrix} \mathbf{A} & \mathbf{c} \\ \mathbf{c}^{\mathsf{T}} & -b \end{bmatrix} \begin{bmatrix} \mathbf{\Omega} - \bar{\mathbf{\Omega}} \\ \tau - \bar{\tau} \end{bmatrix} \right\}, \tag{H.11}$$

where $\bar{\mathbf{\Omega}}$ represents the mean direction with azimuth $\bar{\phi}$ and elevation $\bar{\theta}$, i.e. $\bar{\mathbf{\Omega}} = \mathbf{e}(\bar{\phi}, \bar{\theta})$, $\bar{\tau}$ denotes the mean delay, $[\cdot]^{\mathsf{T}}$ represents the transpose operation, $\mathbf{A} \in \mathbb{R}^{3\times3}$ describes the spread of $f_{\mathrm{ME}}(\mathbf{\Omega}, \tau)$ in direction, $b \in \mathbb{R}$ determines the concentration of $f_{\mathrm{ME}}(\mathbf{\Omega}, \tau)$ in delay, and $\mathbf{c} \in \mathbb{R}^3$ describes the dependence of the spread of $f_{\mathrm{ME}}(\mathbf{\Omega}, \tau)$ in direction and in delay.

The parameters $\mathbf{A}$, $\mathbf{c}$ and b arising in (H.11) are all free parameters. We now determine these parameters under the assumption that the conditional pdfs of (H.11) with respect to delay and direction coincide with the Gaussian pdf and the FB_5 pdf respectively. These two pdfs are selected specifically because they also maximize the entropy with specified first and second moments.

The Gaussian pdf for the variable delay reads

$$f(\tau) \propto \exp\{-b(\tau - \bar{\tau})^2\}. \tag{H.12}$$

The FB_5 pdf reads [15]

$$f_{\mathrm{FB}_5}(\mathbf{\Omega}) \propto \exp\{\kappa \boldsymbol{\gamma}_1^{\mathsf{T}} \mathbf{\Omega} + \zeta[(\boldsymbol{\gamma}_2^{\mathsf{T}} \mathbf{\Omega})^2 - (\boldsymbol{\gamma}_3^{\mathsf{T}} \mathbf{\Omega})^2]\}, \tag{H.13}$$

where $\kappa \geq 0$ and $\zeta \in [0, \kappa/2)$ are respectively the concentration parameter and the ovalness parameter of the distribution on the unit sphere $\mathbb{S}_2$, while $\boldsymbol{\gamma}_1$, $\boldsymbol{\gamma}_2$ and $\boldsymbol{\gamma}_3 \in \mathbb{R}^3$ are unit vectors. The matrix $\mathbf{\Gamma} \doteq [\boldsymbol{\gamma}_1, \boldsymbol{\gamma}_2, \boldsymbol{\gamma}_3]$ is uniquely determined by the three angular parameters $\bar{\phi}$, $\bar{\theta}$ and α according to

$$\mathbf{\Gamma} =$$
$$\begin{bmatrix} \sin(\bar{\theta})\cos(\bar{\phi}) & -\sin(\bar{\phi}) & \cos(\bar{\theta})\cos(\bar{\phi}) \\ \sin(\bar{\theta})\sin(\bar{\phi}) & \cos(\bar{\phi}) & \cos(\bar{\theta})\sin(\bar{\phi}) \\ \cos(\bar{\theta}) & 0 & -\sin(\bar{\theta}) \end{bmatrix} \cdot \begin{bmatrix} 1 & 0 & 0 \\ 0 & \cos(\alpha) & -\sin(\alpha) \\ 0 & \sin(\alpha) & \cos(\alpha) \end{bmatrix},$$
$$\tag{H.14}$$

where $\bar{\theta}$ and $\bar{\phi}$ coincide with respectively the elevation and the azimuth of the mean direction, i.e. the first moment of $f_{\text{FB}_5}(\boldsymbol{\Omega})$. The angle α describes tilt of the pdf on $\mathbb{S}_2$. An illustrative description of the meanings of $\boldsymbol{\gamma}_1$, $\boldsymbol{\gamma}_2$ and $\boldsymbol{\gamma}_3$ can be found in [15].

Under the assumption that the pdf $f_{\text{ME}}(\boldsymbol{\Omega}, \tau)$ in (H.11) has the conditional direction pdf (H.13) and the conditional delay pdf (H.12), the sought pdf (H.11) is calculated to be

$$f_{\text{ME}}(\boldsymbol{\Omega}, \tau) \propto \exp\{\kappa\bar{\boldsymbol{\Omega}}^{\mathsf{T}}\boldsymbol{\Omega} + \boldsymbol{\Omega}^{\mathsf{T}}\mathbf{A}(\tau, \zeta, \alpha, \beta)\boldsymbol{\Omega} \\ - b(\tau - \bar{\tau})^2 - 2\eta\mathbf{g}^{\mathsf{T}}(\boldsymbol{\Omega} - \bar{\boldsymbol{\Omega}})(\tau - \bar{\tau})\}. \quad \text{(H.15)}$$

In (H.15), the matrix $\mathbf{A}$ is a function of the delay τ, the ovalness coefficient ζ, as well as the angles α and β that jointly describe how $f_{\text{ME}}(\boldsymbol{\Omega}, \tau)$ is tilted in the direction–delay space, η describes the dependence between the spread in direction and in delay, and

$$\mathbf{g} = \begin{bmatrix} \sin\bar{\phi}\cos\beta - \sin\bar{\theta}\cos\bar{\phi}\sin\beta \\ -\cos\bar{\phi} - \sin\bar{\theta}\sin\bar{\phi}\sin\beta \\ \cos\bar{\theta}\sin\beta \end{bmatrix}.$$

We assume that the component direction–delay psd $f_d(\boldsymbol{\Omega}, \tau)$ in (H.10) is well approximated by the pdf in (H.15), i.e.

$$f_d(\boldsymbol{\Omega}, \tau) = f_{\text{ME}}(\boldsymbol{\Omega}, \tau; \boldsymbol{\theta}_d), \quad \text{(H.16)}$$

where $\boldsymbol{\theta}_d$ contains the component-specific parameters

$$\boldsymbol{\theta}_d \doteq \begin{bmatrix} \bar{\boldsymbol{\Omega}}_d & \bar{\tau}_d & \kappa_d & \zeta_d & \alpha_d & \beta_d & \eta_d & b_d \end{bmatrix}.$$

The center of gravity of $f_d(\boldsymbol{\Omega}, \tau)$ coincides with $(\bar{\boldsymbol{\Omega}}_d, \bar{\tau}_d)$, while the shape of $f_d(\boldsymbol{\Omega}, \tau)$ is determined jointly by the parameters $\kappa_d, \zeta_d, \alpha_d, \beta_d, \eta_d$ and b_d.
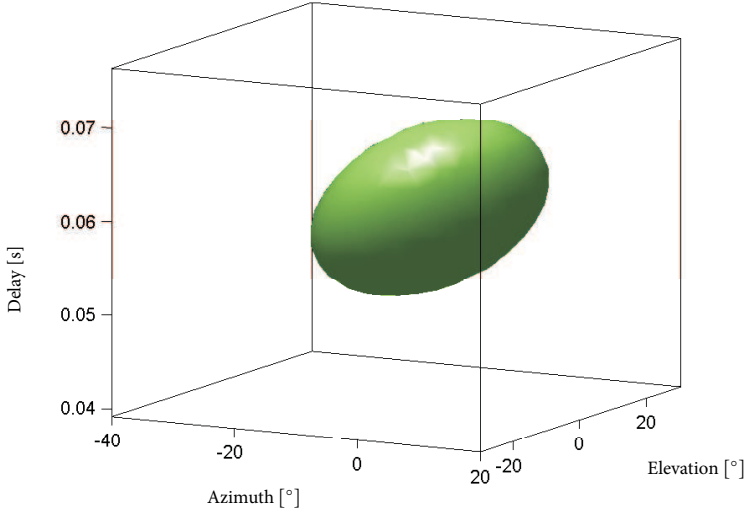
The component azimuth-elevation-delay psd $f_d(\phi, \theta, \tau)$ is induced from $f_d(\boldsymbol{\Omega}, \tau)$ via the mapping $(\phi, \theta, \tau) \mapsto (\boldsymbol{\Omega}, \tau)$ to be

$$f_d(\phi, \theta, \tau) = \sin(\theta) \cdot f_d(\boldsymbol{\Omega}, \tau)\big|_{\boldsymbol{\Omega}=\mathbf{e}(\phi,\theta)} \\ = \sin(\theta) \cdot f_{\text{ME}}(\boldsymbol{\Omega}, \tau; \boldsymbol{\theta}_d)\big|_{\boldsymbol{\Omega}=\mathbf{e}(\phi,\theta)}. \quad \text{(H.17)}$$

Here, $\sin(\theta)$ is the Jacobian resulting from the change of variables. Fig. H.1 depicts an example of the 3 dB-spread surface

$$\left\{(\phi, \theta, \tau) : f_d(\phi, \theta, \tau) = \frac{1}{2}f_d(\bar{\phi}, \bar{\theta}, \bar{\tau})\right\} \quad \text{(H.18)}$$

computed using (H.17) for the parameter setting reported in this figure.

$\bar{\theta}\,[°]$	$\bar{\phi}\,[°]$	$\bar{\tau}\,[\mathrm{ms}]$	κ	ζ	$\alpha\,[°]$	$\beta\,[°]$	η	b
0	0	58	100	0.01	60	270	1000	40000

Fig. H.1: 3 dB-spread surface of the azimuth–elevation–delay psd calculated using (H.15) with the parameter setting given above.

H.4 Parameter Estimator using a SAGE Algorithm

In a scenario with D dispersed components, the unknown parameters in the signal model (H.2) can be concatenated in the vector

$$\boldsymbol{\theta} \doteq \left[P_1, \ldots, P_D, \boldsymbol{\theta}_1, \ldots, \boldsymbol{\theta}_D\right]. \tag{H.19}$$

The ML estimator of $\boldsymbol{\theta}$ can be derived from the signal model (H.2) [16]. However, this estimator requires the solution of a $10D$-dimensional maximization problem, which is too complex for implementation in real applications. As an alternative, we resort to a SAGE algorithm [12, 13] as an approximation of the ML estimator. Due to the limitation of space, we will not describe the SAGE algorithm in this contribution.

H.5 Experimental Investigations

To assess whether the proposed characterization is applicable in real situations, we use the SAGE algorithm to estimate the direction-delay power
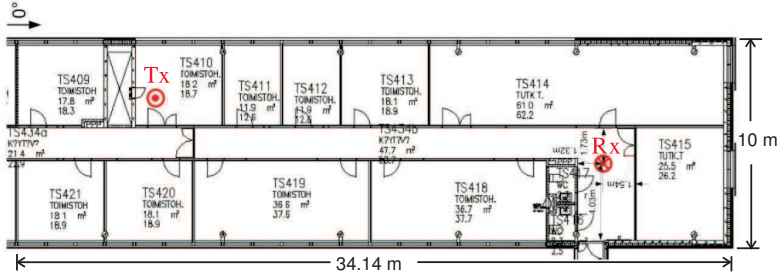
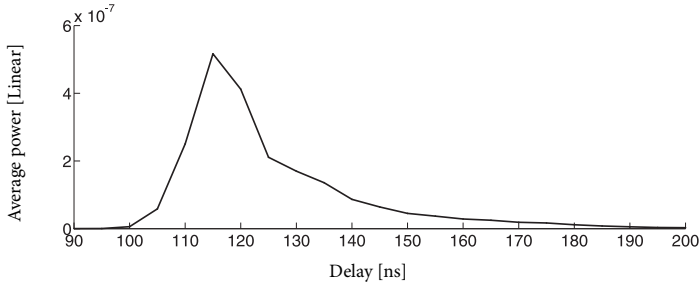Fig. H.2: *Map of the investigated propagation environment.*

Fig. H.3: *Estimated delay power spectrum of the received signal.*

spectrum (H.9) of a propagation channel from measurement data collected using the MIMO wideband channel sounder Propsound CS in the measurement campaign described in [17, 18]. We select a measurement conducted in an office, the premises of which are shown in Fig. H.2. A description of the measurement setting can be found in [10]. The locations of the Rx and Tx were kept fixed during the measurement. A 50-element omni-directional antenna array was used in the Tx. The Rx was equipped with a single omni-directional antenna. A detailed description of the configuration of the Tx antenna array can be found in [19, Fig. 2]. During the measurement, people were moving in the room where the Tx was located. These movements introduced time variations of the channel response.

The data of 200 measurement cycles were collected within a period of 13 seconds. A measurement cycle is referred to as the interval within which all 50 subchannels are sounded once. Fig. H.3 depicts the estimated delay power spectrum calculated from the data.

The SAGE algorithm was used to compute an estimate $\hat{P}(\Omega, \tau)$ of the direction–delay power spectrum $P(\Omega, \tau)$ in (H.9) within the delay ranging
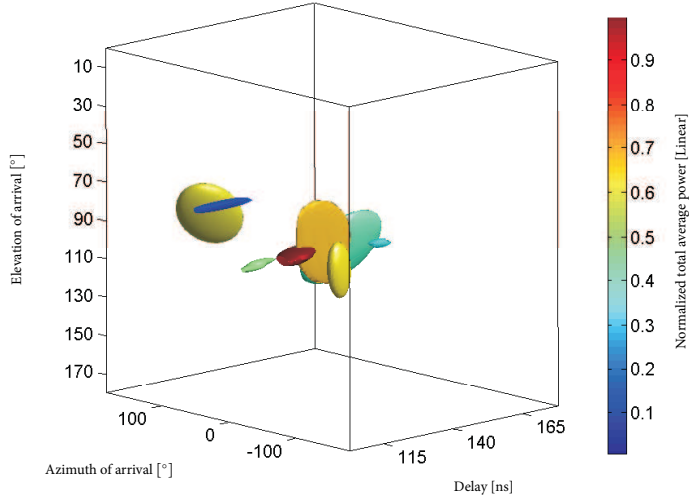
Fig. H.4: 3 *dB-spread surfaces of estimated component azimuth–elevation–delay power spectra. The color of the surfaces codes the component power estimates.*

from 100 ns to 135 ns. The estimated number of components $\hat{D}$ is set according to the number of observed dominant local maxima of the direction-delay Bartlett spectrum computed from the measurement data within this delay range: $\hat{D} = 10$. Fig. H.4 depicts the 3 dB-spread surfaces (H.18) of the estimated component azimuth-elevation-delay psds. The color of the surfaces codes the estimated component power.

Fig. H.5 depicts the estimated azimuth–elevation–delay power spectrum calculated using the Bartlett beamformer [20] and the azimuth–elevation–delay power spectrum estimate

$$\hat{P}(\phi, \theta, \tau) = \sin(\theta) \cdot \hat{P}(\mathbf{\Omega}, \tau)|_{\mathbf{\Omega}=\mathbf{e}(\phi,\theta)}$$

obtained from the parameter estimates computed with the SAGE algorithm. The notation "Bartlett($\mathbf{\Sigma}$)" in Fig. H.5 represents the power spectrum estimate calculated using the Bartlett beamformer applied to the covariance matrix $\mathbf{\Sigma}$ given as an argument. For notational brevity, we call such a spectrum "Bartlett spectrum" in the sequel. The matrices $\hat{\mathbf{\Sigma}}$ and $\mathbf{\Sigma}(\hat{\boldsymbol{\theta}})$ denote respectively the sample covariance matrix and the covariance matrix computed based on $\hat{P}(\mathbf{\Omega}, \tau)$.

It is apparent from Fig. H.5 that the individual components in $\hat{P}(\phi, \theta, \tau)$ are much more concentrated than the corresponding components in both

Bartlett spectra. Furthermore, the symmetry axes of the individual components of $\hat{P}(\phi, \theta, \tau)$ are not parallel to the azimuth and elevation axes. This asymmetry is due to the dependence across different dispersion dimensions. Notice that the Jacobian in (H.17) can also induce an artificial tilting of the components. However, in this particular example most of the components in $\hat{P}(\phi, \theta, \tau)$ are concentrated in an elevation range around $90°$, i.e. over which the impact of the Jacobian is insignificant.

It can be observed from Fig. H.5 that the spectra Bartlett($\hat{\mathbf{\Sigma}}$) and Bartlett($\mathbf{\Sigma}(\hat{\boldsymbol{\theta}})$) are similar. However, some of the foot prints arising in Bartlett($\hat{\mathbf{\Sigma}}$) do not have their counterpart in Bartlett($\mathbf{\Sigma}(\hat{\boldsymbol{\theta}})$), which indicates that the number of components $\hat{D}$ specified in the SAGE algorithm is less than the true number of components in the channel response. Furthermore, Bartlett($\hat{\mathbf{\Sigma}}$) and Bartlett($\mathbf{\Sigma}(\hat{\boldsymbol{\theta}})$) are slightly different in their significant global and local maxima. A possible explanation for this effect is that the derived pdf (H.17) only provides an approximation to the effective psd of individual components.

H.6 Conclusions

In this contribution, we characterized the normalized direction-delay power spectral density of individual dispersed components in the response of the propagation channel with a probability density function (pdf). The proposed pdf maximizes the entropy under the constraint that its first and second moments are specified. A SAGE algorithm was used to estimate the parameters of the component direction–delay power spectra from measurement data. The results showed that the Bartlett spectra obtained from the reconstructed signal covariance matrix computed using the SAGE estimation result look similar to those calculated using the sample covariance matrix. Furthermore, the estimated component direction-delay power spectra are much more concentrated than their counterpart in the Bartlett spectra. These results demonstrate that the proposed pdf along with the SAGE estimator provide an effective tool to characterize direction-delay dispersion in the propagation channel.

References

[1] T. Betlehem, T. D. Abhayapala, and T. A. Lamahewa, "Space-time MIMO channel modelling using angular power distributions," in *Proceedings of the 7th Australian Communications Theory Workshop*, Perth, Australia, February, 1-3 2006, pp. 165 – 170.
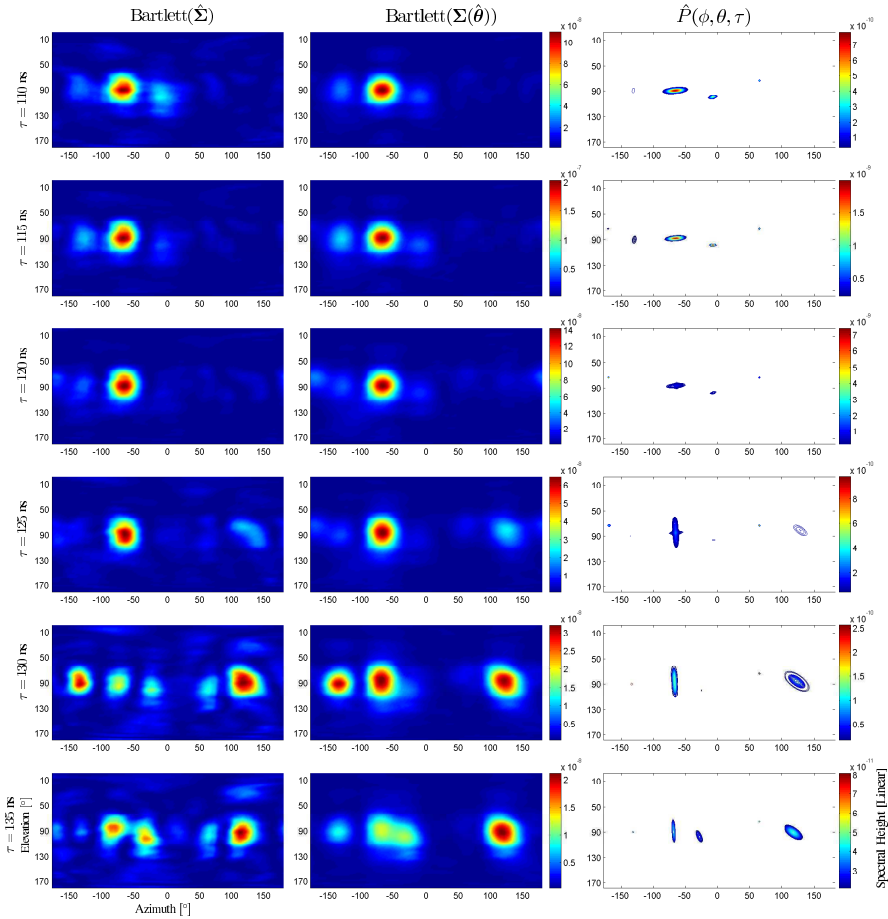
Fig. H.5: Bartlett azimuth–elevation–delay spectrum (first two columns) and estimated azimuth–elevation–delay power spectrum computed from the parameter estimates returned by the SAGE algorithm (third column). Each row is plotted for the delay given to its left.

[2] L. Correia, Ed., *Wireless Flexible Personalised Communications.* John Wiley & Sons, 2001.

[3] J. Medbo, M. Riback, and J. Berg, "Validation of 3GPP spatial channel model including WINNER wideband extension using measurements," in *Proceedings of IEEE 64th Vehicular Technology Conference, (VTC2006-Fall)*, Montréal, Canada, September, 25-28 2006.

[4] N. Czink, X. Yin, H. Özcelik, M. Herdin, E. Bonek, and B. Fleury, "Cluster characteristics in a MIMO indoor propagation environment," *IEEE Transactions on Wireless Communications*, vol. 6, no. 4, pp. 1465–1476, April 2007.

[5] M. Bengtsson and B. Völcker, "On the estimation of azimuth distributions and azimuth spectra," in *Proceedings of the 54th IEEE Vehicular Technology*

Conference (VTC2001-Fall), vol. 3, no. 12, Atlantic City, USA, October 2001, pp.
1612–1615.

[6] T. Trump and B. Ottersten, "Estimation of nominal direction of arrival and
angular spread using an array of sensors," *Signal Processing*, vol. 50, pp. 57–69,
Apr. 1996.

[7] O. Besson and P. Stoica, "Decoupled estimation of DoA and angular spread for
spatially distributed sources," *IEEE Transaction on Signal Processing*, vol. 49, pp.
1872–1882, 1999.

[8] C. B. Ribeiro, E. Ollila, and V. Koivunen, "Stochastic maximum likelihood
method for propagation parameter estimation," in *Proceedings of the 15th IEEE
International Symposium on Personal, Indoor and Mobile Radio Communica-
tions (PIMRC'06)*, vol. 3, Helsinki, Finland, September, 11-14 2004, pp. 1839 –
1843.

[9] E. Jaynes, *Probability theory*.   Cambridge University Press, 2003.

[10] X. Yin, T. Pedersen, N. Czink, and B. H. Fleury, "Parametric characterization
and estimation of bi-azimuth dispersion of path components," in *Proceedings of
the 7th IEEE International Workshop on Signal Processing Advances for Wireless
Communications (SPAWC)*, Nice, France, July 2006.

[11] X. Yin, L. Liu, D. Nielsen, N. Czink, and B. H. Fleury, "Characterization of
the azimuth-elevation power spectrum of individual path components," in
*Proceedings of the International ITG/IEEE Workshop on Smart Antennas (WSA
2007)*, Vienna, Austria, Feb. 2007.

[12] X. Yin, L. Liu, D. Nielsen, T. Pedersen, and B. Fleury, "A SAGE algorithm for
the estimation of direction power spectrum of individual path components," in
*Proceedings of the 50th IEEE Global Telecommunications Conference (GLOBE-
COM 2007)*, Washinton D.C. USA, November 2007.

[13] B. H. Fleury, "First- and second-order characterization of direction dispersion
and space selectivity in the radio channel," *IEEE Transactions on Information
Theory*, no. 6, pp. 2027–2044, Sept. 2000.

[14] K. V. Mardia, "Statistics of directional data," *Journal of the Royal Statistical
Society. Series B (Methodological)*, vol. 37, pp. 349–393, 1975.

[15] J. T. Kent, "The Fisher-Bingham distribution on the sphere," *Journal of the Royal
Statistical Society, Series B (Methodological)*, vol. 44, pp. 71–80, 1982.

[16] H. Krim and M. Viberg, "Two decades of array signal processing research: the
parametric approach," *IEEE Transactions on Signal Processing*, vol. 13, pp. 67–94,
July 1996.

[17] N. Czink, E. Bonek, X. Yin, and B. H. Fleury, "Cluster angular spreads in a
MIMO indoor propagation environment," in *Proceedings of the 16th IEEE In-
ternational Symposium on Personal, Indoor and Mobile Radio Communications
(PIMRC'05)*, vol. 1, Berlin, Germany, September, 11-14 2005, pp. 664–668.

[18] E. Bonek, N. Czink, V. M. Holappa, M. Alatossava, L. Hentilä, J. Nuutinen,
and A. Pal, "Indoor MIMO measurements at 2.55 and 5.25 GHz - a comparison

of temporal and angular characteristics," in *Proceedings of the 15th IST Mobile Summit*, Myconos, Greece, June, 4-8 2006.

[19] X. Yin, T. Pedersen, N. Czink, and B. H. Fleury, "Parametric characterization and estimation of bi-azimuth and delay dispersion of path components," in *Proceedings of The First European Conference on Antennas and Progation (EuCAP'06)*, Acropolis, Nice, France, Nov. 2006.

[20] M. Bartlett, "Smoothing periodograms from time series with continuous spectra," *Nature*, vol. 161, 1948.

A Realistic Radio Channel Model Based on Stochastic Propagation Graphs

Troels Pedersen and Bernard H. Fleury

Conference on Mathematical Modelling, MATHMOD 2006

The layout has been revised.

Abstract

In this contribution a propagation model is derived based on the so-called propagation graph. It is shown by means of Monte Carlo simulations that the obtained model as a result of its inherent structure predicts an exponentially decaying power-delay-profile as commonly reported from measurements. Furthermore, the power-delay-profile obtained with the proposed model exhibit a transition from specular components at small delays to diffuse components at long delays. This feature was also observed, especially in experimental investigations for ultra wide band systems.

I.1 Introduction

The design and optimisation of modern radio communication systems require realistic models of the radio propagation channel, which incorporate dispersion in delay, Doppler frequency, direction of departure, direction of arrival, and polarisation. Often radio communication systems are assessed by Monte Carlo simulations in which stochastic models are used to generate synthetic realisations of the response of the radio propagation channel.

Traditional stochastic radio channel models reflect the statistical properties of the (time-variant or time-invariant) impulse response of the channel between the input of any antenna element at the transmitter site and any antenna element at the receiver site. The probability distributions of the parameters of the channel impulse response are generally difficult to obtain from environment parameters such as the scatterer size and density. Instead, the model parameters are often inferred from measurements. Motivated by experimental results conventional models implement an exponentially decaying power-delay-profile by including various ad-hoc constraints on the random model parameters. The two contributions [1] and [2] follow this approach. In these models a key parameter for modelling the arrival times of individual signal components is the "cluster arrival rate". However this parameter is difficult to derive from a propagation environment. In the model given in [3] the scattering coefficients are corrected to obtain the effects observed from measurements like the exponential decay of the power-delay-profile. These approaches, however, do not reflect the underlying physical mechanisms that lead to this decaying behaviour.

A different approach is followed Franceschetti in [4] where the radio propagation mechanism is modelled as a "stream of photons" performing a continuous random walk in a cluttered environment with constant clutter density. The transmitted signal is a pulse of finite duration. When a photon interacts with an obstacle, it is either absorbed (with a certain probability)

or scattered and changes direction. The Franceschetti model is mainly a descriptive model for the delay power spectrum; it is not possible to obtain realisations of the channel impulse responses from this model. Furthermore, the model does not cover the transition from specular to diffuse signal contributions as observed in [5].

In this contribution we present a stochastic model of the radio-propagation environment based on a random propagation graph. The model can incorporate dispersion in delay, (bi)-directions, Doppler frequency, *etc*. The aim is to obtain a stochastic model that leads to realisations of the channel response with features similar to those observed in measured responses.

The remaining part of the paper is organised as follows. Section I.2 reviews the needed fundamentals of directed graphs. In Section I.3 the stochastic propagation graph is described. Using this model, we give an example of the resulting power-delay-profile in Section I.4. Concluding remarks are adressed in Section I.5.

I.2 *Directed Graphs*

Following [6] we define a directed graph $\mathcal{G}$ as a pair $(\mathcal{V}, \mathcal{E})$ of disjoint sets (of vertices and edges) together with the two mappings init $: \mathcal{E} \rightarrow \mathcal{V}$ and term $: \mathcal{E} \rightarrow \mathcal{V}$ assigning every edge $e \in \mathcal{E}$ an initial vertex init(e) and a terminal point term(e). An edge $e \in \mathcal{E}$ that fulfils init$(e) = $ term(e) is called a loop. Two edges e and e' are parallel if init$(e) = $ init(e') and term$(e) = $ term(e'). A walk (of length K) in a graph $\mathcal{G}$ is a non-empty alternating sequence $\langle v_1, e_1, v_2, e_2, \ldots, e_K, v_{K+1} \rangle$ of vertices and edges in $\mathcal{G}$ such that init$(e_k) = v_k$ and term$(e_k) = v_{k+1}$, $1 \leq k < K$. A path is a walk, with no parallel edges and where the vertices $v_2, \ldots, v_{K-1}$ are distinct. If a path that fulfils $v_1 = v_K$, is called cycle.

I.3 *Propagation graphs*

A propagation graph is a special case of a directed graph. An example of a propagation graph $\mathcal{G} = (\mathcal{V}, \mathcal{E})$ with $\mathcal{V} = \{\text{Tx}, \text{Rx}, \text{S1}, \ldots, \text{S6}\}$ is shown in Fig. I.1. The vertices of a propagation graph model the transmitter (Tx), the receiver (Rx) and the scatterers (S1,…,S6). The edges model the visibility between vertices meaning that a signal emitted from the initial vertex is received delayed and attenuated at the terminal vertex. In the depicted case, the signal emitted from the Tx vertex is observed by the Rx, S1, S4 and S6 vertices, whereas a signal emitted from S3 or S5 is not observable from any vertex. We restrict the discussion to propagation graphs with no loops nor parallel edges.
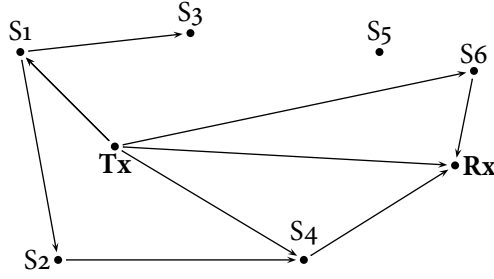
Fig. I.1: One realisation of a propagation graph with six scatterers.

In this case we may identify the edge e with $(\text{init}(e), \text{term}(e)) \in \mathcal{V}^2$ and write $e = (\text{init}(e), \text{term}(e))$ with a slight abuse of notation. With this identification, $\mathcal{E} \subseteq \mathcal{V}^2$. If we consider two vertices $v_1, v_2 \in \mathcal{V}$ then $e = (v_1, v_2) \in \mathcal{E}$ is fulfilled with probability P_e. As the propagation graphs contain no loops, $P_{(v,v)} = 0$. The Tx is a source, and hence there exists no edge with Tx as terminal point, that is $P_{(v,\text{Tx})} = 0$. Likewise, the Rx vertex is considered a sink and therefore $P_{(\text{Rx},v)} = 0$.

The spatial positions of a vertex (a scatterer) $v \in \mathcal{V}$ with respect to some arbitrary origin is given by a spatial displacement $\mathbf{r}_v \in \mathcal{R} \subseteq \mathbb{R}^3$, where $\mathbb{R}$ denotes the real line and $\mathcal{R}$ is the region in which the scatterers that significantly affect the propagation mechanisms between the Tx and Rx are located. The propagation time of the signal propagating along edge $e = (v_1, v_2)$ can be calculated as

$$\Delta\tau_e = \left| \mathbf{r}_{v_1} - \mathbf{r}_{v_2} \right| \cdot c^{-1}, \tag{I.1}$$

where $c \approx 3 \cdot 10^8 \frac{\text{m}}{\text{s}}$ is the speed of light (in air) and $|\cdot|$ denotes the Euclidian norm.

We model a wave interaction with a scatterer v as a scatter-gain g_v weighting all signals arriving at v. The gain can be complex if we work in complex base-band notation (e.g. of narrow-band and wide-band signals) or a real number if we describe the signals directly (e.g. for ultra-wide-band signals). In both cases, we restrict the magnitude of g_v as $|g_v| < 1$. In this contribution we assume that $g_v = g$ for all v, where g is a known constant. In general g_v might be modelled as a random variable. We assume an inverse squared distance power law. Therefore the gain of the signal being scattered by $\text{init}(e)$ observed at $\text{term}(e)$ is given by

$$a_e = g \cdot \Delta\tau_e^{-2}. \tag{I.2}$$

Note that g is not dimensionless; it is given in $[s^2]$. Thus, a_e is dimensionless.

A propagation path $\mathcal{G}$ is defined as a walk $\ell = \langle v_1, e_1, v_2, e_2, \ldots, e_{K_\ell}, v_{K_\ell+1} \rangle$ in $\mathcal{G}$ that fulfils $v_1 = \text{Tx}$ and $v_{K_\ell+1} = \text{Rx}$. The propagation path $\langle \text{Tx}, (\text{Tx}, \text{Rx}), \text{Rx} \rangle$ is called the line-of-sight path provided it exists. The set of all propagation paths in $\mathcal{G}$ is denoted by $\mathcal{L}(\mathcal{G})$. The signal received at the Rx is a superposition of all signal components each propagating via a propagation path $\ell \in \mathcal{L}(\mathcal{G})$. The number of signal components in the received signal therefore equals the cardinality of $\mathcal{L}(\mathcal{G})$. This number can be finite as in the case depicted in Fig. I.1 or infinite if there exists at least one path connecting Tx and Rx with a cycle.

The delay τ_ℓ and gain α_ℓ of a propagation path $\ell \in \mathcal{L}(\mathcal{G})$ can be calculated by repetitively using (I.1) and (I.2) as

$$\alpha_\ell = \prod_{k=1}^{K_\ell} a_{e_k} \quad \text{and} \quad \tau_\ell = \sum_{k=1}^{K_\ell} \Delta\tau_{e_k} \tag{I.3}$$

Hence, the impulse response $h_\mathcal{G}(\tau)$ of the propagation graph can be obtained as

$$h_\mathcal{G}(\tau) = \sum_{\ell \in \mathcal{L}(\mathcal{G})} h_\ell(\tau) \tag{I.4}$$

with $h_\ell(\tau) = \alpha_\ell \delta(\tau - \tau_\ell)$, where $\delta(\cdot)$ is the Dirac unit impulse.

I.4   Simulation Study

In the sequel we investigate the power-delay-profile of the propagation graph model by means of a Monte-Carlo simulation. In this simulation the following scenario is assumed:

1. A constant number N of scatterers is assumed.

2. The region $\mathcal{R}$ is assumed to be a rectangular solid box.

3. The positions of the N scatterers $S1, \ldots, SN$ are drawn according to a uniform distribution defined on $\mathcal{R}$.

4. The Tx and Rx have fixed coordinates, i.e. $\mathbf{r}_{\text{Tx}}, \mathbf{r}_{\text{Rx}} \in \mathcal{R}$ and are known vectors.

5. We define P_e as

$$P_e = \begin{cases} 1 & \text{if } e = (\text{Tx}, \text{Rx}), \\ P_{\text{vis}} & \text{if } e = (v_1, v_2), \text{ where } v_1 \in \mathcal{V}\backslash\{\text{Tx}\}, v_2 \in \mathcal{V}\backslash\{\text{Rx}\}, \text{ and} \\ 0 & \text{otherwise.} \end{cases}$$

Table I.1: Parameter setting for the simulation

Parameters	Values
$\mathcal{R}$	$[0,2] \times [0,3] \times [0,5]\,\mathrm{m}^3$
$\mathbf{r}_{Tx}$	$[1.8, 2.0, 0.5]^{\mathrm{T}}\,\mathrm{m}$
$\mathbf{r}_{Rx}$	$[1.0, 1.0, 4.0]^{\mathrm{T}}\,\mathrm{m}$
N	50
g	$0.1\,\mathrm{s}^2$
P_{vis}	0.08
Number of Monte Carlo runs	100

The settings are given in Table I.1. The region $\mathcal{R}$ has a volume of $30\,\mathrm{m}^3$ which yield an scatter density of roughly $1.7\,\mathrm{m}^{-3}$. In each Monte Carlo run, the propagation graph is generated randomly and the resulting τ_ℓ's and α_ℓ's are computed.

The (averaged) power-delay-profile $\mathrm{E}_{\mathcal{G}}[|h_{\mathcal{G}}(\tau)|^2]$ (assuming a small, but finite observation bandwidth) is reported together with three individual channel realisations in Fig. I.2. It appears from the figure that the proposed model exhibits an exponentially decaying power-delay-profile. Since we assumed an inverse squared distance power law, the exponential power decay stems from the structure of the propagation model alone. The individual channel realisations are depicted as a scatter plot of the $(\tau_\ell, |\alpha_\ell|^2)$'s obtained for each channel realisation. The reported individual channel realisations all exhibit the same behaviour: for $\tau < \Delta\tau_{(\mathrm{Tx,Rx})} = |\mathbf{r}_{Tx} - \mathbf{r}_{Rx}| \cdot c^{-1} \approx 12.4$ ns, the channel impulse response is zero; for $\tau \geq \Delta\tau_{(\mathrm{Tx,Rx})}$ the "occurrence rate" of the signal contribution increases with the delay. As a result the impulse response consists of a specular short-delay part (including the line-of-sight path) and a diffuse tail part for large delay with a transitional mix of specular and diffuse components in the intermediate delay range. This transition effect is observed from measurements in [5]. The behaviour is expected since for a longer delay the signal is spread through the propagation graph and an increasing number of components exist.

I.5   Conclusions

A propagation model based on a stochastic propagation graph was proposed. A propagation graph is defined by a set of vertices (scatterers) and a set of edges (visibility between scatterers). These parameters can be drawn randomly according to some probability density function. Based on measure-
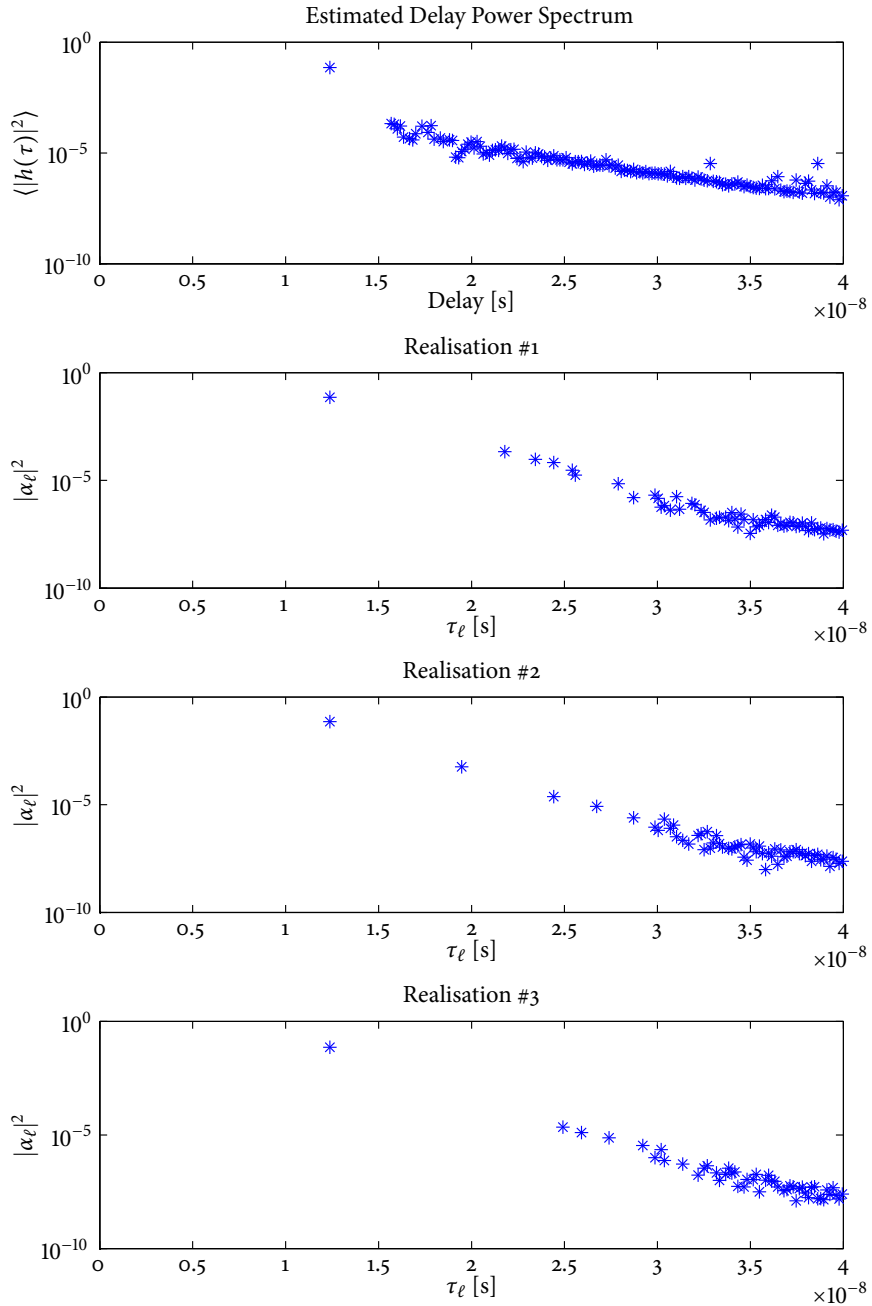
Fig. I.2: *Estimated delay power spectrum and three individual realisations of the channel impulse response. The parameter setting is given in Table I.1.*

ment results conventional models implement an exponentially decaying power-delay-profile by various assumptions. These approaches, however, do not reflect the underlying physical mechanisms that lead to this decaying behaviour. It was shown by simulation that assuming an inverse squared distance power decay, the proposed model yields the often observed exponentially decaying power-delay-profile. This effect stems from the structure of the propagation graph and is not obtained by introducing any artificial assumptions. The channel realisations obtained from the model also exhibit a transition from specular contributions for low delays to a diffuse part at long delays as observed in measurements. The model can be easily extended to include dispersion in directions of departure and arrival.

References

[1] A. A. M. Saleh and R. A. Valenzuela, "A statistical model for indoor multipath propagation channel," *IEEE J. Sel. Areas Commun.*, vol. SAC-5, no. 2, pp. 128–137, Feb. 1987.

[2] Q. H. Spencer, B. Jeffs, M. Jensen, and A. Swindlehurst, "Modeling the statistical time and angle of arrival characteristics of an indoor multipath channel," *IEEE J. Sel. Areas Commun.*, vol. 18, no. 3, pp. 347–360, 2000.

[3] J. Laurila, A. F. Molisch, and E. Bonek, "Influence of the scatterer distribution on power delay profiles and azimuthal power spectra of mobile radio channels," *Proceedings of the IEEE 5th Int. Symposium on Spread Spectrum Techniques and Applications*, vol. 1, pp. 267–271, 1998.

[4] M. Franceschetti, "Stochastic rays pulse propagation," *IEEE Trans. Antennas Propag.*, vol. 52, no. 10, pp. 2742–2752, Oct. 2004.

[5] J. Kunisch and J. Pamp, "Measurement results and modeling aspects for the UWB radio channel," in *Ultra Wideband Systems and Technologies, 2002. Digest of Papers. 2002 IEEE Conf. on*, May 2002, pp. 19–24.

[6] R. Diestel, *Graph Theory*. Springer-Verlag, 2000. [Online]. Available: http://www.math.uni-hamburg.de/home/diestel/books/graph.theory/

Radio Channel Modelling Using Stochastic Propagation Graphs

Troels Pedersen, and Bernard H. Fleury

IEEE International Conference on Communications. ICC 2007

Erratum: Equation (J.1) *on page 216 should read:*

$$A_e(f) = g_e \cdot \exp(-j2\pi\tau_e f), \quad e \in \mathcal{E}.$$

Abstract

In this contribution the radio channel model proposed in [1] is extended to include multiple transmitters and receivers. The propagation environment is modelled using random graphs where vertices of a graph represent scatterers and edges model the wave propagation between scatterers. Furthermore, we develop a closed form analytical expression for the transfer matrix of the propagation graph. It is shown by simulation that impulse response and the delay-power spectrum of the graph exhibit exponentially decaying power as a result of the recursive scattering structure of the graph. The impulse response exhibits a transition from specular to diffuse signal contributions as observed in measurements.

J.1   Introduction

The design and optimisation of modern radio communication systems require realistic models of the radio propagation channel, which incorporate dispersion in delay, Doppler frequency, direction of departure, direction of arrival, and polarisation. Often radio communication systems are assessed by Monte Carlo simulations in which stochastic models are used to generate synthetic realisations of the response of the (radio) propagation channel.

Traditional stochastic radio channel models reflect the statistical properties of the (time-variant or time-invariant) impulse response of the channel between the input of any antenna element at the transmitter site and the output of any antenna element at the receiver site. The probability distributions of the parameters of the channel impulse response are generally difficult to obtain from environment parameters such as the scatterer size and density. Instead, the model parameters are often inferred from measurements. Motivated by experimental results, conventional models implement an exponentially decaying delay-power spectrum and impulse response magnitude by including various ad-hoc constraints on the random model parameters. The two contributions [2] and [3] follow this approach. In these models a key parameter for modelling the arrival times of individual signal components is the "cluster arrival rate". However this parameter is difficult to derive from a propagation environment. In the model given in [4] the scattering coefficients are corrected to account for the effects observed experimentally like the exponential decay of the delay-power spectrum. These approaches, however, do not reflect the underlying physical mechanisms that lead to this decaying behaviour.

A different approach is followed by Franceschetti in [5] where the radio propagation mechanism is modelled as a "stream of photons" performing a

continuous random walk in a cluttered environment with constant clutter density. The transmitted signal is a pulse of finite duration. When a photon interacts with an obstacle, it is either absorbed (with a certain probability) or scattered and changes direction. The Franceschetti model is mainly a descriptive model for the delay-power spectrum; it is not possible to obtain realistic realisations of the channel impulse responses from this model. Furthermore, the model does not cover the transition from specular to diffuse signal contributions as observed in [6] for ultra wide band measurements. This transition effect is well-known within the field of room acoustics [7]. In a recently published work [8] Andersen *et. al* model the exponentially decaying power of the diffuse tail of the impulse response by applying Sabine's reverberation formula commonly used in room acoustics. In the work presented in [1] the propagation environment was modelled using random graphs where vertices of a graph represent scatterers and edges model the wave propagation between scatterers. When a graph is generated, the corresponding realisation of the channel impulse response can be computed by exhaustively searching for propagation paths that connect the transmitter to the receiver. The obtained impulse response exhibits the specular-to-diffuse transition.

In this contribution we extend the model described in [1] to include multiple transmitters and receivers. We develop a closed form analytical expression for the transfer matrix. The derivation is inspired from the method used in the room acoustical model proposed in [9].

The remaining part of the paper is organised as follows. In Section J.2 the modelling concept based directed graphs is presented and a model of the propagation environment is introduced. In Section J.3 an analytical expression for the transfer matrix of the propagation graph is derived. Numerical examples are given in Section J.4 and concluding remarks are addressed in Section J.5.

J.2   *Modelling Propagation Using Graphs*

In the following we describe the underlying principles for modelling the propagation mechanisms using graphs. In a typical propagation scenario, the electromagnetic signal emitted by a transmitter propagates through the environment interacting with a number of objects called scatterers. The receiver, which is usually placed away from the transmitter, picks up the transmitted signal. If a line-of-sight exists between the transmitter and receiver, direct propagation occurs. In other cases, indirect propagation via one ore more scatterers can occur. In the following we represent the propagation environment as a directed graph where the vertices represent the transmitters,

receivers, and scatterers, and the edges represent visibilities between the vertices. First, the necessary notation is introduced.

J.2.1 Directed Graphs

Following [10] we define a directed graph $\mathcal{G}$ as a pair $(\mathcal{V}, \mathcal{E})$ of disjoint sets (of vertices and edges) together with the two mappings init : $\mathcal{E} \to \mathcal{V}$ and term : $\mathcal{E} \to \mathcal{V}$ assigning every edge $e \in \mathcal{E}$ an initial vertex init(e) and a terminal vertex term(e).

Two edges e and e' are parallel if init(e) = init(e') and term(e) = term(e'). When the discussion is restricted to graphs without parallel edges we may identify the edge e with $(\text{init}(e), \text{term}(e)) \in \mathcal{V}^2$ and write $e = (\text{init}(e), \text{term}(e))$ with a slight abuse of notation. With this identification, $\mathcal{E} \subseteq \mathcal{V}^2$.

A walk (of length K) in a graph $\mathcal{G}$ is a non-empty alternating sequence $\langle v_1, e_1, v_2, e_2, \ldots, e_K, v_{K+1} \rangle$ of vertices and edges in $\mathcal{G}$ such that init(e_k) = v_k and term(e_k) = v_{k+1}, $1 \le k < K$. An edge $e \in \mathcal{E}$ that fulfils init(e) = term(e) is called a loop. Thus, by definition, a loop is a walk of length 1. A path is a walk, without parallel edges, where the vertices $v_2, \ldots, v_{K-1}$ are distinct. A path that fulfils $v_1 = v_K$ is called a cycle. The outdegree of a vertex v denoted by $\deg_i(v)$ is the number of edges with initial vertex v.

J.2.2 Propagation Graphs

A propagation graph is a directed graph $\mathcal{G} = (\mathcal{V}, \mathcal{E})$ where the vertices model transmitters, receivers and scatterers, and the edges model the propagation conditions between the vertices.

The vertex set of a propagation graph is a union of three disjoint sets: $\mathcal{V} = \mathcal{V}_t \cup \mathcal{V}_s \cup \mathcal{V}_r$, where $\mathcal{V}_t = \{\text{Tx}1, \ldots, \text{Tx}M_1\}$ is the set of transmit vertices, $\mathcal{V}_r = \{\text{Rx}1, \ldots, \text{Rx}M_2\}$ the set of receive vertices, and $\mathcal{V}_s = \{\text{S}1, \ldots, \text{S}N\}$ is the set of scatterer vertices. Fig. J.1 shows a propagation graph for a communication system with $M_1 = 5$ transmitters, $M_2 = 3$ receivers, and $N = 6$ scatterers. The depicted graph has one cycle. Each vertex $v \in \mathcal{V}$ is assigned a coordinate in space with respect to a coordinate system and arbitrarily selected origin. The vector $\mathbf{r}_v \in \mathcal{R} \subseteq \mathbb{R}^3$, denotes the displacement vector of v from the origin of the coordinate system. The set $\mathcal{R}$ is the region in which contains the scatterers that significantly affect the propagation mechanisms between the transmitters and a receivers in the graph.

In the case depicted in Fig. J.1, all transmit vertices are located in the close proximity of each other, away from the other vertices which is also the case for the receive vertices. This corresponds to the case where the transmitter

and receiver sites are equipped with antenna arrays. This is not the case in multi-user systems, where the transmitters and receivers are spread evenly in space.

The edges of a propagation graph model the propagation, or the visibility, between vertices meaning that a signal emitted from the initial vertex is observed in a filtered (e.g. delayed and attenuated) version at the terminal vertex. Due to this conceptual interpretation of an edge, a propagation graph does not have parallel edges. In this case we may identify the edge e with $(\text{init}(e), \text{term}(e)) \in \mathcal{V}^2$ and write $e = (\text{init}(e), \text{term}(e))$ with a slight abuse of notation. With this identification, $\mathcal{E} \subseteq \mathcal{V}^2$. Notice that $\mathcal{G}$ may have "anti-parallel" edges, i.e. if the edge $e = (v, v')$ is in the graph, the edge $e' = (v', v)$ can exist. We restrict the discussion to propagation graphs where scatterers cannot "see" themselves. Hence we only deal with graphs without loops. However, the propagation graphs may have cycles. The transmit vertices are considered as purely sources with outgoing edges. Likewise, the receivers are considered as sinks with only incoming edges.

The signal propagates in the graph in the following way. Each transmitter emits a signal that propagate via the edges of the graph. The signals observed by a receiver vertex is the sum of the signals arriving via the incoming edges. The scatterers sum up the signals arriving via the incoming edges and re-emit the sum-signals via the outgoing edges. When a signal propagates along an edge, or interacts with a scatterer, the signal undergoes dispersion in time, depending on the length of the edge and the particular scattering mechanisms. The joint mechanism of propagating along an edge and interaction with a scatterer is assumed linear, thus the time dispersion of the signal can be represented as a convolution with an impulse response or, in the Fourier domain, as a multiplication with a transfer function.

J.2.3 *Model of the Propagation Mechanisms*

In the following we discuss a model where the propagation along the edges is assumed to be non-dispersive in delay in the sense that the impulse response of each edge is merely a scaled and delayed Dirac impulse. Let g_e and τ_e denote respectively the complex gain and propagation time of edge e. Thus the edge transfer functions $A_e(f)$ takes the form

$$A_e(f) = g_e \cdot \exp(j2\pi\tau_e f), \quad e \in \mathcal{E}. \tag{J.1}$$

The complex gain g_e includes the gain due to the propagation loss along edge e and the scattering coefficient due to the interaction at $\text{term}(e)$. This scatterer model is suitable in situations where the electromagnetic properties of the
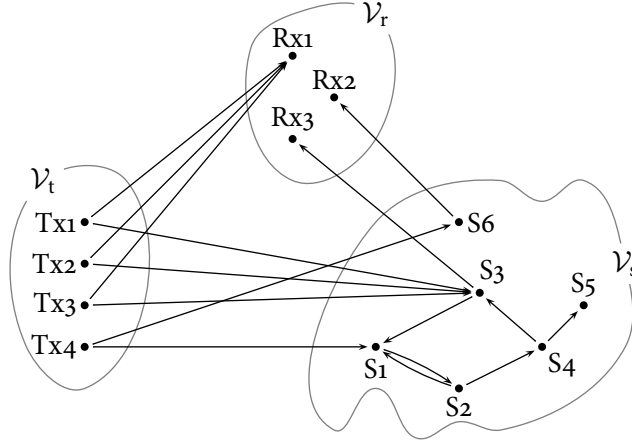
Fig. J.1: A propagation graph with four transmit vertices (M_1 = 4), three receive vertices (M_2 = 3), and six scatterer vertices (N = 6).

scatterers are constant over the bandwidth of the transmitted signal. In the sequel a method for determining the edge gains and attenuations is described.

The propagation time τ_e of a signal propagating along edge $e = (v, v')$ in $\mathcal{E}$ can be calculated from the coordinates of v and v' as

$$\tau_e = \frac{|\mathbf{r}_v - \mathbf{r}_{v'}|}{c}, \tag{J.2}$$

where $c \approx 3 \cdot 10^8$ m/s is the speed of light (in vacuum) and $|\cdot|$ is the Euclidean norm. The power gain $|g_e|^2$ of $e \in \mathcal{E}$ is defined as

$$|g_e|^2 = \left(\frac{g}{1 + |\mathbf{r}_v - \mathbf{r}_{v'}|} \right)^2 \cdot \frac{1}{\deg_o(v)}. \tag{J.3}$$

For large edge lengths $|\mathbf{r}_v - \mathbf{r}_{v'}|$, (J.3) behaves like the standard inverse squared distance power law. Notice that since $\deg_o(v) = 0$ if and only if $e \notin \mathcal{E}$, and the term $1 + |\mathbf{r}_v - \mathbf{r}_{v'}| \geq 1$, the gain $|g_e|^2$ is finite for all $e \in \mathcal{V}^2$. The definition (J.3) ensures that the power leaving a vertex is always smaller than the power entering the vertex. The phase of g_e can be chosen according to some appropriate model. As an example, when a multiuser systems is modelled, this phase can be assumed to be uniformly distributed on the interval $[0; 2\pi)$. However, if the transmitters and receivers forms arrays, then more careful modelling of the phases is necessary.

J.2.4 Modelling Systems With Antenna Arrays

Considering a system where the transmit antennas are spatially grouped such that they form an array, it is customary to make the so-called 'small-scale characterisation'. This assumption states that the overall geometry of each propagation path is the same for all antenna elements of one antenna array. This corresponds to a propagation graph where all elements of an array share the same visibilities. We can distinguish 'small' and 'large' arrays as follows:

An array $\mathcal{A} \subseteq \mathcal{V}_t$ of transmit vertices is a *small array*, if, and only if, for any edge $e = (v, v')$ from a transmitter vertex $v \in \mathcal{A}$ to a receiver or scatterer vertex $v' \in \mathcal{V}_s \cup \mathcal{V}_r$ the set of edges $\{(v'', v') : v'' \in \mathcal{A}\}$ is a subset of $\mathcal{E}$. If an array is not small then it is a *large array*. The generalisation of the definition to include receive antennas is obvious.

In the situation depicted in Fig J.1, the transmit antennas Tx1, Tx2, Tx3 and Tx4 form an array $\mathcal{A} = \{Tx1, Tx2, Tx3, Tx4\}$. As can be seen from the figure, edge $(Tx1, Rx1)$ exists. Since there is not an edge $(Tx4, Rx1)$ in the graph, the array $\mathcal{A}$ is a large array. It can be checked that the sub-array $\{Tx1, Tx2, Tx3\}$ form a small array.

It should be noticed that not all practical arrays are small (see [11] for an example). However, by applying appropriate restrictions on the edge-set of the graph, the propagation graphs can be used to model both small and large arrays. For a small array $\mathcal{A}$, it seems to be natural to assume that the edge gains of the set of edges which connects the elements of $\mathcal{A}$ to a particular vertex $v \notin \mathcal{A}$ all have the same phase.

J.3 The Transfer Matrix of a Propagation Graph

In the following we derive the input-output relation of a propagation graph. By the definition of the propagation graph, there are no other signal sources than the vertices in $\mathcal{V}_t$. Thus by assuming that the propagation mechanisms are linear and time-invariant, the Fourier domain version of the input-output relation can be written as

$$\mathbf{Y}(f) = \mathbf{H}(f)\mathbf{X}(f), \tag{J.4}$$

where $\mathbf{H}(f)$ is $M_2 \times M_1$ transfer matrix. The M_1-dimensional input signal $\mathbf{X}(f)$ is defined as

$$\mathbf{X}(f) = \left[X_1(f), \ldots, X_{M_1}(f)\right]^{\mathsf{T}}, \tag{J.5}$$

where $X_m(f)$ is the signal emitted by transmitter Txm, and $[\cdot]^{\mathsf{T}}$ denotes the transposition operator. The output signal vector $\mathbf{Y}(f)$ is defined as

$$\mathbf{Y}(f) = \left[Y_1(f), \ldots, Y_{M_2}(f)\right]^{\mathsf{T}}, \tag{J.6}$$

where $Y_m(f)$ is the Fourier transform of the signal observed by receiver Rxm.

Similar, to $\mathbf{X}(f)$ and $\mathbf{Y}(f)$ we can define a vector $\mathbf{Z}(f)$ to describe the signal observed at the scatterers as

$$\mathbf{Z}(f) = [Z_1(f), \dots, Z_N(f)]^\mathsf{T}, \tag{J.7}$$

where the nth entry denotes the Fourier transform of the signal observed at scatterer vertex Sn.

We form the $M_1 + M_2 + N$ dimensional complex state vector $\mathbf{C}(f)$ as

$$\mathbf{C}(f) = [C_1(f), \dots, C_n(f), \dots C_{M_1+M_2+N}(f)]^\mathsf{T}, \tag{J.8}$$

where $C_n(f)$ is the state variable of vertex v_n. By selecting the indexing of the vertices according to

$$v_n \in \begin{cases} \mathcal{V}_\mathrm{t}, & n = 1, \dots, M_1 \\ \mathcal{V}_\mathrm{r}, & n = M_1 + 1, \dots, M_1 + M_2 \\ \mathcal{V}_\mathrm{s}, & n = M_1 + M_2 + 1, \dots, M_1 + M_2 + N, \end{cases} \tag{J.9}$$

it is seen that

$$\mathbf{C}(f) = [\mathbf{X}(f)^\mathsf{T}, \mathbf{Y}(f)^\mathsf{T}, \mathbf{Z}(f)^\mathsf{T}]^\mathsf{T}. \tag{J.10}$$

Let us for a moment consider the edge $e = (v_n, v_{n'})$ in $\mathcal{E}$. A filtered version of the signal $C_n(f)$ emitted by vertex v_n is observed at vertex $v_{n'}$. The signal observed at vertex $v_{n'}$ via edge e reads $A_e(f)C_n(f)$ where $A_e(f)$ is the edge transfer function defined in (J.1). In other words, the transfer function $A_e(f)$ describes the propagation along the edge e, i.e. the propagation delay, attenuation, and the scattering coefficient at the initial vertex of e. By collecting the edge transfer functions to a matrix using the indexing described in (J.9) we obtain the weighted adjacency matrix $\mathbf{A}(f) \in \mathbb{C}^{(M_1+M_2+N)\times(M_1+M_2+N)}$ of the entire propagation graph $\mathcal{G}$:

$$[\mathbf{A}(f)]_{nn'} = \begin{cases} A_{(v_n,v_{n'})}(f) & \text{if } (v_n, v_{n'}) \in \mathcal{E}, \\ 0 & \text{otherwise.} \end{cases} \tag{J.11}$$

Element n, n' of $\mathbf{A}(f)$ is the transfer function from vertex v_n to vertex $v_{n'}$ of $\mathcal{G}$. Due to the selected vertex indexing the weighted adjacency matrix can be partitioned as

$$\mathbf{A}(f) = \begin{bmatrix} \mathbf{0} & \mathbf{0} & \mathbf{0} \\ \mathbf{D}(f) & \mathbf{0} & \mathbf{R}(f) \\ \mathbf{T}(f) & \mathbf{0} & \mathbf{B}(f) \end{bmatrix}, \tag{J.12}$$

where $\mathbf{0}$ denotes a zero matrix of the appropriate dimension and

$$\mathbf{D}(f) \in \mathbb{C}^{M_2 \times M_1} \quad \text{connects transmitters to receivers} \tag{J.13}$$

$$\mathbf{R}(f) \in \mathbb{C}^{M_2 \times N} \quad \text{connects scatterers to receivers} \tag{J.14}$$

$$\mathbf{T}(f) \in \mathbb{C}^{N \times M_1} \quad \text{connects transmitters to scatterers} \tag{J.15}$$

$$\mathbf{B}(f) \in \mathbb{C}^{N \times N} \quad \text{interconnects the scatterers.} \tag{J.16}$$

The special structure of $\mathbf{A}(f)$ origins from the structure of the propagation graph. The first M_1 rows are zero because, we do not accept incoming edges into the transmitters. Likewise column $M_1 + 1, \ldots, M_1 + M_2$ are all zero since the receiver vertices have no outgoing edges. Furthermore, since the propagation graph contains no loops the entries of the main diagonal of the adjacency matrix $\mathbf{A}(f)$ are zero. Therefore the entries of the main diagonal of $\mathbf{B}(f)$ are zero.

The state vector $\mathbf{C}(f)$ can be rewritten as the sum

$$\mathbf{C}(f) = \sum_{k=0}^{\infty} \mathbf{C}_k(f), \tag{J.17}$$

where $\mathbf{C}_k(f) = [\mathbf{X}_k(f)^\mathsf{T}, \mathbf{Y}_k(f)^\mathsf{T}, \mathbf{Z}_k(f)^\mathsf{T}]^\mathsf{T}$ denotes the signal contribution that has propagated along k edges. The signal emitted by the transmitters has not propagated via any edges and therefore $\mathbf{X}_0(f) = \mathbf{X}(f)$. For $k = 0$ we have

$$\mathbf{C}_0(f) = [\mathbf{X}(f)^\mathsf{T}, \mathbf{0}^\mathsf{T}, \mathbf{0}^\mathsf{T}]^\mathsf{T}, \tag{J.18}$$

and for $k \geq 1$ we have the recursive relation:

$$\mathbf{C}_{k+1}(f) = \mathbf{A}(f)\mathbf{C}_k(f), \quad k \geq 1. \tag{J.19}$$

As a consequence of (J.17), the output signal vector can be decomposed as the sum

$$\mathbf{Y}(f) = \sum_{k=1}^{\infty} \mathbf{Y}_k(f), \tag{J.20}$$

where $\mathbf{Y}_k(f)$ is the received signal component that has propagated via k edges from the transmitter to the receiver. Thus $\mathbf{Y}_1(f)$ is the component originating from direct propagation from the transmitters to the receivers. By direct computation of $\mathbf{C}_1(f)$ using (J.19) and (J.18) we see that

$$\mathbf{C}_1(f) = \mathbf{A}(f)\mathbf{C}_0(f) = \begin{bmatrix} \mathbf{0} \\ \mathbf{D}(f)\mathbf{X}(f) \\ \mathbf{T}(f)\mathbf{X}(f) \end{bmatrix}. \tag{J.21}$$

It follows from (J.21) that

$$\mathbf{Y}_1(f) = \mathbf{D}(f)\mathbf{X}(f). \tag{J.22}$$

By inspection of the series $\mathbf{A}^2(f), \mathbf{A}^3(f), \dots$ it is readily recognised that

$$\mathbf{A}^k(f) = \begin{bmatrix} \mathbf{0} & \mathbf{0} & \mathbf{0} \\ \mathbf{R}(f)\mathbf{B}^{k-2}(f)\mathbf{T}(f) & \mathbf{0} & \mathbf{R}(f)\mathbf{B}^{k-1}(f) \\ \mathbf{B}^{k-1}(f)\mathbf{T}(f) & \mathbf{0} & \mathbf{B}^k(f) \end{bmatrix}, \ k \geq 2. \tag{J.23}$$

Inserting (J.22) and (J.23) into (J.20) and using (J.19) yields

$$\mathbf{Y}(f) = \mathbf{Y}_1(f) + \sum_{k=2}^{\infty} \mathbf{Y}_k(f) \tag{J.24}$$

$$= \mathbf{D}(f)\mathbf{X}(f) + \sum_{k=2}^{\infty} \mathbf{R}(f)\mathbf{B}^{k-2}(f)\mathbf{T}(f)\mathbf{X}(f) \tag{J.25}$$

$$= \left[\mathbf{D}(f) + \sum_{k'=0}^{\infty} \mathbf{R}(f)\mathbf{B}^{k'}(f)\mathbf{T}(f) \right] \mathbf{X}(f) \tag{J.26}$$

$$= \underbrace{\left[\mathbf{D}(f) + \mathbf{R}(f)(\mathbf{I} - \mathbf{B}(f))^{-1}\mathbf{T}(f) \right]}_{\mathbf{H}(f)} \mathbf{X}(f). \tag{J.27}$$

Identity (J.27) is obtained using geometric series for matrices [12, p. 427], which holds under the condition that the maximum of the eigenvalue magnitudes of $\mathbf{B}(f)$ is less than unity for all frequencies considered. This constraint is always fulfilled for a propagation graph due the definition of the edge gain (J.3).

Equation (J.19) shows the structure of the propagation mechanism. The radio signal is re-scattered successively in the propagation environment. This effect results in the geometric series in (J.26). From (J.27) we see that the transfer matrix $\mathbf{H}(f)$ consists of the two following terms: $\mathbf{D}(f)$ representing direct propagation between the transmitters and receivers and $\mathbf{R}(f)(\mathbf{I} - \mathbf{B}(f))^{-1}\mathbf{T}(f)$ describing indirect propagation.

J.4 Numerical Examples

Using the analytical results from Section J.3 we are able to compute the transfer matrix of a particular propagation graph. The propagation graph is fully defined by the vertex set, the vertex locations, and the edge set of the graph. Thus, a propagation graph can be generated stochastically by randomly placing the vertices and generating the edges set.

In the sequel we investigate the impulse response and the delay-power spectrum of the propagation graph model by means of a Monte-Carlo experiment. The following scenario is assumed:

- The region $\mathcal{R}$ is assumed to be a rectangular solid box.

- To simplify the discussion we consider a single-input single-output ($M_1 = M_2 = 1$) system. The locations of the transmitter and receiver vertices are fixed throughout the experiment.

- The number N of scatterers is assumed constant.

- The positions of the scatterer vertices are drawn according to a uniform distribution defined on $\mathcal{R}$.

- We define the occurrence probability $P_{(v,v')}$ of an edge $(v, v') \in \mathcal{V}^2$ as

$$P_{(v,v')} = \begin{cases} P_{\text{dir}} & \text{if } (v, v') = (\text{Tx, Rx}) \\ 0 & \text{if } v = v' \\ 0 & \text{if } v' = \text{Tx or } v = \text{Rx, and} \\ P_{\text{vis}} & \text{otherwise,} \end{cases}$$

where P_{dir} denotes the probability of the direct propagation between the transmitter and receiver. When $P_{\text{dir}} = 0$ the direct term $\mathbf{D}(f)$ in (J.27) takes the value zero corresponding to a non-line-of-sight scenario. When $P_{\text{dir}} = 1$ direct propagation between transmitter and receiver always occurs which corresponds to a line-of-sight scenario. In this case $\mathbf{D}(f)$ is non-zero.

The parameter settings are given in Table J.1. In each Monte Carlo run the following steps are performed:

1. Generate scatterer positions $\mathbf{r}_v$, $v \in \mathcal{V}_{\text{s}}$.

2. Generate the edge set $\mathcal{E}$.

3. Compute the transfer function $\mathbf{H}(f)$ for the frequencies $f = f_{\text{min}}$, $f_{\text{min}} + \Delta f, \ldots, f_{\text{max}}$

4. Compute the inverse Fourier transform of the transfer function applying a Hanning window to reduce side-lobes.

An example of an obtained transfer function for $P_{\text{dir}} = 0, 1$ and corresponding impulse response are reported in Fig. J.2. The magnitude of the transfer function for the $P_{\text{dir}} = 0$ exhibits fading over the considered frequency band, whereas the function obtained in the $P_{\text{dir}} = 1$ case, which is about 10 dB higher, is more constant. The reported impulse responses magnitudes are roughly exponentially decaying. In the reported case, the impulse responses exhibit a concentration of power into "clusters". Inspection

Table J.1: *Parameter setting for the simulation*

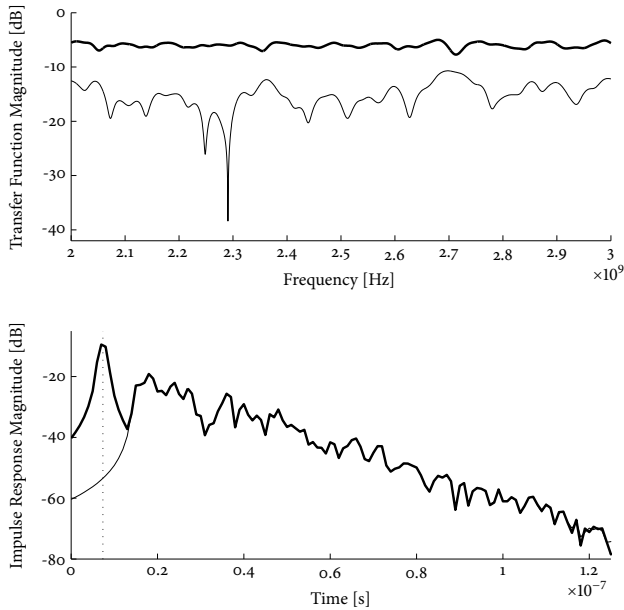| Parameters	Values
$\mathcal{R}$	$[0,5] \times [0,10] \times [0,3.5]\,\text{m}^3$
$\mathbf{r}_{\text{Tx}}$	$[1.8,\ 2.0,\ 0.5]^{\text{T}}\,\text{m}$
$\mathbf{r}_{\text{Rx}}$	$[1.0,\ 4.0,\ 1.0]^{\text{T}}\,\text{m}$
N	20
g	$0.8\,\text{s}^2$
P_{vis}	0.8
Number of Monte Carlo runs	1000
Signal bandwidth $[f_{\min}, f_{\max}]$	$[2,3]\,\text{GHz}$
Δf	$0.5\,\text{MHz}$
IFFT window	Hanning

Fig. J.2: *Examples of transfer functions (top) and the corresponding impulse responses (bottom) for $P_{\text{dir}} = 1$ (thick line) and $P_{\text{dir}} = 0$ (thin line). The dotted vertical line marks the propagation delay of the direct edge between the transmitter and the receiver (line-of-sight). The parameter setting used in the simulations is listed in Table J.1.*
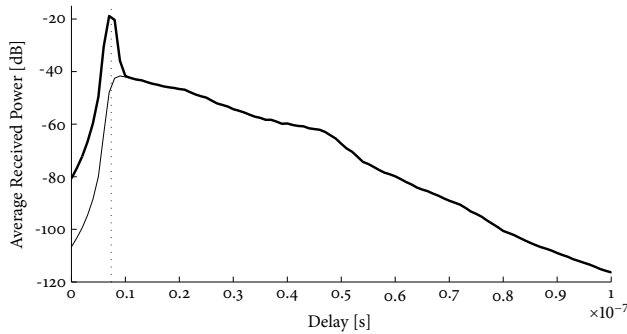
Fig. J.3: Delay-power spectrum computed from the Monte Carlo experiment for $P_{dir} = 1$ (thick line) and $P_{dir} = 0$ (thin line). The dotted vertical line marks the propagation delay of the direct edge between the transmitter and the receiver. The parameter setting is listed in Table J.1.

of the vertex positions of the particular realisation revealed that this effect is not caused by geometrically clustering of the scatterers but is an effect of the structure of the graph.

An estimate of the delay-power spectrum can be obtained by computing the mean squared-magnitude of the generated impulse response realisations. Estimates of the delay-power spectra for $P_{dir} = 0, 1$ each obtained from 1000 realisations of the impulse response are shown in Fig. J.3. Apart from the high-magnitude of the direct component in the $P_{dir} = 0, 1$, both delay-power spectra in Fig. J.3 show similar behaviour: the tails of the delay-power spectra in exhibit an exponential decay in both cases. This exponentially decaying power, which is not obtained by ad-hoc restrictions on the model parameters, is a result of recursive scattering in the graph.

To investigate the finer structure of the impulse response, it is necessary to have a better resolution in the delay domain. Therefore, we report in Fig. J.4 the absolute value of an impulse respons obtained with $P_{dir} = 1$ using the parameter settings given in Table J.1, but with the frequency range extended such that $f_{max} = 10\,\mathrm{GHz}$. The impulse response in this case exhibits a specular-to-diffuse transition, i.e. the early part of the profile, dominated by specular contributions, is preceded by a diffuse tail. This shows that the model is able to jointly treat the specular and diffuse components of the impulse response.

J.5   Conclusions

A propagation model based on a stochastic propagation graph was proposed. The propagation model proposed [1] was extended to account for multi-
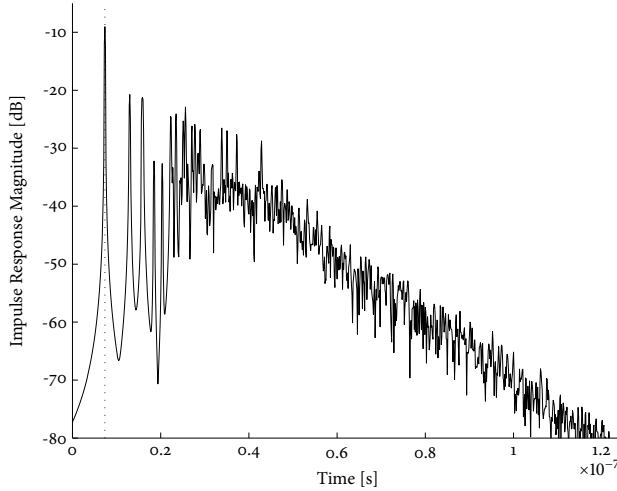
Fig. J.4: Impulse response magnitude obtained from the model with $P_{dir} = 1$. The parameter setting is as listed in Table J.1, but f_{max} has been set to 10 GHz.

input multi-output systems. Moreover, a closed form expression for the input-output relation was obtained.

A propagation graph is defined by a set of vertices (transmitters, receivers, and scatterers) and a set of edges (visibility between vertices). These parameters can be drawn randomly according to some joint probability density function.

Based on measurement results conventional models implement an exponentially decaying absolute impulse response and delay-power spectrum by various assumptions. These approaches, however, do not reflect the underlying physical mechanisms that lead to this decaying behaviour. It was shown by Monte Carlo simulations that assuming an inverse squared distance power decay, the proposed model yields the often observed exponentially decaying absolute impulse response and delay-power spectrum. This effect stems from the structure of the propagation graph and is not obtained by introducing any artificial assumptions.

The realisations of the impulse response obtained from the proposed model also exhibit a transition from specular contributions for low delays to a diffuse part at long delays as observed in measurements. The model can be easily extended to include dispersion in directions of departure and arrival.

References

[1] T. Pedersen and B. H. Fleury, "A realistic radio channel model based on stochastic propagation graphs," *Proceedings 5th MATHMOD Vienna – 5th Vienna Symposium on Mathematical Modelling*, vol. 1,2, p. 324, Feb. 2006, iSBN 3–901608–30–3.

[2] A. A. M. Saleh and R. A. Valenzuela, "A statistical model for indoor multipath propagation channel," *IEEE J. Sel. Areas Commun.*, vol. SAC-5, no. 2, pp. 128–137, Feb. 1987.

[3] Q. H. Spencer, B. Jeffs, M. Jensen, and A. Swindlehurst, "Modeling the statistical time and angle of arrival characteristics of an indoor multipath channel," *IEEE J. Sel. Areas Commun.*, vol. 18, no. 3, pp. 347–360, 2000.

[4] J. Laurila, A. F. Molisch, and E. Bonek, "Influence of the scatterer distribution on power delay profiles and azimuthal power spectra of mobile radio channels," *Proceedings of the IEEE 5th Int. Symposium on Spread Spectrum Techniques and Applications*, vol. 1, pp. 267–271, 1998.

[5] M. Franceschetti, "Stochastic rays pulse propagation," *IEEE Trans. Antennas Propag.*, vol. 52, no. 10, pp. 2742–2752, Oct. 2004.

[6] J. Kunisch and J. Pamp, "Measurement results and modeling aspects for the UWB radio channel," in *Ultra Wideband Systems and Technologies, 2002. Digest of Papers. 2002 IEEE Conf. on*, May 2002, pp. 19–24.

[7] H. Kuttruff, *Room Acoustics*.   London: Taylor & Francis, 2000.

[8] J. B. Andersen, J. Ødum Nielsen, G. Bauch, and M. Herdin, "The large office environment-measurement and modeling of the wideband radio channel," in *The 17th Annual IEEE Int. Symposium on Personal Indoor and Mobile Radio Commun.*, 2006.

[9] R. Gerlach and V. Mellert, "Der Nachhallvorgang als Morkoffsche Kette Theorie un erste experimentelle überpruüfung," *Acustica*, vol. 32, no. 4, pp. 211–227, Apr. 1975.

[10] R. Diestel, *Graph Theory*.   Springer-Verlag, 2000. [Online]. Available: http://www.math.uni-hamburg.de/home/diestel/books/graph.theory/

[11] E. Bonek, M. Herdin, Werner, and H. Özcelik, "MIMO — study propagation first!" in *Proceedings of the 3rd IEEE Int. Symposium on Signal Processing and Information Technology, ISSPIT 2003*, Dec. 2003, pp. 150–153.

[12] G. Strang, *Introduction to Linear Algebra*, 3rd ed.   Wellesley-Cambridge Press, 2003.